SOURCE AND FLUX OF METHANE RELEASED FROM CORPUS CHRISTI COASTAL AREA

A Dissertation

by

HAO YU

BS, Ocean University of China, China, 2000
MS, East China Normal University, China, 2007

Submitted in Partial Fulfillment of the Requirements for the Degree of

DOCTOR OF PHILOSOPHY

in

COASTAL AND MARINE SYSTEM SCIENCE

Texas A&M University-Corpus Christi
Corpus Christi, Texas

May 2022

May 2022

SOURCE AND FLUX OF METHANE RELEASED FROM CORPUS CHRISTI COASTAL AREA

A Dissertation

by

HAO YU

This dissertation meets the standards for scope and quality of
Texas A&M University-Corpus Christi and is hereby approved.

Richard Coffin, PhD
Chair

James Gibeaut, PhD
Committee Member

Ahmed Mahdy, PhD
Committee Member

Joseph David Felix, PhD
Committee Member

Alexandra Theodossiou, PhD
Graduate Faculty Representative

May 2022

ABSTRACT

Methane (CH_4) is the second most abundant greenhouse gas after carbon dioxide (CO_2), with an atmospheric warming potential of approximately 28-34 times and 84-86 times that of CO_2 over 100 years and 20 years, respectively (IPCC 2014). Coastal areas, particularly vegetated coastal ecosystems, including seagrass meadows, salt marshes, and mangroves, referred to as major reservoirs of blue carbon, have a high potential for the emission of CH_4 and other greenhouse gases to the atmosphere due to their high capability of carbon storage. Hence, the effect of coastal areas on global warming is based on the balance between carbon deposition and greenhouse gas emissions. Located at the interface of land and ocean, coastal areas are more vulnerable to the consequences of human activities and climate change, e.g., global warming, eutrophication, sea-level rise, and hypoxia, which could influence carbon sequestration and emissions of greenhouse gases, including CH_4, as feedback.

In this project, we determined the sources and fluxes of CH_4 released from the Corpus Christi coastal area to the atmosphere, explored the mechanisms influencing CH_4 emissions, and estimated the contributions of natural processes and anthropogenic activities to the local atmospheric CH_4 budget. Water and air samples were collected from Corpus Christi Bay and Nueces Bay, Upper Laguna Madre, and Aransas Bay from June 2018 to May 2021 to determine dissolved CH_4 concentrations and CH_4 fluxes at the sea-air interface. We also measured CH_4 fluxes at the sediment-water interface using the porewater CH_4 profile and incubation experiments. Half-year continuous atmospheric CH_4 monitoring was performed at Ingleside, Texas, in 2021 to determine the impact of anthropogenic CH_4 emissions on the residential

community. We also applied aircraft observations over the Ingleside industrial area in August 2021 to measure industrial emissions of CH_4.

We observed highly spatial and temporal variations in CH_4 emissions from these estuaries. The annual sea-air CH_4 flux was largest at Upper Laguna Madre and lowest at Aransas Bay. Such discrepancies could be attributed to the distribution of different environmental characteristics, i.e., seagrass, mangroves, channels, and open bays in each estuary. Tidal processes, amplitude (spring and neap), and topographic characteristics are crucial factors controlling CH_4 cycling in mangrove estuaries. Dissolved CH_4 concentrations in creeks were higher during ebbs due to the export of CH_4 from inside mangroves and porewater tidal pumping. During floods, CH_4 concentrations in water were dependent on the balance between CH_4 input from sediment and bay water dilution. Elevated CH_4 concentrations in spring tides compared with neap tides could be attributed to additional CH_4 emissions from upper intertidal sediment. The annual CH_4 emissions offset approximately 0.17% of local organic carbon deposits, indicating that these estuarine mangrove creeks are a weak CH_4 source.

In seagrass meadows, both diurnal and long-term variations showed a tight relationship between CH_4 concentration and dissolved oxygen, dissolved inorganic carbon and pH, which was driven by photosynthesis and respiration of the seagrass ecosystem. Photosynthetic oxygen transported by seagrass to sediment played a significant role in reducing CH_4 production and transport. Seasonal variations in CH_4 concentrations in seagrass meadows coincided with seagrass growth patterns, indicating a possible plant mediation of CH_4 emissions from sediment to water. The CH_4 emissions were estimated to offset 1.4%~2.2% of the blue carbon deposited in local seagrass meadows. This study reported the largest CH_4 emissions from global seagrass meadows to date. In comparison with mangrove creeks, seagrass meadows were a more significant CH_4

source. Further analyses showed that tidal processes could largely decrease CH_4 emissions, by exporting CH_4 from mangroves to open bays during ebbs and diluting CH_4 concentrations by bay water during floods. It implied a strategy of applying tidal processes in coastal wetland restoration.

Extreme weather was found to enhance CH_4 emissions in these coastal areas. Higher CH_4 concentrations were observed after the extreme cold event in February 2021, which was related to more organic carbon deposits induced by the high mortality of mangrove forests during the extremely cold days. The larger riverine discharge in November 2018 caused by heavy precipitation delivered more CH_4 from freshwater to coastal water, temporarily enhancing CH_4 concentrations and sea-air CH_4 flux in the Nueces Bay.

Daily CH_4 flux was highest in the channel at Upper Laguna Madre, suggesting that the disturbance of vegetated sediment could severely enhance CH_4 emissions in comparison with less vegetated sediment. In addition, maritime transportation and gas pipeline leakage are direct anthropogenic CH_4 sources in these estuaries, which have been widely overlooked. The long-term monitoring at a fixed station and aircraft observations at Ingleside estimated that one third of the CH_4 input to the residential community was related to fugitive emissions during crude oil loading and offloading operations. At least 11% of CH_4 fluxes corresponded to emissions from Ingleside industrial areas, much larger than the emissions reported to EPA in previous years. The overall anthropogenic emissions, including from large facilities in industrial areas and fugitive sources during maritime operations and from sediment disturbance, have been largely underestimated.

The estimated CH_4 budget in Corpus Christi coastal area was at least 6.3×10^9g/yr, among which 90% was from anthropogenic sources and 10% from natural sources. It suggested that anthropogenic emissions contributed the majority to local atmospheric CH_4 levels.

DEDICATION

This dissertation is dedicated to Yong and Ruiqi.

ACKNOWLEDGEMENTS

I'm extremely grateful to my advisor, Dr. Richard Coffin. Without his support, I would not have completed this dissertation research. I was so lucky to join Dr. Coffin's group four and a half years ago. Not only helped me out of difficulty, but Dr. Coffin also gave me excellent graduate training in the following years, which is invaluable for my professional development. He always encouraged me to do my independent research following my interests and gave me his strong support and instructions. Besides acquiring professional knowledge and skills from him, I was always inspired by his enthusiasm for science and his generosity.

I would like to express my deepest appreciation to my committee members, Dr. Ahmed Mahdy, Dr. James Gibeaut, and Dr. Joseph Felix for the support and guidance on my dissertation research all along. Lots of thanks for Dr. Mahdy's support on the unmanned aircraft observation, which broaden my experiences in a new research field. Many thanks to Dr. Gibeaut for his valuable advice on data collection and analyses. Especially thank Dr. Felix's recommendation for me to set up a long-term observation at the Ingleside community, which let me acquire valuable data about the local methane budget for this research as well as future research opportunities.

I would also like to extend my deepest gratitude to Mr. Michael Cancienne for his generous assistance in obtaining aircraft observation data last summer. The flight experience for me was incredible, and the data were invaluable.

I am grateful to Dr. Jessica Labonte at TAMUG for teaching proposal writing and editing my first graduate student grant proposal.

Many thanks to Dr. Wetz Michael, Dr. Simon Geist, and their groups, Ms. Natasha Breaux, Ms. Elani Morgan, and Ms. Polly Hajovsky for helping in fieldwork. Many thanks to Mr. Kenneth

Hayes for sharing YSI data. Lots of thanks to Dr. Xinping Hu, and his group, Mr. Cory Staryk, Dr. Hongjie Wang and Dr. Hongming Yao for helping in lab work. I also appreciate my colleagues, Ms. Hannah Organ and Mr. Derry Xu for helping with fieldwork.

I wish to thank Ms. Alessandra Garcia and the staff in PENS, for making my study enjoyable and providing strong assistance in lab maintenance.

I very much appreciate Dr. Xinping Hu, Dr. Dorina Murgulet, and CMSS committees for providing CMSS research assistantships. Many thanks to Dr. Jennifer Smith-Engle, Dr. Jeffery Spirko, and Ms. Galina Reid for helping in teaching assistantships.

Many thanks to all my friends who are near or far from me for their help and encouragement, for bringing me many happy times. These friendships have made me no longer lonely and become braver, and they are priceless treasures in my life.

I sincerely appreciate the financial support from the Texas Sea Grant Grants-in-Aid of Graduate Research Program, Texas A&M University-Corpus Christi Texas Comprehensive Research Funds, and Geological Society of America Graduate Student Grants, as well as NSF MRI-Development of Integrated Gas Monitoring UAS.

Final but not least, I would express my deep gratitude to my family, my parents, my husband, my daughter, my younger sister, and my parents-in-law, for their support, care, and love for me, which are the warmest company in my Doctoral journey and life journey.

TABLE OF CONTENTS

Page

LIST OF FIGURES

Page

LIST OF TABLES

Page

CHAPTER I: INTRODUCTION

1.1 Global methane budget and climate change

Methane (CH_4) is the second most abundant greenhouse gas after carbon dioxide (CO_2), with an atmospheric warming potential approximately 28-34 times and 84-86 times that of CO_2 over 100 years and 20 years, respectively (IPCC 2014). The Paris Agreement effective in 2016 calls for reducing CH_4 emissions to realize the goal of limiting global warming to 1.5°C compared to preindustrial levels (UNFCCC 2015). In addition to its effect on climate change, CH_4 is a precursor of ozone in the lower troposphere, which can influence human health (Fiore et al. 2008). On the other hand, CH_4 is also a primary component in natural gas and a significant component of other fossil fuel products, which can serve as an efficient and economic energy source. In particular, shale gas, primarily composed of CH_4, occupies a significant proportion in the energy market and is becoming a critical part of future energy. Global production of shale gas increased from 31 billion m^3 per year in 2005 to 435 billion m^3 per year in 2015, accounting for 63 percent of the worldwide increase in all natural gas production (Howarth 2019). According to the US Department of Energy, CH_4 use will reach 1,500 billion m^3 per year by 2040. As we enjoy the convenience brought by CH_4 as an important energy source, we have to consider potential risks in global and regional climate change caused by the emission of CH_4 to the atmosphere.

1.1.1 Variations in atmospheric methane and explanations

Since the industrial revolution, the CH_4 concentration in the atmosphere has increased from ~ 790 ppb to over 1800 ppb. Observations of atmospheric CH_4 since 1983 show that global CH_4 levels increased from 1983 to 1999, reached a plateau from 1999 to 2006, and then amplified again after 2007 to hit a new high (Lindsey and Scott 2017; Nisbet et al. 2014; Nisbet et al. 2019). In particular, the annual rate of increase of atmospheric CH_4 (> 5 ppb/year) from 2014 to 2017 was

much larger than those in previous decades (Nisbet et al. 2019). The highest annual CH_4 growth since 1983 occurred in 2020, which is up to 15.1 ppb (Dlugokencky 2021). The emission of CH_4 from the fossil fuel industry was explained as the primary reason leading to a rise in the CH_4 concentration in air before 1999 (Lindsey and Scott 2017). However, corresponding to the growth rate of CH_4 concentrations since 2007, stable carbon isotopic ratios of CH_4 continued to decrease, from approximately -47.0‰ to -47.5‰ from 2005 to 2021 (Nisbet et al. 2019; Schwietzke et al. 2016; Tollefson 2022), indicating that more CH_4 has been released from microbial sources in recent years (Nisbet et al. 2016; Schaefer et al. 2016). Nisbet et al., 2016 suggested that it was increased tropical wetland and tropical agricultural emissions causing the post-2006 atmospheric CH_4 elevation (Nisbet et al. 2016). In contrast, Schaefer, et al., 2016 proposed that more CH_4 emissions came from agriculture rather than wetlands (Schaefer et al. 2016).

Although variation in the stable carbon isotopic signature of atmospheric CH_4 did not indicate an increase in fossil fuel sources, considering that fossil fuel has a broad range of $\delta^{13}C$-CH_4 (-47‰ to -53‰), the contribution from fossil fuel needs more evaluation (Nisbet et al. 2019). Schwietzke, et al., 2016 applied both box model and stable isotopic analyses to upward CH_4 emissions from fossil fuel industries up to 150~200 Tg/yr (Schwietzke et al. 2016). A report compiled by the National Academies of Sciences in 2018 estimated that 145±23 Tg CH_4/yr was emitted from global fossil fuel production and usage from 2003 to 2012 (National Academies of Sciences 2018). A later study increased this value up to 194±34 Tg CH_4/yr, which accounts for nearly half of anthropogenic emissions (Hmiel et al. 2020). Worden et al. (2017) explained that the decrease in biomass burning CH_4 emissions could reconcile the increase in emissions from fossil fuels (Worden et al. 2017). Howarth et al. (2019) proposed that emissions from shale gas production in North America were an essential contribution to the increased CH_4 emissions

globally. Milkov et al. (2020) disputed this viewpoint using $\delta^{13}C$ data of CH_4 from shale gas formations worldwide.

Alternatively, the decrease in CH_4 sinks, e.g., hydroxyl radicals, could also explain the variation in CH_4 concentrations in the atmosphere (Rigby et al. 2017; Turner et al. 2017). Moreover, another CH_4 sink, soil CH_4 uptake, also decreased in forests. The decline in CH_4 uptake in global forest soils reached 77% from 1988 to 2015 (Ni and Groffman 2018).

Some recent studies have searched explanations from both sources and sinks of CH_4. Estimates acquired using the inverse model of Jackson et al., 2020 showed that both agriculture and waste and fossil fuel were likely the primary reasons, while the decrease in both atmospheric and soil sinks was too slow to explain CH_4 growth in the atmosphere (Jackson et al. 2020). However, Lan et al., 2021 found that neither the increase in fossil fuel CH_4 nor the decrease in hydroxyl radicals could explain the post-2006 CH_4 variation using a three-dimensional model of CH_4 flux and $\delta^{13}C$-CH_4. However, tropospheric chloride (Cl) as a sink of CH_4, as well as the application of a static versus a dynamic wetland map, could influence the estimates of CH_4 emissions from fossil fuel (Lan et al. 2021a).

1.1.2 Estimation of the global methane budget

A critical reason for the difficulties in discovering the mechanisms that lead to the variations in CH_4 is the significant uncertainties in assessing the global CH_4 budgets (Saunois et al. 2016; Saunois et al. 2020). Generally, there are still substantial discrepancies in CH_4 emission fluxes between the top-down (observations of atmospheric flux) and bottom-up (measurements of individual inventory) approaches at local, national and global scales because of the limitations of these two methods (National Academies of Sciences 2018).

The most recently updated global CH_4 budget showed that the global CH_4 emissions from 2008 to 2017 were estimated to be 576 $TgCH_4$/yr (550~594 $TgCH_4$/yr) using the atmospheric inversion method, which is 29 $TgCH_4$/yr larger than a previous estimate for 2000-2009 (Saunois et al. 2020). This updated budget improved the partition of some sources, e.g., wetlands and other inland waters, and re-estimated the atmospheric lifetime of CH_4. However, it only reduced the overall discrepancy between bottom-up and top-down estimates by 5% in comparison with the results four years ago (Saunois et al. 2020). The CH_4 emission acquired using bottom-up methods averaged 737 $TgCH_4$/yr (594~881 $TgCH_4$/yr), which was 30% larger than the outcomes obtained by top-down inversion (Saunois et al. 2020). Sources with higher estimates from bottom-up measurements primarily included natural wetlands, other inland water systems and geological sources, and the higher estimation was probably caused by overestimation of individual emissions (Saunois et al. 2016; Saunois et al. 2020). A review of four decades of CH_4 measurements published in September 2021 further pointed out that large uncertainties in the global CH_4 budget still remain, particularly in sink processes and wetland emissions, and the exact causes of the accelerating increase in atmospheric CH_4 since 2007 are not yet clear (Lan et al. 2021b).

On the other hand, although the uncertainties in global estimates of the anthropogenic CH_4 budget were relatively lower than those in natural sources, local discrepancies could also not be negligible. Aircraft observations of CH_4 emitted from landfills in the Baltimore-Washington area showed that emissions were 9 times larger than the landfill inventory reported to the Environmental Protection Agency (EPA) (Ren et al. 2018). Approximately 60% of global atmospheric CH_4 comes from anthropogenic origins (e.g., agriculture, petroleum and natural gas industry, waste disposal) (National Academies of Sciences 2018). Compared to natural sources of CH_4, anthropogenic CH_4 emissions have great potential to mitigate anthropogenic climate forcing

by improving production efficiency. For instance, although CH_4 emissions from fossil fuel industries increased, CH_4 emissions per unit of production declined from 8% to 2% in the past decade (Schwietzke et al. 2016). Hence, the accurate quantification of anthropogenic CH_4 emissions is more meaningful to global and regional strategies of reducing greenhouse gas emissions.

1.2 Methane emissions from global coastal areas

1.2.1 Methane offset to coastal blue carbon reservoirs

Coastal areas, particularly vegetated coastal ecosystems, including seagrass meadows, salt marshes, and mangroves, are referred to as major reservoirs of blue carbon, indicating a high capability of carbon storage (Macreadie et al. 2019). On the other hand, the large amount of deposited organic carbon provides potential for the emission of CH_4 and carbon dioxide, which can be returned to the atmosphere by the metabolization of organic matter (Macreadie et al. 2019; Rosentreter et al. 2018b). Weber et al., 2019 proposed that CH_4 emissions from shallow coastal water constituted the majority of the global marine CH_4 flux (Weber et al. 2019). Saunois et al., 2020 reported an average of 6 Tg CH_4/yr (4-10 Tg CH_4/yr) from coastal and open oceans, including 4~5 Tg CH_4/yr from estuaries (Saunois et al. 2020). Hence, the effect of coastal areas on global warming is based on the balance between carbon deposition and greenhouse gas emissions (Rosentreter et al. 2021a). Rosentreter et al., 2018 estimated that the offset of CH_4 in global mangrove sediment could reach 18% to 22% (Rosentreter et al. 2018b). Al-Haj and Fulweiler, 2020 assessed that global mangroves, salt marshes and seagrasses with an annual mean CH_4 flux of 0.23~0.25 Tmol/yr, 0.071 Tmol/yr, and 0.0311~0.065 Tmol/yr, could offset ~9%, ~7% and <0.5% carbon buried in mangroves, salt marshes and seagrasses, respectively (Al-Haj and Fulweiler 2020). Considering the corresponding CO_2 sequestered in sediment, CH_4 emissions from

mangroves and salt marshes could fully offset (>100%) their burial of ~160 Tg CO_2/yr (Al-Haj and Fulweiler 2020). However, Taillardat et al., 2020 demonstrated a cooling effect of most coastal wetlands on the global climate to date (Taillardat et al. 2020). Research on CO_2 offset by the enhancement of CH_4 and N_2O after the restoration of seagrass meadows in Virginia, U.S. showed that despite CH_4 and N_2O emissions increasing after restoration, the restored seagrass meadow could remove far more CO_2 from the atmosphere than the equivalent CO_2 amount of CH_4 and N_2O emissions (Oreska et al. 2020). The debate about the offset effect of CH_4 is largely due to the high spatial and temporal variability of CH_4 fluxes, paucity of data and limitations in measurement approaches (Rosentreter et al. 2021a).

Coastal ecosystems are vulnerable to human activities and climate change, which would bring more risk in releasing greenhouse gases, including CH_4. Degraded ecosystems have been reported to release more CH_4 than their undegraded status (Macreadie et al. 2019). Deforestation of mangroves by shrimp cultivation could increase greenhouse gas emissions (Ahmed and Thompson 2019; Kauffman et al. 2017; Kauffman et al. 2018). Loss of seagrass caused by shading and grazing could also enhance CH_4 growth and emissions from sediment (Lyimo et al. 2018). More CH_4 emitted from dead mangrove stems than from living stems was observed along the Gulf of Carpentaria in Australia (Jeffrey et al. 2019). Both incubation and mesocosm experiments showed that warming could enhance CH_4 release from seagrass sediment (Burkholz et al. 2020; George et al. 2020).

1.2.2 Anthropogenic methane emissions in coastal areas

Anthropogenic CH_4 (e.g., agriculture, petroleum and natural gas industry, waste disposal) has been estimated to be approximately 60% of the global budget (National Academies of Sciences 2018). Although many coastal areas in the world are densely populated, only a few studies about

anthropogenic CH_4 emissions from coastal areas have been reported (Guha et al. 2020; Plant et al. 2019). Take the fossil fuel industry as an example since it is one of the major anthropogenic sources of atmospheric CH_4. Extensive investigations have been performed in production sites and distribution systems to evaluate their CH_4 emissions (Allen et al. 2013; Hugenholtz et al. 2021; Li et al. 2020b; Lowry et al. 2020; Ren et al. 2019; Rodriguez and Philp 2010). However, recent studies have found fugitive emissions from urban end use and fossil fuel product industries to be underestimated and poorly characterized (Guha et al. 2020; Plant et al. 2019; Plant et al. 2022; Sargent et al. 2021). Aircraft observations over San Francisco found that CH_4 emissions from five refineries were 4 to 23 times larger than the reported emissions (Guha et al. 2020). Satellite-based measurements over eight United States east coast cities found more urban emissions than the EPA estimate (Plant et al. 2022). Anthropogenic emissions in coastal urban areas not only originate from landfills, vessel exhaust, and the usage of natural gas but also come from coastal-specific pollution, such as oil spilling, maritime exhaust, dredging and filling.

Due to the convenience of maritime transportation, many fossil fuel-related industries have been built in coastal cities, which brings more potential for elevated CH_4 emissions. All these anthropogenic CH_4 emissions could directly enhance the local atmospheric CH_4 level, influencing the local climate. Hence, it is necessary to have a thorough understanding of the anthropogenic CH_4 emissions in coastal areas.

1.2.3 Study methods and limitations

As described in the previous section (1.1.2), the study approaches for CH_4 emissions can be briefly categorized into two types: bottom-up and top-down. Based on spatial scales, CH_4 measurements can be classified from large scales (e.g., global, continental, and regional) to small scales (e.g., a source region, individual source). Measurements on temporal scales include long-

term (e.g., monthly, annual, multiannual) and short-term (e.g., hourly, daily) observations. Bottom-up measurement intends to determine CH_4 emissions at the water-atmosphere or land-atmosphere interfaces or from specific sources and regions (e.g., landfills, facilities, petroleum fields, wetlands, etc.). It primarily focuses on CH_4 emissions at small and intermediate scales and can be short-term and long-term. Top-down observation applies tools (e.g., tower, aircraft, satellite) that perform at higher altitudes (several meters to kilometers) to monitor CH_4 emissions from a larger scale (e.g., regional, continental, and global). This type of measurement is often carried out over a long period of time.

In coastal areas, naturally original CH_4 can be released from sediments, the water column, plants, and vegetated/unvegetated soils to the atmosphere. A variety of methods are utilized based on different CH_4 sources and objectives. Similar to terrestrial observations, satellites, aircraft, and towers are also suitable for measurements on a large spatial scale in coastal areas. Important challenges include disturbance signals caused by marine environments for satellites, the availability of launch/land off sites for aircraft, and suitable sites for the building and maintenance of towers. Different from observations on land, a more complicated environment in coastal areas makes CH_4 cycling more complex, bringing more difficulties in designing measurement strategies, particularly when measuring CH_4 emissions related to a short-term process (hourly/diurnal). The selected methods should be sufficiently sensitive to short-term variations.

Based on my dissertation research, this section will primarily introduce methods used in measuring CH_4 emissions from water to the atmosphere and large-scale observations using aircraft and unmanned aircraft. Figure 1.1 briefly illustrates the approaches applied in this study, except for satellites (marked by dashed lines), at spatial and temporal scales using bottom-up and top-down methods.

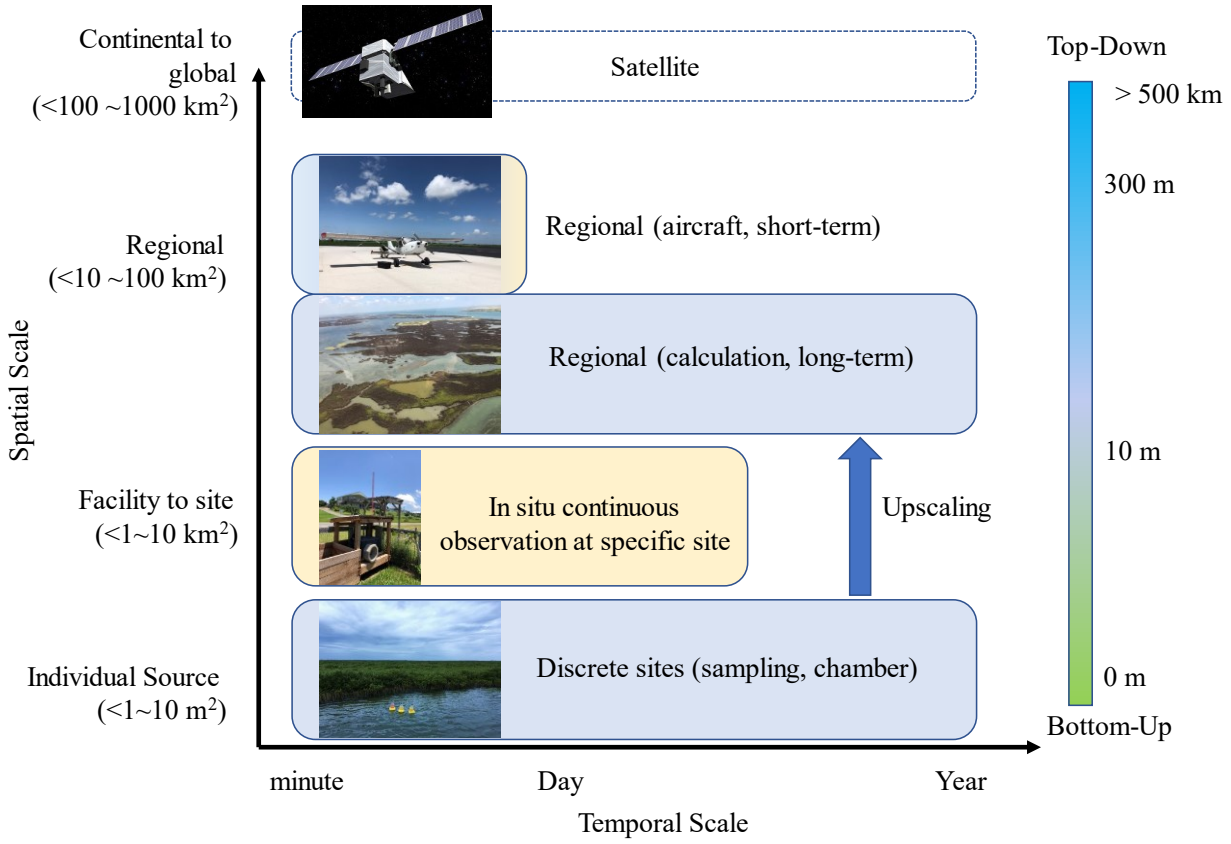

Figure 1.1 Study approaches (modified based on (National Academies of Sciences 2018)).

1.2.3.1 Water-air (sea-air) methane emissions

There are three widely used approaches in measuring CH_4 flux at the water-air interface: the gas transfer model, floating chamber technique and eddy covariance. Gas transfer models are empirical equations developed to calculate diffusive CH_4 flux at the water-air interface based on natural tracers (e.g., oxygen, ^{14}C) or artificially distributed tracers (SF_6). The floating chamber represents the smallest scale (~ $1m^2$) measurement with the advantages of a simple principle, easy operation, high sensitivity, and low cost. Eddy covariance is suitable for large scales (km^2) of measurement, preferred by meteorologists.

1.2.3.1.1 Gas transfer model

Diffusive CH_4 flux at the water-air interface is generally estimated using a bulk flux equation (Wanninkhof 1992; Wanninkhof 2014).

$$F = k_v \cdot (C_w - C_a) \quad (1)$$

where F is the flux of gas to the atmosphere ($mmol \cdot m^{-2} \cdot d^{-1}$ or $\mu mol \cdot m^{-2} \cdot h^{-1}$); C_w represents the measured concentration of dissolved CH_4 in water ($nmol \cdot L^{-1}$); C_{eq} is the concentration of CH_4 in equilibrium with the atmosphere at in situ temperature ($nmol \cdot L^{-1}$), calculated for each sample from the temperature- and salinity-dependent equilibrium relationship (Wiesenburg and Guinasso 1979); and k_v is the gas transfer velocity ($m \cdot d^{-1}$ or $cm \cdot h^{-1}$). k_v is normalized to Schmidt number (Sc) as follows (k, k_{660} or k_{600}):

Seawater: $k_{660} = k_v \cdot (660/Sc)^n$

Freshwater: $k_{600} = k_v \cdot (600/Sc)^n$

where 660 is the Sc of CO_2 in seawater at 20°C, 600 is the Sc of CO_2 in freshwater at 20°C (Wanninkhof 1992), n is -0.5 for an interface with waves (Wanninkhof 1992), and Sc is defined as the kinematic viscosity of water divided by the diffusion coefficient of the gas, which is a function of temperature and salinity (Wanninkhof 1992).

Since the dissolved CH_4 concentration in the water and atmospheric CH_4 can be precisely measured, a large challenge in estimating the water-air (sea-air) CH_4 flux comes from calculating the gas transfer velocity normalized by Sc, k (k_{600} or k_{660}), since there is currently no universal applicable relationship between k and some easily measured environmental variables (Ho et al. 2014). Table 1.1 lists the most commonly used equations in calculating k for CH_4 flux in references. For open water where wind speed is the primary driver of gas exchange, empirical models built and developed by Wanninkhof in 1992 and 2014 based on bomb-$^{14}CO_2$ have been

widely used (Chuang et al. 2017; Fenwick and Tortell 2018; Kelley and Jeffrey 2002; Ye et al. 2016; Zang et al. 2020). The updated empirical equation in 2014 (W2014) is suitable for gas exchange at intermediate winds (3-15 m/s), which could cover most ocean water since 94% of the winds over the ocean are within this range (Wanninkhof 2014). That is, $k_{660} = 0.251\mu^2$ (μ: wind speed at 10-m height). Sc was also extended for application at temperatures from -2 to 40°C.

By comparison, the gas transfer velocity in coastal water can be affected by a variety of factors, including not only wind speed (Raymond and Cole 2001) but also turbulence caused by water currents (Borges et al. 2004; Jeffrey et al. 2018; O'Connor and Dobbins 1958), turbidity and estuarine surface area (Abril et al. 2009). The summary of studies from different estuaries (Table 1.1) showed that it is difficult to form a universal equation to estimate CH_4 emissions from coastal water due to the high spatial variability in gas transfer velocity. Even for the same estuary, there existed high temporal variation in the gas transfer velocity, and therefore, site-specific k has been recommended to be measured in highly dynamic areas, particularly mangrove estuaries (Rosentreter et al. 2017). However, it is not easy to do this in this way in consideration of the time and cost consumption. Some studies chose the equations that best fit their situations (Banerjee et al. 2018). Some research acquired the k value by averaging data obtained from different equations (Call et al. 2015; Call et al. 2019).

It should also be noted that most studies used the k values obtained from CO_2 exchange at the water-air interface combined with the Sc of CH_4 (Wanninkhof 2014) to calculate CH_4 flux (Barbosa et al. 2020; Myllykangas et al. 2020). Only a few studies calculated the gas exchange of CH_4 directly (Ho et al. 2016; McGinnis et al. 2015; Prairie and del Giorgio 2013; Rosentreter et al. 2017). In these studies, floating chambers and purposeful tracers (^3He and SF_6) were applied to determine the CH_4 flux from water and the atmosphere. At the same time, environmental

parameters such as wind speed, current velocity and water depth were measured, attempting to build the relationship with CH_4 flux. However, the equations based on different estuaries (e.g., microtidal vs. macrotidal estuaries and among different macrotidal estuaries) are different and cannot thoroughly explain the variation in CH_4 flux, probably due to high spatial and temporal heteroscedasticity of geophysical and biogeochemical characteristics in coastal areas. Moreover, empirical equations for predicting gas exchange during daytime and nighttime could be distinct (Van Dam et al. 2019). Trifunovic et al., 2020 also found that the gas transfer velocities of both CH_4 and CO_2 in different tidal stages (high tide, low tide, ebb and flood) were different in a microtidal estuary (Trifunovic et al. 2020).

Different from CO_2, except for Fickian diffusion, CH_4 exchange at the sea-air interface can also occur in the form of microbubbles related to the degree of CH_4 supersaturation (Prairie and del Giorgio 2013; Rosentreter et al. 2017). Rosentreter et al., 2017 found that microbubble flux could contribute up to 73% of the total CH_4 flux in mangrove-dominated estuaries in Queensland, Australia and Florida, USA. Hence, in estuaries with high CH_4 supersaturation or when only CH_4 concentration data are available, a microbubble flux was suggested to add to the diffusive flux as follows (Rosentreter et al. 2017).

$$F_{MB} = -1.568 + 0.0017CH_{4sat} + 0.953v + 0.011T \ (R^2=0.53)$$

In three river-dominated mangrove-lined estuaries in Australia, another equation was applied to estimate microbubble flux (Rosentreter et al. 2018a):

$$F_{MB} = -1.166 + 0.0028 \times Sat_{CH4} + 0.042 \times Temp$$

where F_{MB} is the CH_4 flux of the microbubble; CH_{4sat} is the saturation of CH_4 between water and air; v is the current velocity (cm/s); and T is the temperature (°C). Alternatively, the gas transfer velocity of the microbubble, k_{MB}, is 2.1 m/d (Prairie and del Giorgio 2013).

Table 1.1 Methods of gas transfer velocity (k_{660} or k_{600})

Abbr.	Study location	Method	Equation	Suggested application	Reference
O1958	river	oxygen balance	$k_{600} = 1.539 v^{0.5} h^{-0.5}$	turbulent flow	(O'Connor and Dobbins 1958)
S1983	wetland pond	chamber	$k_{600,CH4} = 1.70$ (μ = 0 m/s) $k_{600,CH4} = 1.1 + 1.2\mu^{1.96}$ (μ = 1.4 to 3.5 m/s)	wind speed <3.5 m/s	(Sebacher et al. 1983)
W1992	open ocean	bomb-$^{14}CO_2$	$k_{660} = 0.31\mu^2$	wind speed 5-7 m/s water temperature 0~30°C	(Wanninkhof 1992)
R2001	rivers and estuaries	integration using previous data	$k_{600} = 1.91e^{0.35\mu}$ (all data, R^2=0.53) $k_{600} = 2.06e^{0.37\mu}$ (dome data, R^2=0.53) $k_{600} = 1.58e^{0.30\mu}$ (nondome data, R^2=0.46)	wind speed < 7 m/s (Jiang et al. 2008)	(Raymond and Cole 2001)
B2004	Scheldt estuary in European (macrotidal)	floating chamber	$k_{600} = 1.0 + 1.719 v^{0.5} h^{-0.5} + 2.58\mu$ $k_{600} = 4.045 + 2.58\mu$ $k_{600} = -3.065 + 7.302\mu^{0.646}$ $k_{600} = 5.141\mu^{0.758}$		(Borges et al. 2004)
J2008	estuaries at Georgia, US	integration using previous data	$k_{600} = 0.314\mu^2 - 0.436\mu + 3.990$	high wind speed	(Jiang et al. 2008)
W2014	open ocean	bomb-$^{14}CO_2$	$k_{660} = 0.251\mu^2$ (uncertainty: 20%)	wind speed 3-15 m/s water temperature -2~40°C	(Wanninkhof 2014)

M2015	Lake Stechlin, Germany (oligotrophic)	floating chamber	$k_{600,CH4} = 3.2K_{600,CO2} - 3.4$	presence of microbubbles	(McGinnis et al. 2015)
H2016	Shark River, mangrove tidal estuary, Florida, US	$^3He/SF_6$ dual tracers	$k_{600} = 0.77v^{0.5}h^{-0.5} + 0.266\mu^2$		(Ho et al. 2016)
R2017	mangrove estuaries (macrotidal) in Australia and Florida, US	floating chamber and $^3He/SF_6$ dual tracers	$k_{600,CH4} = -1.07 + 0.36v + 0.99u + 0.87h$ (R^2=0.57) $k_{600,CH4} = -0.77 + 0.45v + 0.92u$ (R^2=0.54) $k_{600,CH4} = 2.03 + 0.43v$ (R^2=0.48)	macrotidal mangrove estuary with high tidal amplitudes and strong water currents	(Rosentreter et al. 2017)
VD2019	New River estuary (microtidal), North Carolina, US	Eddy covariance and pCO_2 measurement	Day: $k_{600} = 2.3 + 1.9u$ (R^2=0.92) Night: $k_{600} = 18.5 - 5.3\mu + 0.64\mu^2$ (R^2=0.95) Combined: $k_{600} = 4.2 + 1.5u$ (R^2=0.78)	microtidal estuary, diel processes	(Van Dam et al. 2019)

μ: wind speed at 10 m height (m/s); ν: current velocity (cm/s); h: water depth (m)

1.2.3.1.2 Chamber technique

The floating chamber technique has been widely used to determine CH_4 emissions at the water-air interface due to its ease and simplicity in measuring a short-term change in gas fluxes (Raymond and Cole 2001; Silva et al. 2015). However, some problems may arise, including an increase in temperature and pressure in the chamber, introducing artificial gradients of gas concentration, perturbing turbulence in the air and the water-filled chamber spaces, reducing diffusive exchange, and suppressing advective exchange (Bahlmann et al. 2015). The influence of temperature, pressure and gas concentration gradient can be minimized in a short-term deployment (Rosentreter et al. 2017). Moreover, various designs of floating chambers were applied to minimize these problems. For example, insulation around chambers can decrease the thermal exchange and keep inside temperatures stable (Rosentreter et al. 2017). The chamber can be equipped with a fan inside the chamber to evenly disperse air circulation to diminish the possible gas gradient, mimic air turbulence outside the chamber, and supplement the absence of diffusive exchange caused by wind (Kankaala and Bergström 2004; Yang et al. 2021). In addition, the shape, height, volume and material of chambers, selection of surrounding floats, attachment of thermometer and pressure gauge are all possible considerations based on specific observation objectives (Bastviken et al. 2010; Jacotot et al. 2018; Lorke et al. 2015; Rosentreter et al. 2017).

In addition, the floating chamber technique has been primarily criticized because of its disturbance of the turbulence at the boundary layer of surface water (Raymond and Cole 2001). There are three opinions about the disturbance of water turbulence. Lorke et al., 2015 found that floating chambers could overestimate fluxes of CH_4 and CO_2 because the chamber walls penetrating the water could enhance turbulence. Using drifting chambers rather than anchored chambers and/or applying a flexible plastic foil collar to seal the chamber and water surface to

avoid rigid chamber walls penetrating into the water could reduce such bias (Lorke et al. 2015). In addition to these suggestions, Rosentreter et al., 2017 also recommended designing a chamber with a large ratio of water surface area to chamber volume and a frame with minimal contact with the water surface (Rosentreter et al. 2017). Nevertheless, another study found that floating chambers could reduce turbulence, so they would underestimate the gas transfer velocity and fluxes from lakes (Davidson et al. 2018). The turbulence and wave height are key drivers of gas transfer velocity. Some researchers also found good agreement or no significant difference between floating chamber methods and other methods, e.g., dissipation methods, particularly in conditions with little wave breaking (Gålfalk et al. 2013; Tokoro et al. 2008).

In addition to diffusive gas flux, chambers can also catch bubbles. To distinguish two types of input, some floating chambers have been carefully designed. Bastviken et al., 2010 equipped chambers with a plastic shield under the water surface to prevent gas bubbles from entering the chambers (Bastviken et al. 2010). Schilder et al., 2016 modified the shield to be slightly concave so that the bubbles could be caught by the chambers to determine the bubble input of CH_4 (Schilder et al. 2016). Yang et al. covered or uncovered the opening of the chamber using a thin gauze (pore diameter 0.001 mm) to determine diffusive and bubble CH_4 input (Yang et al. 2021)

A significant linear increase in CH_4 concentrations (e.g., R^2>0.85) in floating chambers in a short time (45 or 60 minutes) is generally taken as the input from diffusive CH_4, while a dramatic increase is attributed to bubble CH_4 (Chuang et al. 2017; Deborde et al. 2010; Yang et al. 2021). However, Silva et al., 2015 tested the floating chamber technique at a tropical anaerobic pond and suggested that nonlinear regression models should be used when the correlation coefficient of the nonlinear model was larger than that of the linear model, and the percentage of the curve that could be accepted was 93.6% for CH_4 (Silva et al. 2015).

In comparison with static floating chambers, dynamic chambers can realize long-term observations. Dynamic chambers have been used in terrestrial ecosystems for a long time but have been introduced into aquatic gas emission studies only in the recent few decades (Bahlmann et al. 2015; Gao et al. 1997; Huang et al. 2019a; Yang et al. 2018). In dynamic chambers, air inside the chamber is pumped out at a predefined flow rate to an in situ continuous monitoring system. The flux in the chamber is calculated from the difference between the CH_4 concentrations inside the chamber and in ambient air (Gao et al. 1997). According to different objectives, dynamic chambers include floating dynamic chambers designed to measure water-air CH_4 flux as static floating chambers and benthic dynamic chambers for the measurement of CH_4 flux from sediment to air (Bahlmann et al. 2015; Huang et al. 2019a; Yang et al. 2018; Yang et al. 2017). Some dynamic chambers were designed to adjust different objectives by adjusting the float system to be floating or benthic (Yang et al. 2017). Different from static benthic chambers that are insensitive to hydrodynamic conditions, although dynamic benthic chambers were also inserted into surface sediment to separate the experimental sediment from the surroundings, some chambers were equipped with a U-tube at the bottom to ensure water exchange and pressure equilibrium between the chamber and the water body (Bahlmann et al. 2015).

1.2.3.2 Aircraft and unman aircraft observations

1.2.3.2.1 Aircraft campaigns

Aircraft observations have been performed to obtain large-scale data (regional and continental) quickly and efficiently. Generally, there are two kinds of aircraft observations: aircraft campaigns and cargo or commercial aircraft. Cargo and commercial aircraft are often used to observe CH_4 in the upper troposphere (e.g., over 4 km) by in situ measurement or flask collection (Umezawa et al. 2014; Wofsy 2011). These flights provide us with more detailed data about the

spatial and temporal variations in CH_4 mixing ratios in the atmosphere, efficiently connecting the ground measurements and satellite observations.

Aircraft campaigns are the most regular method. The most famous and longest duration is the Global Greenhouse Gas Reference Network (GGRN)'s aircraft program carried out by the National Oceanic and Atmospheric Administration/Earth System Research Laboratory Global Monitoring Division (NOAA/ESRL GMD) since 1992. This program uses aircraft to collect flask samples at different altitudes (up to 13279 m) over North America and analyzes the CO_2, CO, N_2O, CH_4, H_2, and other components as well as isotopes of CO_2 and CH_4 in the on-land labs (available at https://www.esrl.noaa.gov/gmd/ccgg/aircraft/index.html). It aims to acquire the seasonal and annual changes in these trace gas mixing ratios over the long term. Other campaigns were performed in a relatively short term, focusing on specific objectives. For example, the Atmospheric Carbon and Transport-America (ACT-America) campaign investigated CH_4 emissions from the south central United States using 5 flights in 2017 and found that the emissions from oil/gas sectors were 1.8±0.7 (2σ) times larger than EPA inventory estimates (Barkley et al. 2019). Flights over Baltimore-Washington in the winters of 2015 and 2016 also discovered that the mean winter CH_4 emission rates from these urban areas were larger than the average U.S. Inventory-based emission rate. Urban natural gas systems contribute approximately 40~60% of total CH_4 emissions (Ren et al. 2018).

The most extensive flight campaigns in wetland and coastal areas were performed in the Arctic, particularly on the North Slope of Alaska. The Carbon Arctic Rservoirs Vulnerability Experiment (CARVE) from 2012 to 2014 observed that CH_4 emissions for the northern slope of Alaska accounted for 24% of the total statewide flux (Chang et al. 2014; Miller et al. 2016). Airborne Measurements of Methane Emissions (AirMeth) campaigns in 2012-2013 measured CH_4

emissions from natural sources in this region (Hartmann et al. 2018). The Airborne Carbon Measurement (ACME-V) aircraft campaign across the North Slope of Alaska was the most detailed airborne survey of northern Alaska, carrying out 38 flights between late May and mid-Sept 2015. They estimated a CH_4 flux from the North Slope of Alaska of 0.64±0.13 Tg during June through August 2015, and the contribution of tundra in this region to the overall Alaskan CH_4 flux during the study period was ~27% (Tadić et al. 2021). Another flight campaign in the Arctic was the Arctic-Measurements, process studies and Modeling (MAMM) project, which determined CH_4 flux and stable isotopic signatures above wetland regions of northern Fennoscandia, Arctic, in 11 flights from 2012 to 2013 using a BAe 16 research aircraft (Fisher et al. 2017). In addition, over the Arctic, only a few campaigns were executed in wetland and coastal areas in the Amazon basin, Atlantic coasts, and Africa (Beck et al. 2012; Nisbet et al. 2022; Wolfe et al. 2018).

Some campaigns applied aircrafts to collect air samples with similar methods of GGRN, such as the flights at Western Siberia from 2005 to 2009 using NIES aircrafts and over Japan from 1988 to 2010 using Cessna 172 chartered aircrafts by Tokoku University (Umezawa et al. 2014; Umezawa et al. 2012). The more recent aircraft observations preferred to use in situ measurements, particularly cavity ring-down spectroscopic sensors from Picarro Inc. and LGR Inc. (Barkley et al. 2019; Chang et al. 2014; Li et al. 2019; Tadić et al. 2021; Wolfe et al. 2018; Yu et al. 2020). Although aircraft campaigns have been well developed and are being widely applied in greenhouse gas emission monitoring, large investments and multiple cooperation make them impractical for small projects.

1.2.3.2.2 Unmanned aircraft observations

In comparison with aircrafts, unmanned aircraft vehicle (UAV) observation is a more economical and convenient approach. In particular, the updated development of UAVs makes

them more promising for broader applications in monitoring air quality and greenhouse gases. The payloads used to measure atmospheric CH_4 on UAVs can be classified into three types: sampling facilities such as Tedlar bags (Brownlow et al. 2016; Greatwood et al. 2017; Thomas et al. 2015), in situ observations by remote sensors (e.g., LIDAR, nondispersive infrared sensor) (Clow and Smith 2016; Shah et al. 2019), and in situ Greenhouse Gas Analyzer (GGA) produced by LGR or Picarro (Berman et al. 2012; Golston et al. 2017; Wolf et al. 2017). The payload limitation of UVAs is a primary factor influencing UAV observations. The progress of portable GGA has made it meet the size, weight and power requirements of UAVs in the recent decade. The earlier trials of a NASA SIERRA UAV deployed by a GGA at Crow's Landing, California and Svalbard, Norway in 2009 proved the capabilities of the UAV-GGA system to work at low altitudes and in remote or dangerous conditions (Berman et al. 2012).

Aircraft measurements of the GGRN program from approximately 300 meters and most other aircraft observations from a few hundred meters focus on the atmospheric dynamics of CH_4, while UAVs have the advantage of studying CH_4 flux at the ecosystem-atmospheric interface. The flights of the hexacopter system at the ScaleX field campaign in Germany in 2015 and 2016 showed the profile of CH_4 at different altitudes at different times, indicating a substantial variation in lower height (Golston et al. 2017; Wolf et al. 2017). Moreover, the variations that occurred overnight reflected the influence of the natural boundary layer and the role of soil that transferred from the source to the sink of CH_4. Such variations indicate that the observation of CH_4 from the ground to a few hundred meters is valuable for the assessment of the CH_4 budget (Golston et al. 2017; Wolf et al. 2017). Other applications of UAVs also include point-, facility-scale or other small-scale sources of CH_4, such as landfills and leaks on pipelines (Allen et al. 2019; Gålfalk et al. 2021; Li et al. 2020a; Shah et al. 2019).

1.3 Methane emissions from coastal areas of the Gulf of Mexico

1.3.1 Atmospheric methane over the Corpus Christi coastal area

Aircraft flight samples collected over the Gulf of Mexico off the coast of Corpus Christi, Texas, showed that average CH_4 levels in this region were higher than the global average, and their annual variation trends were consistent with global observation results from 2013 to the end of 2017 (https://www.esrl.noaa.gov/gmd/ccgg/aircraft; Figure 1.2). This result agrees with the estimation from the global CH_4 budget that biogenic CH_4 from the tropics and subtropics is probably attributed to a rapid increase in atmospheric CH_4 (Nisbet et al. 2019). Hence, this project expects to obtain valuable clues in deciphering the secretion of the global CH_4 increase in recent years from the local CH_4 budget.

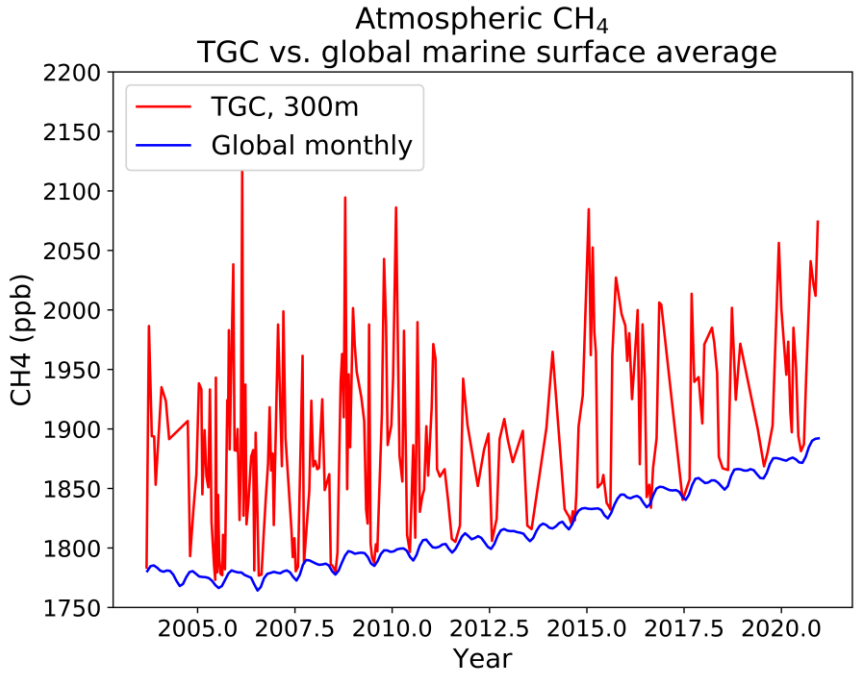

Figure 1.2 Atmospheric CH_4 concentration at 300 m altitude of TGC and average CH_4 concentration over the global marine surface.

Data available at https://www.esrl.noaa.gov/gmd/ccgg/aircraft.

1.3.2 Methane emissions from the Gulf of Mexico

1.3.2.1 Geological methane emissions from petroleum platforms and methane hydrate seeps

Offshore, sea-to-air exchange is one of the vital sources of atmospheric CH_4, where release from sediments or existing in the water column can enter the air through bubble rising or turbulent diffusion (Borges et al. 2016; Hu et al. 2012). Although CH_4 can be emitted from marine hydrate seeps and several hydrate seeps have been found on the seafloor of the northern Gulf of Mexico, most studies have discovered that CH_4 bubble plumes cannot reach the air-water interface. Instead, diffusive CH_4 in the water column was the primary contributor to atmospheric CH_4 because the CH_4 concentration in surface water was supersaturated with respect to atmospheric equilibrium. However, some researchers believe that diffusive CH_4 from hydrate seeps is a significant contributor to atmospheric CH_4 (Solomon et al. 2009), while some believe that this contribution is insignificant (Hu et al. 2012). The impact of the Deepwater Horizon oil spill on sea-air CH_4 flux was assessed to be minimal (i.e., <0.01% of the CH_4 emitted to the atmosphere) due to the consumption of CH_4 by methanotrophs in the water column (Kessler et al. 2011; King et al. 2015), which seemed to support the latter viewpoint.

1.3.2.2 Natural methane emissions from vegetated areas

The Gulf of Mexico coastal vegetated areas are an important blue carbon hot spot in North America, with mangrove carbon stocks dominating its south half, salt marsh occupying the northwestern coasts, and seagrass omnipresent (Thorhaug et al. 2019). Studies on CH_4 emissions from these vegetated areas focused on the north, east and south coasts of the Gulf. Early studies on the Florida coast found that the metabolic process of seagrass could influence the production of CH_4 in sediment (Oremland 1975; Oremland and Taylor 1977). A later study on CH_4 fluxes

from sediments of both live seagrass and dead seagrass in Florida Bay suspected the significance of plant mediation of CH_4 flux from seagrass (Barber and Carlson 1993). Mangrove creeks in southwestern Florida were found to be a minor CH_4 source (Cabezas et al. 2018), while mangrove swamps and Florida Bay and mangrove-dominated lagoons at Yucatán on the south coast of the Gulf were significant CH_4 sources (Barber et al. 1988; Chuang et al. 2017). The CH_4 fluxes from degraded mangrove forests at the Tampamachoco coastal lagoon, in the southwest of the Gulf, were up to 9-fold those of preserved mangroves (Romero-Uribe et al. 2021). There was a large spatial discrepancy in CH_4 emissions from coastal ecosystems along the Gulf of Mexico.

1.3.3 Preliminary study

Although the lagoonal estuaries around Corpus Christi, South Texas, are dominated by seagrass meadows and poleward migrating mangrove forests, to our knowledge, CH_4 emissions from this area have seldom been reported before this project. We also noticed anthropogenic emissions from industrial areas. Our preliminary investigations in the estuaries of Corpus Christi (Corpus Christi Bay, Nueces Bay, Aransas Bay and Upper Laguna Madre) in May and June 2018 showed that the sea-air CH_4 flux (mangrove: 0.012~0.10 mmol/m^2·d; seagrass: 0.068~0.31 mmol/m^2·d; channel: 0.004~0.85 mmol/m^2·d) was much higher than that in previous studies in the northern Gulf of Mexico (0.00419 ~ 0.086 mmol/m^2·d (Hu et al. 2012); 0.024×10^{-3} mmol/m^2·d (Yvon-Lewis et al. 2011)), which suggested a significant contribution of coastal areas to local and global atmospheric CH_4 levels. In comparison with CH_4 released from mangrove areas, channels and seagrass regions were more significant CH_4 sources. Such results were surprisingly different from previous studies that viewed mangroves as a primary biogenic source of CH_4. Meanwhile, much higher salinity was observed at Upper Laguna Madre than at Aransas Bay and Corpus Christi Bay, which was opposite to the knowledge that sulfate can inhibit methanogenesis. Hence, it

triggered the curiosity to explore whether it was a random phenomenon and what were the drivers that influenced CH_4 emissions in these coastal estuaries.

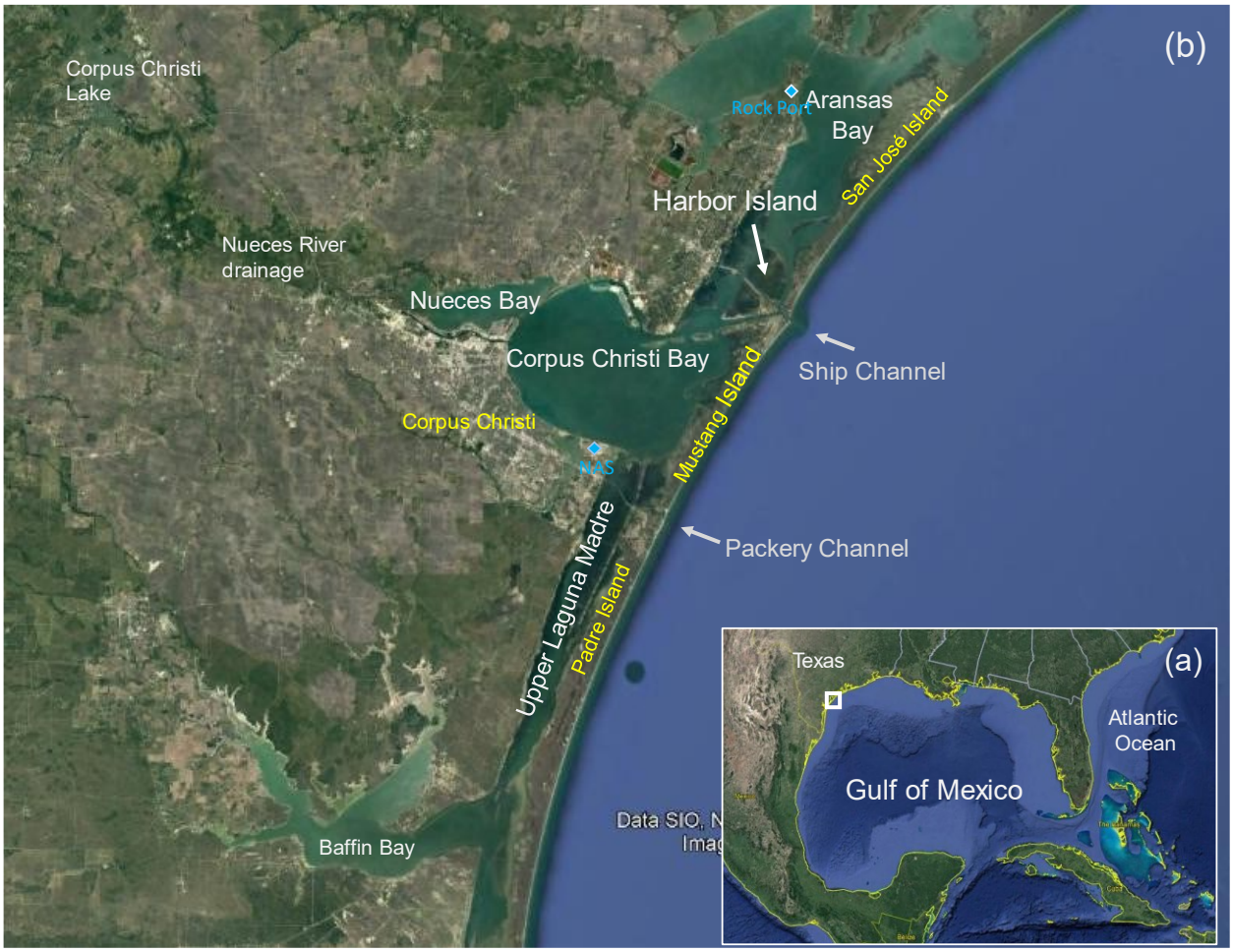

Figure 1.3 Overview of the whole study area in the project.

(a) An overview of the Gulf of Mexico. The study area is northwest of the Gulf of Mexico and southeast of Texas, USA, marked by the white rectangle. (b) Study area in detail, including Nueces Bay, Corpus Christi Bay, Upper Laguna Madre, and Aransas Bay. Rock Port and NAS are meteorological stations in the study area where wind data were collected (blue diamond).

Moreover, EPA data of annual CH_4 released by facilities in Nueces County (including Corpus Christi) from 2010 showed that the CH_4 emitted from anthropogenic sources (e.g.,

industry, landfill) has increased gradually since 2013 (Figure 1.3). Hence, the contribution of anthropogenic emissions to local atmospheric CH_4 also needs to be considered.

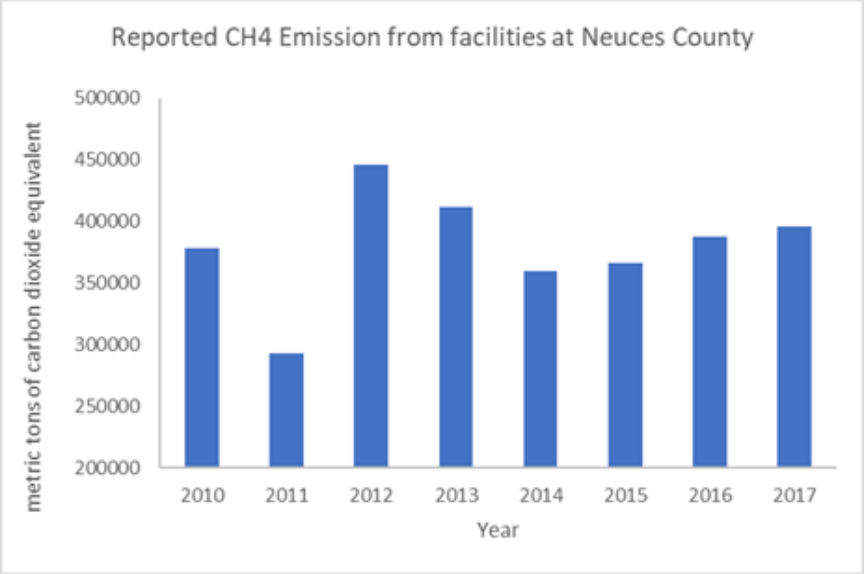

Figure 1.4 CH_4 emissions from facilities reported to the EPA in Nueces County. Data are available at http://ghgdata.epa.gov/ghgp.

1.4 Purpose, Objectives and Hypotheses

1.4.1 Purpose

The overall goal of this project is to determine the sources and fluxes of CH_4 released from the Corpus Christi coastal area to the atmosphere and estimate the contributions of natural processes and anthropogenic activities to the local atmospheric CH_4 budget.

1.4.2 Objective

This project aims to achieve two objectives:

Objective 1: To acquire the spatial and temporal variation in CH_4 released from the Corpus Christi estuary, estimate the contribution from natural sources to the atmosphere and characterize the mechanisms influencing the emission of CH_4.

Objective 2: Apply the aircraft coupled with the greenhouse gas analyzer to measure CH_4 emitted from industrial areas; build long-term monitoring at the Ingleside community to determine how the atmospheric CH_4 level over the community is affected by adjacent industrial operations.

1.4.3 Hypotheses

Based on preliminary studies, there are three hypotheses in this project:

Hypothesis 1: Sediment in shallow coastal water around Corpus Christi is a more significant local source of CH_4 to the atmosphere than deeper bays. A higher fraction of CH_4 released from sediment in shallow water is transported to the atmosphere rather than oxidized in the water column.

Hypothesis 2: Seagrass meadows contribute more significantly than mangrove creeks to local atmospheric CH_4. Compared with mangroves, seagrass meadows are a more significant sink of carbon.

Hypothesis 3: Anthropogenic CH_4 emissions from industrial areas have been underestimated.

CHAPTER II: TIDAL CONTROL AND EXTREME COLD IMPACT ON METHANE EMISSIONS AT SUBTROPICAL MANGROVE CREEKS

Abstract

Mangrove ecosystems with high sediment deposition and active water column carbon cycling are a source of methane (CH_4) to the coastal atmosphere. We investigated diurnal and seasonal scale variations in CH_4 emissions from a subtropical mangrove estuary in South Texas, northwest Gulf of Mexico, from 2018 to 2021. Tidal processes, amplitude (spring and neap) and topographic characteristics are crucial factors controlling CH_4 cycling in mangrove estuaries. Dissolved CH_4 concentrations in creeks were higher during ebbs due to export of CH_4 from inside mangroves and porewater tidal pumping. During floods, CH_4 concentrations in water were determined by the balance between CH_4 input from sediment and bay water dilution. Elevated CH_4 concentrations in spring tides compared with neap tides could be attributed to additional CH_4 emissions from upper intertidal sediment. Moreover, higher CH_4 concentrations were observed after the extreme cold event in February 2021, which was probably related to more organic carbon deposits induced by the high mortality of mangrove forests during the extreme cold days. Diffusive CH_4 fluxes at the sea-water interface in different months were 85.2 ± 84.2 ~ 206.2 ± 213.3 $\mu mol/m^2 \cdot d$ during the study period. The annual CH_4 emissions offset approximately 0.17% of local organic carbon deposits, indicating that these estuarial mangrove creeks are a weak CH_4 source. However, CH_4 fluxes two months after the extreme cold event in 2021 were four times those in the same months in a previous normal year, indicating the potential for enhanced CH_4 emissions caused by extreme weather conditions needs further attention to provide a more accurate estimate related to climate change.

2.1 Introduction

Coastal vegetated ecosystems such as mangroves, saltmarshes, and seagrass are large carbon reservoirs and are crucial for evaluating global carbon sinks (Macreadie et al. 2019). High deposition of organic carbon in these systems provides robust carbon sources for microbial production and respiration, leading to a high potential for greenhouse gas emissions (Macreadie et al. 2019; Rosentreter et al. 2018b). Methane (CH_4) is the second most abundant greenhouse gas after carbon dioxide (CO_2), with a warming potential of approximately 28-34 times that of CO_2 over 100 years (IPCC 2014). As a major CH_4 source in coastal areas, mangroves were estimated to emit 0.23~ 0.25 Tmol CH_4-C/year, which would offset ~9% of the carbon buried in mangrove sediment (Al-Haj and Fulweiler 2020). Due to high spatial and temporal variability in CH_4 released from different mangrove ecosystems, there is a large uncertainty in global estimates, and the data are continuously updated (Rosentreter et al. 2021a; Saunois et al. 2020).

Mangrove ecosystems (rivers, estuaries, lagoons, creeks, etc.) play a significant role in CH_4 emissions (Cabezas et al. 2018; Gnanamoorthy et al. 2021; Maher et al. 2015; Purvaja et al. 2004; Serrano-Silva et al. 2014). A recent global dataset shows that the gas contribution from mangrove water and sediment is higher than previous estimates (Saunois et al. 2020). In these systems, tidal processes often significantly impact CH_4 emissions through water or porewater exchange. CH_4 fluxes in mangrove creeks were higher during low tides due to porewater exchange or progressive enrichment of diffusive CH_4 in the water column controlled by tidal pressure and mixing (Call et al. 2015; Jacotot et al. 2018; Lekphet et al. 2003; Linto et al. 2014). However, elevated CH_4 emissions have also been reported to appear during high tides in mangrove-covered estuaries on the Andaman coast or a couple of days following high tides in mangrove estuaries along west Bengal Bay (Jha et al. 2014; Lekphet et al. 2005). In some mangrove ecosystems, tidal inundation during spring tides could release more CH_4 from upper intertidal sediment (Bahlmann

et al. 2015; Call et al. 2019; Dutta et al. 2015; Jacotot et al. 2018). Call et al. (2019) explained such variation using a "first flush" model of porewater exchange in mature macrotidal mangrove systems (tidal range > 4 m). Higher CH_4 emissions have also been observed at neap tides rather than spring tides in a subtropical mangrove ecosystem due to an input of older groundwater enriched in CH_4 during neap tides, which was speculated to be in microtidal systems (tidal range < 2 m) (Call et al. 2015). In riverine estuaries, CH_4 emissions could also be driven by riverine and groundwater inputs, in situ production, and terrestrial input (Rosentreter et al. 2018a). It seems that hydrological drivers are important factors that cause the large heteroscedastic distribution of CH_4 emissions from mangrove ecosystems.

Furthermore, mangrove forests are vulnerable to climate changes, such as extreme events (Osland et al. 2018), which could exacerbate CH_4 emissions. Along the coast of the Gulf of Carpentaria, Australia, tree stems of dead mangroves were observed to release eight-fold more CH_4 than those of living trees (Jeffrey et al. 2019). A recent study in the Tampamachoco coastal lagoon, Mexico, in the southwest position of the Gulf of Mexico, showed that CH_4 emissions from soils of degraded mangrove forests were up to 9-fold those of preserved mangroves (Romero-Uribe et al. 2021).

In recent decades, mangroves have shown poleward expansion from tropical to subtropical areas primarily due to the reduced frequency of extreme cold events (days colder than -4°C) (Cavanaugh et al. 2014). Mangrove forests at Aransas Bay, Texas, are a key area of northward mangrove expansion and replacement of salt marshes along the Gulf of Mexico. Between 1990 and 2010, mangrove coverage increased 75% (Armitage et al. 2015; Osland et al. 2018). The transfer from salt marsh to mangroves deposited more carbon in the sediment; hence, the poleward expansion of mangroves would benefit local carbon sequestration (Bianchi et al. 2013; Vaughn et

al. 2020). On the other hand, we need to consider the offset of greenhouse gas emissions to carbon storage for a precise evaluation of the function of ecosystem change. Unlike the eastern and southern coasts of the Gulf of Mexico (Cabezas et al. 2018; Chuang et al. 2017; Oremland 1975; Romero-Uribe et al. 2021; Wilson et al. 2015), few studies on CH_4 emissions in this region, northwest coast of the Gulf, have been reported. Moreover, the freezing event that occurred between February 14th and 17th 2021 caused the death of a large area of mangroves at Aransas Bay (Figure 1). Although there has been no report about the exact mangrove mortality until now, this event would undoubtedly lead to a dramatic increase in local carbon sinks.

There is a wide range of factors that control mangrove carbon emissions to the atmosphere, and these factors occur over large and small spatial and temporal intervals. This study contributes to this effort with a focus on the spatial and temporal overview of CH_4 emissions that is compared with the impact of mangrove freezing, contributing to understanding of the mechanisms between the carbon sequence and greenhouse gas emission offset during a changing climate. This is addressed across diurnal and seasonal variations in CH_4 emissions and related parameters in mangrove creeks to examine potential drivers that control CH_4 emissions. We also evaluated the CH_4 offset of carbon deposits and assessed the impact of extreme cold events on CH_4 emissions.

2.2 Materials and Method

2.2.1 Study area

This study is located at Harbor Island of Aransas Bay, southern Texas, northwest of the Gulf of Mexico (Figure 1.3 for overview and Figure 2.1 for detail in this chapter). Aransas Bay is separated from the Gulf of Mexico by the sandy barrier island of San José Island, and the Gulf of Mexico water inflow to the bay is only through the Ship Channel at Port Aransas. It has a subtropical climate and diurnal microtides (tide range 0.3~0.6 m) (Montagna et al. 2011; Whitfield

and Elliott 2011). Harbor Island is a flood tidal delta located at the Ship Channel inlet (Montagna et al. 2011). The area is covered by black mangroves (*Avicennia germinans*) and salt marshes (*Spartina alterniflora* and other grass and forb species) (Armitage et al. 2015). From the 1930s to the present, the coverage of black mangroves at Harbor Island had a notable increase, and salt marsh decreased significantly (Armitage et al. 2015; Montagna et al. 2011). It has become a dominant black mangrove habitat (Montagna et al. 2011), and provides vital nursery habitat to many bird, fish, and invertebrate species and serves as a major area for public recreation, e.g., boating and fishing.

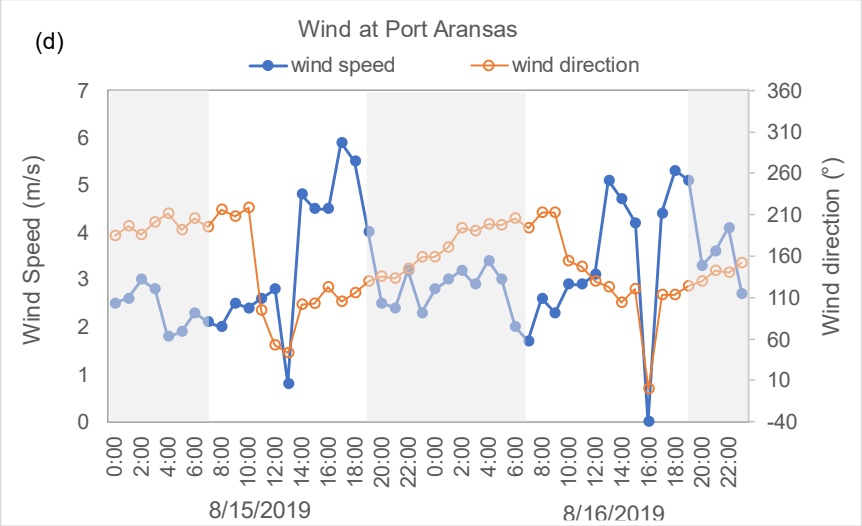
(d)
Wind at Port Aransas
wind speed
wind direction
Wind Speed (m/s)
Wind direction (°)
8/15/2019
8/16/2019

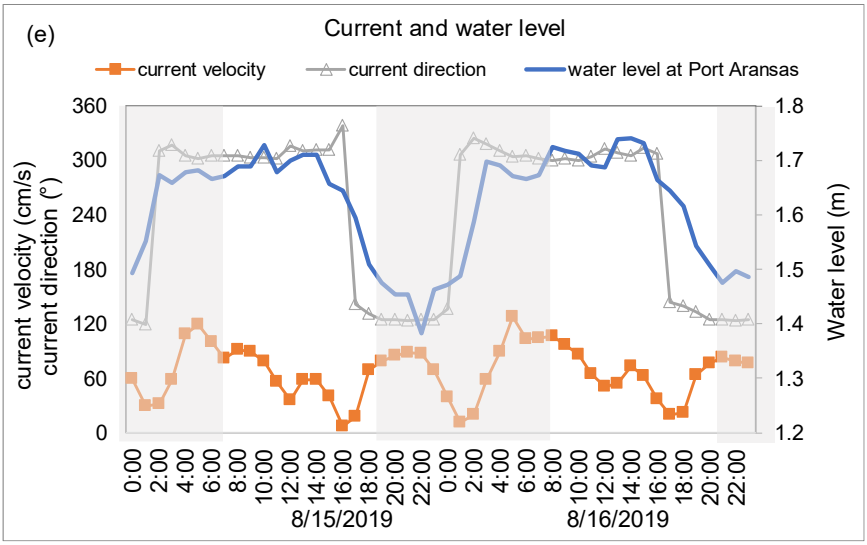
(e)
Current and water level
current velocity
current direction
water level at Port Aransas
current velocity (cm/s)
current direction (°)
Water level (m)
8/15/2019
8/16/2019

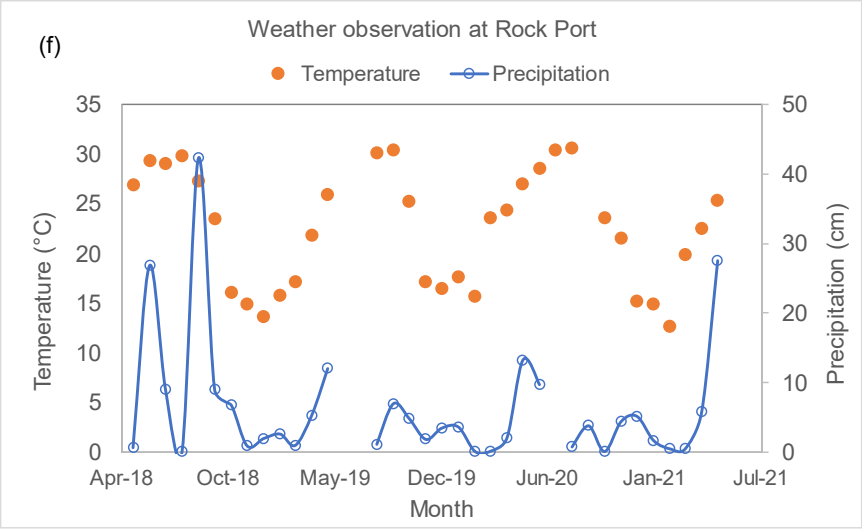
(f)
Weather observation at Rock Port
Temperature
Precipitation
Temperature (°C)
Precipitation (cm)
Apr-18
Oct-18
May-19
Dec-19
Jun-20
Jan-21
Jul-21
Month

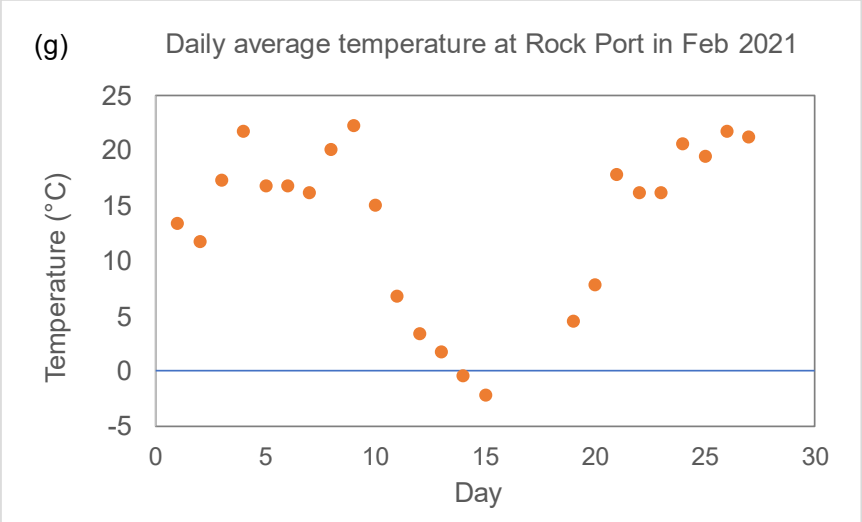

Figure 2.1 Study sites at Harbor Island, Aransas Bay.

(c) Sampling sites. Yellow sites are at Harbor Island mangrove creeks, which are the objectives of this paper. White sites are in channels or bays around the Harbor Island mangrove area. AM4, AM5 and AM6 are located at the southern creek; AM16, AM7 and AM17 are at the middle creek; AM17 is outside of a creek mouth; and AM8 is inside of the north creek. (d) Wind speed and direction during diurnal study at Port Aransas station (8775237) (Figure 2.1c, blue diamond). Shading areas represent nighttime. (e) Current velocity and direction at Channel View, Port Aransas (cc0301) (Figure 2.1c, write triangle), and water level at Port Aransas station (8775237) (Figure 2.1c, blue point). (f) Monthly temperature and precipitation over the study period at a

nearby meteorologic station (Rock Port, Texas, Figure 1.3, blue). (g) Daily average temperature in February 2021 at a nearby meteorologic station (Rock Port, Texas, Figure 1.3, blue). (h, i) Mangrove forests at Harbor Island before and after the freezing event in February 2021.

2.2.2 Study method and sampling

Long-term observations and sampling were performed at sites in creeks of Harbor Island, south Texas, USA (Figure 1.3 and Figure 2.1), in June 2018, January, March, May, July, August 2019, and bimonthly from January 2020 to May 2021. Diurnal observations were carried out at site AM5 (27°51'54.85"N, 97° 3'35.91"W) of Harbor Island on August 15th and 16th, 2019, during spring tide (Figure 2.1).

Surface water and ambient air samples were collected to determine dissolved CH_4, sea-air CH_4 flux, dissolved inorganic carbon (DIC), and chlorophyll-*a* (Chl-*a*). Simultaneous water parameters (salinity, pH, dissolved oxygen (DO), temperature) were measured using a multiparameter meter (HI98194, Hanna Instruments). In addition, weather (wind speed, wind direction, and temperature), water level, and current data from nearby meteorological and hydrological stations were acquired online (NOAA Tides & Current, https://tidesandcurrents.noaa.gov/, station: Port Aransas, Texas (8775237), Figure 2.1c; and U.S. Local Climatological Data, https://www.ncdc.noaa.gov/cdo-web/datasets/LCD/stations/WBAN:12972/detail, station: Rockport Aransas Co Airport, Figure 1.3). These data were applied to calculate the CH_4 flux and analyze factors controlling CH_4 emissions at the sea-air interface (Chuang et al. 2017; Lorenson et al. 2016). During diurnal observations, all sampling and in situ measurements were performed every 4 hours to determine 24-hour variations.

Floating chambers were set up to measure the total in situ CH_4 emissions from surface water to the atmosphere and calculate the standard gas transfer velocity. During diurnal observations, they were built in both daytime and night. Thorough data evaluation for this study includes coupling a linear increase in chamber CH_4 concentration (R^2 >0.95) during the first hour through a diffusive flux with the inclusion of undissolved advective gas advection.

2.2.2.1 Surface water collection

For each site, water samples were taken in 160 ml serum glass bottles, immediately capped without headspace using airtight butyl rubber septa and crimp sealed and preserved in cool with an addition of 1 ml saturated $CuSO_4$ (Coffin and Mueller 2020; Rose et al. 2013). For background CH_4 concentrations and calculation of sea-air CH_4 flux, ambient air samples were collected at approximately 1 meter above the water surface using 30 ml syringes and injected into serum vials by replacing the filled Mili-Q water. Water and air samples were stored in an ice-packed cooler during boat operations and stored in the refrigerator at the end of the day. For the incubation experiment, fourteen bottles of additional samples were collected simultaneously as the first samples at AM5, and $CuSO_4$ solution was added to duplicate samples at 1, 2, 3, 4, 5, 6 and 12 hours.

2.2.2.2 Floating chamber capture

Three floating chambers were placed at AM5 to observe the in situ CH_4 flux at the water-air interface. In the diurnal experiment, four were set in the daytime and one at night. Polyester bottles made floating chambers with a volume of 3 liters and an area of 154 cm^2. The chambers were kept floating on the water surface with foam and counterweight to minimize turbulence (McGinnis et al. 2015). The sample chamber top was predrilled with a small hole (1/16 inch) and sealed by black airtight tape. In the first hour, air samples in floating chambers were collected

every 15 minutes using a 30 ml syringe from the chamber's top by piercing a small gauge needle into the small hole through the tape. Once the samples were collected and the needle was withdrawn, the chamber was resealed. Air samples were immediately injected into vials filled with Milli-Q water that had previously been sparged with ultra-high purity N_2. During the diurnal observation, air samples in the chambers were collected every four hours after the first hour to determine the CH_4 source for whole day-night cycling.

2.2.3 Analytical Methods

The dissolved and airborne CH_4 concentrations were measured by the headspace equilibration technique and gas chromatography (GC, Agilent 6890N) (Magen et al. 2014; Reeburgh 2007). DIC concentrations were determined using a UIC CM5017 Coulometer. Chlorophyll *a* (Chl-*a*) concentrations were measured using a Turner 10-AU fluorometer. Sulfide in porewater was determined by colorimetric analysis of the methylene blue method using a spectrophotometer (Cline 1969; Reese et al. 2011). The above works were performed in the Isotope Core Laboratory at Texas A&M University-Corpus Christi. The $\delta^{13}C$-CH_4 of some samples was analyzed at the Stable Isotope Lab of the University of California-Davis, with a precision of ±0.14‰.

2.2.4 Calculation of fluxes

2.2.4.1 Floating chamber methane flux

The sea-air CH_4 flux acquired using floating chambers is called the chamber flux in this paper. If the CH_4 concentration increased linearly (R^2>0.95), the flux was calculated using the CH_4 concentration growth rate (ppm/minute).

$$F_{fc} = s \times \frac{P}{R \times T} \times \frac{V_{chamber}}{A_{chamber}} \times t \qquad (1)$$

where F_{fc} is chamber flux (μmol/m^2·h or μmol/m^2·d); s is the growth rate of CH_4 concentration (ppm/min) in the linear increase; P is gas pressure inside the chamber (Pa); R is universal gas law constant (8.314510 m^3 Pa K^{-1} mol^{-1}); $\frac{P}{R \times T}$ is to convert volume concentration to molar concentration based on Law of Avogadro's; $V_{chamber}$ is the volume of the chamber (m^3); $A_{chamber}$ is the area of the chamber connecting surface water (m^2); and t is time efficient (convert from min to hour or day). Here, we assumed that P was 1 atm since the observation lasted only 1 hour.

2.2.4.2 Diffusive methane flux

The diffusive CH_4 flux at the sea-air interface was calculated using the gas-transfer model (Wanninkhof 1992).

$$F = k_v \cdot (C_{obs} - C_{eq}) \quad (2)$$

where F is the flux of CH_4 to the atmosphere (μmol/m^2·d or μmol/m^2·h); C_{obs} represents the measured concentration of dissolved CH_4 in water (nmol/L); C_{eq} is the concentration of CH_4 in equilibrium with the atmosphere at in situ temperature (nmol/L), calculated for each sample from the temperature- and salinity-dependent equilibrium relationship (Wiesenburg and Guinasso 1979); and k_v is the gas transfer velocity (cm/h), calculated using the relationship between the standard gas transfer velocity (k_n) and Schmidt number (Sc).

$$k_v = k_n \times (\frac{Sc}{n})^{-\frac{1}{2}} \quad (3)$$

where Sc is defined as the kinematic viscosity of water divided by the gas diffusion coefficient, which is dependent on water temperature and salinity (Wanninkhof 1992; Wanninkhof 2014). The calculation of Sc followed Wanninkhof (2014) since water temperatures exceeded 30°C. We use *n* of 660 to calculate k_v and diffusive flux since salinity in this region is high (>30) (Wanninkhof 1992). k_n is calculated using five methods, in situ floating chamber flux (k_{fc}) and

four empirical equations (k_{model}). Except in the equation of W2014, an n of 600 was previously used in the other three equations because they were developed for rivers and estuaries with lower salinity (Raymond and Cole 2001). Here, we still used these equations because the standard gas transfer velocity was not related to salinity in the equations, so we assumed that the difference caused by salinity could be ignored.

Floating chambers: $k_{fc} = F_{fc}/(C_{obs} - C_{eq})$ (4)

R2001 (Raymond and Cole 2001): $k_{R2001} = 2.06e^{0.37\mu}$ (5)

J2008 (Jiang et al. 2008): $k_{J2008} = 0.314\mu^2 - 0.436\mu + 3.990$ (6)

W2014 (Wanninkhof 2014): $k_{W2014} = 0.251\mu^2$ (7)

VD2019 (Van Dam et al. 2019): $k_{VD2019} = 2.3 + 1.9u$ (daytime)

$k_{VD2019} = 18.5 - 5.3\mu + 0.64\mu^2$ (night) (8)

where μ is the mean wind speed at 10 m at nearby weather stations acquired online (monthly and daily average data from the station of Rockport Aransas Co Airport in NOAA National Centers for Environmental Information Climate Dataset, https://www.ncdc.noaa.gov/cdo-web/datasets/LCD/stations/WBAN:12972/detail and hourly data from station of Port Aransas in NOAA Tides & Current, https://tidesandcurrents.noaa.gov/stationhome.html?id=8775237). In the diurnal observations, the hourly mean wind speed was applied to calculate the in situ hourly CH_4 flux (μmol/m^2·h), while in the seasonal investigations, the monthly average daily wind speed was used in the calculation to obtain a monthly average daily CH_4 flux (μmol/m^2·d). The fluxes calculated using equations were collectively called F_{model}. The fluxes calculated using each standard gas transfer velocity were F_{fc}, F_{R2001}, F_{J2008}, F_{W2014}, and F_{VD2019}. The whole-day sea-air CH_4 flux during the diurnal observations was calculated using the average hourly CH_4 flux over 24 hours.

2.2.5 Statistical analysis

R software (version 3.6.1) was applied for statistical analysis. Linear regression models were used to test whether there were significant relationships between CH_4 concentrations/CH_4 flux and other parameters. ANOVA comparison with the Shaffer test was applied to check the impact of tidal process and amplitude on CH_4 emissions.

2.3. Results

2.3.1 Temporal variation in methane and other parameters

During the diurnal observation, dissolved CH_4 concentrations increased from noon, reached the highest level at midnight, and then decreased. $\delta^{13}C$-CH_4 was -61.9‰ ~ -60.9‰, suggesting a biogenic CH_4 source (Coffin et al. 2015). The variation in $\delta^{13}C$-CH_4 was opposite to that in the CH_4 concentration (Figure 2.2a). Salinity had a similar variation as the CH_4 concentration, highest at midnight and lowest at noon, which was obviously caused by tidal processes rather than evaporation in the daytime (Figure 2.2b). Temperature and pH were highest in the late afternoon, decreased overnight, and increased the following morning. DIC varied similarly to CH_4 concentration (Figure 2.2c).

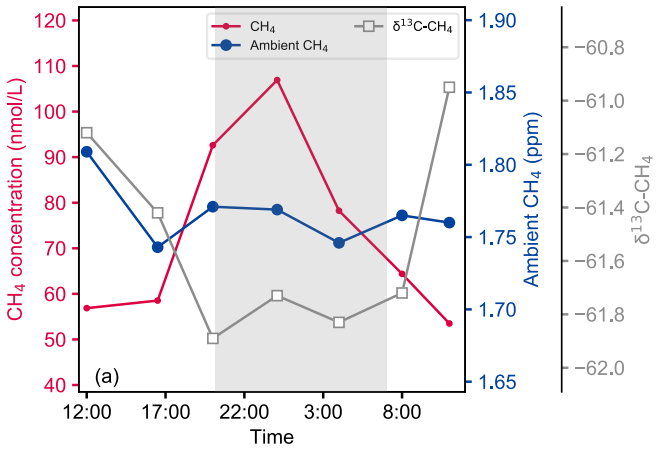

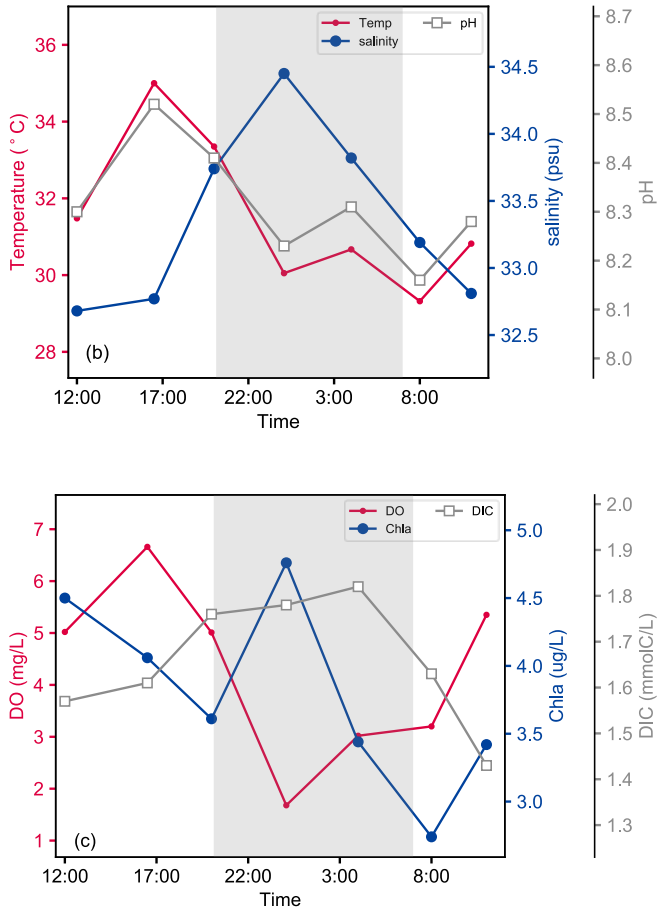

Figure 2.2 Diurnal variations in CH_4 and other parameters.

(a) diurnal variation in dissolved CH_4 concentration, ambient CH_4 and $\delta^{13}C$-CH_4; (b) diurnal variation in temperature, salinity, and pH; (c) diurnal variation in DO, Chl-*a* and DIC

From July 2020 to May 2021, dissolved CH_4 concentrations decreased from summer/early autumn in 2020 to winter in 2020/2021 and then increased in spring 2021, following a pattern related to variations in monthly temperature (Figure 2.3). Viewed from the annual difference, CH_4 concentrations at AM4 and AM5 in March and May 2021 were higher than those in the same months in 2019.

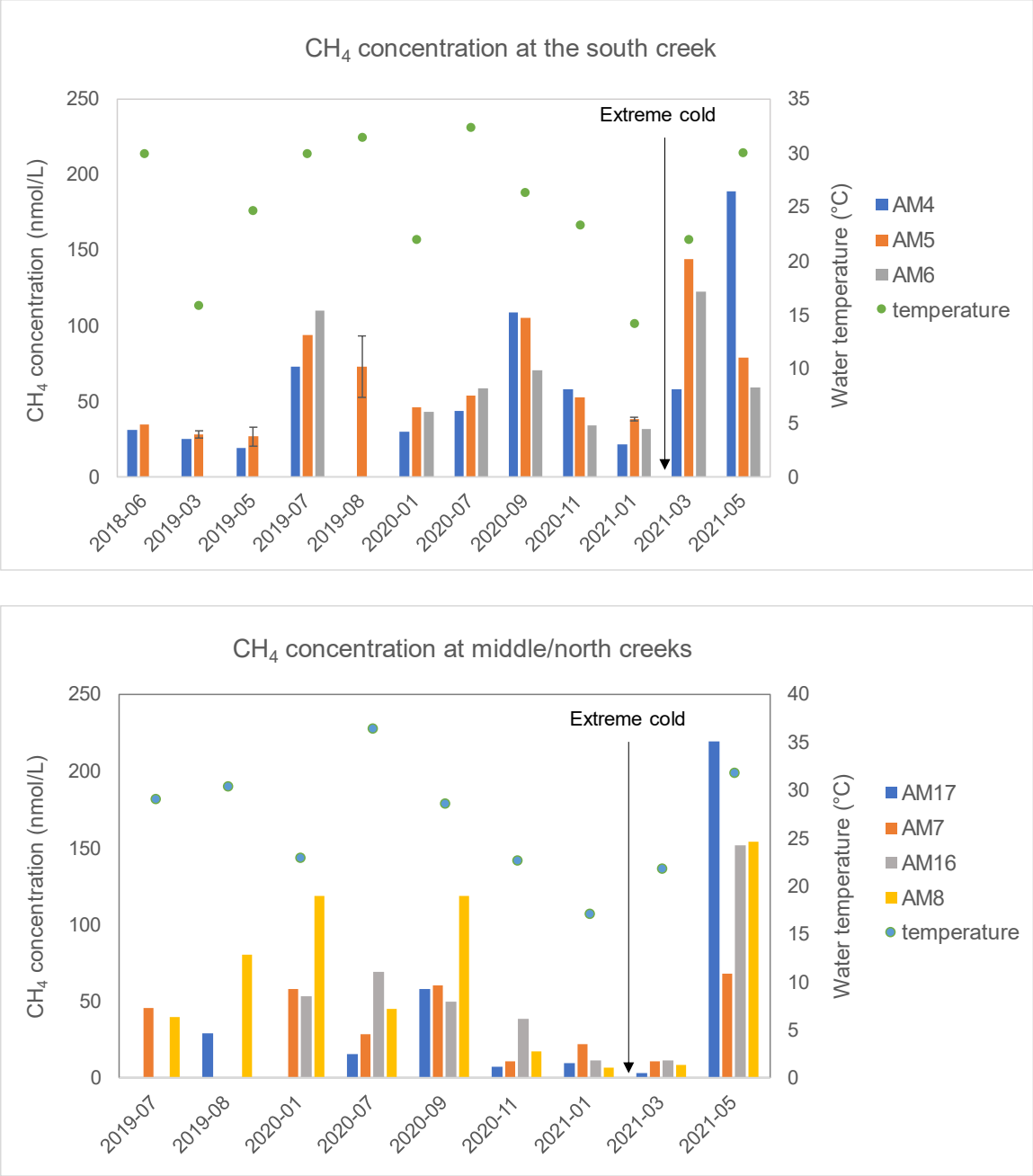

Figure 2.3 Monthly variation in dissolved CH_4 concentrations in mangrove creeks (upper: south creek; lower: middle and north creeks) and corresponding water temperatures

2.3.2 Variation of methane in floating chambers

Floating chambers were built at AM5 to determine the in situ CH_4 emissions from the water column to the atmosphere and the gas transfer velocity. In one hour, the CH_4 concentrations in

chambers except in March 2019 increased linearly, indicating that there was no contribution from bubbles (Figure 2.4). The linearity of the CH_4 increase in the chambers in March 2019 was poor, and the growth rates were very low, indicating minimal CH_4 emissions at the water-air interface over the study period. The increase rate was highest in September 2020, suggesting the largest CH_4 emissions over the study period. Then, the CH_4 increase rate decreased in autumn and winter and increased again in the spring of 2021. The floating chamber experiments also showed that more CH_4 was released from water to the atmosphere in March and May 2021 than in the same months of 2019.

During diurnal observations, average growth rates of the CH_4 concentration in chambers at AM5 built in the daytime (0.008±0.001 ppm/min) were larger than those at night (0.006 ppm/min, Figure 2.4), revealing that more CH_4 was released from water to air during daytime than at night. $\delta^{13}C$-CH_4 was negatively related to CH_4 concentration in floating chambers. The Keeling plot of $\delta^{13}C$-CH_4 and $1/CH_4$ (Garcias-Bonet and Duarte 2017) indicated that $\delta^{13}C$ of CH_4 entering the chamber should be -61.8‰, consistent with that of dissolved CH_4 in water.

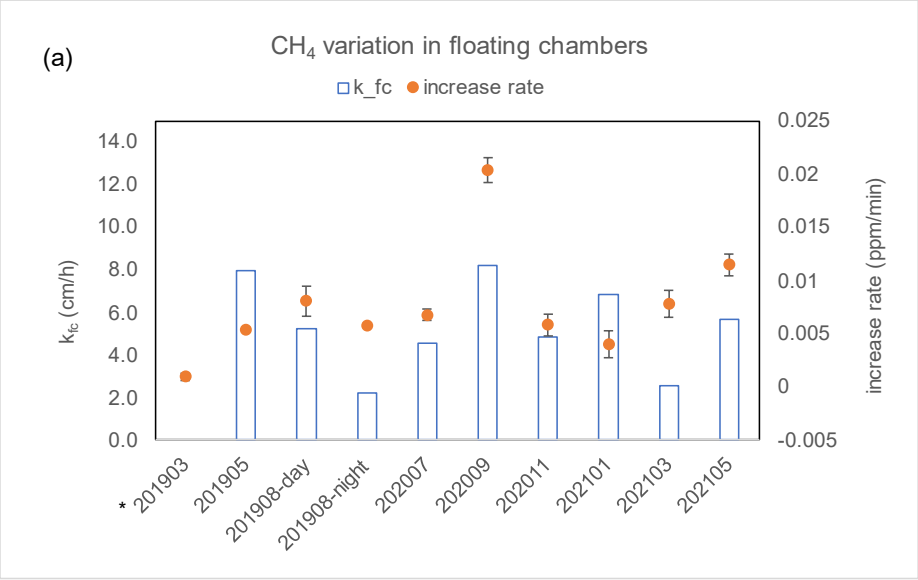

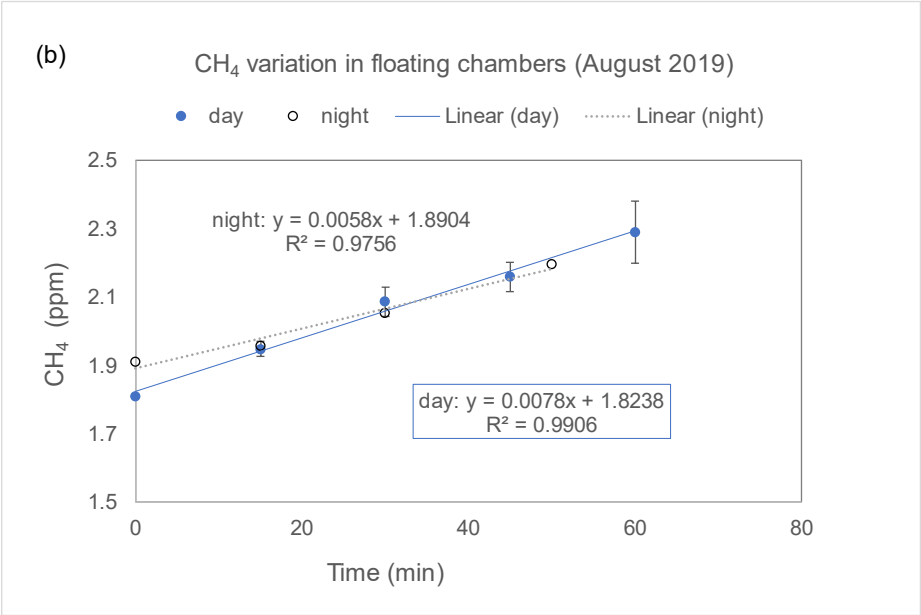

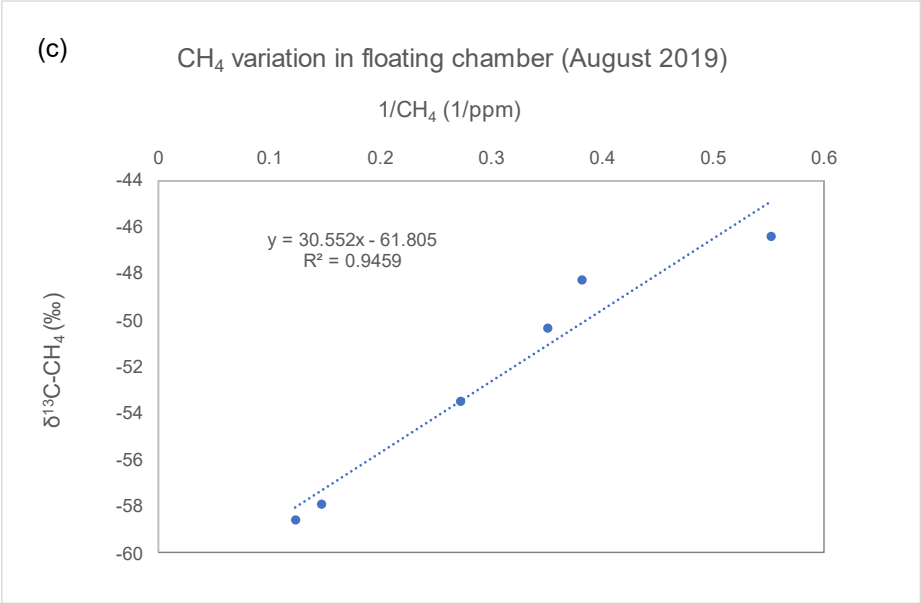

Figure 2.4 CH_4 variation in floating chambers.

(a) CH_4 variation in floating chambers and standard gas transfer velocity acquired by floating chamber (k_{fc}), * The linearity in chambers at AM5 in March 2019 was poor; (b) CH_4 concentration in floating chambers in the first hour at AM5 in daytime and nighttime on August 15th, 2019; (c) Relationship between $\delta^{13}C$-CH_4 and the inverse of CH_4 in the floating chamber on August 15th, 2019.

2.3.3 Methane fluxes at the sea-air interface

2.3.3.1 Standard gas transfer velocity

The standard gas transfer velocities at AM5 calculated using chamber fluxes (k_{fc}) were 2.2~8.2 cm/h (average: 5.3±2.1 cm/h, Figure 2.4a, Figure 2.5a). The values of k_{W2014} were always smallest among the k_{model} (Figure 2.5a). Its average (4.8±3.0) was closest to that of k_{fc}. The k_{fc} in May 2019, July 2020, and November 2020 was similar to k_{W2014}, while in August 2019 (daytime), it was close to k_{VD2019}. Unlike k_{model}, k_{fc} did not follow a similar pattern as wind speed.

2.3.3.2 Sea-air methane flux

Since there are no universally applicable standard gas transfer velocities, we used k_{fc} and k_{model} to estimate sea-air CH_4 fluxes (F_{fc} and F_{model}). During the diurnal observations (Figure 2.5b), the overall average of F_{W2014} (2.6±2.0 μmol/m^2·h) was closest to that of F_{fc} (3.3±0.7 μmol/m^2·h). The F_{fc} values in the daytime were similar to those in F_{J2008} and F_{R2001}, except in the late afternoon. In the late afternoon, all F_{model} values were much larger than F_{fc} due to the largest wind speed during the diurnal period. At night, the F_{fc} values were close to F_{W2014}.

A comparison of monthly average sea-air CH_4 fluxes (Figure 2.5c) showed that the values of F_{fc} were close to F_{W2014} in months except September 2020, consistent with the diurnal observations. In September 2020, F_{fc} was similar to F_{J2008}.

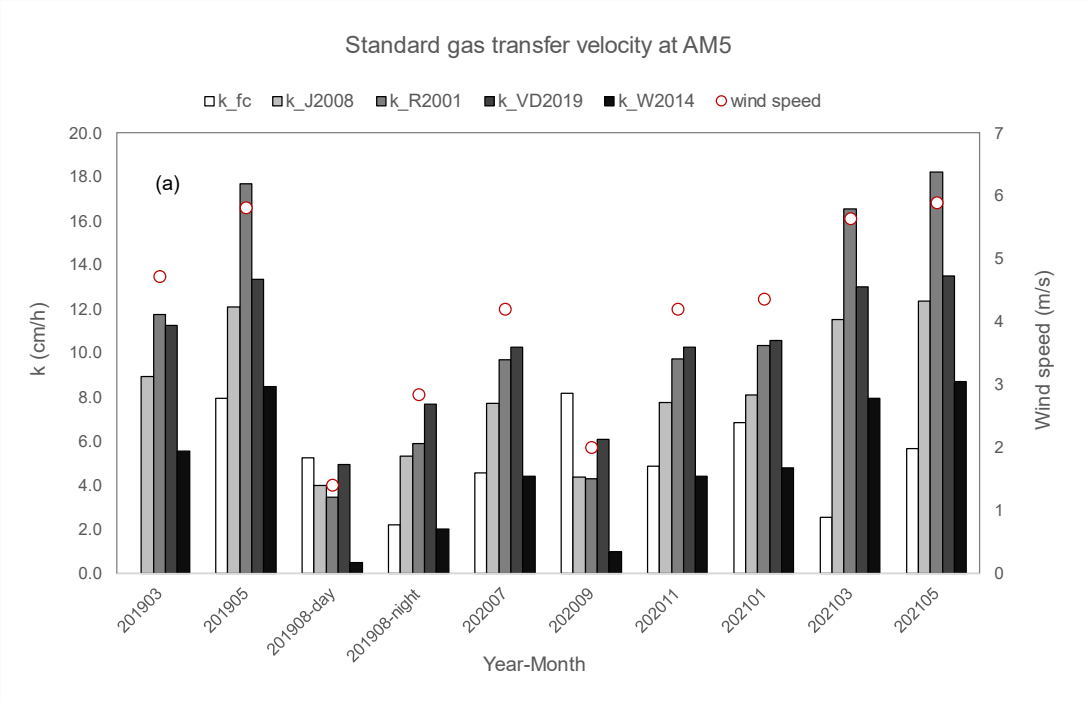
Standard gas transfer velocity at AM5
k_fc
k_J2008
k_R2001
k_VD2019
k_W2014
wind speed
(a)
k (cm/h)
Wind speed (m/s)
Year-Month
201903
201905
201908-day
201908-night
202007
202009
202011
202101
202103
202105

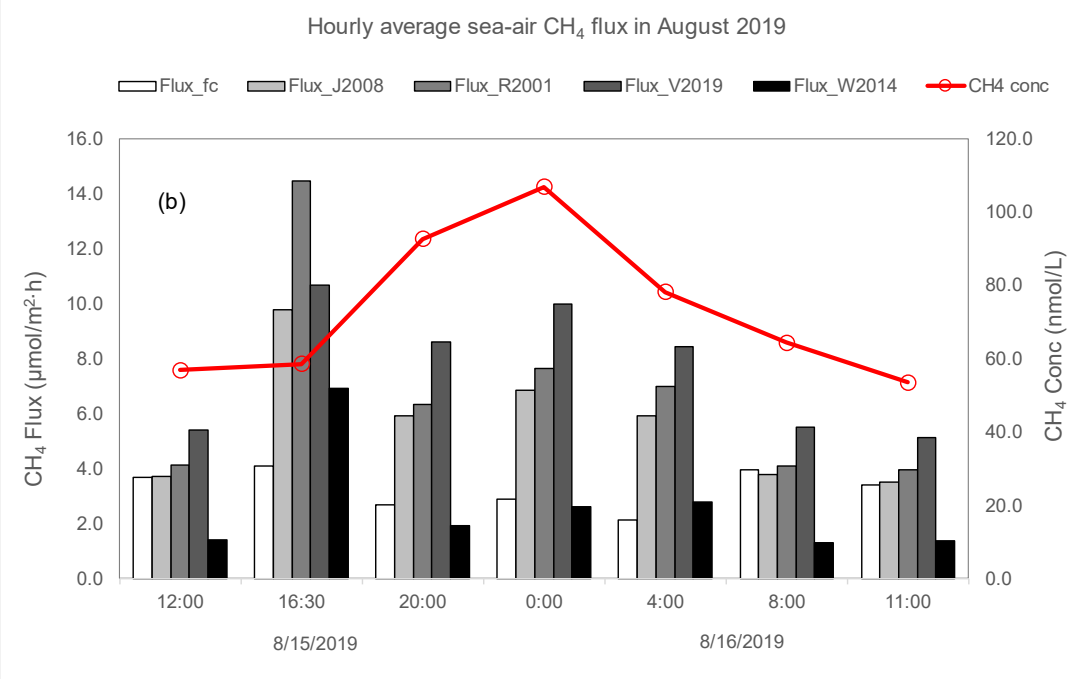
Hourly average sea-air CH4 flux in August 2019
Flux_fc
Flux_J2008
Flux_R2001
Flux_V2019
Flux_W2014
CH4 conc
(b)
CH4 Flux (μmol/m2·h)
CH4 Conc (nmol/L)
12:00
16:30
20:00
0:00
4:00
8:00
11:00
8/15/2019
8/16/2019

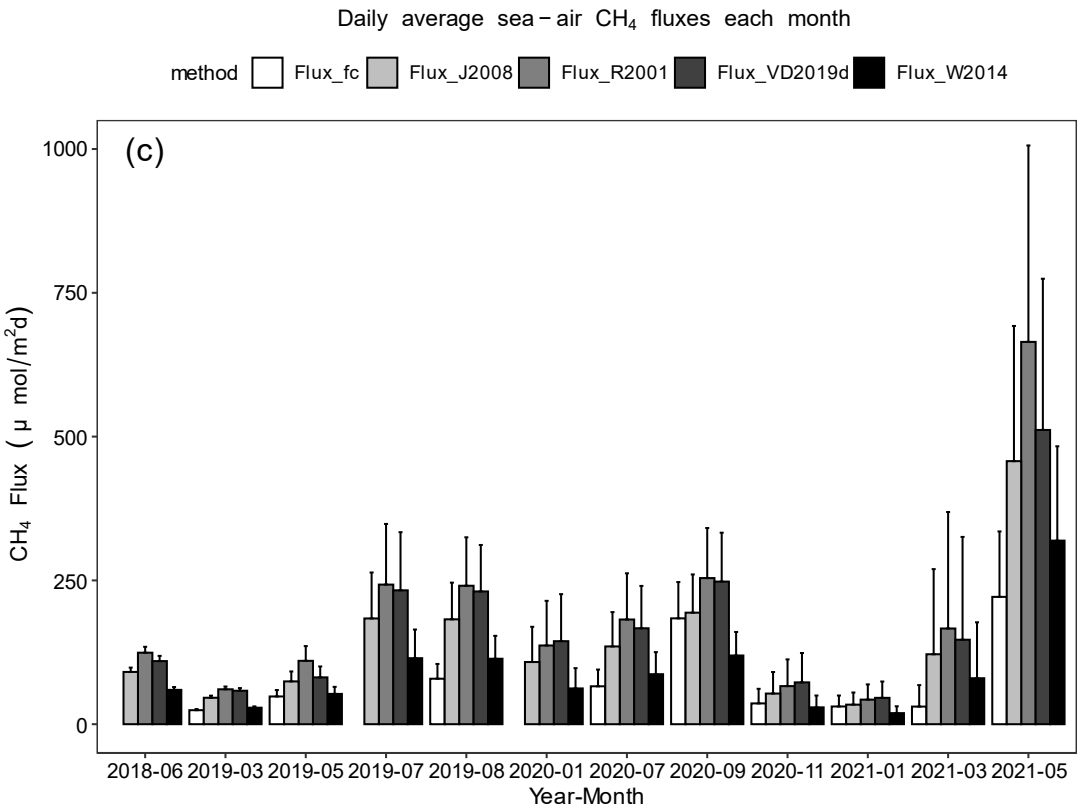

Figure 2.5 (a) Standard gas transfer velocities; (b) Hourly sea-air CH_4 flux in diurnal observations; and (c) Daily average sea-air CH_4 fluxes each month.

2.3.4 Water incubation

The first incubation experiment performed in March 2019 lasted 70 hours for the sample at AM5 (Figure S1). Due to the limited variation in CH_4 concentration in the long term, incubations were performed for no more than 24 hours. The initial dissolved CH_4 concentrations at AM5 (mangrove) were 20~140 nmol/L. The largest decrease in CH_4 concentration appeared in July 2020, which was up to 35%. In addition, the CH_4 concentration decreased by no more than 20% in summer and fall. In winter and spring, the reduction in CH_4 concentration was no more than 10%. More decomposition of dissolved CH_4 in summer and fall than in winter and spring was probably related to seasonal variation in methanotrophs. The CH_4 concentration in the AM5 samples decreased gradually in the first few hours, and then the CH_4 concentration slightly

returned and remained stable. Both the rate of decrease and duration indicated that there was a low level of bacterial consumption and production in the water column.

2.4. Discussion

2.4.1 Sea-air methane flux

The whole-day CH_4 fluxes at AM5 calculated using different methods were 62.7~195.1 μmol/m^2·d during the diurnal observation on August 15-16, 2019. Hourly CH_4 fluxes were all highest in the late afternoon, which was caused by the highest wind speed (5.9 m/s), 2~3 times the wind speeds at other times (2.8~3.4 m/s). Under low wind speeds (i.e., <3.4 m/s), F_{model} had a significantly positive linear relationship with dissolved CH_4 concentration (e.g., R^2=0.55 (p=0.0931) in F_{W2014}, R^2> 0.8 (p<0.01) in other F_{model}) but no significant relationship with wind speed (p>0.2).

The daily CH_4 fluxes of different months over the study period using different methods were 85.2±84.2 ~ 206.2±213.3 μmol/m^2·d. Although there was annual variance, they were generally lowest in winter, increased in spring and reached a high level in summer and early autumn, having a weak association with temperature (R^2>0.18, p<0.001). Moreover, all CH_4 fluxes were more significantly related to dissolved CH_4 concentrations (F_{fc}: R^2=0.78; others: R^2≥0.90, p<2×10^{-16}) than to monthly average wind speed (R^2: 0.15~0.29, p<0.005).

F_{fc} was similar to F_{W2014} in March, May and August 2019 and F_{J2008} in January and September 2020 and January 2021. In other months, F_{fc} was closest to F_{W2014}. Equation J2008 was developed for CO_2 flux estimation in estuaries and has been applied to study CO_2 flux in this region (Yao et al. 2020). Although Equation W2014 was developed based on open-ocean data, it has been used in some estuaries and lakes (Call et al. 2015; Chuang et al. 2017). In this study, Equations J2008 and W2014 seemed to match F_{fc} in some conditions. Hence, we unify monthly CH_4 fluxes

using empirical equations J2008 or W2014 based on relationships with F_{fc} and temperature, wind speeds and tidal characteristics.

The artificially unified CH_4 fluxes ranged from 0.6 to 395.1 μmol/m^2·d (94.7±81.3 μmol/m^2·d, median: 70.7 μmol/m^2·d). Similar to the original fluxes (F_{fc} and F_{model}), they were significantly related to CH_4 concentrations (R^2=0.83, p<2×10^{-16}) and weakly related to temperature (R^2=0.18, p<0.0005). Our estimated fluxes were comparable to CH_4 emissions from some mangrove creeks at similar latitudes, e.g., south Moreton Bay, Queensland, Australia (13.1~632.9 μmol/m^2·d, average 213.7 μmol/m^2·d, 25-30°S) (Call et al. 2015) and southwest Florida at 25-30°N (-62.5 ~ 231.2 μmol/m^2·d) (Cabezas et al. 2018). In contrast, this was a lower CH_4 diffusion in comparison to mangrove swamps at Mrazek Pond near Florida Bay (3369.9~7315.1 μmol/m^2·d, average 5123.3 μmol/m^2·d, 25-30°N), where there was a lower salinity (1~12‰) (Barber et al. 1988).

With comparison across the Gulf of Mexico coast, diffusive CH_4 fluxes in this study were also much lower than the tropical lagoons at Yucatán, south coast of the Gulf (2.3 to 15000 μmol/m^2·d) (Chuang et al. 2017). Although the highest CH_4 concentrations (up to 8378 nmol/L) were related to pollution, a great magnitude of CH_4 emissions was supposed from natural sources, i.e., mangrove sediment, considering its large CH_4 transport at the sediment-water interface (Chuang et al. 2016). This difference is reasonable because the mangrove habitat at Yucatán, Mexico (93171 ha) is approximately 30 times that at Texas (3316 ha), with approximately 20 times the organic carbon stock (Thorhaug et al. 2019). Moreover, such difference also could be related to different species of mangrove forests. CH_4 emissions from soils of red mangrove were found higher than from soils of black mangroves in Veracruz Mexico (Hernández and Junca-Gómez 2020). Ebullitive CH_4 has been observed in mangrove swamps at Yucatán, Mexico and at Mrazek

Pond near Florida Bay (Barber et al. 1988; Chuang et al. 2017), which was probably related to the high CH_4 concentrations in these regions. In contrast, we did not catch any bubble input in this study, which seemed to be comparable to the lower CH_4 concentrations.

2.4.2 Impact of tidal processes on methane emissions

2.4.2.1 Diurnal observations

2.4.2.1.1 Ebb and flooding tides

The diurnal variation in dissolved CH_4 concentration in the mangrove creek (AM5) has a strong positive linear relationship with salinity (R^2=0.92, p=0.000564, Figure S2). The CH_4 concentration and salinity variations were opposite to the tidal water level at Port Aransas. During ebb tide, both CH_4 concentration and salinity increased, and during flooding, they decreased. Nevertheless, it is different from the variations in riverine estuaries, where CH_4 concentration increased during ebb due to riverine input enriched in dissolved CH_4 but depleted in salinity (Matoušů et al. 2017; Ye et al. 2019). Elevated CH_4 concentrations have been widely observed in freshwater aquatic systems because there is less competition in electrons for methanogenesis in a less sulfate environment (DeLaune et al. 1983). Although the relationship between CH_4 concentration and salinity in this study area was opposite to those in riverine estuaries, it is not inconsistent with this universal observation, given that the CH_4 concentration in the local freshwater, e.g., the Nueces River (621.9±89.4 nmol/L, January to June 2019), was approximately 10-fold the CH_4 concentration in coastal waters.

The finding that CH_4 concentrations were positively related to salinity during diurnal observation in the mangrove creek is related to two factors. First, sulfate-reducing bacteria can coexist with methanogens in mangrove sediments, probably because abundant sedimentary organic deposits provide a broad range of substrates that simultaneously support both communities

in a noncompetitive situation (Lee et al., 2008). The $\delta^{13}C$-CH_4 at AM5 was -61.9‰ ~ -60.9‰, proving this biogenic source of CH_4 (Coffin et al. 2015; Kirschke et al. 2013). The decrease in $\delta^{13}C$-CH_4 during ebb also suggested an increase in biogenic CH_4 at AM5.

Second, the synchronic variations in salinity and CH_4 concentration were probably caused by tidal processes. Since AM5 is located in the middle of the mangrove creek, elevated salinity at midnight should be attributed to export of water with higher salinity from the inside mangrove water or exchange of porewater during ebb rather than evaporation. Because of high evaporation and less freshwater input (e.g., precipitation and riverine input) in summer, it is reasonable that shallower water inside the mangrove forests has a higher salinity than that outside the bay area. A decreasing salinity gradient (32.5, 32.1, 32.0, 31.5) from inside to outside along the creek was observed one month before this observation (July 2019) (Figure S3). Similarly, the dissolved CH_4 concentration at AM5 was elevated during ebb tide, probably due to the transport of water with a higher CH_4 level from inside shallower water. Corresponding to salinity in July 2019, a decreasing dissolved CH_4 concentration gradient (109.7 nmol/L, 93.4 nmol/L, 72.5 nmol/L, 24.8 nmol/L, and 12.7 nmol/L) was observed along this creek to the Ship Channel (Figure S3). In this study, the CH_4 concentration at AM8, a site inside mangrove water, was higher than that at AM5. Hence, the increasing CH_4 concentration at AM5 during ebb tide could be explained by exporting water from inside to outside the creek. Comparably, export of CH_4 from coastal systems to the open bay and ocean during ebbs has been reported in Cadiz Bay, Spain (Burgos et al. 2018).

During ebb tide, elevated CH_4 concentrations could also come from sediment porewater by tidal pumps (Deborde et al. 2010). However, the porewater CH_4 concentration (20.0 ~ 85.9 nmol/L in the top 16 cm) at AM5 was slightly higher and even lower in some layers than CH_4 in the water column (Chapter 4), which could not explain the variation (58.5~106.9 nmol/L) during

ebb tide. This is different from the mangrove creeks in southern Moreton Bay, Queensland, Australia, where porewater with a high CH_4 concentration could enhance CH_4 levels in the water column by tidal pumping (Call et al. 2015) and is further compared to our data in subsequent text.

The DO concentrations decreased from noon to midnight and then increased, indicating that DO at the middle of the creek was probably not entirely related to the respiration process but was influenced by water exchange during the tidal process. The increase in DO overnight accompanied by a decrease in salinity appeared during flooding, indicating that bay water containing less salinity and higher DO reduced the salinity and elevated the DO concentration at AM5. The dissolved CH_4 concentration decreased synchronously due to the dilution of bay water with less CH_4 during the flood or oxidation of CH_4 caused by bay water enriched in DO. Elevated $\delta^{13}C\text{-}CH_4$ in flooding also manifested the influence of bay water. The investigation in July 2020 showed that the $\delta^{13}C\text{-}CH_4$ in mangrove creeks (-64.61‰ and -64.14‰ at AM16 and AM5, respectively) was lower than that at the channel/bay site (AM14: -57.52‰, site location can refer Figure 1).

2.4.2.1.2 Tidal inundation

Diurnal observations showed that the dissolved CH_4 concentration decreased dramatically a few hours after the start of the flood tide but increased slightly a few hours before ebb tide, although the water level at Port Aransas remained relatively stable at a high level during this period. This result indicated that there appeared to be a change in the role of flood tides on CH_4 cycling in this mangrove aquatic system.

During high tide, the CH_4 concentration in the water column depended on a balance between CH_4 released from intertidal porewater and dilution of bay water depleted of CH_4. In the first few hours of high tide, dilution exceeded the release of CH_4 from sediment; hence, the

dissolved CH_4 concentration decreased. A rapid increase in $\delta^{13}C$-CH_4 also suggested that the proportion of biogenic CH_4 in the total dissolved CH_4 was decreased, further proving the dilution of bay water. In later hours, as more CH_4 was emitted from upper intertidal sediment and the dilution effect decreased, dissolved CH_4 concentrations slightly increased. $\delta^{13}C$-CH_4 decreased synchronously, suggesting more input of biogenic sources of CH_4 due to inundation. A similar time lag of peak CH_4 emissions post inundation was also reported in a mangrove creek in the Amazon region (Call et al. 2019).

During diurnal observations, hourly CH_4 fluxes varied following a different pattern than CH_4 concentrations. In the late afternoon, as more CH_4 was transported to the atmosphere under a large wind, the CH_4 concentration continued to increase. This further illustrated that more CH_4 was input from inside mangrove creek and subtidal sediment during ebb tide.

2.4.2.2 Long-term observation: spring vs. neap tides

Our long-term investigation also showed the impacts of tidal processes and tidal amplitudes on dissolved CH_4 concentrations. As in the diurnal observations, CH_4 concentrations in spring tides were highest during ebb tide. Although there were no data about CH_4 concentrations during low and high tides in neap tides, CH_4 concentrations were also higher during ebb tides than during flood tides (Figure 7). Moreover, CH_4 concentrations during both ebbs and floods were higher in spring tides than in neap tides, indicating that tidal amplitudes (spring and neap) had a significant influence on CH_4 emissions, probably due to more CH_4 released from upper intertidal sediment during the inundation of water (Call et al. 2019). The highest CH_4 concentration appeared during ebb tide in spring, which was consistent with the findings in mangrove water in New Caledonia in the South Pacific (Jacotot et al. 2018).

The $\delta^{13}C$-CH_4 at mangrove creeks during ebb in neap tide (-64.61‰ and -64.14‰ at AM16 and AM5, respectively, July 11th, 2020) were lower than those in spring tide (-61.89~-61.42‰ at AM5, August 15th, 2019). Similar to the explanation for the variation in CH_4 concentration during floods, the difference in $\delta^{13}C$-CH_4 between spring and neap tides could be attributed to two possibilities. First, the higher $\delta^{13}C$-CH_4 in spring tide was probably related to more oxidation of porewater CH_4 in intertidal sediment than in subtidal sediment since subtidal sediment has less exposure potential than intertidal sediment. Second, elevated $\delta^{13}C$-CH_4 in spring tide could also be led by more dilution of bay water than in neap tide, which decreased the proportion of biogenic CH_4 in the water column. Regardless of the possible reasons, in comparison with spring tides, less water immersion occurred during neap tides. Hence, consistent with other studies (Call et al. 2015; Deborde et al. 2010), the increase in CH_4 concentration during ebbs in neap tides more likely came from subtidal porewater input under the effect of tidal pumping.

Since sea-air CH_4 fluxes were significantly related to dissolved CH_4 concentrations, it is reasonable that the highest CH_4 fluxes were observed during ebb tide in spring tides (Figure 2.6). However, in neap tides, there was no obvious variation in CH_4 fluxes between ebb and flood tides, probably due to the combined effect of wind. Unlike the hourly CH_4 flux in the diel observation, monthly average wind speeds were applied to estimate the monthly average daily CH_4 fluxes. Although the impact of short-term (e.g., hourly) wind speed on CH_4 emissions was hidden, it is valuable to understand the drivers on long-term variations in CH_4 emissions.

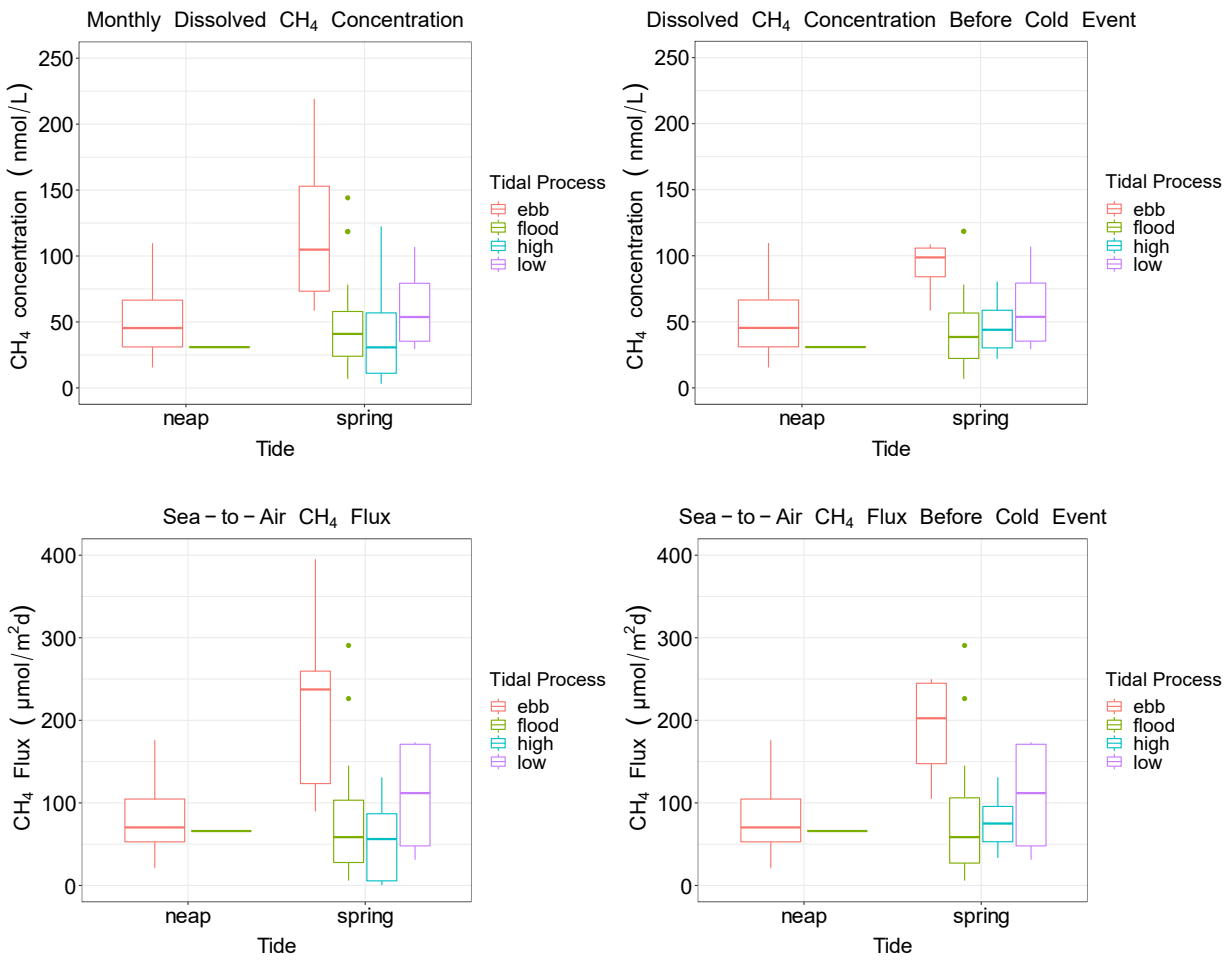

Figure 2.6 Boxplots of dissolved CH_4 concentrations in mangrove creeks under different tidal processes (left: over study period; right: before the extreme cold event in February 2021).

Although this study area is located in a microtidal estuary, CH_4 concentrations in both ebbs and floods were higher in spring tide than in neap tide, similar to the observations at mangrove-dominated macrotidal creeks in the Amazon region (Call et al. 2019), rather than the findings in the microtidal estuary in southern Moreton Bay, Queensland, Australia (Call et al. 2015). We speculate that it was not only related to tidal magnitude but also associated with local topographic characteristics, e.g., the relative elevation of high tide lines and slopes of banks and the amount of floodwater. Although the local tidal range is small, even in neap tide, flood water can immerse upper tidal sediment due to its low elevation. Hence, the immersion area during flood/high tide

could determine the possible additional porewater CH_4 exchange. The larger the area of flood water inundation was, the greater the potential of CH_4 input from the upper intertidal sediment/soil. Furthermore, the amount of seawater with less CH_4 flushing into upper streams during flood/high tide should be taken into account because it is the balance between CH_4 input from sediment and the dilution of seawater depleted of CH_4 that controls the dissolved CH_4 concentration.

Higher CH_4 emissions in spring tides were caused by CH_4 input from upper intertidal sediment during water inundation (Call et al. 2019). Hence, as in Amazon mangrove creeks, a larger immersion area caused by macrotides could undoubtedly release more CH_4 (Call et al. 2019). By comparison, at Kangaroo Island in southern Moreton Bay, Queensland, Australia, the water inundation effect on CH_4 emissions from upper tidal sediment was probably not large enough to exceed the seawater dilution effect during flooding in spring tides due to the smaller amplitude of micro tides. In contrast, the release of porewater CH_4 by tidal pumping in neap tide was more significant (Call et al. 2015). Although Harbor Island is located in a microtidal estuary and the tidal amplitude is small even during spring tide, it is a flood tidal delta. Therefore, a larger area of upper intertidal sediment could be immersed during floods in spring tides than in neap tides, leading to more CH_4 exchange from upper intertidal sediment, which exceeded the dilution effect. Tidal control of CH_4 concentrations is a combined effect of tidal processes, tidal magnitude, topographic characteristics, the amount of porewater exchange, and the dilution effect of flooding water during floods.

2.4.3 Extreme cold event and precipitation/water level

Bimonthly investigations from July 2020 to May 2021 showed that CH_4 concentrations in creeks of Harbor Island were high in July and September, then decreased during the fall until winter or early spring, and then increased. It should be noted that CH_4 concentrations at AM4 and

AM5 along the south mangrove creek in March and May 2021 were much larger than those in the same months in 2019 (Figure 2.3). The same was true for CH_4 fluxes in May 2021 (Figure 2.5c). They were even larger or comparable to those in the summer months. The floating chamber CH_4 fluxes in March and May 2021 were also much larger than those in March and May 2019 (Figure 2.5b). There was no doubt that extra CH_4 was released from the sediment to the water column and to the atmosphere in March and May 2021.

Previous discussions have shown that CH_4 concentrations and fluxes in mangrove creeks were highest during ebb in spring tides. The investigation in May 2021 was in this period; therefore, the progressive export of CH_4 along the creek during ebb plus the addition of porewater CH_4 in upper intertidal sediment under water inundation were possible factors that caused high CH_4 emissions (Call et al. 2019; Jacotot et al. 2018). To avoid elevated CH_4 concentrations caused by other factors after the extreme cold interfering with understanding the impact of the tidal process, we compared the tidal effect on both all data and data before the cold event. As Figure 2.6 shows, although CH_4 concentrations during ebb tide in spring tides slightly decreased, the influences of tidal process and amplitude were similar. On the other hand, there probably existed other drivers for the unexpected increase in CH_4 emissions after the cold event.

Another possibility was that more organic carbon was buried due to the death of mangrove forests during extreme events, which provided more carbon sources for methanogenesis. In addition, less salinity in May 2021 caused by large precipitation (Figure 2.1f) could benefit the production of CH_4 in sediment porewater due to less competition from sulfate reduction (Chuang et al. 2016; Lee et al. 2008).

In Figure 2.8a, dissolved CH_4 concentrations increased slightly with increasing salinity except in May 2021, which was consistent with the diel variation in CH_4 concentrations in August

2019. Notably, the extraordinarily high CH_4 concentrations corresponded to less salinity in May 2021, implying an extra input of CH_4 to the mangrove creeks. In contrast to flood tides, lower salinity was probably caused by heavy rain (Figure 2.1f). Similar to the situation in May 2021, low salinity also occurred in May 2019 (Figure S4) due to rain (Figure 2.1). However, the dissolved CH_4 concentrations in May 2019 were 3.5~10-fold lower than those in May 2021. Hence, less salinity was probably not a sufficient reason to explain the elevated CH_4 concentration. Moreover, the dissolved CH_4 concentrations in May 2021 were higher than others, including those in the same tidal status. Hence, the extra input CH_4 might be related to the additional carbon sources deposited in sediment from dead mangroves.

Although the mortality of mangrove forests occurred in February 2021, the increase in dissolved CH_4 concentration in March was not as remarkable as that in May. The primary increase occurred in the south creek of Harbor Island (AM4, AM5, AM6), which was comparable to the previous summer and early-autumn months and much larger than those under the same tidal status (flood in spring) and similar tidal levels in March 2019 (Figure 2.8b). The higher monthly average temperature in March 2021 than in March 2019 was probably a driver for more CH_4 production in March 2021. However, since the monthly average temperature in May 2019 was slightly higher than that in March 2021, elevated CH_4 concentrations might be triggered by other factors rather than temperature. The salinity in March 2021 was similar to that of the majority of mangrove creek samples, and DO was within the range of all samples (Figure 2.8). Although we did not measure the organic carbon deposited in sediment after the death of mangrove forests, it is most likely that more carbon sources for methanogenesis in the mangrove sediment were the primary factor leading to more CH_4 production and transport, which caused a dramatic increase in dissolved CH_4 in mangrove creeks and higher chamber fluxes.

After the freeze event, compared to March 2021, the lower salinity in May 2021 probably further promoted the production of CH_4 due to less competition in electrons for methanogenesis in a less sulfate environment (DeLaune et al. 1983). The opposite tidal processes during the investigation in March (flood/high) and May (ebb) might be another reason why CH_4 concentrations in creeks were relatively lower in March. However, although the dissolved CH_4 concentrations in the middle and northern creeks (AM16, AM6, AM17 and AM8) were low in March 2021, the CH_4 concentrations in the southern creek were high (Figure 2.8b). These results indicated high spatial variations in methanogenesis and CH_4 exchange between sediment porewater and the water column.

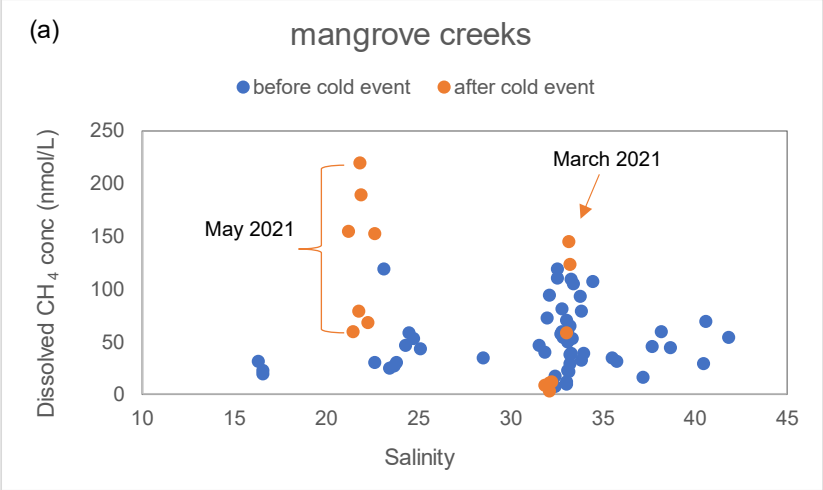

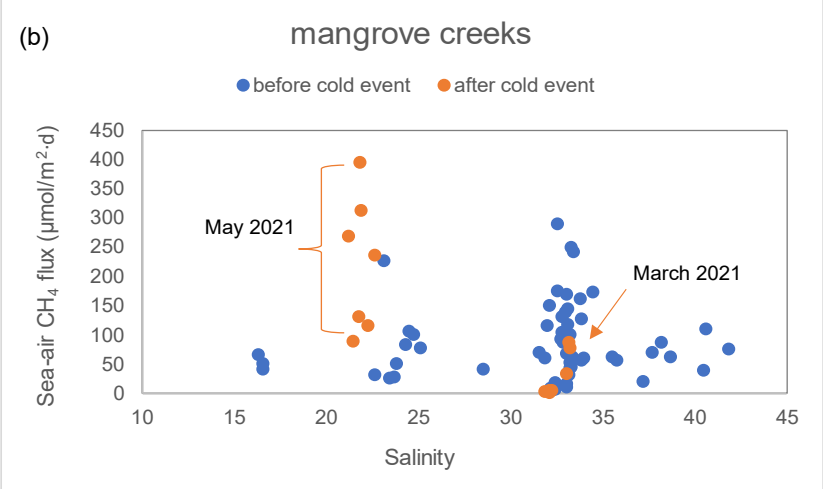

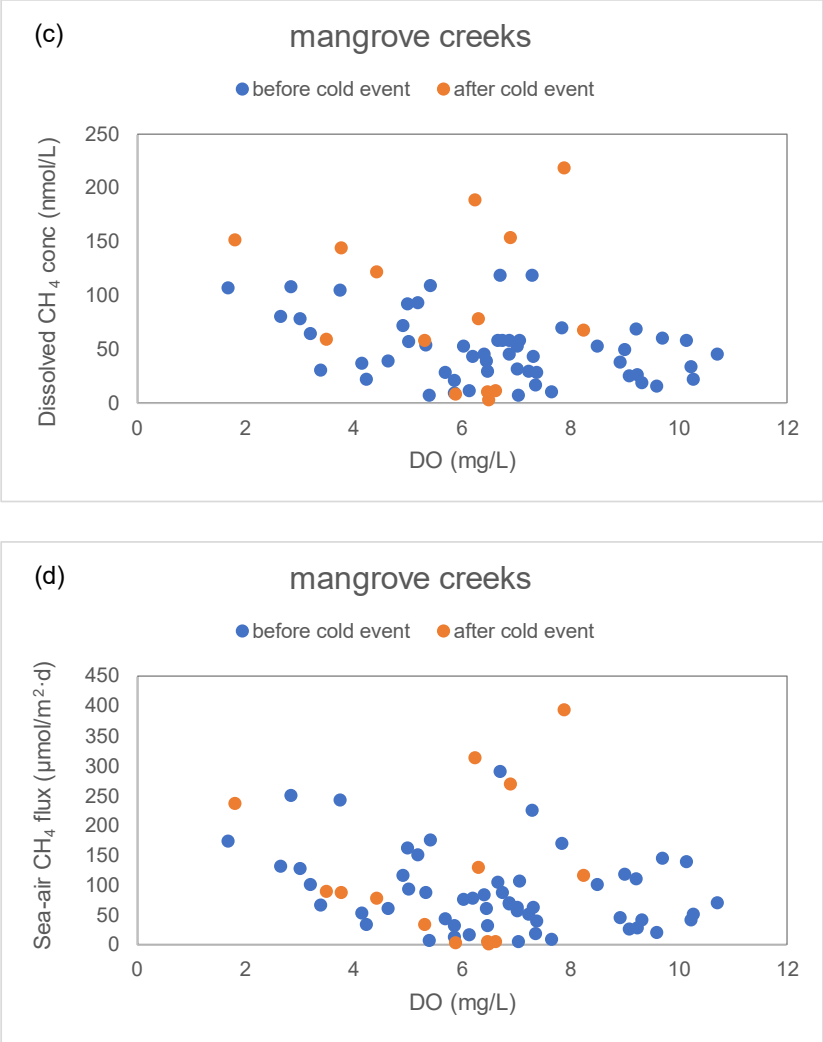

Figure 2.7 Relationships between dissolved CH_4 concentration and salinity (a) and DO (c) in mangrove creeks, as well as sea-air CH_4 flux and salinity (b) and DO (d)

After the extreme cold event in 2021, a pronounced increase in sea-air CH_4 fluxes appeared in May 2021 (221.4±113.8 ~ 664.7±341.5 μmol/m^2·d) (Figure 2.5), which was higher than the second highest fluxes in September 2020 (119.4±40.9 ~ 254.0±87.0 μmol/m^2·d) and four times those in the same month in 2019 (48.2±11.2 ~ 110.2±25.6 μmol/m^2·d). Although they were much lower than the CH_4 emissions from dead mangrove soils in lagoons in the southwestern Gulf of Mexico (up to 1300±270 μmol/m^2·d in the rainy season and 9-fold higher than those of preserved mangroves) (Romero-Uribe et al. 2021), we are probably concerned that there will be more CH_4

emissions than in previous years because we have no idea about the duration of mangrove debris degradation and recovery in these forests.

2.4.4 Methane offset to local carbon sequestration

Calculating using the monthly average CH_4 flux from July 2020 to May 2021 (97.2±88.4 μmol/m^2·d), the annual CH_4 flux from the mangrove creeks at Harbor Island was estimated to be 35.5 mmol/m^2·y. Accounting for a carbon sequestration rate at Harbor Island of 253 g/m^2·y (Bianchi et al. 2013), CH_4 emissions from mangrove creeks could offset 0.17% of the buried carbon in mangrove forests. This evaluation was only ~2% of the global mangrove offset (~9%) (Al-Haj and Fulweiler 2020)). This result is reasonable because the global mean value (4557.0±1102.1 μmol/m^2·d) applied in the estimation of mangrove CH_4 offset was over 45 times that in this study (97.21±88.4 μmol/m^2·d), and the carbon burial rates used in the two estimates were similar (225.6 g C/m^2·y globally vs. 253 g C/m^2·y at Harbor Island).

As in previous comparisons, CH_4 emissions from mangrove forests located in low salinity water or polluted areas could be up to two orders of magnitude higher than those in saline estuaries with less disturbance (Barber et al. 1988; Chuang et al. 2017). Such heteroscedasticity in CH_4 emissions worldwide exists, causing a positively skewed distribution (mean > median); thus, the statistical assumptions and method selection are very sensitive to the estimates (Rosentreter et al. 2021b). Both local and global data showed that CH_4 fluxes were positively skewed (mean > median), indicating that more fluxes were in a low-level range. In comparison with the difference between the mean and media values in regional CH_4 fluxes, there was a much larger discrepancy in the global dataset (e.g., mean: 4557.0±1102.1 μmol/m^2·d and median: 279.2 μmol/m^2·d) (Al-Haj and Fulweiler 2020). Hence, caution should be taken when applying the mean value in

upscaling calculations, which could probably cause an overestimate. In future work, we need to develop more reliable and precise approaches to estimate regional and global CH_4 emissions.

Upscaling CH_4 emissions to all mangrove forests in Texas (33.16 km^2) (Thorhaug et al. 2019), the annual CH_4 emissions from the Texas costal mangrove were approximately 14.12×10^6 gC/year. Compared with global estimates of the CH_4 offset to carbon deposits in mangrove ecosystems, this region is a weak CH_4 source.

2.5 Conclusion

Diurnal and seasonal variations in CH_4 concentrations revealed that not only tidal processes and tidal amplitude (spring and neap) but also topographic characteristics are crucial factors that control CH_4 cycling in mangrove creeks at our study site. Export of CH_4 from inside creeks to outside bay and tidal pumping of porewater led to CH_4 concentration increase during ebbs. Flushing of bay water during flood/high tide could decrease CH_4 concentrations in creeks by dilution and release more CH_4 emissions due to inundation of upper intertidal sediment. The balance between dilution and CH_4 exchange from intertidal porewater determines the variation in CH_4 during flood/high tide. Elevated CH_4 emissions appeared in spring tides than in neap tide, which can be explained by the larger area of water immersion of upper intertidal sediment that released additional CH_4. Unlike some microtidal-dominated estuaries, CH_4 emissions were higher during spring tides than during neap tides due to the different water inundation areas of upper intertidal sediment. Although there was a small tidal range in neap tides, flood water could still immerse a part of the upper intertidal area over this tidal flat delta. This result indicated that topographic characteristics should be considered in combination with tidal amplitudes in interpreting tidal controls on CH_4 emissions.

Elevated CH_4 concentrations after the freeze were interpreted to result from large deposits of organic matter created by dead mangroves during the freezing event. Heavy precipitation was another factor that further enhanced CH_4 emissions from mangrove sediments and soils by forming a broader area of water inundation and by decreasing salinity. Although we do not know the mortality data of mangroves and carbon deposits after extreme cold events, current data suggest more potential CH_4 emissions as feedback of such extreme weather events in the future.

Diffusive CH_4 fluxes at the sea-water interface in different months acquired using the floating chamber approach and empirical equations were 85.2±84.2 ~ 206.2±213.3 μmol/m^2·d during the study period. Under some conditions, the fluxes obtained using floating chambers could match those from empirical equations. The artificially unified annual CH_4 fluxes from July 2021 to May 2022 ranged from 0.6 to 395.1 μmol/m^2·d (mean: 94.7±81.3 μmol/m^2·d, median: 70.7 μmol/m^2·d). Calculated using the mean value, the CH_4 emissions could offset 0.17% of the locally buried organic carbon in Harbor Island, indicating that local mangrove ecosystems are a weak CH_4 source and have a main function as blue carbon reservoirs.

CHAPTER III: TEMPORAL VARIATIONS IN METHANE EMISSIONS FROM SEAGRASS MEADOW

Abstract

Seagrass meadows are considered to be pertinent blue carbon reservoirs but have the potential to release methane (CH_4) into the atmosphere. To study the dynamics of CH_4 emissions in subtropical seagrass, we investigated seasonal variations in CH_4 concentrations and related environmental parameters from June 2018 to July 2021, as well as diurnal variations in August 2019 at lagoonal estuaries of southern Texas, USA, northwest coast of the Gulf of Mexico. Both diurnal and long-term variations showed a tight relationship between CH_4 concentration and dissolved oxygen, dissolved inorganic carbon, and pH, which was driven by photosynthesis and respiration of the seagrass ecosystem. Seagrass photosynthetic oxygen in sediment played a significant role in reducing CH_4 production and transport. Seasonal variations in CH_4 concentrations in seagrass meadows coincided with seagrass growth patterns, indicating a possible plant mediation of CH_4 emissions from sediment to water. The unified diffusive CH_4 fluxes were 12.3~816.2 μmol/m^2·d over the range of the current global seagrass CH_4 database (1.2~401.5 μmol/m^2·d). These CH_4 emissions were estimated to offset 1.4%~2.2% of the blue carbon deposited in local seagrass meadows. This study reported the largest CH_4 emissions from seagrass meadows to date.

3.1 Introduction

Seagrass meadows are not only crucial blue carbon reservoirs in coastal areas but also have great capabilities in climate mitigation due to their efficiency in capturing and converting light energy into organic matter and utilizing additional dissolved inorganic carbon (Purvaja et al. 2020; Ricart et al. 2020). However, as in other coastal vegetated ecosystems, e.g., mangroves and salt

marshes, large deposits of organic matter in seagrass also provide plenty of carbon sources for microbial production and subsequent respiration, leading to a high potential of greenhouse gas emissions, e.g., methane (CH_4) (Macreadie et al. 2019; Rosentreter et al. 2018b). The global CH_4 flux at seagrass was estimated to be 0.031 to 0.065 Tmol CH_4-C/year (Al-Haj and Fulweiler 2020). Although CH_4 has a warming potential 28 times that of carbon dioxide (CO_2) at a 100-year horizon (IPCC 2014; Saunois et al. 2020), in comparison with CO_2 captured by seagrass, the offset of CH_4 is minor; hence, seagrass ecosystems are still taken as a sink of atmospheric CO_2 (Al-Haj and Fulweiler 2020; Banerjee et al. 2018; Rosentreter et al. 2021a). The restoration of seagrass meadows in Virginia Coast Reserve Long-Term Ecological Research at South Bay Virginia, US showed that although CH_4 and N_2O emissions were enhanced after the restoration of seagrass, their offset to CO_2 removed by seagrass was quite limited, particularly compared with the large amount of CO_2 sequestration in the long term, e.g., 15 years, which provided a promising approach in climate mitigation (Oreska et al. 2020).

Located in vulnerable coastal areas, seagrass meadows are easily destroyed by human activities (e.g., dredging, filling, and vessel grounding) or degraded due to eutrophication, hypoxia, sea-level rise, and extensive extreme climate events (Burkholder et al. 2007; Che et al. ; Congdon et al. 2019; Hicks et al. 1998; Saunders et al. 2013; Thorhaug et al. 2017; Wilson and Dunton 2018). Some studies have shown that seagrass loss could trigger an increasing risk of more CH_4 emissions (Burkholz et al. 2020; George et al. 2020; Lyimo et al. 2018). Lyimo et al., 2018 found that shading and grazing could release more CH_4 from seagrass sediment because the degradation of the biomass of seagrass can support both sulfate-reducing bacteria and methanogens. The absence of an oxygen supply derived from photosynthesis due to the death of seagrass could lead to a more hypoxic sediment environment that would benefit sulfate reduction and methanogenesis

(Lyimo et al. 2018). Moreover, both sediment incubation experiments in the Red Sea and in situ mesocosm experiments in Tanzania have demonstrated that warming can increase CH_4 fluxes from seagrass sediment (Burkholz et al. 2020; George et al. 2020). High temperatures could enhance CH_4 emissions and sulfide (H_2S) concentrations in sediment and decrease seagrass photosynthesis (George et al. 2020). That $\delta^{13}C$-CH_4 in sediment exposed to a higher temperature became more negative indicated that the increase in CH_4 concentration was caused by more methanogen production (Burkholz et al. 2020).

Seagrass meadows along the Gulf of Mexico coastal areas are ubiquitous blue carbon sinks (Thorhaug et al. 2019). An early study at Caesar Creek, Florida, found higher methanogenic activities in seagrass *Thalassia testudinum* sediment than in sediment of *Syringodium sp.* and two coral reefs, suggesting that metabolic processes such as photosynthetic oxygen could affect the production of CH_4 (Oremland 1975). Diel variations in O_2, N_2, and CH_4 in sediment bubbles and rhizome gases in the seagrass *T. testudinum* further verified that O_2 produced during photosynthesis could be delivered via the rhizome system to sediment, and O_2 concentrations were negatively related to CH_4 concentrations in sediment and rhizome gases (Oremland and Taylor 1977). However, a later study on CH_4 fluxes from sediments of both live seagrass and dead seagrass in Florida Bay suspected the significance of plant mediation of CH_4 flux from seagrass (Barber and Carlson 1993). This was opposite to the plant-mediated transport of CH_4 observed in many emergent and submerged macrophytes (Chanton et al. 1992; Fonseca et al. 2017; Laanbroek 2009; Whiting and Chanton 1992; Zhang et al. 2019).

Although the northwest coasts of the Gulf of Mexico are essential seagrass habitats, few studies have been published about CH_4 emissions from this region. As the most extensive seagrass habitat in the northwestern Gulf, Laguna Madre is among the most hypersaline lagoons in the

world (Thorhaug et al. 2017). It is covered primarily by *Halodule wrightii*, *Thalassia testudinum*, and *Syringodium filiforme* (Wilson and Dunton 2018). In recent decades, seagrass meadows in this region have experienced extensive human activities, e.g., dredging and climate change events, e.g., hurricanes and drought events, which have undoubtedly changed seagrass coverage, biomass, and species distributions (Congdon et al. 2019; Dunton et al. 2003; Erftemeijer and III 2006; Wilson and Dunton 2018). In this study, we observed the seasonal and diurnal variations in CH_4 emissions in this subtropical seagrass meadow and discussed the factors that influence CH_4 transport from sediment to the water column and from water to atmosphere. Data presented supplement sparse CH_4 data along the Gulf of Mexico and provide a more thorough understanding of CH_4 cycling in subtropical areas.

3.2 Materials and Method

3.2.1 Study area

Upper Laguna Madre is the northern part of Laguna Madre, located on the southeast coast of Texas, northwest of the Gulf of Mexico (Figure 1.3 for overview, and Figure 3.1 for detail this chapter). It is separated from the Gulf of Mexico by sandy barrier islands of Padre Island, and only through the Packery Channel can it access the water of the Gulf of Mexico. It has a semiarid subtropical climate, with little precipitation and high evaporation. With little freshwater inflow, low tidal range, and shallow bathymetry (~1 m), it is one of the hypersaline lagoons in the world (Eldridge and Morse 2000; Onuf 2007; Tunnell et al. 2002). In the middle of the lagoon, there is a channel 125 feet wide and 12 feet deep for boating and marine transportation. It is a part of the Gulf Intracoastal Waterway of Texas (GIWW-T), which is 379 miles in length along the Texas coastline and handles 67% of all GIWW traffic (Kruse et al. 2016).

Upper Laguna Madre is a crucial seagrass habitat, with seagrass meadows covering approximately 66% of the floor (Dunton and Reyna 2019). *H. wrightii* (56.0 ± 39.1%, 2018) dominated the region, followed by *S. filiforme* (9.2 ± 23.1%, 2018) and *H. engelmannii* (0.5 ± 4.7%, 2018) (Dunton and Reyna 2019). *H. wrightii* (shoal grass) prefers to root at a surface in the oxic zone. Its rhizome internodes are 0.75~3.5 cm long (Phillips and Menez 1988). Due to the supersalinity in Upper Laguna Madre, only a few submerged phytoplankton can survive, e.g., the harmful "brown tide" organism *Aureoumbra lagunensis* (Cira et al. 2021). Seagrass meadow covering the Upper Laguna Madre provides vital nursery habitat to many birds, fish, and invertebrate species. It also serves as a major area for public recreation, e.g., boating and fishing.

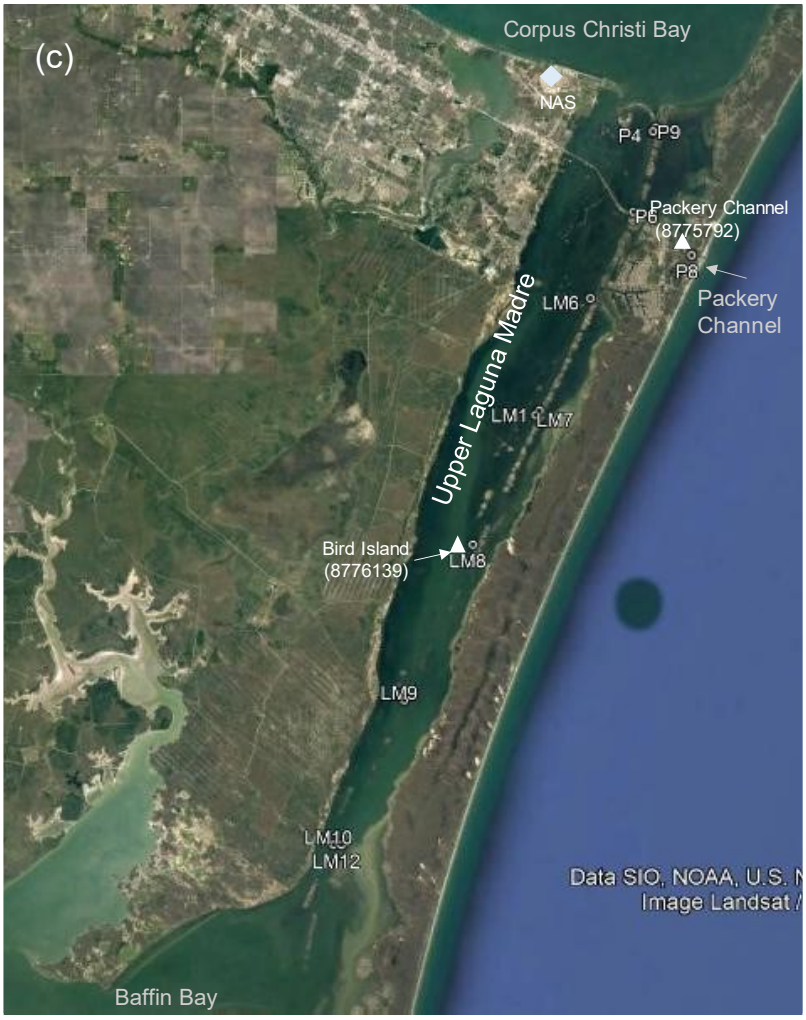

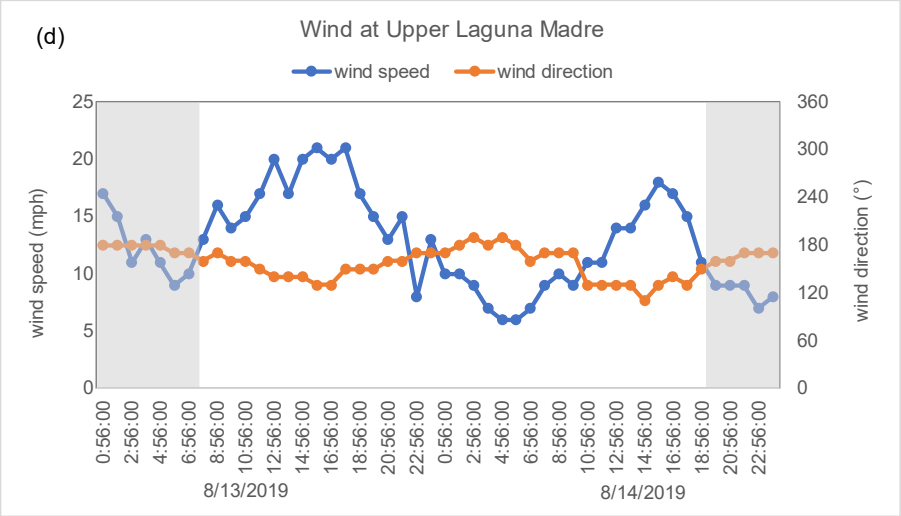
(d)
Wind at Upper Laguna Madre
wind speed
wind direction
wind speed (mph)
wind direction (°)
25
20
15
10
5
0
360
300
240
180
120
60
0
0:56:00
2:56:00
4:56:00
6:56:00
8:56:00
10:56:00
12:56:00
14:56:00
16:56:00
18:56:00
20:56:00
22:56:00
8/13/2019
8/14/2019

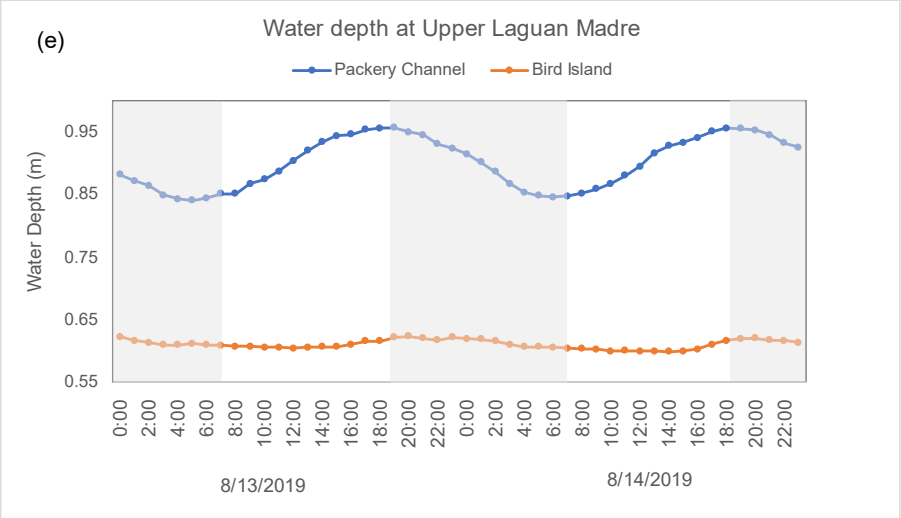
(e)
Water depth at Upper Laguan Madre
Packery Channel
Bird Island
Water Depth (m)
0.95
0.85
0.75
0.65
0.55
0:00
2:00
4:00
6:00
8:00
10:00
12:00
14:00
16:00
18:00
20:00
22:00
8/13/2019
8/14/2019

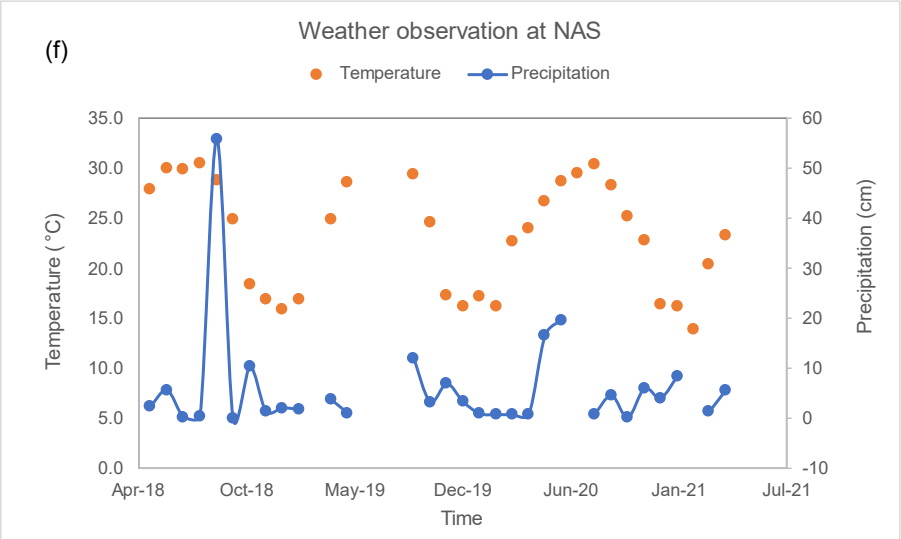
(f)
Weather observation at NAS
Temperature
Precipitation
Temperature (°C)
Precipitation (cm)
35.0
30.0
25.0
20.0
15.0
10.0
5.0
0.0
60
50
40
30
20
10
0
-10
Apr-18
Oct-18
May-19
Dec-19
Jun-20
Jan-21
Jul-21
Time

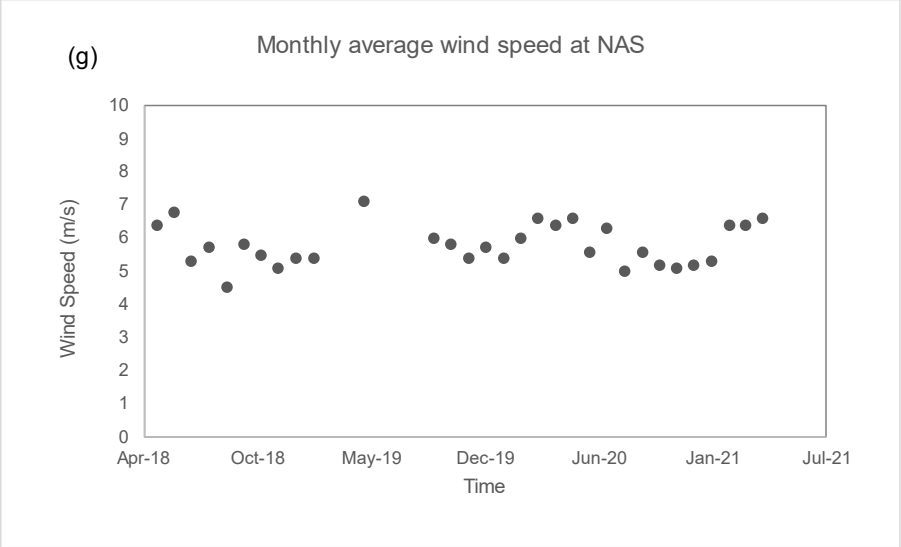

Figure 3.1 Study sites at Upper Laguna Madre

(c) Sampling sites. LM1, LM9, P7, and P9 are located in the seagrass meadow; LM7, LM11, P4 and P6 are located in the Gulf Intracoastal Water Way (channel); LM7 and LM11 are close to LM1 and LM9, respectively; and P7 and P9 are close to P4. Sites at seagrass meadow are the primary study objects in this study. (c) Wind speed and wind direction at the Corpus Christi NAS meteorological station (Figure 3.1c, blue diamond) during diurnal observation in August 2019. (d) Water depth at the Packery Channel station (8775792) (Figure 3.1c, write triangle) connecting the Gulf of Mexico and Bird Island hydrological station (8776139) (Figure 3.1c, write triangle) close to the sampling sites during diurnal observation in August 2019. Shading areas in (c) and (d) represent nighttime. (f) and (g) Monthly average temperature, total precipitation and monthly average wind speed at the Corpus Christi NAS meteorological station (Figure 3.1c, blue diamond) during the study period.

3.2.2 Study method and sampling

Sampling was performed at Upper Laguna Madre (LM) in June 2018, January, March, May, July, August 2019, and bimonthly from January 2020 to May 2021 (Figure 3.1). Diurnal

observations and sampling were carried out at site LM1 (27°32'39.16"N, 97° 17'9.5"W, seagrass) of Upper Laguna Madre on August 13th and 14th, 2019 (Figure 3.1). To thoroughly understand the transport of CH_4 from sediment to the atmosphere via the water column, we investigated CH_4 emissions at both the water-air and sediment-water interfaces.

3.2.2.1 Water and air sampling

Surface water and ambient air samples were collected to determine dissolved CH_4, sea-air CH_4 flux, dissolved inorganic carbon (DIC), and chlorophyll-*a* (Chl-*a*). Simultaneous water parameters (salinity, pH, dissolved oxygen (DO), temperature) were measured using a multiparameter meter (HI98194, Hanna Instruments). Another fourteen bottles of water were collected at the same time as the first samples at LM1 and/or LM7 for the water incubation experiment. In addition, weather (wind speed, wind direction, and temperature), water level, and current data from nearby meteorological and hydrological stations were acquired online (https://tidesandcurrents.noaa.gov/, station: Bird Island (8776139); https://www.ncei.noaa.gov/maps/lcd/, station: NAS, (Figure 3.1c)). These data were applied to calculate the CH_4 flux and analyze factors controlling CH_4 emissions at the sea-air interface (Chuang et al. 2017; Lorenson et al. 2016).

During diurnal observations, all sampling and in situ measurements were performed every 4 hours to determine 24-hour variations at LM1. For comparison with this location, water and air samples were collected at another seagrass site (LM9) and two channel sites (LM7 and LM11) close to seagrass sites, respectively, on August 13th, 2019 (Figure 3.1).

Floating chambers were set up at LM1 to measure the total in situ CH_4 emissions from surface water to the atmosphere and calculate the standard gas transfer velocity. During diurnal observations, they were built in both daytime and night. A linear increase in the CH_4 proportion

(R^2 >0.95) in the chamber in one hour indicated diffusive emission. If there was a dramatic rise in the CH_4 proportion, bubble CH_4 would be released from water.

To determine CH_4 emissions at the sediment-water interface, sediment cores were collected, and sediment chambers were established for sediment incubation experiments at LM1, and LM9. Porewater CH_4 profiles through sediment cores were applied to calculate diffusive CH_4 fluxes at the sediment-water interface. The variation in CH_4 in the overlying water of sediment chambers before and after incubation could indicate total sediment-water CH_4 fluxes during the experiment.

3.2.2.2 Sediment core collection and sediment incubation experiment

Sediment cores were collected at LM1 and/or LM9 using 50 cm polycarbonate tubing 6.67 cm in diameter in May, August 2019 and September 2020. For each core, porewater samples were drawn using Rhizon samplers (Coffin et al. 2013; Seeberg-Elverfeldt et al. 2005; Treude et al. 2014) and 30 ml syringes from the 2 cm interval holes predrilled in a 1/8 inch and sealed as soon as the cores were collected. The core samples inserted with Rhizon samplers were stored in an ice box and transported to the lab at the same time as other samples. Once the syringe was full, porewater samples were transferred to 30 ml vials previously filled with ultrahigh purity N_2 gas, and 0.2 ml saturated $CuSO_4$ solution was injected immediately and then stored in the refrigerator until measurement.

Sediment incubation experiments were carried out using 70 cm polycarbonate tubing 6.67 cm in diameter at LM1 and LM9 in August 2019. At LM1, the sediment chamber was inserted into the sediment until the chamber was submerged into water entirely. It stood up in situ for nearly 24 hours. Sediment chambers at LM9 were collected in the same way as sediment cores and moved to LM1, submerged and fixed along with the LM1 sediment chamber. After in situ incubation, the

overlying water of each chamber was collected using 60 mL serum glass bottles, the septa were sealed immediately, and 1 ml saturated $CuSO_4$ solution was added.

3.2.3 Analytical Methods

All samples were stored in a refrigerator and measured within two months after they were collected. Concentrations of dissolved and airborne CH_4 were measured by the headspace equilibration technique and gas chromatography (GC, Agilent 6890N) (Magen et al. 2014; Reeburgh 2007). DIC concentrations were determined using a UIC CM5017 Coulometer. Chlorophyll *a* (Chl-*a*) concentrations were measured using a Turner 10-AU. Porewater H_2S in porewater was determined by colorimetric analysis of the methylene blue method (Cline 1969; Reese et al. 2011). The above works were performed in the Isotope Core Laboratory at Texas A&M University-Corpus Christi. The $\delta^{13}C$-CH_4 values of some samples were analyzed at the Stable Isotope Lab of the University of California-Davis.

3.2.4 Calculation of fluxes

3.2.4.1 Floating chamber methane flux

The sea-air CH_4 flux acquired using floating chambers is called the chamber flux in this paper. If the CH_4 proportion increased linearly, the flux was calculated using the growth rate (ppm/minute) of the CH_4 proportion in the chamber during observation. If there was a dramatic increase, the flux was calculated using the difference between the final and initial proportions.

$$F_{fc} = s \times \frac{P}{R \times T} \times \frac{V_{chamber}}{A_{chamber}} \times t \qquad (1)$$

where F_{fc} is the chamber flux (μmol/m^2·h or μmol/m^2·d); s is the growth rate of CH_4 proportion (ppm/min) in linear increase or CH_4 proportion variation before and after observation (ppm/hr) in surge increase; P is gas pressure inside the chamber (Pa); R is universal gas law constant (8.314510 m^3 Pa K^{-1} mol^{-1}); $\frac{P}{R \times T}$ is to convert volume proportion to molar proportion

based on Law of Avogadro's; $V_{chamber}$ is volume of the chamber (m^3); $A_{chamber}$ is area of the chamber connecting surface water (m^2); and t is time efficient (convert from min to hour or day).

3.2.4.2 Diffusive methane flux at the sea-air interface

The diffusive CH_4 flux at the sea-air interface was calculated using the gas-transfer model (Wanninkhof 1992).

$$F = k_v \cdot (C_{obs} - C_{eq}) \quad (2)$$

where F is the flux of gas to the atmosphere ($mmol/m^2 \cdot d$ or $\mu mol/m^2 \cdot h$); C_{obs} represents the measured concentration of dissolved CH_4 in water (nmol/L); C_{eq} is the concentration of CH_4 in equilibrium with the atmosphere at in situ temperature (nmol/L), calculated for each sample from the temperature- and salinity-dependent equilibrium relationship (Wiesenburg and Guinasso 1979); and k_v is the gas transfer velocity (cm/h), calculated based on the Schmidt number (Sc) normalized to k_{660}, which is called the standard gas transfer velocity.

$$k_v = k_{660} \times (\frac{Sc}{660})^{-\frac{1}{2}} \quad (3)$$

where Sc is defined as the kinematic viscosity of water divided by the diffusion coefficient of the gas, which is dependent on the water temperature and salinity (Wanninkhof 1992; Wanninkhof 2014). The calculation of Sc followed Wanninkhof 2014 since water temperatures exceeded 30°C. k_{660} is calculated using four methods: in situ floating chamber flux (k_{fc}) and empirical equations (k_{model}).

Floating chambers: $k_{fc} = F_{fc}/(C_{obs} - C_{eq})$ (4)

Empirical equations:

J2008 (Jiang et al. 2008): $k_{J2008} = 0.314\mu^2 - 0.436\mu + 3.990$ (5)

W2014 (Wanninkhof 2014): $k_{W2014} = 0.251\mu^2$ (6)

VD2019 (Van Dam et al. 2019): $k_{VD2019} = 2.3 + 1.9u$ (daytime)

$k_{VD2019} = 18.5 - 5.3\mu + 0.64\mu^2$ (night) (7)

R2001 (Raymond and Cole 2001): $K_{600} = 2.06e^{0.37\mu}$ (8)

where μ is the hourly mean wind speed at 10 m at nearby weather stations acquired online: Monthly and daily average data from the station of NAS (WBAN:1926) in NOAA National Centers for Environmental Information Climate Dataset, https://www.ncdc.noaa.gov/cdo-web/datasets/LCD/stations/WBAN:12926/detail, and hourly data from station of Bird Island (8776139) in NOAA Tides & Current, https://tidesandcurrents.noaa.gov/stationhome.html?id=8775237).

3.2.4.3 Diffusive methane flux at the sediment-water interface

The diffusive CH_4 flux at the sediment-water interface was calculated using Fick's first law (Berner 1980).

$$J_s = -\emptyset(D_0 \cdot \theta^{-2})\left[\frac{dc}{dz}\right] \quad (9)$$

J_s is the diffusive CH_4 flux at the sediment-water interface; $\emptyset$ is the porosity of sediment, measured from the weight loss of sediment dried at 80°C (Coffin et al. 2014; Coffin et al. 2013; Morin and Morse 1999); D_0 is the diffusion coefficient for CH_4 in water (1.5×10^{-5} $cm^2 \cdot s^{-1}$) (Broecker and Peng 1974); θ is tortuosity, calculated using $\theta^2 = 1 - ln(\emptyset^2)$ (Boudreau 1996); and $\frac{dc}{dz}$ is the CH_4 gradient in porewater. Both the gradient of the first two layers of porewater and the gradient between bottom water and the first layer of porewater were applied to represent sediment-water CH_4 fluxes.

The incubation CH_4 flux at the sediment-water interface was calculated through the variation in CH_4 concentration in the overlying water before and after incubation.

$$F_{inc} = S \times \frac{V_{chamber}}{A_{chamber}} \times t \quad (10)$$

where F_{inc} is the sediment-water flux ($\mu mol/m^2 \cdot h$ or $\mu mol/m^2 \cdot d$); S is the variation in the CH_4 concentration in the overlying water of the sediment chamber before and after observation

(nmol/L); $V_{chamber}$ is the volume of overlying water in the chamber (m^3); $A_{chamber}$ is the area of the chamber (m^2); and t is the time coefficient (converted from min to hour or day).

3.2.5 Statistical analysis

Statistical analyses were performed using R software (version 3.6.1). Dissolved CH_4 concentrations were logarithmized before analysis. General linear models were built to determine the factors that influence CH_4 concentrations. Akaike information criterion correlation (AICc) was used in model selection. The variance information factor (VIF) was used to check collinearity. The Shapiro–Wilk W test at the $p<0.05$ level of significance was used to assess normality of residuals in the model. Homoscedasty was tested by the Brevsch-Pagan test with $p>0.05$.

3.3 Results

3.3.1 Diurnal and seasonal variation in dissolved methane and other parameters

Diurnal observations found that the dissolved CH_4 concentration at seagrass site LM1 decreased and reached its lowest value (28.3 nmol/L) before sunset, while the overnight CH_4 concentration increased and reached its highest value (79.1 nmol/L) before sunrise (Figure 3.2). Such variation in dissolved CH_4 concentration had a similar trend with DIC and was the opposite of pH, Chl-*a*, DO, and temperature. The $\delta^{13}C$-CH_4 in water was -57.8‰ ~ -57.3‰, indicating its biogenic origin (Kirschke et al. 2013; Schroll et al. 2020; Whiticar et al. 1986). When the CH_4 concentration was relatively higher, the corresponding $\delta^{13}C$-CH_4 was lower, and vice versa. Salinity varied from 31.8 to 32.7‰, combined with minor changes (0.02 m, Figure 3.1) in water depth, indicating that water exchange in this study area was weak.

During the whole study period, the dissolved CH_4 concentrations over the seagrass meadow were 62.3±49.9 nmol/L (11.5~258.2 nmol/L). The concentrations in winter (42.6±40.2 nmol/L, 11.6~133.6 nmol/L) were lower than those in other seasons. The dissolved CH_4 concentrations in

autumn (70.9±79.2 nmol/L, 14.4~258.2 nmol/L) and summer (67.9±48.8 nmol/L, 14.3~244 nmol/L) were relatively higher, and those in spring (61.1±34.2 nmol/L, 12.2~149.7 nmol/L) were in the middle. During the bimonthly observations from July 2020 to May 2021, CH_4 concentrations were highest in early autumn, decreased dramatically to their lowest values in winter, and then increased in spring (Figure 3.2d).

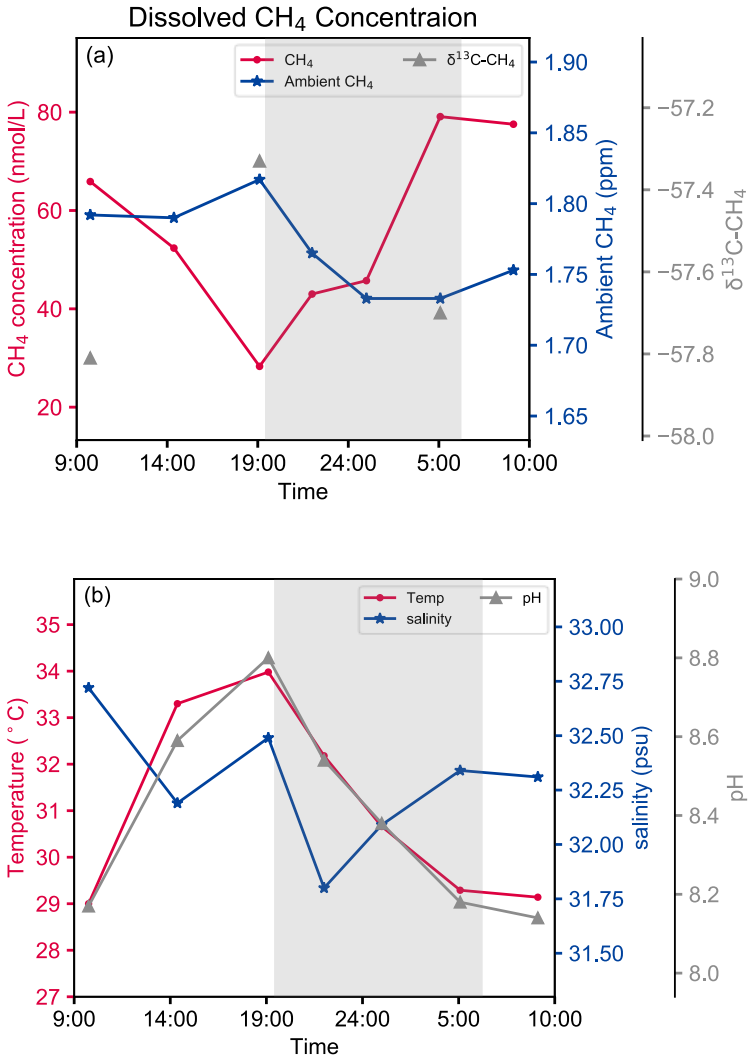

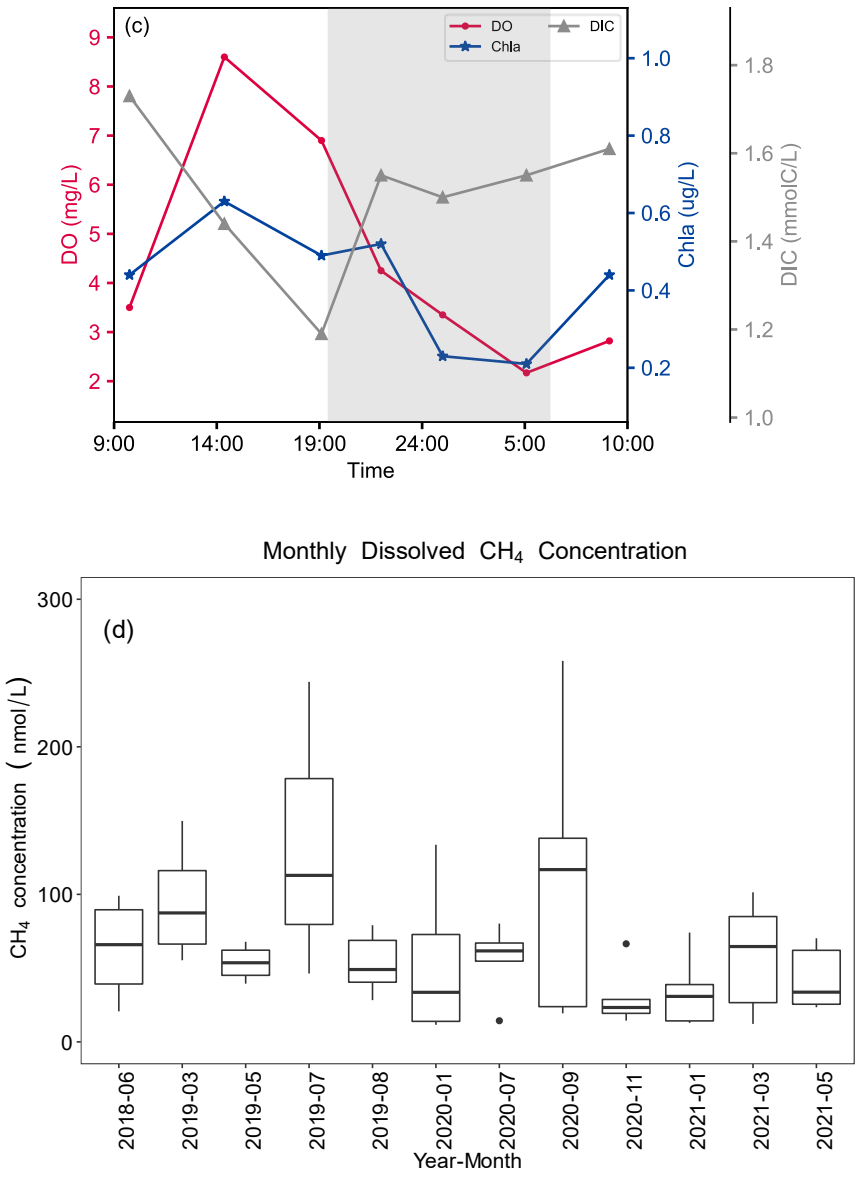

Figure 3.2 Temporal variations in CH_4 concentration and other parameters

(a)-(c) Diurnal variation in dissolved CH_4 concentration and other parameters: (a) dissolved CH_4 concentration, ambient air CH_4 and $\delta^{13}C$-CH_4; (b) temperature, salinity, and pH; (c) DO, Chl-*a* and DIC. (d) Seasonal variations in dissolved CH_4 concentration.

3.3.2 Variation of methane in floating chambers

Except in July 2020, the variations in CH_4 in floating chambers in one hour increased linearly (R^2>0.95), indicating that diffusion was a primary pathway of CH_4 at the sea-air interface

(Figure S1). The highest increase occurred in September 2020, suggesting that the transport of diffusive CH_4 from water to the atmosphere was largest in early autumn (Figure 3.2d). In July 2020, although the increase in CH_4 concentration in the floating chamber caused by diffusive transport was not as large as that in September 2020, there was a dramatic increase in one chamber at 30 minutes after the start of the experiment, which could be attributed to the input of ebullitive CH_4. This was the first and only time that bubble CH_4 was observed until now. During the diurnal observations, the increase rate of CH_4 concentration in chambers built in the daytime was larger than that set up at night. This result revealed that more CH_4 was released from water to the air in the daytime than at night.

Based on the increase in CH_4 concentration in the floating chamber, we found that during the bimonthly investigations in 2020-2021, the diffusive CH_4 flux at LM1 was highest in September and then decreased (Figure 3.3). In winter, floating chamber fluxes were lowest and then increased during spring. However, the floating chamber flux at LM1 in March 2019 was much larger than that in March 2021, although the dissolved CH_4 concentrations at both times were similar. Meanwhile, the large standard deviation among the three chamber fluxes in March 2019 indicated a high heteroscedascity of CH_4 emissions. The ebullitive CH_4 flux was observed in July 2020 and was 16.7 times the diffusive flux.

Changes in $\delta^{13}C\text{-}CH_4$ were negatively related to CH_4 concentration in floating chambers. Based on the relationship between $\delta^{13}C\text{-}CH_4$ and $1/CH_4$ (Figure 3.3c) obtained by conducting keeling plots (Garcias-Bonet and Duarte 2017), the $\delta^{13}C$ of dissolved CH_4 entering the chamber in August 2019 and July 2020 should be -57.7‰, which agreed with that of dissolved CH_4 in water. The $\delta^{13}C$ of ebullitive CH_4 was -65.8‰, much lower than that of diffusive CH_4, indicating possible oxidation of dissolved CH_4.

Calculated using the CH_4 fluxes in chambers, the standard gas transfer velocities (k_{fc}) ranged from 5.1 to 28.0 (Figure 3.3a), showing a large temporal discrepancy. During the diurnal observations in August 2019, k_{fc} in the daytime (12.9) was slightly larger than that at night (11.3). Different from floating chamber CH_4 fluxes, the highest k_{fc} appeared in November 2021.

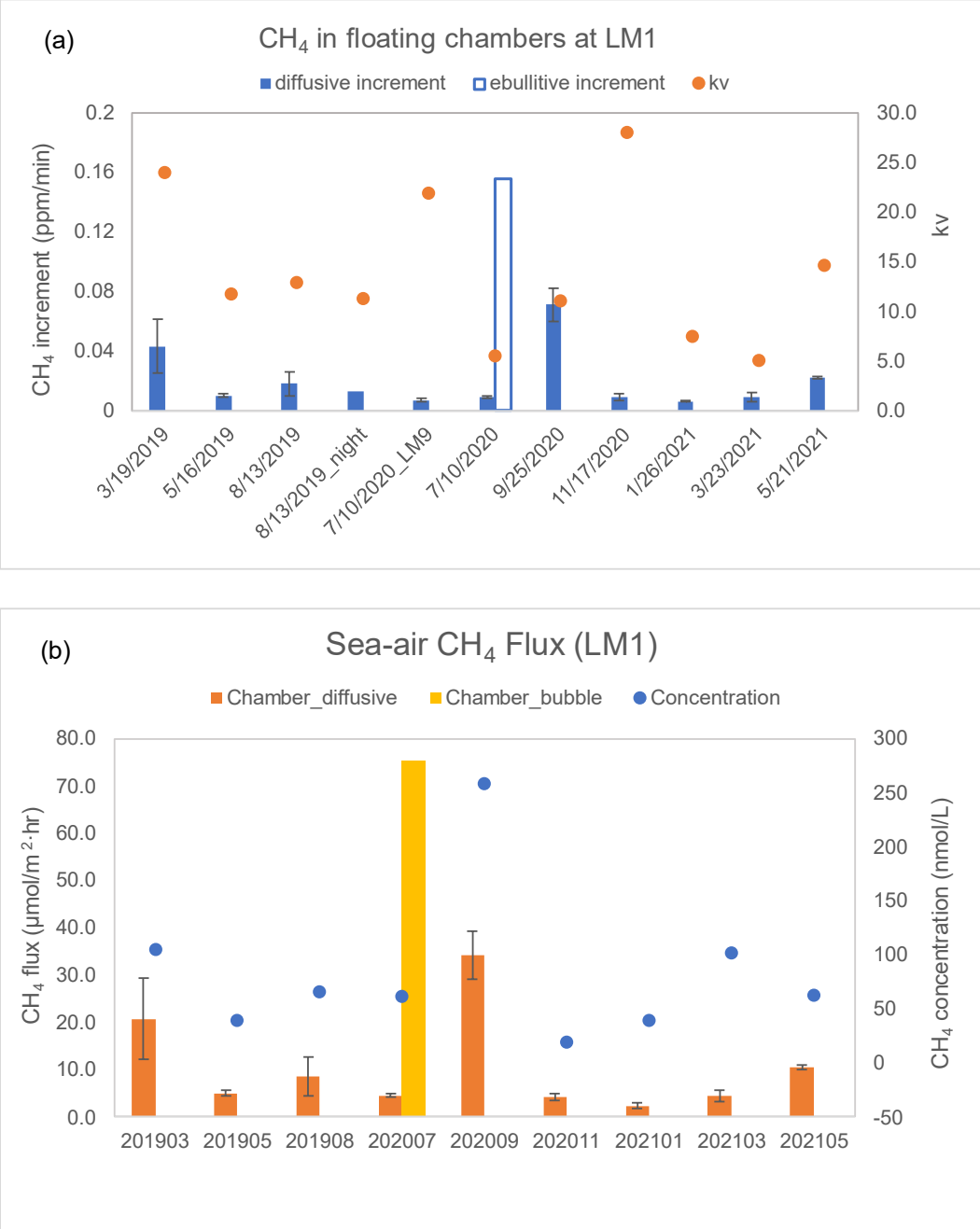

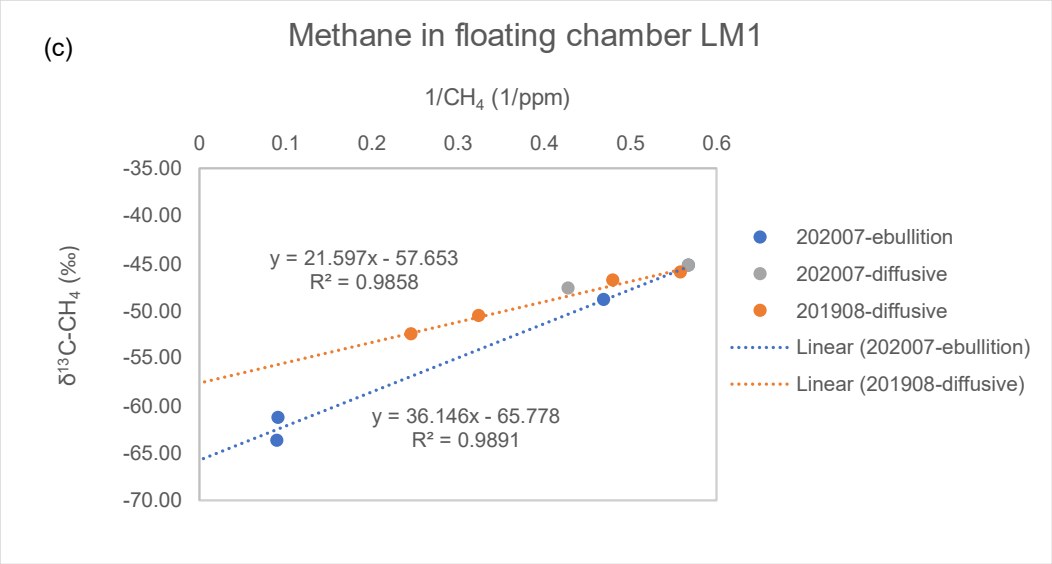

Figure 3.3 a: Increase rate of CH_4 concentrations in floating chambers and k_{fc} during the study period; b: Sea-air CH_4 fluxes acquired using floating chambers; c: Relationship between $\delta^{13}C$-CH_4 and the inverse of CH_4 concentration in floating chambers at LM1 in August 2019 and July 2020.

3.3.3 Sea-air methane flux

Sea-air diffusive CH_4 fluxes were calculated using four types of gas transfer velocities, k_{fc} acquired from in situ floating chambers, and k_{model} derived using three empirical equations (Figure 3.4). During the diurnal observations, although hourly CH_4 fluxes were somewhat different, they were all lower at night than during the daytime, demonstrating that more CH_4 was released from water to the atmosphere in the daytime than overnight. From July 2020 to May 2021, the monthly average daily diffusive CH_4 fluxes were highest in summer and early autumn, decreased to their lowest values in winter and then increased during spring. This further revealed that more CH_4 was released from water to the atmosphere in summer and autumn than in winter.

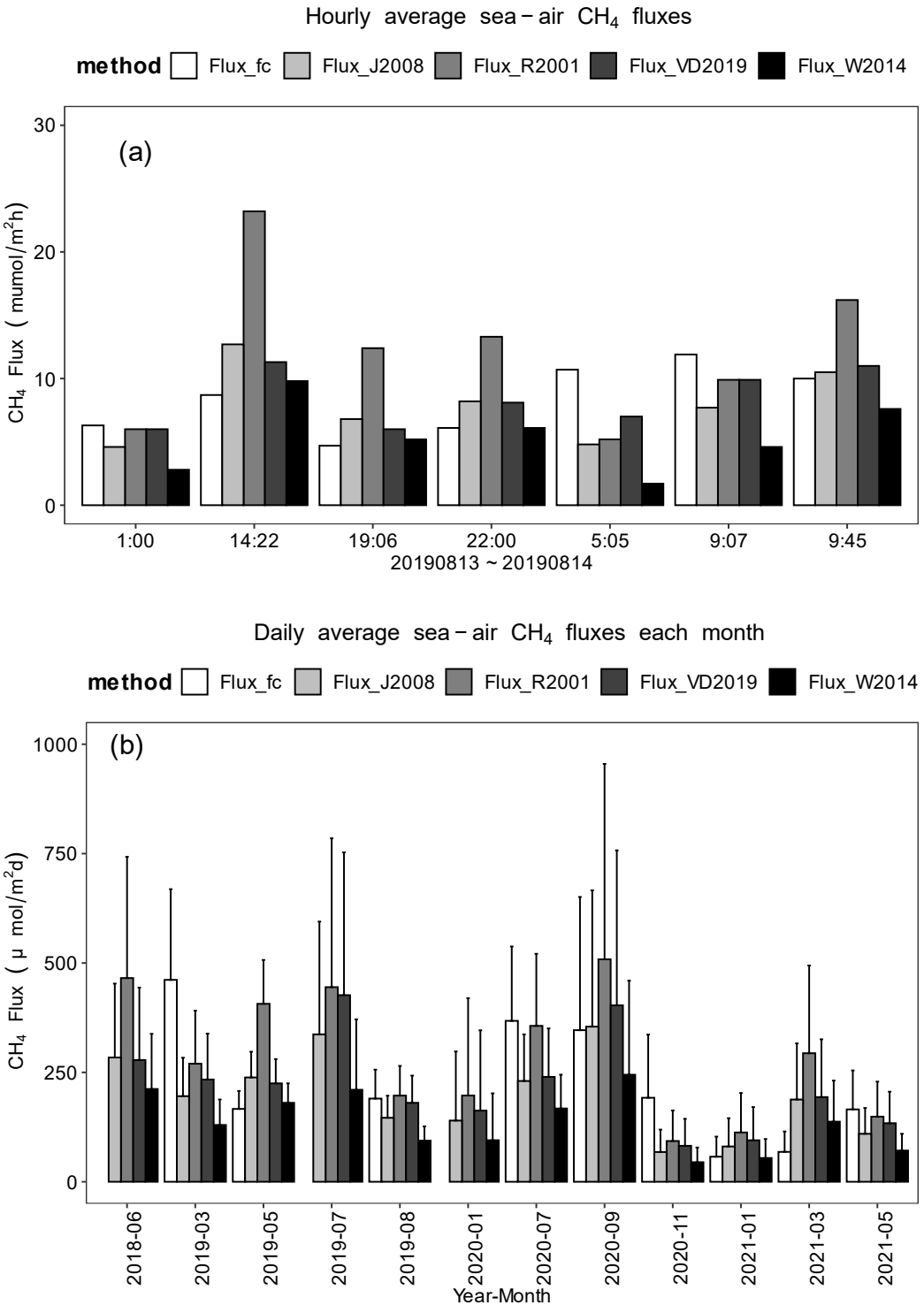

Figure 3.4 Diffusive sea-air methane fluxes calculated using different gas transfer velocities.

(Flux_fc: flux from k_{fc}; Flux_W2014: flux from the W2014 equation; Flux_VD2019: flux from the VD2019 equation; Flux_J2008: flux from the J2008 equation). (a) Hourly fluxes during the diurnal observation in August 2019; (b) Monthly average daily fluxes during the study period.

3.3.4 Water incubation

During the study period, variations in dissolved CH_4 concentration in the incubation experiments at sites LM1 and LM7 were no more than 20% in 24 hours (Figure S2), indicating that bacterial water column consumption and production were limited. In most cases, a decrease in the dissolved CH_4 concentration occurred in the first hour, and then the CH_4 concentration slightly increased.

3.3.5 Sediment-water methane flux

Profiles of porewater CH_4, DIC and sulfide concentrations in seagrass meadows showed a significant temporal variation (Figure S3), indicating a dynamic biogeochemical process in the surface sediment. After nearly 24 hours of incubation, CH_4 concentrations in overlying water increased 81.0 nmol/L and 135.0 nmol/L in the sediment chambers at LM1 and LM9, respectively.

Sediment-water CH_4 fluxes were calculated through two approaches: the variation in CH_4 concentrations in the overlying water of sediment incubation chambers before and after incubation (chamber flux) and Fick's first law of diffusion at the sediment-water interface (diffusive flux) (Table 3.1). The diffusive fluxes were calculated using the largest CH_4 concentration gradient at the interface of the surface sediment and a deep sediment layer. Incubation fluxes at LM1 and LM9 were larger than all diffusive fluxes at the sediment-water interface of the seagrass meadow, indicating that diffusive transport was not a primary way of CH_4 exchange from sediment to water.

Table 3.1 CH_4 flux at the sediment-water interface

μmol/m^2·d		LM1	LM9
Diffusive flux	May-19	0.052	-
	Aug-19	0.008	0.023
	Sep-20	0.613	-
Incubation flux	Aug-19	37.655	47.017

3.4 Discussion

3.4.1 Sea-air methane flux over the seagrass meadow

3.4.1.1 Diffusive flux

During diurnal observations, F_{VD2019} (8.2±2.7 μmol/m^2·h) was closest to F_{fc} (8.3±2.7 μmol/m^2·h) and then F_{J2008} (7.9±3.0 μmol/m^2·h), and F_{W2014} was lowest (5.4±2.8 μmol/m^2·h). Although the fluxes calculated using different methods are somewhat different, they were all lower in the nighttime than in the daytime, indicating less CH_4 emissions from water to the atmosphere. The CH_4 emissions over the whole day were approximately 189.6~199.9 μmol/m^2·d based on k_{fc}, k_{VD2019} and k_{J2008}.

The overall mean value of the monthly average daily F_{fc} (217.8±181.9 μmol/m^2·d) during the study period was closest to that of F_{VD2019} (211.8±173.9 μmol/m^2·d). However, F_{VD2019} was not the most suitable empirical model for estimating CH_4 flux in individual months. In different months, F_{fc} matched different $F_{model.}$ For example, F_{fc} was close to F_{R2001} in March and August 2019, July 2020 and May 2021, while F_{fc} in May 2019 and January 2021 was consistent with F_{W2014} (Figure 3.6). The F_{fc} in September 2020 was similar to F_{J2008}. Although no unified equation can currently be used to calculate the sea-air CH_4 flux, all these equations are reasonable. VD2019 was developed from a microtidal shallow estuary (Van Dam et al. 2019), with aquatic conditions similar to those of this study area. J2008 can be used for scenarios of high wind speed (Jiang et al.

2008), which have been applied in the study of CO_2 systems in estuaries near this study area (Yao and Hu 2017). W2014 was derived from the open ocean (Wanninkhof 2014) and widely applied in lakes and some lagoons (Chuang et al. 2017). R2001 was developed from floating chamber-based approaches in estuaries (Raymond and Cole 2001). Hence, we applied the same approach as in the estimation of CH_4 fluxes in mangrove creeks to unify the sea-air diffusive CH_4 fluxes over seagrass meadows (221.1±190.7 μmol/m^2·d). These unified diffusive CH_4 fluxes were significantly related to the dissolved CH_4 concentration (R^2=0.75, $p<0.01$).

3.4.1.2 Ebullitive flux

Only one chamber set up at LM1 (seagrass) in July 2020 caught bubble CH_4, as viewed from the nonlinearly dramatic increase in the CH_4 proportion in the chamber. The CH_4 proportion in the other chambers increased linearly in one hour, indicating no ebullitive CH_4. It should be noted that the ebullitive CH_4 flux was approximately 17-fold as large as the synchronic diffusive flux and over 2 times the largest diffusive flux (September 2020) during the study period (Figure 3.3). Hence, although ebullitive CH_4 was only occasionally observed due to the limit in observation methods, it needs more concern. Most bubble transport of CH_4 from sediment to the water column has been reported from lakes, reservoirs and freshwater wetlands (Davidson et al. 2018; DelSontro et al. 2016; Engram et al. 2020; Horn et al. 2017; Linkhorst et al. 2021; Scandella et al. 2016). A few observations were reported from coastal areas, where dissolved CH_4 in the water column and/or porewater was much higher than that in our study area (Chuang et al. 2017; Martens and Val Klump 1980; Padhy et al. 2020; Purvaja et al. 2004).

3.4.2 Factors that influence methane emissions

3.4.2.1 Relationship between methane concentration and environmental parameters

During the long-term observations, among the environmental parameters, DO%, pH, temperature, and DIC were factors that could influence temporal variations in dissolved CH_4 concentrations in seagrass meadows. Temperature and DIC were significantly positively related to CH_4 concentration ($p<0.01$), while pH was negatively ($p<0.01$) and DO% was slightly positively related ($p=0.057$). The positive relationship between CH_4 concentration and temperature was consistent with the results of the seagrass sediment incubation experiments in the Red Sea, where warming could release more CH_4 from sediment (Burkholz et al. 2020). However, the best regression model composed of temperature, pH and DO% could only explain 26.9% of the temporal variations in CH_4 concentrations. The one made by temperature and DIC accounted for 22.1%. There should be other factors that control CH_4 emissions.

The diel variations in environmental parameters and CH_4 concentrations provided more detailed information. As shown in Figure 3.5, the dissolved CH_4 concentration profiles were inversely related to DO and Chl-*a* concentrations and positively correlated with DIC. In particular, the relationship between CH_4 concentration and DO and Chl-*a* became more significant when comparing CH_4 concentrations with DO and Chl-*a* concentrations four hours later (Figure 3.6b, d). The dissolved CH_4 concentration was also positively related to DIC but negatively related to pH, which was similar to the long-term observations. Different from the long-term observations, the opposite relationship between CH_4 concentration and water temperature suggested more CH_4 in the water overnight when the water temperature was relatively lower.

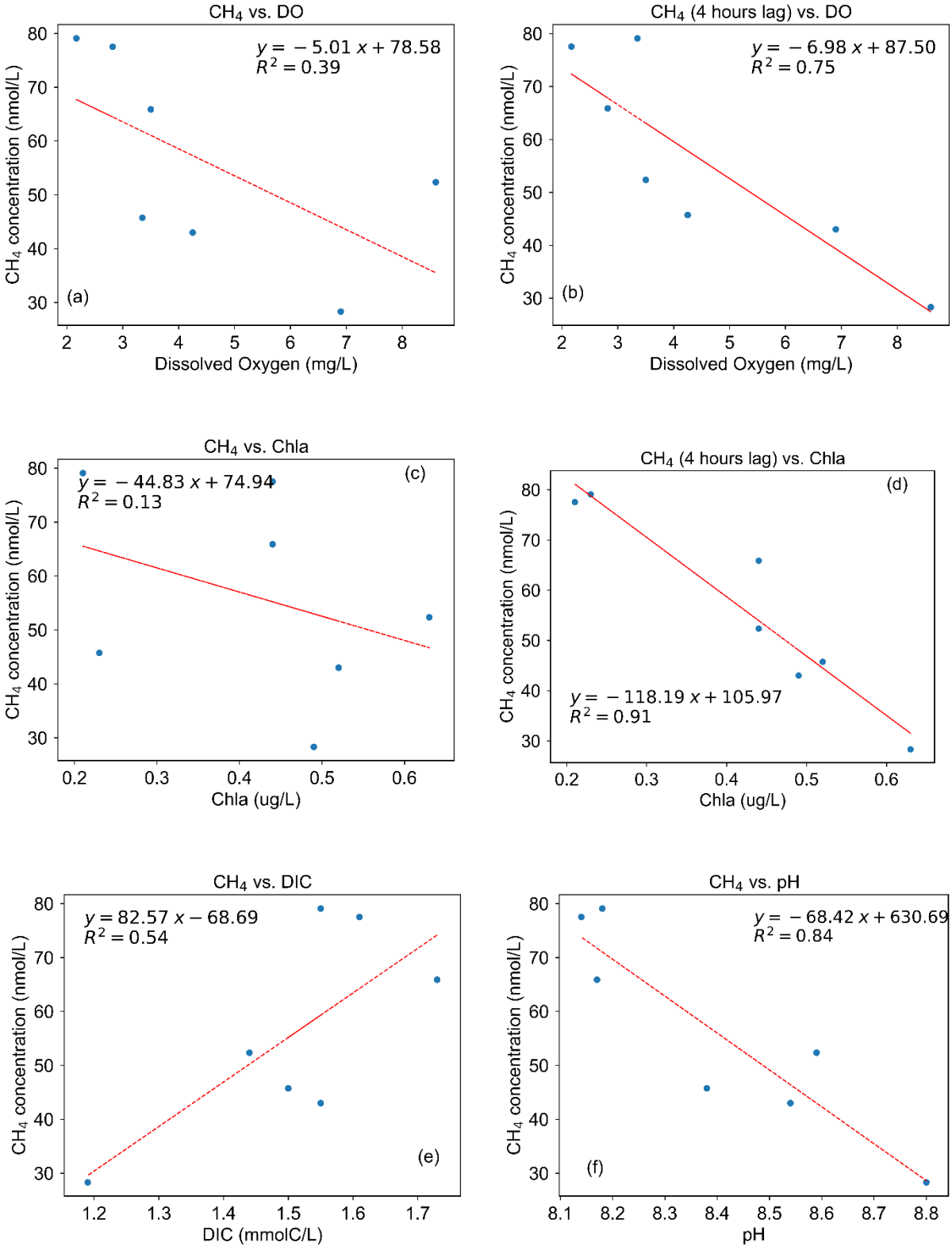
CH4 vs. DO
y = −5.01 x + 78.58
R2 = 0.39
(a)
CH4 concentration (nmol/L)
Dissolved Oxygen (mg/L)
CH4 (4 hours lag) vs. DO
y = −6.98 x + 87.50
R2 = 0.75
(b)
CH4 concentration (nmol/L)
Dissolved Oxygen (mg/L)
CH4 vs. Chla
y = −44.83 x + 74.94
R2 = 0.13
(c)
CH4 concentration (nmol/L)
Chla (ug/L)
CH4 (4 hours lag) vs. Chla
y = −118.19 x + 105.97
R2 = 0.91
(d)
CH4 concentration (nmol/L)
Chla (ug/L)
CH4 vs. DIC
y = 82.57 x − 68.69
R2 = 0.54
(e)
CH4 concentration (nmol/L)
DIC (mmolC/L)
CH4 vs. pH
y = −68.42 x + 630.69
R2 = 0.84
(f)
CH4 concentration (nmol/L)
pH

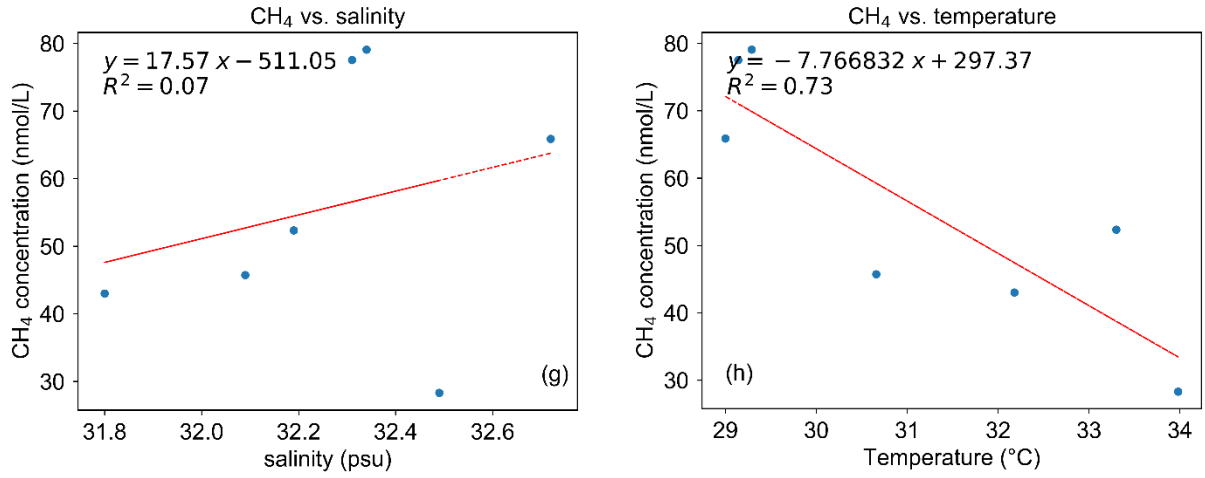

Figure 3.5 Relationship between dissolved CH_4 concentration and other parameters in the water column

3.4.2.2 Coincidence variation in methane concentration with photosynthesis and respiration in seagrass ecosystems

°Diel variations in dissolved CH_4 concentration and environmental parameters as well as their relationships were coincident with the physiologic processes in this seagrass ecosystem. In seagrass ecosystems, DO increases in the daytime due to photosynthesis (light + $6CO_2$ + $6H_2O$ -> $C_6H_{12}O_6$ + $6O_2$) and decreases in the dark because of oxygen consumption by dominant respiration ($C_6H_{12}O_6$ + $6O_2$ -> $6CO_2$ + $6H_2O$ + ATP) (Borum et al. 2007; Marbà et al. 2006). Chl-*a* was highest in the afternoon, indicating the peak time of photosynthesis; therefore, it is reasonable that DO was highest at the same time (Figure 3.2). DIC and pH varied following the change in DO, suggesting that they were related to CO_2 in the ecosystem (CO_2 + H_2O ⇔ HCO_3^- + H^+) (Marbà et al. 2006). Similar diel curves of DIC and DO in seagrass meadows were reported at Laguna Madre in September 1996 (Ziegler and Benner 1998).

Photosynthetic oxygen is essential to seagrass not only due to the metabolism of seagrass plants but also because oxygen can be delivered to seagrass rhizome sediment to inhibit toxic

compounds such as H_2S (Borum et al. 2007; Eldridge and Morse 2000). The DO percentages in this study changed in a large range, from 22.4% before sunset to 139.1% in the mid-afternoon. When oxygen is delivered to sediment via seagrass, in addition to inhibiting the growth of H_2S, it also oxidizes CH_4 and impedes methanogenesis (Alongi et al. 2008; Oremland and Taylor 1977). Both the diel variation in CH_4 concentration and the relationship between CH_4 concentration and DO suggested that the variations in CH_4 in the water were related to photosynthetic oxygen. Although DO concentrations were far more than enough to oxidize all CH_4 in the water, our water incubation experiments showed that less than 20% of CH_4 was decomposed in 24 hours, while the difference in diurnal variations (28.3 ~ 79.1 nmol/L) was up to 2.8 times. Hence, the majority of changes should be associated with the sedimentary environment.

In particular, the lowest CH_4 concentration appeared four hours after the DO peak in the water column, and the overall CH_4 concentrations were more significantly related to DO concentrations four hours earlier. This time lag suggested that the oxidization of CH_4 occurred in the sediment. Considering the passive diffusive migration of oxygen inside seagrass, it was reasonable that it took some time for oxygen to be delivered to rhizome sediment via seagrass lacunae from leaves to roots (Borum et al. 2007). Similar to this study, Oremland and Taylor 1997 also noted lag periods between methanogenesis and gaseous composition from the diurnal variation in photosynthetic oxygen and CH_4 in sediment bubbles and gases in the rhizome of the seagrass *T. testudinum* in Florida Bay (Oremland and Taylor 1977). Moreover, the highest $\delta^{13}C$-CH_4 (-57.3‰) appeared when the dissolved CH_4 concentration was lowest (Figure 3.2), implying oxidation of the dissolved CH_4 source by methanotrophs (Garcias-Bonet and Duarte 2017).

As the DO concentration decreased overnight due to DO consumption in ecosystem respiration, the CH_4 concentration increased correspondingly, indicating that methanogenesis was

dominant at night. The highest CH_4 concentration before sunrise had a lower $\delta^{13}C$ (-57.7‰), suggesting less oxidation of CH_4.

The $\delta^{13}C$-CH_4 in the water at LM7 (channel) was -59.5‰ and -59.8‰ in August 2019 and July 2020, respectively, approximately 2‰ lower than those at LM1. Since these sites were only 300 meters away from each other and there was less living seagrass on the floor of this channel site, the higher $\delta^{13}C$-CH_4 at LM1 could probably be attributed to CH_4 oxidation in seagrass sediment. Moreover, the ebullition input caught by the floating chamber at LM1 in July 2020 showed that CH_4 in the bubble was -65.8‰, which could represent the initial isotopic signature of biogenic CH_4 produced in sediment. However, the $\delta^{13}C$ of diffusive CH_4 in the floating chambers in both August 2019 and July 2020 was similar to $\delta^{13}C$-CH_4 in the water, approximately 8‰ larger than ebullitive CH_4 (Figure 3.3a), further proving the oxidation of CH_4 before being delivered to the water.

DIC and pH during the study period had similar relationships with dissolved CH_4 concentration as in the diurnal observations, indicating the long-term impact of the photosynthetic process of seagrass meadows on CH_4 emissions. Since Upper Laguna Madre is a relatively isolated lagoon with minor water exchange with other aquatic systems and seagrass meadows are thought to be responsible for much of the primary production, the variation in DIC and pH is tightly related to photosynthesis and respiration of seagrass ecosystems (Ziegler and Benner 1998). Hence, random sampling over a long period further proved that seagrass metabolic processes could affect CH_4 emissions from sediment.

4.3 Methane transport at the sediment-water interface

The chamber fluxes at seagrass sites LM1 and LM9 were 37.65 and 47.02 $\mu mol/m^2 \cdot d$, respectively, which were similar to the sediment-water fluxes of CH_4 at the *Thalassia testudinum*

seagrass meadow in Florida Bay in spring (40.9±21.6 μmol/m^2·d) but lower than those in fall (341±121 μmol/m^2·d) (Barber and Carlson 1993). Seagrass meadows with various species along the Red Sea reported a large range of CH_4 production of 0.09 ~ 565.27 μmol/m^2·d (85.09±27.8 μmol/m^2·d) (Garcias-Bonet and Duarte 2017). The chamber flux at LM11 (118.98 μmol/m^2·d) was similar to that of the dead seagrass zone in Florida Bay in fall (158±65.4 μmol/m^2·d). However, the calculated diffusive fluxes were over 6 times less than the chamber fluxes, indicating that diffusion at the sediment-water interface was not a primary way of CH_4 transport from sediment to water.

Different from freshwater aquatic ecosystems and mangroves, where porewater CH_4 concentrations could reach the mmol/L level (Chuang et al. 2016; Huttunen et al. 2006), porewater CH_4 concentrations in seagrass sediment were at the nmol/L to μmol/L level. Hence, it is reasonable that diffusive transport was not a primary mechanism for CH_4 emissions at the sediment-water interface. Other possible transport approaches include advection of fluid, ebullition of bubbles and plant mediation. Advective transport of porewater CH_4 reported in the seagrass meadow at Ria Formosa Lagoon in southern Portugal was prompted by tidal processes (Bahlmann et al. 2015). Upper Laguna Madre has weak water exchange, and the water depth changed little in this study (Figure 3.1). Hence, the tidal impact on CH_4 emissions could be ignored. We caught ebullitive emissions in July 2020, as shown in Figure 3.4. Therefore, although it was the only time, bubbles, as a potential way to deliver CH_4 from sediment to the water column, need more study in this region.

Plant-mediated transport of CH_4 has been reported in many emergent and submerged macrophytes (Chanton et al. 1992; Fonseca et al. 2017; Laanbroek 2009; Whiting and Chanton 1992; Zhang et al. 2019). CH_4 has also been found in the rhizome of the seagrass *Thalassia*

testudinum, which was undoubtedly from an inward diffusion of CH_4 in sediment (Oremland 1975; Oremland and Taylor 1977). However, there is no direct evidence of CH_4 transport by seagrass to the water column (Al-Haj and Fulweiler 2020). A study on CH_4 emissions from *Thalassia testudinum* in Florida Bay proposed that the concentration gradient, not plant mediation, resulted in a higher CH_4 flux in the live zone than in the dead zone (Barber and Carlson 1993). They found that although higher CH_4 flux in chambers was observed in the live seagrass zone, exchange coefficients at the sediment-water interface were lower than those at the dead seagrass zone. However, calculated by inputting the largest variance between porewater and bottom CH_4 concentrations (3380 and 2690 nmol/L in the live zone and 776 and 532 nmol/L in the dead zone, September 1990) into Fick's first law equation, the CH_4 flux at the sediment-water interface was no more than 4.5 and 1.6 $\mu mol/m^2 \cdot d$, much lower than the chamber fluxes of 341 and 158 $\mu mol/m^2 \cdot d$ (Supporting Information). Hence, the concentration gradient could not explain the transport of CH_4 from sediment to water. An assumption is that the lacunal structure of dead seagrass could still deliver gases before the structure was totally decomposed. Dead mangrove tree stems have been found to release more CH_4 than living tree stems (Jeffrey et al. 2019). The CH_4 fluxes at the sediment-water interface in this paper could also not be explained by diffusive transport.

It should be noted that we observed the highest CH_4 concentrations in early autumn and the lowest concentrations in winter, which was coincident with the seasonal pattern of biomass in seagrass. *Halodule wrightii* in the southern Gulf of California peaked during autumn and had the lowest biomass in winter-spring (Pérez-Estrada et al. 2021). Moreover, both in 2019 and 2021, more CH_4 was emitted in March than in May, which can be partly explained by the sprout of seagrass. Plenty of organic carbon deposits due to seagrass mortality in winter in combination with

more active methanogenesis as temperature increases in early spring can produce a large amount of CH_4 in sediment. Since diffusive transport is minor and temperature in early spring is not high, the growing of seagrass in March is the most likely way to mediate CH_4 from sediment to water. With the growth of seagrass in spring, increase in photosynthesis, and reduction in CH_4 accumulation in sediment, the emissions decreased in May. Hence, we speculate that plant mediation of seagrass plays an important role in CH_4 emissions.

3.4.4 Dynamics of methane cycling in seagrass meadows

3.4.4.1 A semi-quantitative analysis of diurnal methane cycling in the seagrass meadow

Methane emissions to the atmosphere from shallow coastal areas depend on all periods of CH_4 biogeochemical cycling, including CH_4 production, oxidation, and transport. CH_4 is primarily produced from methanogenesis and can be oxidized by methanotrophy in sediment and water columns. The remaining CH_4 in the water can finally be transported to the atmosphere. The input and output of CH_4 generally determine the dissolved CH_4 concentration in the water column. For the seagrass meadow in this study, as in the previous discussion, the primary source of CH_4 was the CH_4 transported from sediment to water, and the major output included CH_4 released from water to the air and bacterial decomposition in the water column. These factors were integrated into equation (10) to estimate the diurnal variation in CH_4 cycling. Considering that the incubation of sediment and overlying water was carried out in sealed chambers, the impacts from limited DO and sea-air transport could be ignored (11).

In situ:

$$[CH_4]_{remain} = [CH_4]_{sed\text{-}water} - [CH_4]_{oxidation} + [CH_4]_{methanogensis} - [CH_4]_{sea\text{-}air} \quad (10)$$

Incubation:

$$[CH_4]_{remain} = [CH_4]_{sed\text{-}water} - [CH_4]_{oxidation} + [CH_4]_{methanogensis} \quad (11)$$

Here,

- $[CH_4]_{remain}$: dissolved CH_4 in the water column;

- $[CH_4]_{sed\text{-}water}$: CH_4 flux at the sediment-water interface;

- $[CH_4]_{oxidation}$: oxidization of CH_4 by bacteria in water;

- $[CH_4]_{methanogensis}$: methanogenesis of CH_4 in water;

- $[CH_4]_{sea\text{-}air}$: CH_4 transported at the sea-air interface, determined by wind speed and dissolved CH_4 concentration.

An overall important assumption is that decomposition and production of CH_4 in the water body ($-[CH_4]_{oxidation} + [CH_4]_{methanogenesis}$) in daytime and night were the same, less than 20% based on the incubation experiments. In the diurnal observations, the calculated daytime $[CH_4]_{sea\text{-}air}$ was larger than the nighttime $[CH_4]_{sea\text{-}air}$.

During 13 hours of daytime, the dissolved CH_4 concentration decreased at an average of -4.02 nmol/L·hr (Supporting Information). In contrast, dissolved CH_4 increased overnight (11 hours) at an hourly rate of +5.15 nmol/L·hr. The total daily variance was the sum of the daytime decrease and night increase, that is, +4.5 nmol/L. There was 4.5 nmol/L dissolved CH_4 accumulation each day in summer. Assuming oxygen in the sediment chamber was enough to support seagrass photosynthesis in the daytime during incubation, the increase in CH_4 concentration in overlying water (81.0 nmol/L, 37.66 μmol/m^2·d) was produced and transported overnight. That is, approximately 7.4 nmol/L·hr (3.4 μmol/m^2·hr) CH_4 was transported from sediment to water overnight.

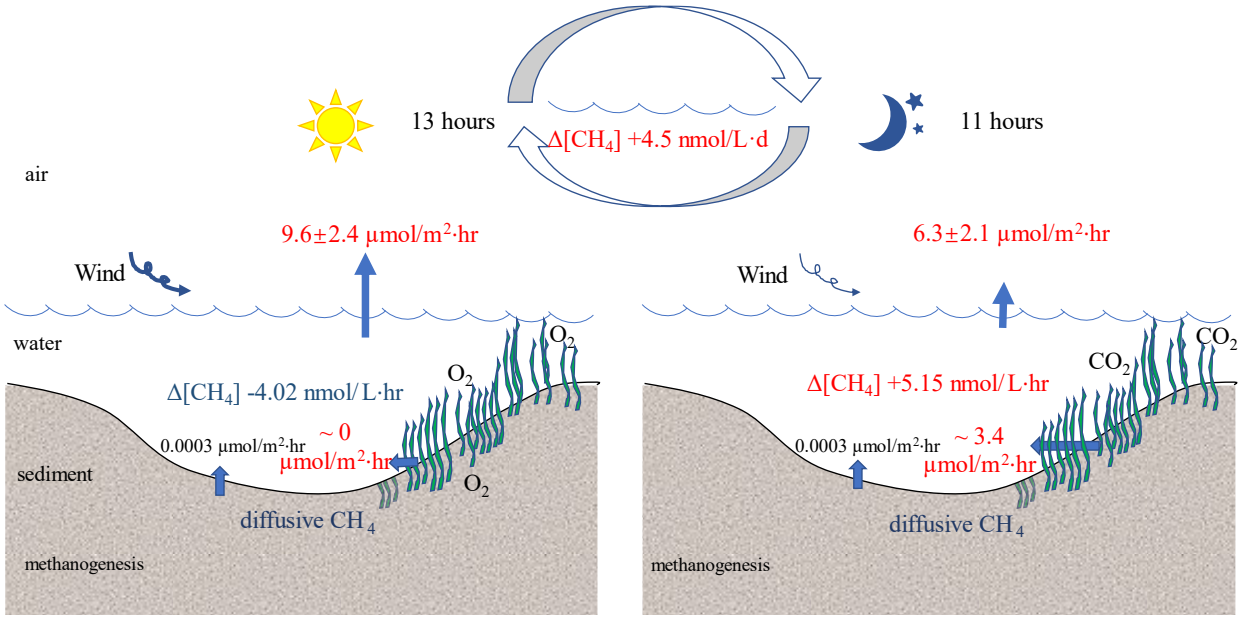

Figure 3.6 Daily CH_4 cycling in the seagrass meadow.

Left: daytime (13 hours); Right: nighttime (11 hours). CH_4 fluxes at the water-air interface were averages of diffusive fluxes in the daytime and nighttime. The variation in CH_4 concentration in the water body was calculated based on diurnal observations. The diffusive CH_4 flux at the sediment-water interface was calculated using Fick's first law.

3.4.4.2 Implications of seagrass photosynthesis for methane cycling

As in the previous discussion, photosynthetic oxygen at least partly contributed to the decrease in CH_4 concentration in the water column, which would consequently reduce sea-air CH_4 emissions. Assuming a scenario without photosynthesis in our study, the daily accumulation of CH_4 in the water column will be 123.6 nmol/L (+5.15 nmol/L × 24 hours). Considering a larger flux from water to the atmosphere in the daytime, this value would be smaller but would still be much larger than +4.5 nmol/L·d. Hence, the seagrass photosynthetic process coupled with its plant mediation of oxygen enhances the carbon capture capability of seagrass by decreasing CH_4 production and emission. As a comparison, elevated CH_4 concentrations at the adjacent channel

sites could further prove this point, e.g., LM7 (58.2 ~ 479.9 nmol/L) vs. LM1 (19.3 ~ 258.2 nmol/L).

However, the role of seagrass photosynthesis in decreasing CH_4 production in sediment has easily been hidden by measurement methods for CH_4 fluxes at sea-air interfaces and/or sediment-water interfaces. In this study, sea-air CH_4 fluxes were larger in the daytime than at night, although more CH_4 was produced and transported to the water column overnight. Viewing only the variation in the sea-air CH_4 flux would lead to a misunderstanding of the factors and mechanisms that influence CH_4 emissions.

3.4.5 Methane offset to seagrass carbon sequestration

The CH_4 fluxes at the sea-air interface of seagrass meadows in this study were 12.3~816.2 μmol/m^2·d (221.0±190.7 μmol/m^2·d, median: 163.7 μmol/m^2·d) over the range of seagrass globally (1.2~401.5 μmol/m^2·d, 108.2±104.3 μmol/m^2·d, median: 64.8 μmol/m^2·d) (Al-Haj and Fulweiler 2020). Accounting for the carbon burial rates in seagrass meadows of 41~66 gC/m^2·y from seagrass production (Kennedy et al. 2010), the CH_4 flux could offset 1.4%~2.2% of blue carbon deposited in seagrass at LM, which was over 3 times higher than global estimates (i.e., <0.5%) (Al-Haj and Fulweiler 2020). Upscaling CH_4 fluxes to seagrass meadow (94289 ha) along the coast of Texas, annual CH_4 emissions from seagrass were 854.3×10^6 gC. They were approximately 0.011% of the total stock organic carbon in seagrass sediment (7.5 Tg) (Thorhaug et al. 2019). Unexpectedly, seagrass meadows along the Texas coast play a more significant role in CH_4 emissions than in other regions.

3.5 Conclusion

The diurnal variation in the dissolved CH_4 concentration in the seagrass meadow was opposite to the DO and Chl-*a* concentrations but positively correlated with DIC in August 2019,

indicating that CH_4 cycling was related to photosynthesis and respiration in the seagrass ecosystem. Photosynthetic oxygen delivered via seagrass lacunae to sediment could oxidize CH_4 and inhibit methanogenesis in sediment, which would reduce the CH_4 concentration in the water column. Long-term variations in CH_4 concentration and pH and DIC had similar relationships, further suggesting the impact of seagrass metabolic processes on CH_4 emissions. The dissolved CH_4 concentrations were highest in autumn and lowest in winter, coincident with the seasonal seagrass growth pattern, indicating the potential of plant mediation on CH_4 emissions.

The diurnal variation in CH_4 concentration further proved the common dilemma of greenhouse gas studies about when to sample during the day using the chamber-based method and discrete sampling (Bansal et al. 2018). However, it also discovered the mechanisms that control CH_4 cycling, which was often hidden from flux observations over the water surface.

Although discrepancies existed among CH_4 fluxes acquired using floating chambers and different empirical models, F_{fc} could match F_{model} in some conditions. Hence, we unified the sea-air diffusive CH_4 fluxes using the relationship between F_{fc} and F_{model}. The unified diffusive CH_4 fluxes were significantly positively related to CH_4 concentrations. They were 12.3~816.2 $\mu mol/m^2 \cdot d$ (221.0±190.7 $\mu mol/m^2 \cdot d$, median: 163.7 $\mu mol/m^2 \cdot d$) over the range of the current global seagrass CH_4 database (1.2~401.5 $\mu mol/m^2 \cdot d$). Calculated using the carbon burial rates in seagrass meadows of 41~66 $gC/m^2 \cdot y$ from seagrass production, CH_4 emissions could offset 1.4%~2.2% of blue carbon deposited in local seagrass meadows. This study reported the largest CH_4 emissions from seagrass meadows to date. Moreover, the ebullitive CH_4 from seagrass sediment need more concerns in the future study.

CHAPTER IV: METHANE EMISSIONS FROM SUBTROPICAL ESTUARIES AT SOUTHERN TEXAS

Abstract

Coastal vegetated ecosystems are major marine methane (CH_4) sources. Lagoonal estuaries in southern Texas are important seagrass and poleward mangrove habitats along the northwest Gulf of Mexico. Methane emissions from this region were investigated to evaluate the contributions to atmospheric CH_4 from different sources and factors influencing CH_4 transport. The annual sea-air CH_4 flux was largest at Upper Laguna Madre and lowest at Aransas Bay. The high spatial variation in CH_4 emissions was attributed to the distribution of different environmental characteristics, i.e., seagrass, mangroves, channels, and open bays in each estuary. Both annual and daily average CH_4 fluxes to the atmosphere in seagrass meadows were higher than those in mangrove creeks, indicating that local seagrass meadows were a more significant CH_4 source than mangrove creeks. Further analyses showed that tidal processes could largely decrease CH_4 emissions, implying a strategy of applying tidal processes in coastal wetland restoration. Daily CH_4 flux was highest in the channel at Upper Laguna Madre, suggesting that the disturbance of vegetated sediment could severely enhance CH_4 emissions in comparison with less vegetated sediment. In addition to dredging, pollution caused by maritime transportation and gas pipeline leakage are direct anthropogenic CH_4 inputs to the atmosphere, which have been widely overlooked. Except for elevated CH_4 emissions from mangrove creeks after the extreme cold event, a larger riverine discharge caused by heavy precipitation could deliver more CH_4 from freshwater to coastal water. Similar to the majority of coastal areas, southern Texas estuaries were a source of atmospheric CH_4. Anthropogenic disturbances and coastal vulnerability to extreme weather might enhance CH_4 emissions, which needs more attention.

4.1 Introduction

Methane (CH_4) is the second most important greenhouse gas after carbon dioxide (CO_2), with an atmospheric warming potential of approximately 28-34 times and 84-86 times that of CO_2 over 100 years and 20 years, respectively (IPCC 2014). Coastal areas are net CH_4 sources globally, with total emissions of 5.3~6.2 Tg CH_4/year (Al-Haj and Fulweiler 2020), accounting for most marine CH_4 emissions (4-10 Tg CH_4/yr with a mean of 6 Tg CH_4/yr), although coastal shallow water only covers 7% of the ocean surface (Saunois et al. 2020; Weber et al. 2019). Vegetated ecosystems such as mangroves, salt marshes and seagrass are crucial coastal CH_4 sources due to their large amount of organic carbon deposition and active biogeochemical cycling (Al-Haj and Fulweiler 2020; Rosentreter et al. 2021b; Weber et al. 2019). A recent study showed that global CH_4 fluxes from mangroves, salt marshes and seagrass were 0.23±0.01, 0.071±0.027, and 0.031±0.006 Tmol/yr, respectively, approximately 8.9%, 7.1% and 0.3% of the carbon deposited in sediment (Al-Haj and Fulweiler 2020).

The emission of CH_4 from coastal areas is controlled by complicated physical and biogeochemical processes (Wilson et al. 2020). Located at the interface of land and ocean, coastal areas are more vulnerable to the consequences of human activities and climate change, e.g., global warming, eutrophication, sea-level rise and hypoxia, which could influence the carbon sequences and emissions of greenhouse gases, including CH_4, as feedback (Al-Haj and Fulweiler 2020; Macreadie et al. 2019; Myllykangas et al. 2020). For example, deforestation of mangroves by shrimp cultivation could increase greenhouse gas emissions (Ahmed and Thompson 2019; Kauffman et al. 2017; Kauffman et al. 2018). Both outdoor mesocosm experiments and laboratory incubation experiments have displayed an increase in CH_4 emissions from seagrass sediment caused by warming (Burkholz et al. 2020; George et al. 2020). The grazing of seagrass could

increase CH_4 emissions in a tropical seagrass meadow (Lyimo et al. 2018). As the most densely populated area in the world, human activities along the coasts not only release greenhouse gases directly but also significantly influence natural processes on greenhouse gas emissions (Allen et al. 2011; Kroeger et al. 2017). In mangrove-dominated lagoons on the Yucatan Peninsula, Mexico, the highest CH_4 concentration was found in areas with pollution input (Chuang et al. 2017).

Coasts along the Gulf of Mexico are important salt marsh, mangrove and seagrass habitats in the world. Located northwest of the Gulf coast, Laguna Madre is one of two major seagrass territories along the Gulf coast (Thorhaug et al. 2017). Seagrass meadows along the Texas coast have been estimated to be 94,389 ha and stock 7.5 Tg organic carbon (Thorhaug et al. 2019). In recent decades, seagrass meadows in this region have experienced extensive human activities (e.g., dredging) and climate change events (e.g., hurricanes and drought events), which have undoubtedly changed seagrass coverage, biomass, and species distributions (Congdon et al. 2019; Dunton et al. 2003; Eldridge et al. 2004; Erftemeijer and III 2006; Wilson and Dunton 2018). Although the coverage of mangroves in the northwestern Gulf (Texas) is only approximately 1.4% of that in Florida (Osland et al. 2018), mangrove forests at Aransas Bay, Texas, have been a key area of poleward mangrove expansion and replacement of salt marshes along the Gulf since the 1930s (Montagna et al. 2011). Mangrove coverage increased 75% between 1990 and 2010 (Armitage et al. 2015; Osland et al. 2018). Mangrove northward expansion in Texas was primarily due to a reduced frequency of extreme cold events, particularly since 1989 (Cavanaugh et al. 2014). The transition from salt marshes to mangroves resulted in the deposition of more carbon in the sediment (Bianchi et al. 2013). Mangroves along the Texas coast have been extended to 3316 ha, where 1.12 Tg organic carbon are deposited (Thorhaug et al. 2019). However, the freezing event

that occurred between February 14th and 17th caused the mortality of a large area of mangroves at Aransas Bay (Figure 4.1).

Due to the development of the fossil fuel industry and the rapid growth of the population in Texas, this region has undoubtedly been highly disturbed by human activities. Located at Corpus Christi Bay, the Port of Corpus Christi is the 3rd largest port in the U.S. in total revenue tonnage and a leader in U.S. Crude Oil exports (Port Corpus Christi 2018-2019 Annual Report, https://portofcc.com/). As the third-busiest inland waterway in the US, the Gulf Intracoastal Waterway (GIWW) runs from Florida to Texas along the Gulf of Mexico. The portion in Texas (GIWW-T) handles 67% of all GIWW traffic (Kruse et al. 2016). Moreover, mangrove and seagrass habitats also provide essential public recreation, such as boating and fishing.

Complicated natural environments and extensive anthropogenic activities make South Texas estuaries have various sources of CH_4 emissions. In this study, we investigated the seasonal and spatial variations in CH_4 emissions from these estuaries and evaluated the flux of CH_4 in this region. We also discussed factors controlling the release of CH_4, particularly the variations in CH_4 emissions by human disturbances and under the effect of extreme weather. Drivers that influence CH_4 emissions from seagrass meadows and mangrove creeks have been discussed in detail in previous publications. In this paper, we compared CH_4 emissions from these two environments to acquire a thorough understanding of the regional CH_4 budget.

4.2 Materials and Method

4.2.1 Study area and sampling sites

The study area of this paper is located on the semiarid subtropical coast of southern Texas, northwest of the Gulf of Mexico, including Corpus Christi Bay, Nueces Bay, Aransas Bay and Upper Laguna Madre (Figure 1.3). They are isolated from the Gulf of Mexico by sandy barrier

islands, i.e., Padre Island, Mustang Island, and San José Island, and only through the Packery Channel at Mustang Island and the Ship Channel at Port Aransas can they access water from the Gulf of Mexico. Dominated by diurnal microtides, these coastal waters have limited water exchange with the Gulf of Mexico (Smith 1979). For convenience, we call all these bays and lagoons estuaries.

Corpus Christi Bay is approximately 490 km^2 and has an average depth of 3 m, with a large area of open water (Figure 4.1c). It has two secondary bays, Nueces Bay and Oso Bay, through which freshwater from the Nueces River and Oso Creek enters Corpus Christi Bay. Oso Bay and Oso Creek will not be discussed in this study because they only occasionally had minor input to Corpus Christi Bay (Wetz et al. 2016). Across Corpus Christi Bay from the Ship Channel to the channel for Port of Corpus Christi, there is a deep maritime channel. Here, we take Corpus Christi Bay and Nueces Bay as a whole system, Corpus Christi/Nueces bays. Sampling site NC1 is near the Nueces River mouth. NC2 is at the interface of two bays. NC3 is located in the middle of Corpus Christi Bay and the maritime channel. NC4 is the eastern site closest to the Gulf of Mexico relative to the other sites.

Upper Laguna Madre is south of Corpus Christi Bay (Figure 4.1e) and is the northern part of Laguna Madre, a hypersaline lagoon. It is a crucial seagrass habitat, with seagrass meadows covering approximately 66% of the bottom (Dunton and Reyna 2019). In the middle of the narrow water body of the upper Laguna Madre is GIWW-T, a channel for boating and marine transportation. GIWW-T is 379 miles of Texas coastline, 125 feet wide and 12 feet deep (Kruse et al. 2016). Upper Laguna Madre connects with the Gulf of Mexico via the Packery Channel. Sampling sites LM1, LM9, LM10, P7 and P9 are in seagrass meadows. Among them, P7 and P9

are close to the mouth of Corpus Christi Bay and saltmarsh/mangrove vegetation. LM6, LM8, LM11, LM12, P4, and P6 are located at GIWW-T. P8 is at the Packer Channel.

Aransas Bay is north of Corpus Christi Bay. Study sites in the region focus on the southern part of the bay, including Redfish Bay and Harbor Island (Figure 4.1d). Harbor Island is near the inlet of the Ship Channel. It is covered by black mangroves (*Avicennia germinans*) and salt marshes (*Spartina alterniflora* and other grass and forb species) (Armitage et al. 2015). It has become one of the primary populations of black mangroves on the Texas coast (Montagna et al. 2011). GIWW-T also crosses this area. Sampling site AM1 is at the waterway connecting the Ship Channel and Corpus Christi Bay. AM2 and AM3 are located in the open bay area. AM4, AM5, AM6, AM7, AM8, and AM16 are at the mangrove creeks of Harbor Island. Among them, AM4, AM5, and AM6 are at the southern creek from outside to inside the mangrove. Along the creeks where AM7, AM8, and AM16 are located, there are both salt marsh and mangrove vegetation. AM17 is at the mouth of a mangrove/salt marsh creek. AM13, AM14 and AM15 are located at GIWW-T close to Redfish Bay, which is west of Harbor Island and surrounded by mangroves and salt marshes. AM9, AM10, and AM11 are at GIWW-T northwest extending from the Ship Channel. AM12 is located in the middle of the Ship Channel, connecting with the Gulf of Mexico.

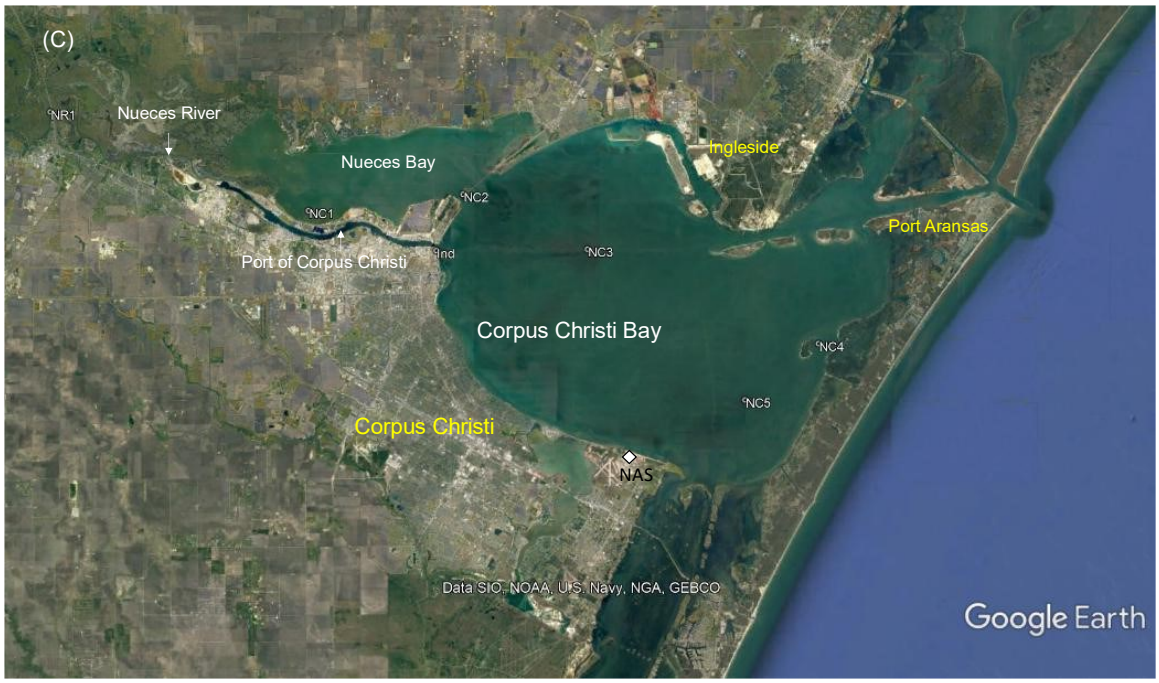
(C)
NR1
Nueces River
Nueces Bay
Ingleside
NC2
NC1
Port Aransas
Port of Corpus Christi
2nd
NC3
Corpus Christi Bay
NC4
NC5
Corpus Christi
NAS
Data SIO, NOAA, U.S. Navy, NGA, GEBCO
Google Earth

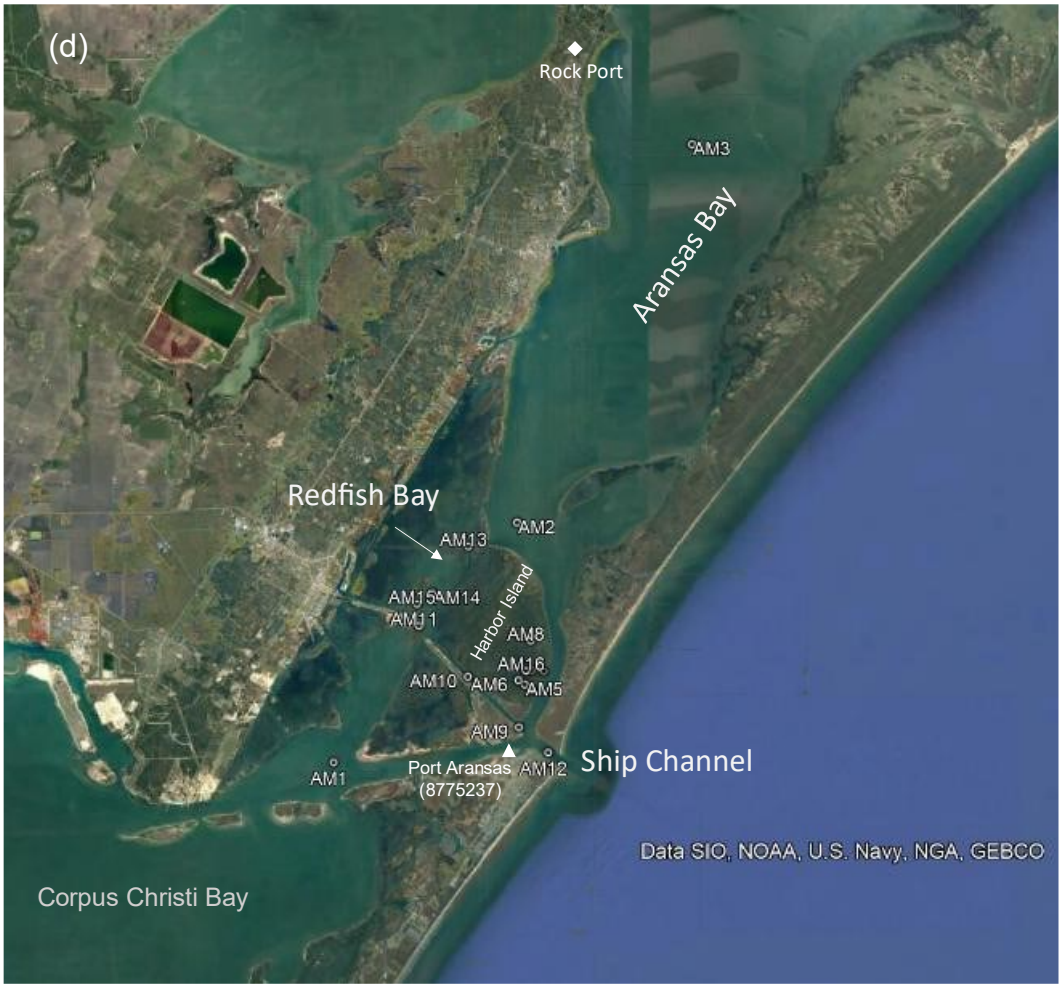
(d)
Rock Port
AM3
Aransas Bay
Redfish Bay
AM13
AM2
AM15
AM14
AM11
Harbor Island
AM8
AM16
AM10
AM6
AM5
AM9
AM1
Port Aransas
(8775237)
AM12
Ship Channel
Data SIO, NOAA, U.S. Navy, NGA, GEBCO
Corpus Christi Bay

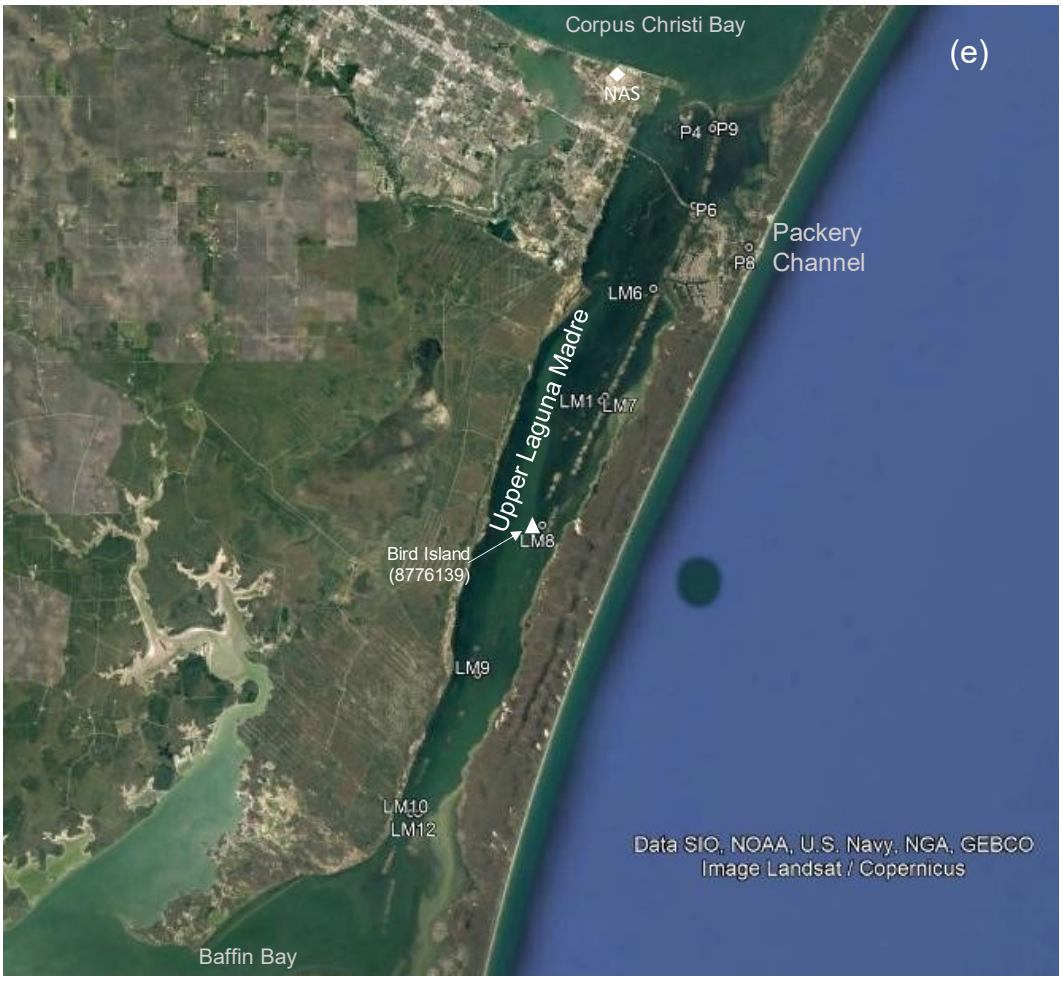

Figure 4.1 Study sites in Corpus Christi Bay, Nueces Bay, Aransas Bay and Upper Laguna Madre.

(c) Sampling sites in Corpus Christi Bay and Nueces Bay. (d) Sampling sites in Aransas Bay, including its subsystem of Harbor Island and Redfish Bay. (e) Sampling sites in Upper Laguna Madre.

4.2.2 Study method

4.2.2.1 Sample collection

Sampling was performed at Corpus Christi/Nueces Bay (NC) each month from May 2018 to January 2020 and July 2020; at Upper Laguna Madre (LM) and Aransas Bay (AM) in June 2018, January, March, May, July, August 2019, and bimonthly from January 2020 to May 2021.

All the water and air sampling and measurement methods applied in this study have been described in previous chapters in detail. Briefly, surface water and ambient air were collected to determine dissolved CH_4, sea-air CH_4 flux, dissolved inorganic carbon (DIC), and chlorophyll-*a* (Chl-*a*). Synchronically, water parameters (salinity, pH, dissolved oxygen (DO), water temperature) were measured using a multiparameter meter (HI98194, Hanna Instruments). Weather (wind speed, wind direction, and temperature) and tidal (water level) data at nearby meteorological and hydrological stations were acquired online (NOAA National Centers for Environmental Information Climate Data Online https://www.ncdc.noaa.gov/cdo-web/, station: NAS and Rockport Aransas Co Airport, for monthly average daily wind speed; NOAA TIDES & CURRENTS https://tidesandcurrents.noaa.gov/, station: Port Aransas (8775237) and Bird Island (8776139) for hourly wind speed and direction, and water level; Figure 4.1). These parameters were applied to calculate the CH_4 flux and analyze factors controlling CH_4 emissions at the sea-air interface (Chuang et al. 2017; Lorenson et al. 2016). Floating chambers were set up at AM5 and LM1 synchronically with sampling to measure in situ CH_4 flux from surface water to the atmosphere and in situ gas transfer velocity.

Sediment cores were collected at LM1, LM7 and AM5 in May 2019; LM1, LM7, LM9, LM11, AM5, AM8 and AM17 in August 2019; and LM1, AM5 and AM16 in September 2020 using 50 cm polycarbonate tubing with a 6.67 cm diameter. As soon as the cores were collected,

porewater samples were drawn using Rhizon samplers (Coffin et al. 2013; Seeberg-Elverfeldt et al. 2005; Treude et al. 2014).

Sediment incubation experiments were carried out using 70 cm polycarbonate tubes 6.67 cm in diameter at AM5, AM8, AM17, LM1, LM9, LM7 and LM11. At AM5 and LM1 the sediment chambers were inserted into the sediment until the chamber was submerged into water entirely. Sediment chambers collected at other sites were moved to stand submerged in water with AM5 or LM1. They stood up in situ for nearly 24 hours. After in situ incubation, the overlying water of each chamber was collected using 60 mL serum glass bottles, the septum was sealed immediately, and 1 ml saturated $CuSO_4$ solution was added. All water and air samples were stored in an icebox onboard, moved to the lab each day, and stored in refrigerators.

4.2.2.2 Analytical Methods

Concentrations of dissolved and airborne CH_4 were measured by the headspace equilibration technique and gas chromatography (GC, Agilent 6890N) (Magen et al. 2014; Reeburgh 2007). DIC concentrations were determined using a UIC CM5017 Coulometer. Chlorophyll *a* (Chl-*a*) concentrations were measured using a Turner 10-AU. Sulfide in porewater was determined by colorimetric analysis of the methylene blue method (Cline 1969; Reese et al. 2011). These works were performed in the Isotope Core Laboratory at Texas A&M University-Corpus Christi. The $\delta^{13}C$-CH_4 values of some samples were analyzed at the Stable Isotope Lab of the University of California-Davis, with a precision of ±0.14‰.

4.2.2.3 Calculation

4.2.2.3.1 Floating chamber flux

Sea-air CH_4 flux (μmol/m^2·hr or μmol/m^2·d) acquired using floating chambers, which is called chamber flux in this paper, was calculated from the variation in CH_4 concentration in the

chambers during in situ observation. The slope of the linear curve in one hour with R^2>0.95 was taken as the emission rate of CH_4 used to calculate the diffusive CH_4 flux. If the CH_4 concentration dramatically increases in one hour, the difference between the final and initial concentrations of CH_4 was used to calculate the ebullition CH_4 flux. An important assumption here was that the pressure inside the chamber was kept at 1 atmospheric pressure in one-hour observations.

The emission rate of CH_4 (ppm) was converted to a metric expression (mol/L), and then the CH_4 flux in the chamber was calculated as follows.

$$F_{fc} = s \times \frac{P}{R \times T} \times \frac{V_{chamber}}{A_{chamber}} \times t \quad (1)$$

where F_{fc} is the chamber flux (μmol/m^2·hr or mmol/m^2·d); s is the emission rate of CH_4 concentration (ppm/min) in a linear increase; for bubble input, s is the variation before and after observation (ppm/h) in a surge increase; P is the gas pressure inside the chamber (Pa); R is the universal gas law constant (8.314510 m^3 Pa K^{-1} mol^{-1}); $\frac{P}{R \times T}$ is to convert volume concentration to molar concentration based on Law of Avogadro's; $V_{chamber}$ is the volume of the chamber (m^3); $A_{chamber}$ is the area of the chamber connecting surface water (m^2); and t is time efficient (converted from min to hour or day).

4.2.2.3.2 Sea-air diffusive methane flux

The diffusive CH_4 flux in the sea-air interface was calculated using the gas-transfer models (Wanninkhof 1992).

$$F = k_v \cdot (C_{obs} - C_{eq}) \quad (2)$$

where F is the flux of gas to the atmosphere (μmol/m^2·d); C_{obs} represents the measured concentration of dissolved CH_4 in water (nmol/L); C_{eq} is the concentration of CH_4 in equilibrium with the atmosphere at in situ temperature (nmol/L), calculated for each sample from the temperature- and salinity-dependent equilibrium relationship (Wiesenburg and Guinasso 1979);

and k_v is the gas transfer velocity (cm/h), calculated using the relationship between the standard gas transfer velocity (k_n) and Schmidt number (Sc).

$$k_v = k_n \times (\frac{Sc}{n})^{-\frac{1}{2}} \quad (3)$$

where Sc is calculated following Wanninkhof 2014 since water temperatures exceeded 30°C. (Wanninkhof 1992; Wanninkhof 2014). We use n of 660 to calculate k_v and diffusive flux since salinity in this region is high (>30) (Wanninkhof 1992). k_n is calculated using five methods, in situ floating chamber flux (k_{fc}) and four empirical equations (k_{model}).

Floating chambers: $k_{fc} = F_{fc}/(C_{obs} - C_{eq})$ (4)

Empirical equations:

R2001 (Raymond and Cole 2001): $k_{R2001} = 2.06e^{0.37\mu}$ (5)

J2008 (Jiang et al. 2008): $k_{J2008} = 0.314\mu^2 - 0.436\mu + 3.990$ (6)

W2014 (Wanninkhof 2014): $k_{W2014} = 0.251\mu^2$ (7)

VD2019 (Van Dam et al. 2019): $k_{VD2019} = 2.3 + 1.9u$ (8)

where μ is the mean wind speed at 10 m at nearby weather stations acquired from the NOAA National Centers for Environmental Information Climate Dataset (https://www.ncdc.noaa.gov/cdo-web/, station: NAS and Rockport Aransas Co Airport, for monthly average wind speed). Data from NAS were used in calculations for NC and LM; data from Rockport were applied in calculations for AM. The diffusive fluxes calculated using equations were collectively called F_{model}. The fluxes calculated using each standard gas transfer velocity were F_{fc}, F_{R2001}, F_{J2008}, F_{W2014}, and F_{VD2019}.

4.2.2.4 Sediment-water methane flux

The dissolved CH_4 flux at the sediment-water interface was calculated using Fick's first law (Berner 1980).

$$J_s = -\emptyset(D_0 \cdot \theta^{-2})\left[\frac{dc}{dz}\right] \quad (9)$$

J_s is the diffusive CH_4 flux at the sediment-water interface; $\emptyset$ is the porosity of sediment, measured from the weight loss of sediment dried at 80°C (Morin and Morse 1999); D_0 is the diffusion coefficient for CH_4 in water ($1.5x10^{-5}$ $cm^2 \cdot s^{-1}$) (Broecker and Peng 1974); θ is tortuosity, calculated using $\theta^2 = 1 - ln(\emptyset^2)$ (Boudreau 1996); and $\frac{dc}{dz}$ is the CH_4 gradient in porewater. Both the gradient of the first two layers of porewater and the gradient between bottom water and the first layer of porewater were applied to represent sediment-water CH_4 fluxes.

4.3 Results

4.3.1 Spatial and temporal variation in dissolved methane concentration and other parameters

4.3.1.1 Spatial variation

The dissolved CH_4 concentrations during the study period ranged from 1.7 to 479.9 nmol/L, corresponding to dissolved CH_4 saturations from 72% to 26659%. Except for the one at AM3 (Aransas Bay, Figure 4.1) in January 2021, CH_4 saturations were all larger than 100%, suggesting a long-term source of atmospheric CH_4. Although these estuaries are connected with each other, there were significant differences in CH_4 concentrations among them. The dissolved CH_4 concentrations in surface water were 20.6±29.8 nmol/L (2.5~167.6 nmol/L) at NC, 38.8±38.4 nmol/L (1.7~219.2 nmol/L) at AM, and 81.5±74.6 nmol/L (7.1~479.9 nmol/L) at LM. The highest CH_4 concentration over the whole region appeared at a channel site of Upper Laguna Madre (LM7) in August 2020 (479.9 nmol/L).

The ambient CH_4 concentrations in the above three estuaries were 1.93±0.19 ppm, 1.88±0.38 ppm and 1.84±0.16 ppm in NC, AM and LM, respectively. High ambient CH_4 concentrations (larger than 2.5 ppm) were detected at a pipeline platform at Redfish Bay (AM14)

in July and September 2020 and March and May 2021, suggesting a potential fossil fuel input to atmospheric CH_4.

Salinities in the three estuaries also showed significant differences, from highest to lowest, 34.0±7.1, 30.2±5.9 and 26.4±7.1 at LM, AM and NC, respectively. The lowest salinities (0.71 and 5.03) occurred at the NC1 site at the Nueces River mouth in October and November 2018, probably due to large riverine runoff. In contrast to salinity, Chl-*a* concentrations were highest in NC (3.99±1.73 µg/L) and lowest in LM (2.84±1.70 µg/L).

At NC, the sites in the maritime channel had higher dissolved CH_4 concentrations than open bay water (Figure 4.2). Similarly, at LM, a higher dissolved CH_4 concentration often appeared along the channel instead of in the seagrass meadow. The CH_4 concentrations in the open bay area of AM were always lower than those in mangrove creeks and channels. In most months, the CH_4 concentration in mangrove creeks was higher than that in channels.

4.3.1.2 Temporal variation

Water temperature followed a similar pattern as air temperature, lowest in the winter and highest in the summer. In this study, the water temperatures ranged from 12.5°C to 37.3°C (Figure S3). An extreme cold event in February 2021 lasted a few days with temperatures below 0°C, and the temperature recovered quickly (Figure 2.1g). Hence, the water temperatures in March 2021 were still higher than those in January and even higher than those in March 2019. Similar to the water temperature, the Chl-*a* concentration and pH increased from spring to summer and autumn and decreased from autumn to winter (Figure S3). The variation in DO was the opposite, with a higher concentration and percentage in the winter and a lower concentration and percentage in the summer. Except for differences among estuaries, salinity was higher in summer and lower in winter due to variations in precipitation, river discharge and evaporation.

Although the overall CH_4 concentrations were lowest in winter and highest in summer (Figure S3), the temporal variation among each estuary was somewhat different. In corpus Christi/Nueces bays, CH_4 concentrations were generally higher in channels than in bay water in most months (Figure 4.2). The most significant exception was in November 2018, when the highest CH_4 concentration appeared in the bay site (NC1) close to the mouth of the Nueces River, suggesting a potential riverine input. Sometimes the highest CH_4 concentration occurred at NC2, the waterway under the bridge, probably due to traffic pollution. In Aransas Bay, the highest CH_4 concentration appeared in mangrove creeks in May 2021, although CH_4 concentrations were generally higher in summer and early autumn. Unlike at AM, the highest CH_4 concentrations occurred in the channel in August 2019 at LM, and in most months, CH_4 concentrations were higher in the channel than in seagrass. Both CH_4 concentrations in the channel and in seagrass were lower in winter (Figure 4.2).

To offset the discontinuity of monthly observations, seasonal variation was taken into account. Based on local climate characteristics, March, April, and May are classified as spring; June, July and August are classified as summer; September, October and November are classified as fall; and the remaining months (December, January and February) are classified as winter. The dissolved CH_4 concentrations were highest in summer and lowest in winter at AM and LM (Figure 4.2). The same was true at the mangrove and seagrass sites. Those at NC were highest in autumn and lowest in summer.

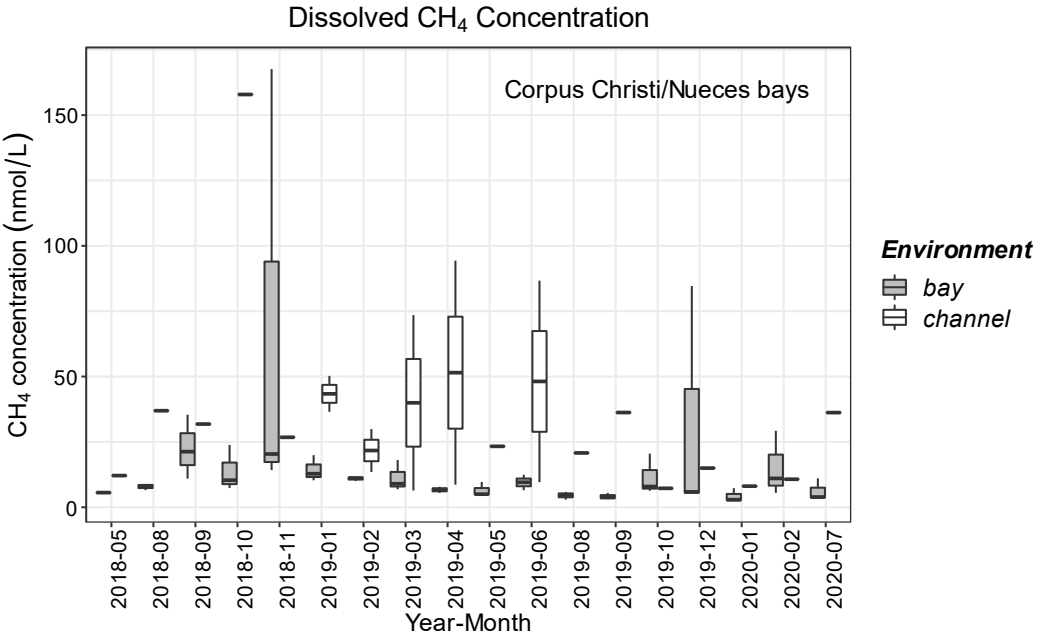
Dissolved CH_4 Concentration
Corpus Christi/Nueces bays
CH_4 concentration (nmol/L)
150
100
50
0
2018-05
2018-08
2018-09
2018-10
2018-11
2019-01
2019-02
2019-03
2019-04
2019-05
2019-06
2019-08
2019-09
2019-10
2019-12
2020-01
2020-02
2020-07
Year-Month
Environment
bay
channel

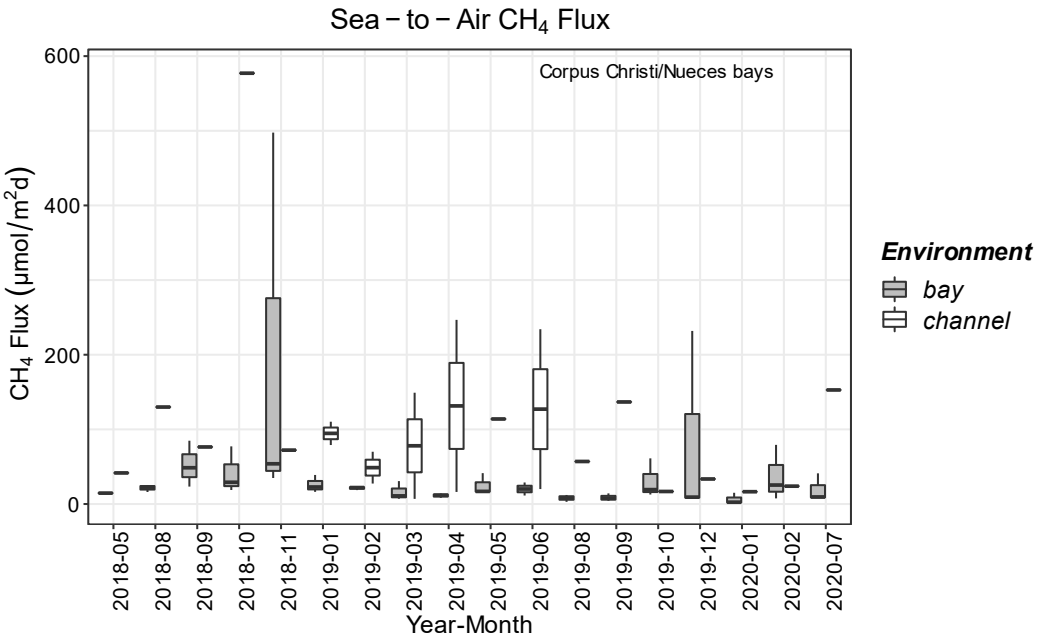
Sea − to − Air CH_4 Flux
Corpus Christi/Nueces bays
CH_4 Flux (µmol/m^2d)
600
400
200
0
2018-05
2018-08
2018-09
2018-10
2018-11
2019-01
2019-02
2019-03
2019-04
2019-05
2019-06
2019-08
2019-09
2019-10
2019-12
2020-01
2020-02
2020-07
Year-Month
Environment
bay
channel

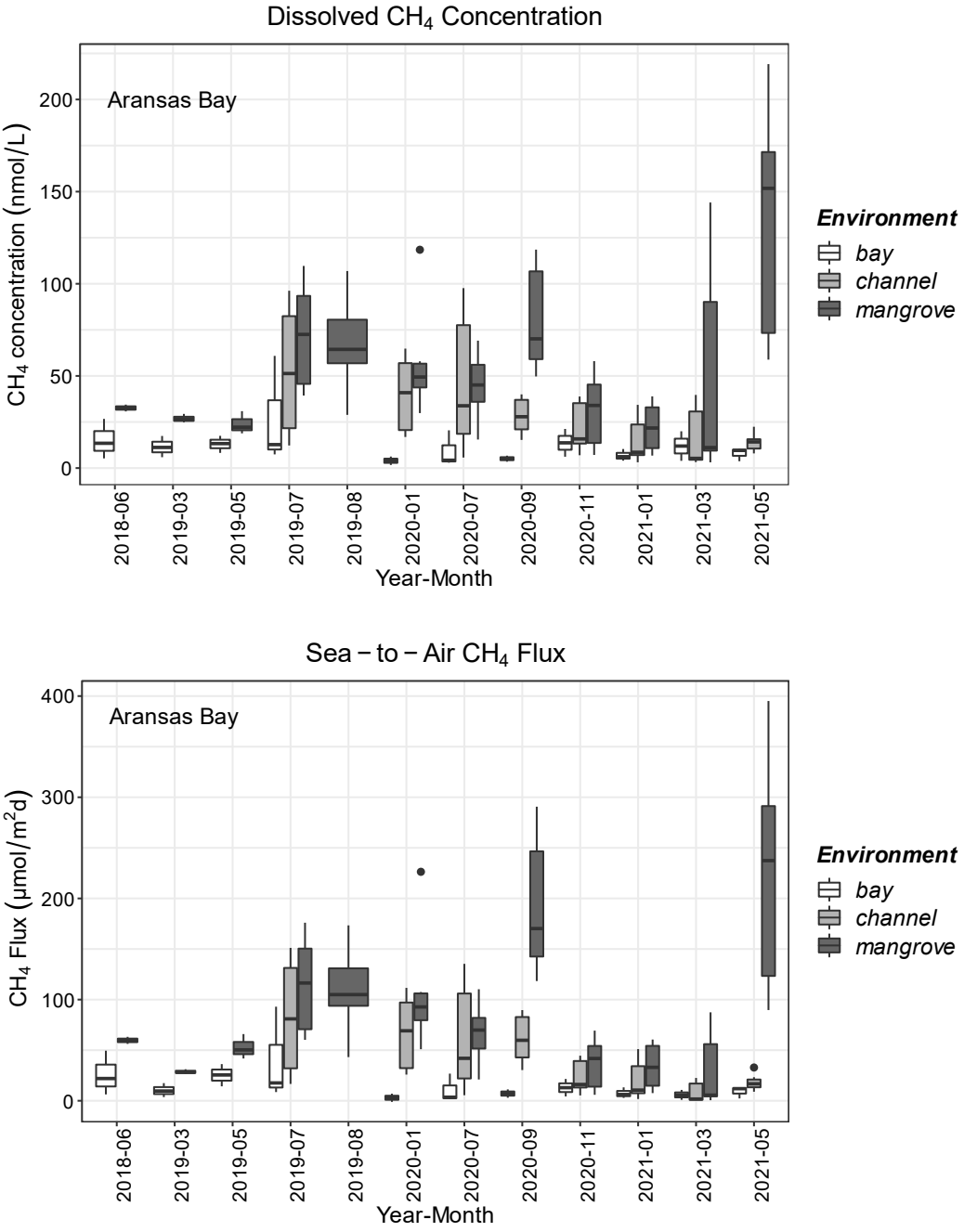
Dissolved CH_4 Concentration
Aransas Bay
CH_4 concentration (nmol/L)
0
50
100
150
200
2018-06
2019-03
2019-05
2019-07
2019-08
2020-01
2020-07
2020-09
2020-11
2021-01
2021-03
2021-05
Year-Month
Environment
bay
channel
mangrove
Sea − to − Air CH_4 Flux
Aransas Bay
CH_4 Flux (μmol/m^2d)
0
100
200
300
400
2018-06
2019-03
2019-05
2019-07
2019-08
2020-01
2020-07
2020-09
2020-11
2021-01
2021-03
2021-05
Year-Month
Environment
bay
channel
mangrove

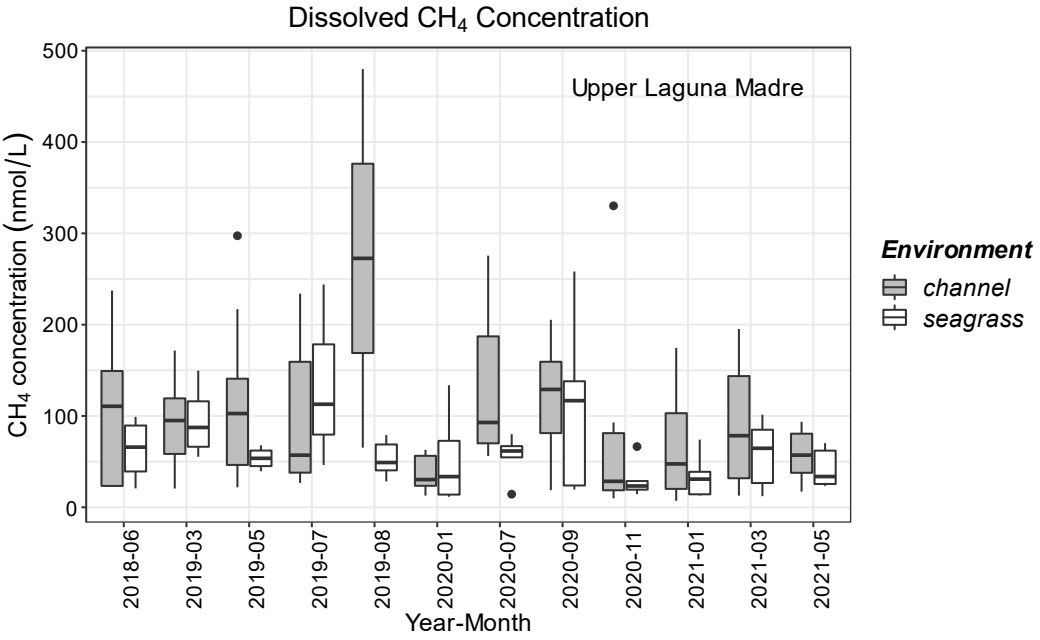
Dissolved CH_4 Concentration
Upper Laguna Madre
CH_4 concentration (nmol/L)
500
400
300
200
100
0
2018-06
2019-03
2019-05
2019-07
2019-08
2020-01
2020-07
2020-09
2020-11
2021-01
2021-03
2021-05
Year-Month
Environment
channel
seagrass

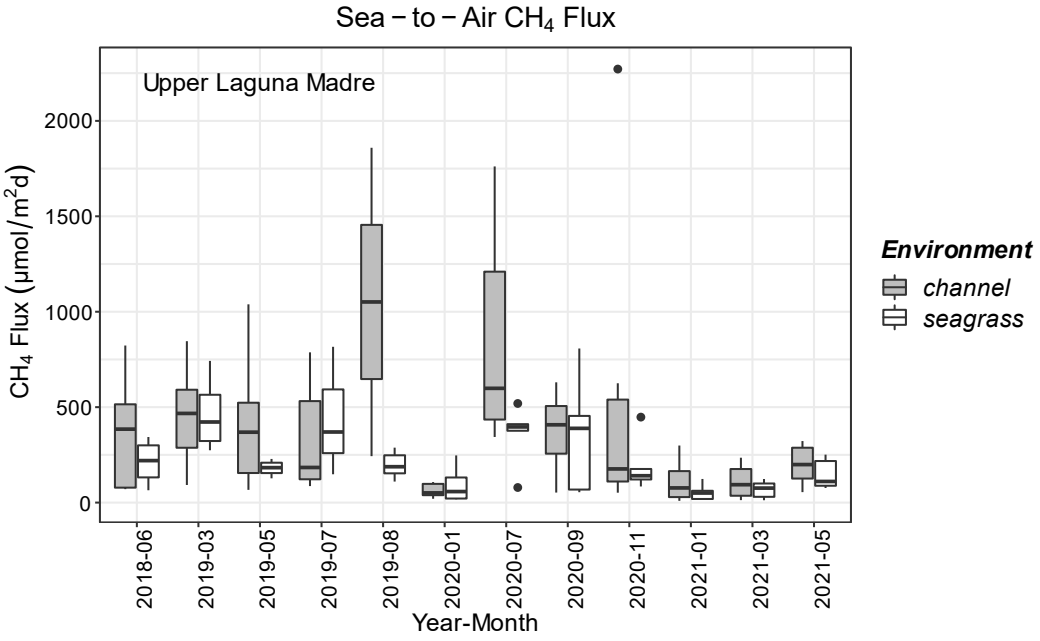
Sea − to − Air CH_4 Flux
Upper Laguna Madre
CH_4 Flux (µmol/m^2d)
2000
1500
1000
500
0
2018-06
2019-03
2019-05
2019-07
2019-08
2020-01
2020-07
2020-09
2020-11
2021-01
2021-03
2021-05
Year-Month
Environment
channel
seagrass

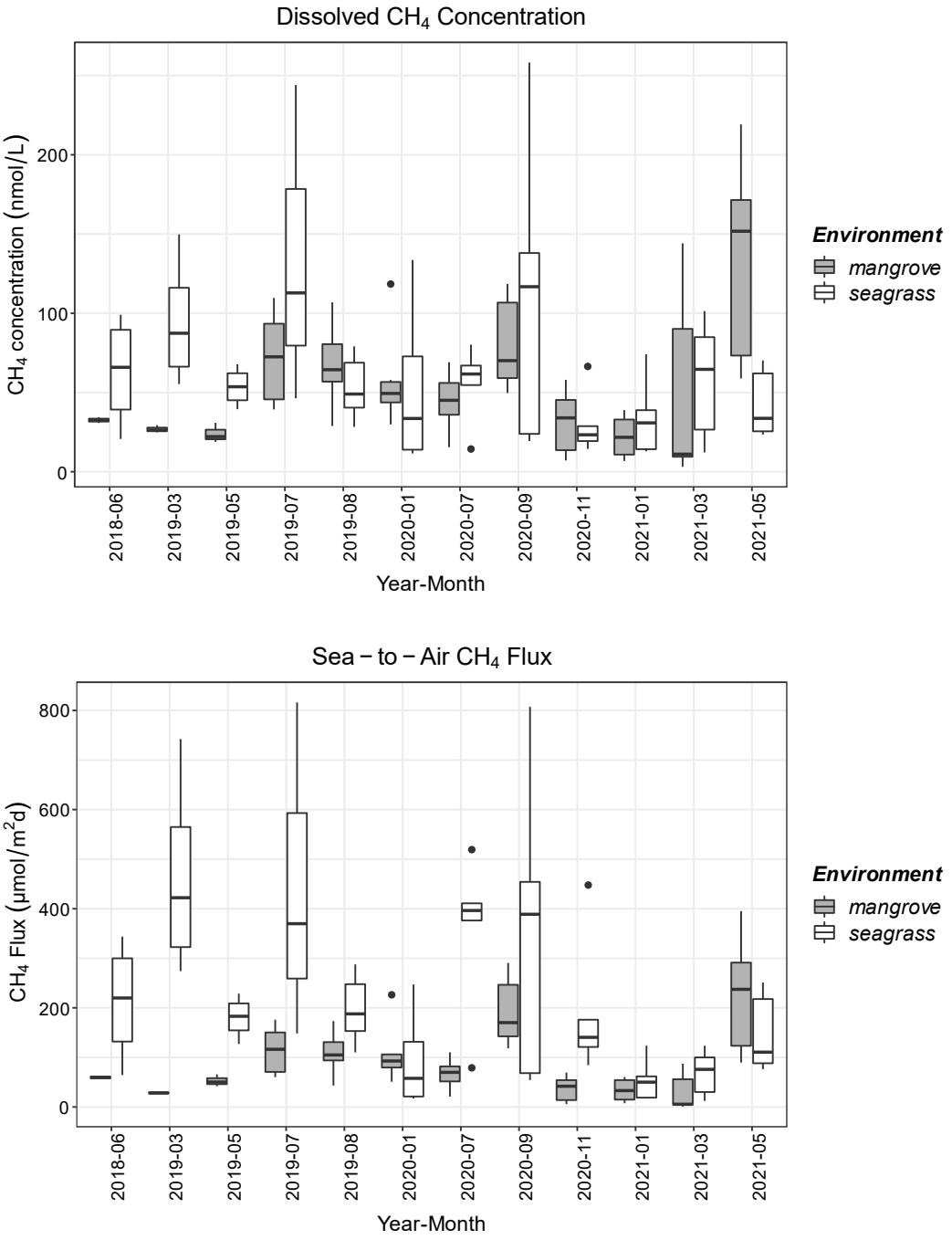

Figure 4.2 Monthly variation in dissolved CH_4 concentration and sea-air CH_4 flux in Nueces/Corpus Christi Bays, Aransas Bay, Upper Laguna Madre, and comparison between mangroves and seagrass during the study period.

4.3.2 Variations in methane in floating chambers

Floating chambers were built at LM1 (seagrass meadow) and AM5 (mangrove creek) to determine the in situ CH_4 emission from the water column of seagrass meadow and mangrove creek to the atmosphere and gas transfer velocity. As described in the previous chapters, except for floating chambers at AM5 in March 2019 and one chamber at LM1 in July 2020, the CH_4 concentrations in chambers at both sites increased linearly (R^2>0.95), indicating a primary diffusive transport of CH_4 from both ecosystems to the atmosphere. However, the CH_4 increasing rates at LM1 (0.009±0.001 ~ 0.071±0.011 ppm/min) were larger than those at AM5 (0.004±0.001 ~ 0.020±0.001 ppm/min). The diffusive floating chamber fluxes calculated using the increase rate of CH_4 concentrations were also lager at LM1 than AM 5 (Figure 4.3a). They indicated that there was more CH_4 released from seagrass meadows than from mangrove creeks.

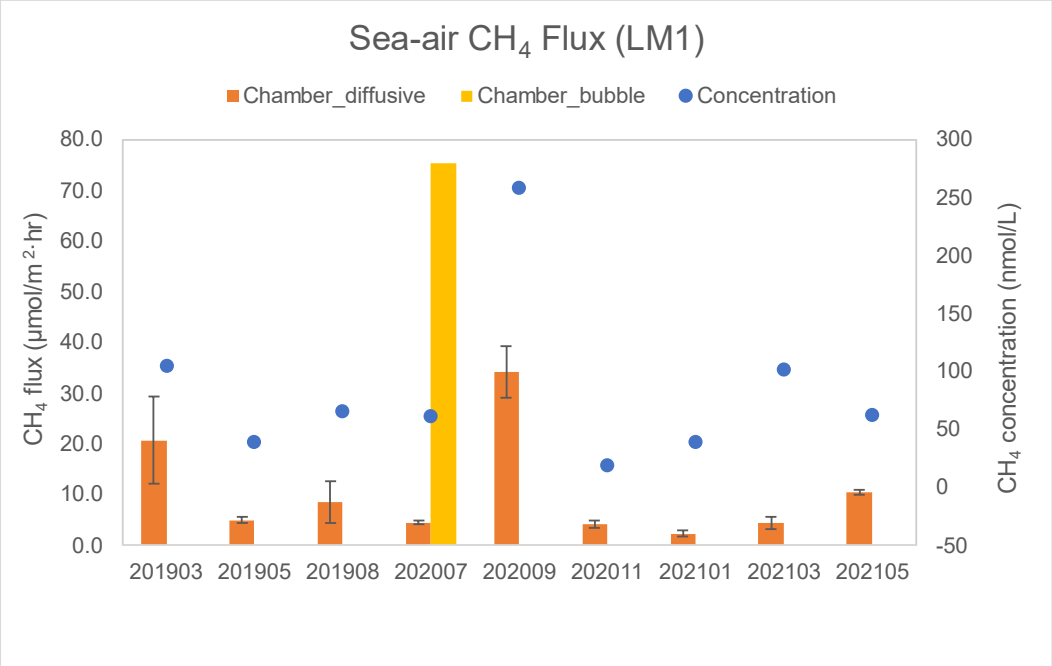

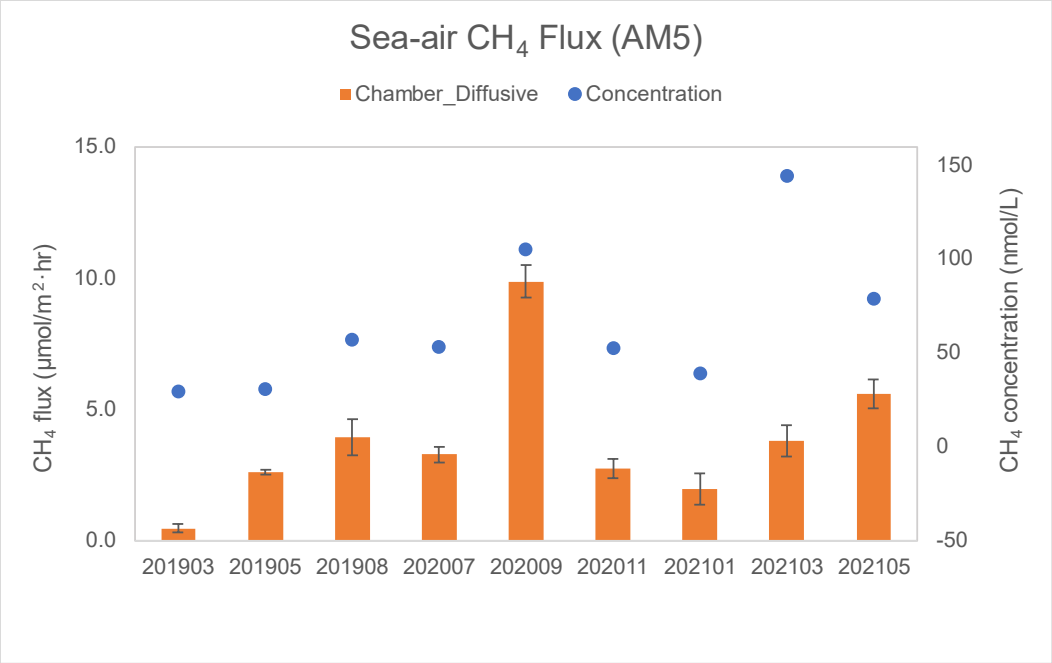

Figure 4.3a Floating chamber CH_4 fluxes and corresponding dissolved CH_4 concentrations at LM1 (seagrass) and AM5 (mangrove)

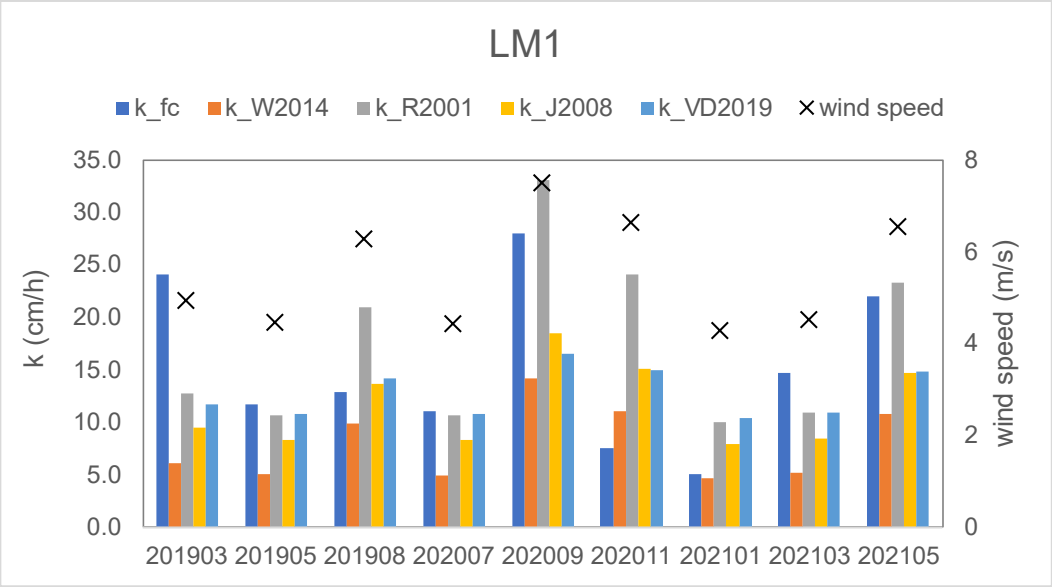

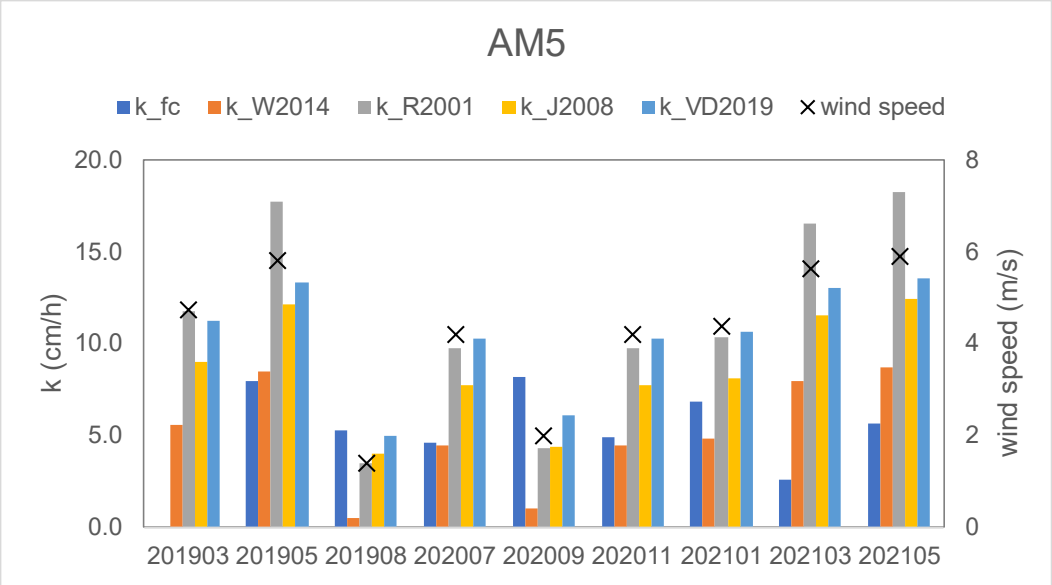

Figure 4.3b Standard gas transfer velocities acquired using floating chamber (k_fc) and empirical models (k_W2014, k_R2001, k_J2008, k_VD2019) and corresponding wind speeds at LM1 (seagrass) and AM5 (mangrove)

4.3.3 Sea-air methane flux

4.3.3.1 Gas transfer velocity

Standard in situ gas transfer velocities (k_{fc}) were calculated using floating chamber fluxes at LM1 and AM5. The average k_{fc} values at LM1 and AM5 were 14.0±7.6 cm/h and 5.3±2.0 cm/h, respectively. Most k_{fc} values at LM1 were higher than those at AM5 (Figure 4.3b), further indicating a stronger gas exchange at the water-air interface over the seagrass meadow than at the mangrove creek.

4.3.3.2 Diffusive methane flux

Diffusive sea-air CH_4 fluxes were calculated using fixed k_{fc} acquired using a floating chamber, and various k_{model} values were obtained using equations based on the relationship between gas exchange and wind speed. The overall average sea-air diffusive flux calculated using k_{fc} was similar to that calculated using equation VD2019 and then that of J2008 (Table 4.1). The

average flux calculated using W2014 was lowest and that calculated using R2001 was highest. However, the average F_{fc} at AM was similar to the average F_{W2014}. Among the fluxes acquired using empirical equations, F_{R2001} was highest in all estuaries, and F_{W2014} was the smallest.

Table 4.1 Diffusive sea-air CH_4 fluxes estimated using different methods ($\mu mol/m^2 \cdot d$)

	F_{fc}	F_{W2014}	F_{R2001}	F_{VD2019}	F_{J2008}
NC	NA	36.2±61.1	76.1±127.5	60±100.9	52.8±88.6
AM	53.6±68.8	61.3±82	129.7±171.1	117.9±140.7	95.9±120.8
LM	317.1±377.9	179.9±189.9	384.2±412.3	283±282.2	257.2±264.3
Average	171.9±289.1	101.2±145.3	215.5±312.8	168.65±221.3	148.29±204.2

Although fluxes calculated using various gas transfer velocities are different, they followed similar spatial and monthly variation patterns. All types of fluxes were highest at LM and then AM. The sea-air CH_4 fluxes at NC were lowest in this region. At NC, the highest sea-air CH_4 fluxes appeared in October and November 2018, and the lowest flux appeared in January 2020. There was no obvious seasonal variation in other months. At AM, the highest sea-air CH_4 fluxes were observed in May 2021. In addition, CH_4 fluxes at AM increased from spring to summer in 2019 and from winter to spring in 2020-2021 and decreased from summer and early autumn to winter in 2020-2021. At LM, the lowest CH_4 fluxes appeared in winter months, January and November 2020 and January 2021. In other months, CH_4 fluxes were all at a higher level.

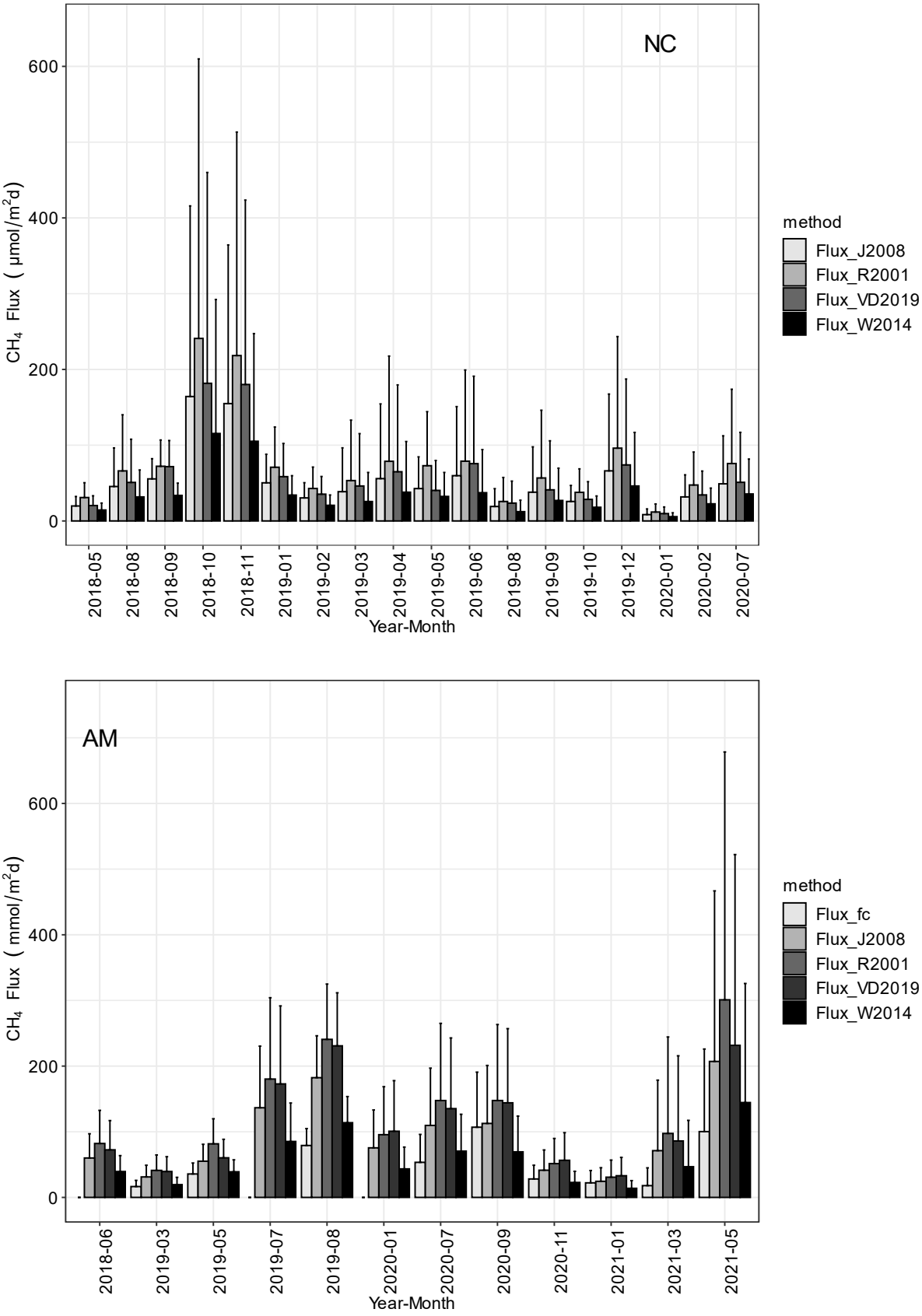
NC
AM
CH4 Flux (μmol/m2d)
CH4 Flux (mmol/m2d)
Year-Month
method
Flux_J2008
Flux_R2001
Flux_VD2019
Flux_W2014
Flux_fc

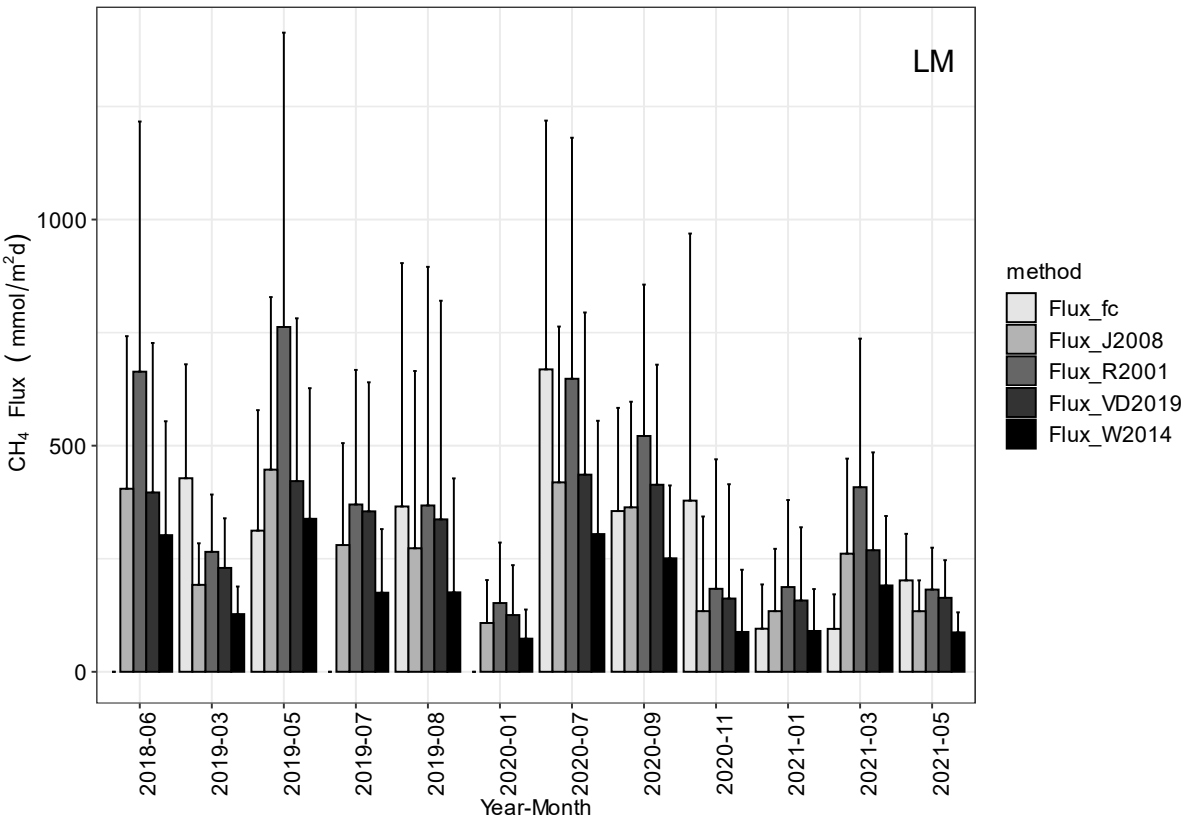

Figure 4.4 Diffusive CH_4 fluxes (mean±sd) at NC, AM and LM. There was no F_{fc} at NC.

4.3.4 Methane in sediment porewater and flux at the sediment-water interface

Porewater CH_4 concentrations in seagrass, mangrove and channel sediment showed high spatial and temporal variation (Figure S4). At LM1 (seagrass), the overall porewater CH_4 in sediment cores was highest in September 2020 (< 3200 nmol/L) and lowest in August 2019 (<60 nmol/L). However, all the top 10 cm sediments had lower CH_4 concentrations than the deeper sediments. Therefore, porewater sulfide concentrations were highest in September 2020 (up to 1700 μmol/L) and lower in May and August 2019 (< 130 μmol/L). This result indicated a synchronic variation in CH_4 and sulfide. Porewater CH_4 concentrations in the sediment core (10 cm) collected at LM9, another seagrass site, were also minor (< 25 nmol/L), corresponding to zero sulfide.

At AM5 (mangrove creek), porewater CH_4 concentrations were lowest in August 2019 (< 100 nmol/L). In May 2019 and September 2020, CH_4 concentrations increased from top to deeper sediment, with a maximum of nearly or over 14000 nmol/L at approximately 12 cm depth, indicating a maximal CH_4 production layer. Sulfide concentrations in sediment were also much higher in May 2019 (up to 900 µmol/L) and September 2020 (< 750 µmol/L) than in August 2019 (<150 µmol/L). The variation in sulfide followed a similar pattern as CH_4 in sediment. Porewater CH_4 concentrations collected at AM8, another mangrove site, in August also increased with sediment depth but were less than those at AM5 (up to 8000 nmol/L). However, sulfide (up to 1800 µmol/L) was much larger than at AM5. The CH_4 (< 160 nmol/L) and sulfide concentrations (< 270 µmol/L) in porewater at AM17 (mouth of mangrove creek) were much lower than those at AM8 but higher than those at AM5.

Porewater CH_4 concentrations at channel sites LM7 and LM11 were also at low levels (< 100 and < 250 nmol/L) in August 2019. The sulfide concentrations at LM7 and the top 12 cm at LM11 were zero, indicating a less anoxic environment. CH_4 and sulfide concentrations (< 70 nmol/L and 0 µmol/L) were also measured at NC1, an open bay site. In May 2019, CH_4 and sulfide concentrations in porewater at LM7 were much higher (up to 800 nmol/L and 2050 µmol/L).

4.4 Discussion

4.1 Methane emission at the sea-air interface

4.4.1.1 Standard gas transfer velocity

Since the flux is defined as the product of the gas transfer velocity (i.e., kinetic forcing) and the gas concentration difference between air and well-mixed water below (i.e., thermodynamic potential), factors that control these two parts can affect the upscaling of the sea (water)-air flux (Wanninkhof et al. 2009). The k_{fc} at the seagrass meadow (LM1) was 5.1~28.0 cm/h (14.0±7.6

cm/h), larger than that at AM5, indicating more gas exchange at the water-air interface over the seagrass-dominated lagoon than at the mangrove creek. Wind speed is a possible reason, considering that the wind speeds over LM1 (4.3~8.9 m/s, 5.8±1.5 m/s) were larger than those at AM5 (1.4~5.9 m/s, 4.1±1.6 m/s). Moreover, in comparison with AM, water exchange and tidal processes were weak at LM. Hence, the higher gas exchange at LM was more likely due to wind speed.

The overall k_{fc} had a weak quadratic relationship with wind speed (R^2=0.33, $p<0.01$). The k_{fc} at LM1 was positively related to wind speed (Figure 4.5a, R^2=0.23, $p<0.01$). However, the k_{fc} data at AM5 did not show any relationship with wind speed (Figure 4.5b). Nevertheless, when we artificially classified k_{fc} by high (>60 nmol/L) and low (<60 nmol/L) dissolved CH_4 concentrations, there was a significant relationship between k_{fc} and wind speed at low CH_4 concentrations (R^2=0.68, $p<0.01$, Figure 4.5c). It seemed that the impact of wind speed on the gas transfer velocity was more significant when the dissolved CH_4 concentration was low. We also found that the difference in temperature between air and surface water was negatively related to k_{fc} in the daytime at LM1. The air temperature was higher than the surface water temperature during the day. A larger temperature difference between air and surface water seemed to impede the gas exchange between water and atmosphere in the daytime. However, no such relationship was observed at AM5. By comparison, the temperature difference seemed to have a greater impact on larger k_{fc}, e.g., > 10 cm/h. Our current dataset was quite limited, and we still need more observations to verify the influence of wind and temperature on the gas transfer velocity.

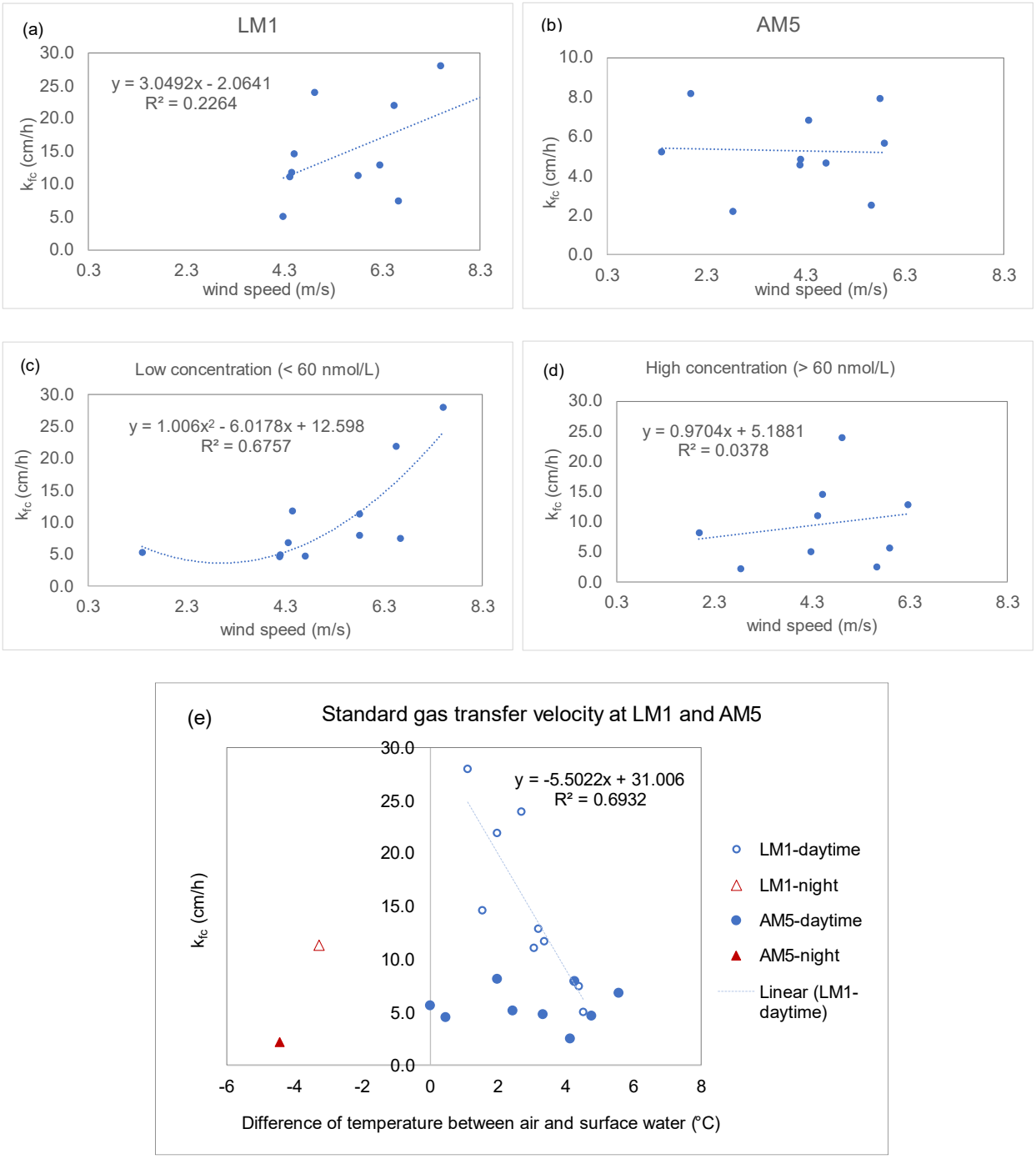

Figure 4.5 Relationships between standard gas transfer velocity k_{fc} and wind speed (a~d) and temperature difference (e).

Most k_{fc} values were within the range of the k_{model} at each site (Figure 4.3b). At LM1, k_{fc} was relatively closer to k_{W2014} in winter (November 2020 and January 2021) but closer to k_{R2001},

k_{J2008} and k_{VD2019} in other warmer months. Exceptionally, k_{fc} in March 2019 was much larger than the others. At AM5, k_{fc} was relatively closer to k_{W2014} when the wind speed was larger than 2 m/s. Otherwise, k_{fc} was similar to k_{VD2019}. However, although wind speeds were larger than 5 m/s, k_{fc} was much smaller than the four k_{model} in March and May 2021. Hence, empirical models could be applied in parameterizing the standard gas transfer velocity in some conditions in this region. Similar to other studies, it is not easy to obtain a unified equation to parameterize the standard transfer velocities in these estuaries in all months/seasons (Rosentreter et al. 2017).

4.4.1.2 Diffusive sea-air flux

As discussed in previous chapters about mangrove creeks and seagrass meadows, during the study period, we found that the monthly F_{fc} could match the F_{model} acquired from some empirical models (Figure 4.6). Since the assumption is that chamber flux (F_{fc}) could reflect in situ sea-air CH_4 flux, data of F_{model} that did not match F_{fc} were modified based on their relationships (slope of the trendline) to obtain a final sea-air CH_4 flux for further analysis. In months without floating chamber observations at AM and LM, F_{model} was selected as the final sea-air CH_4 flux, referring to months with similar environmental conditions (e.g., wind speed, temperature, month, etc). The final sea-air CH_4 fluxes at NC were estimated using the average of four sets of F_{model}.

The unified monthly sea-air CH_4 fluxes at LM were highest, and those at NC were lowest (Figure 4.2). Similar to the dissolved CH_4 concentration, the CH_4 fluxes at the channel sites of NC were higher than those at the bay sites except in November 2018. The variation in CH_4 fluxes at AM was also similar to the dissolved CH_4 concentration. Sea-air CH_4 fluxes over mangrove creeks increased from spring to summer and decreased from summer-early autumn to winter. However, the flux at mangrove creeks in May 2021 was exceptionally large. CH_4 fluxes at channel sites were smaller than those at mangrove water. Unlike at AM, diffusive CH_4 fluxes in the channel were

larger than those in the seagrass meadow at LM. Despite the highest dissolved CH_4 concentration at LM7 in August 2019, the highest diffusive CH_4 flux appeared at LM11, another channel site, in November 2020, caused by a larger monthly average wind speed. Overall, there was a significantly positive relationship between diffusive CH_4 flux and dissolved CH_4 concentration (R^2=0.76, $p<0.01$).

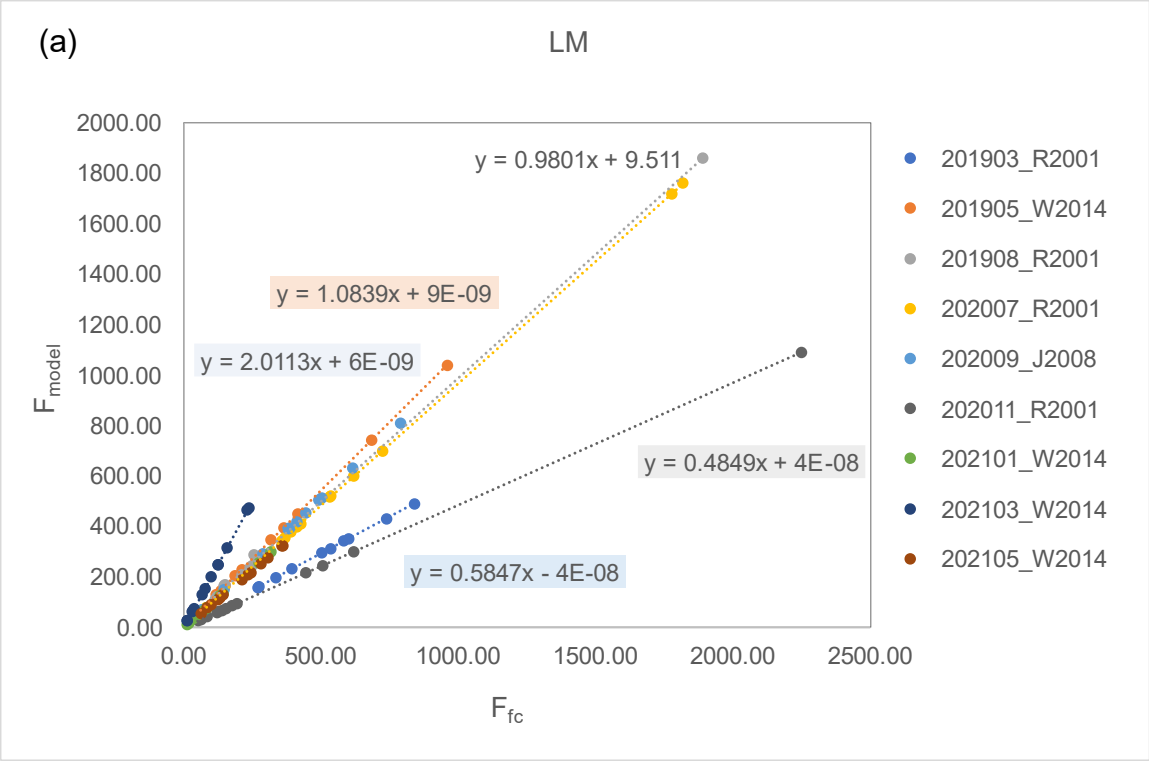

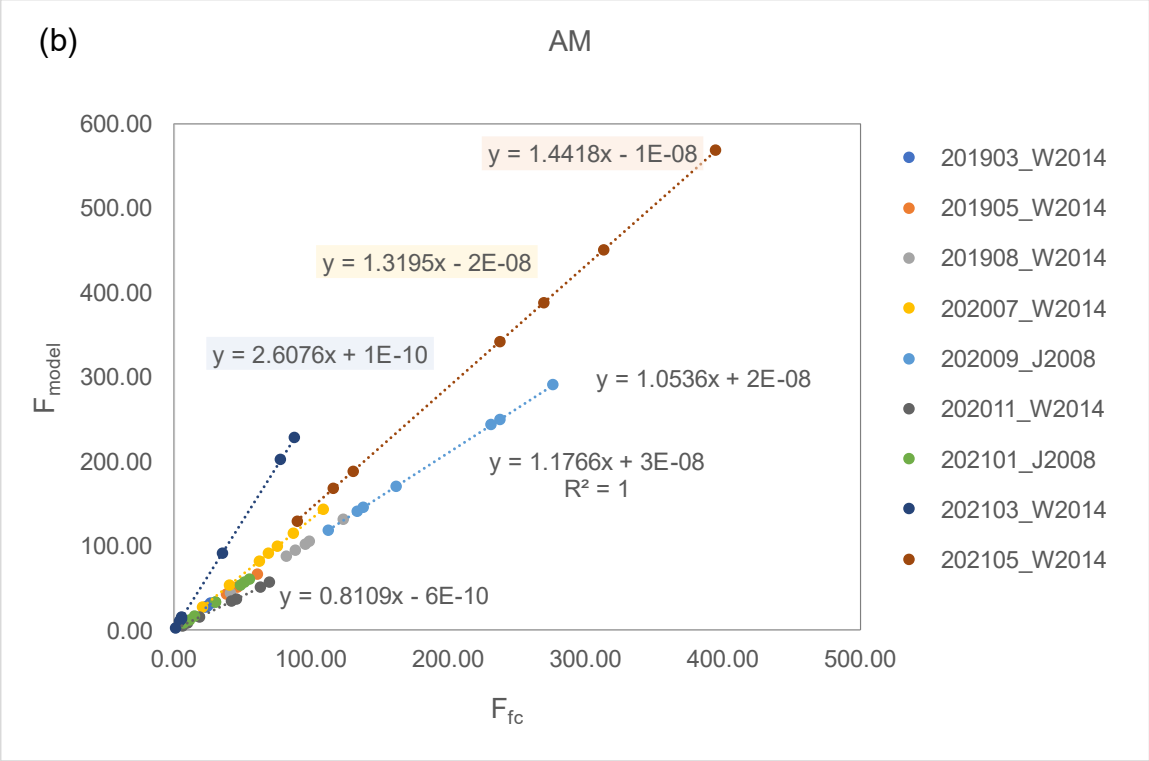

Figure 4.6 Linear relationships between floating chamber fluxes (F_{fc}) and fluxes acquired using empirical equations (F_{model}).

(a) Upper Laguna Madre; (b) Aransas Bay. Only the F_{model} with values close to those of F_{fc} are shown. The slopes of the trendline near 1 represented F_{model} matched F_{fc}. Otherwise, the slopes represent the ratio between F_{model} and F_{fc}.

4.4.1.3 Factors that influence methane emissions

In comparison with the standard gas transfer velocity, which was weakly correlated with the CH_4 flux (R^2=0.20, $p<0.01$), the CH_4 concentration had a more significant relationship with the flux (R^2=0.76, $p<0.01$). The variation in CH_4 concentration is the key process related to CH_4 cycling, including CH_4 production, consumption, and transport, which can be affected by complicated biological, hydrological, and geological processes in estuaries. Moreover, the dissolved CH_4 concentration has already been capable to be measured precisely compared with the

gas transfer velocity. Hence, it is necessary to recognize the factors that affect the dissolved CH_4 concentration.

4.4.2 Variation among different environmental settings

Although Corpus Christi/Nueces Bays, Aransas Bay (Harbor Island) and upper Laguna Madre are adjacent waters connected with each other, they have different environmental characteristics. NC is primarily composed of a large area of open bay and a deep maritime channel connecting the Gulf of Mexico and the Port of Corpus Christi. LM is dominated by seagrass, and in the middle of the lagoon, it is a dredged intercoastal waterway for domestic transportation and recreational boating. AM is composed of mangrove/salt marshes, bays, and intercoastal waterways.

The variation in CH_4 concentration among different environmental characteristics, such as seagrass, mangroves, channels and bays, could partly explain the discrepancy in these estuaries. The average CH_4 concentration was largest in the channel (77.5±80 nmol/L, 3.1~480 nmol/L), followed by seagrass (62.3±49.9 nmol/L, 11.6~258.2 nmol/L) and mangroves (57.8±44.2 nmol/L, 3.1~219.2 nmol/L). The CH_4 concentration was significantly lowest in the open bay (13.3±22.6 nmol/L, 1.6~167.6 nmol/L). Although channels were dredged across all three estuaries, the dissolved CH_4 concentration at LM was highest (94.4±85.2 nmol/L, 7.1~479.9 nmol/L), followed by NC (36.2±36.3 nmol/L, 6.4~157.9 nmol/L) and AM (27.6±23.6 nmol/L, 3.1~97.6 nmol/L). Hence, it is reasonable that the dissolved CH_4 concentrations in LM were higher than those in the other two estuaries due to its seagrass and intercoastal coverage. Since AM is composed of mangrove/salt marsh, bay, and intercoastal waterway, its average dissolved CH_4 concentration was higher than NC primarily occupied by the bay but lower than LM.

4.4.3 Comparison of methane emissions from seagrass meadow and mangrove aquatic systems

The average dissolved CH_4 concentration in the seagrass meadow was similar to and even slightly higher than that in mangroves in this region, although the carbon deposit rate in seagrass sediment (global average from seagrass production, 41~66 gC/ m^2·yr (Kennedy et al. 2010)) was much less than that in mangrove sediment (e.g., at Harbor Island, 253~270 gC/m^2·yr (Bianchi et al. 2013)). In some months, CH_4 concentrations in seagrass meadows were higher than those in mangrove creeks (Figure 4.2). Although globally more CH_4 was emitted from mangroves than from seagrass, there were few comparisons of CH_4 emissions between mangroves and seagrass in the same region.

4.4.3.1 Methane emissions at the sediment-water interface

Sediment cores collected in spring, summer and autumn showed higher porewater CH_4 concentrations in mangrove sediment than in seagrass sediment (Figure S4). This result is reasonable because more CH_4 was produced in mangrove sediment than in seagrass sediment due to larger carbon deposits. Diffusive CH_4 fluxes at the sediment-water interface of mangrove sediment were also larger than those of seagrass sediment. However, in situ sediment incubation experiments observed more CH_4 emissions from seagrass than from mangrove sediment (Figure 4.7). This result suggested that CH_4 in the porewater of seagrass sediment has other ways to enter overlying water.

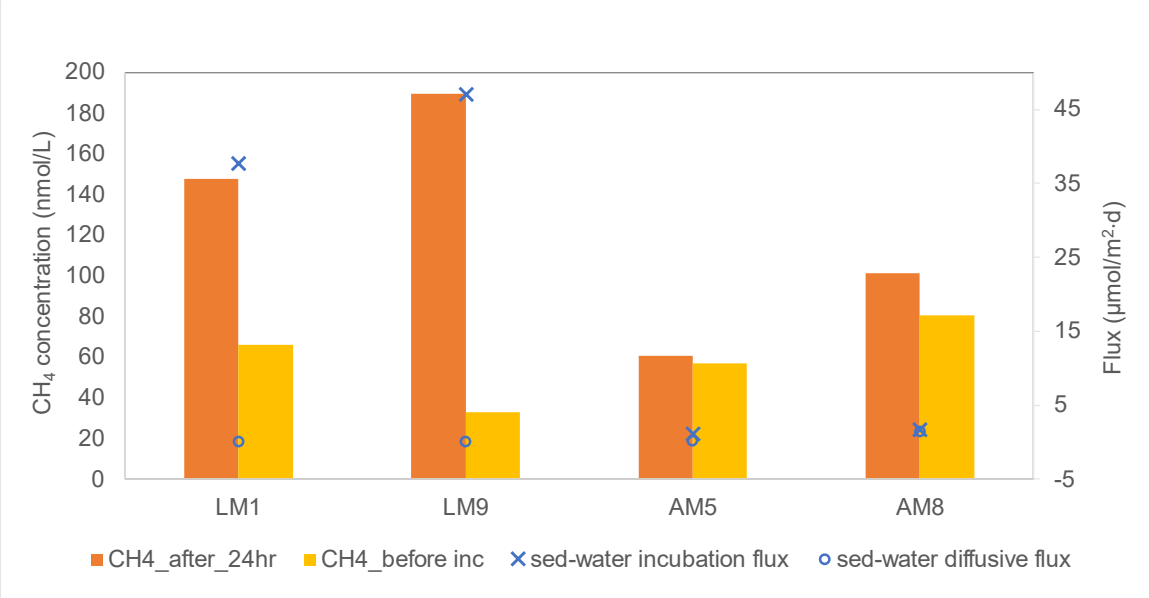

Figure 4.7 Comparison of diffusive fluxes and incubation fluxes at the sediment-water interface. LM1 and LM9 are at seagrass meadow; AM5 and AM8 are at mangrove creeks.

4.4.3.2 Methane emissions at the water-air interface and decomposition in the water column

Both sea-air CH_4 fluxes at seagrass and standard gas transfer velocities at LM1 were larger than those at mangrove creeks, implying more CH_4 emissions at the sea-air interface of seagrass than mangrove creeks. Obviously, the evasion of CH_4 from surface water to the atmosphere cannot explain the higher CH_4 concentration in the seagrass area. Additionally, water incubation showed that the decomposition of CH_4 in the water column was similar at LM1 and AM5, which also cannot account for the higher CH_4 concentration in seagrass water.

4.4.3.3 Implication from diurnal methane variations

The diurnal variations in CH_4 in seagrass meadows were found to be related to photosynthesis and respiration in seagrass ecosystems (Chapter III), while in mangrove creeks, CH_4 was controlled by tidal processes (Chapter II). Taking the diurnal variation in spring tide as an example (Supporting Information, Figure 4.8), the dissolved CH_4 concentration at the middle

of the creek increased at a rate of +6.45 nmol/L·h during the ebb due to input from inside the mangrove creek and/or porewater exchange. Moreover, as the CH_4 concentration in the middle of the creek increased during the ebb, it also indicated that CH_4 was being exported from the mangrove to the outside bay area, similar to observations in some other estuaries (Burgos et al. 2018; Dutta et al. 2015). During the flood, bay water with a lower CH_4 concentration flushed into the creek and diluted the CH_4 concentration in the creek at -4.85 nmol/L·h. Bay water could also dilute porewater CH_4 concentrations by flushing into the sediment through crab burrows or under pressure. By the end of flooding, the CH_4 concentration increased at a low rate of +0.91 nmol/L·h due to CH_4 input from upper intertidal sediment, which often occurred during spring tides (Call et al. 2019). The variation in diffusive CH_4 concentration at AM5 after the whole tidal process was +2.8 nmol/L·d, which was lower than the CH_4 left in the water of seagrass meadows after diel cycling two days ago (+4.5 nmol/L·d, Chapter 3). Hence, it further proved that tidal processes could reduce CH_4 emissions from mangrove aquatic systems. A reduction of CH_4 emissions under tidal flow management has been observed in a restored estuarine wetland in southeast China (Yang et al. 2020). Although the dominated plants there were saltmarsh, not mangrove, our finding was consistent with it that tidal process is helpful in reducing CH_4 emissions.

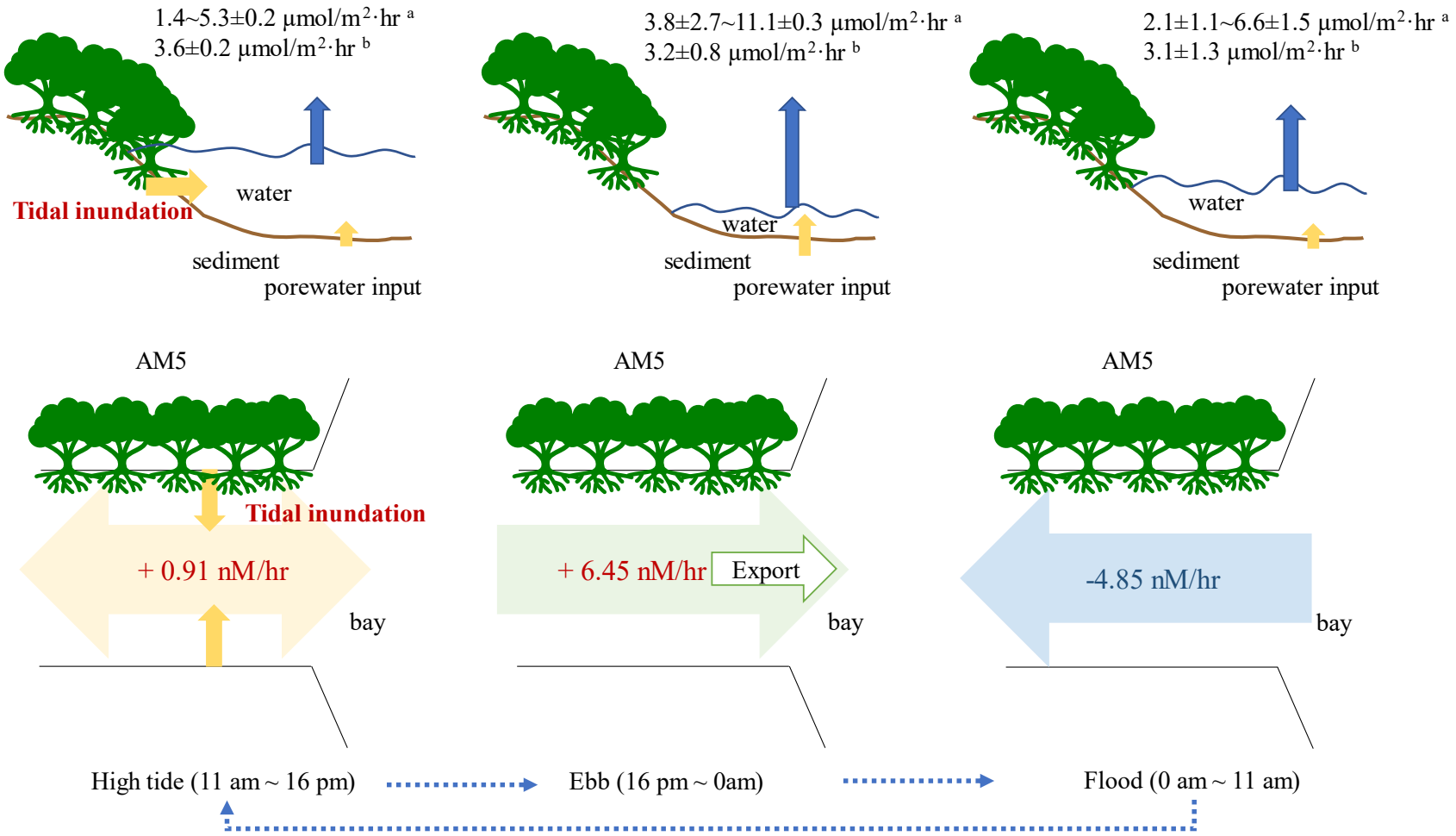

Figure 4.8 CH_4 cycling at the mangrove creek.

Three periods were defined based on tidal procession (high tide, ebb, and flood). [a] Sea-air flux calculated using the gas transfer models; [b] Sea-air flux calculated using k_{fc}. +: increase; -: decrease.

4.4.3.4 Extreme cold event

Although CH_4 emissions were higher from seagrass meadows than from mangrove creeks in most months, in May 2021, more CH_4 was released from mangrove creeks (Figure 4.2). As discussed in Chapter II, this unexpectedly high level of CH_4 emissions was caused by a large amount of carbon deposits due to the mortality of mangrove forests during the extreme cold event in February 2021. In contrast to mangroves, dissolved CH_4 concentrations in March and May 2021 in seagrass did not significantly change after the cold event. CH_4 concentrations were higher in March and May, similar to those in 2019, while sea-air CH_4 fluxes were higher in May due to the higher standard gas transfer velocity. Since the extreme cold lasted only a few days, seagrass meadows submerged under water were probably kept from suffering from the cold because of their higher heat capacity than air. Moreover, *Halodule wrightii* has good chill tolerance (McMillan 1979).

4.4.4 Riverine input and exchange with the Gulf of Mexico

Open Bay has the lowest CH_4 concentration, which is the primary reason why NC had a lower CH_4 concentration than the other two estuaries. The dissolved CH_4 concentrations at NC1, the site close to the Nueces River, were always at a low level except in November 2018 (Figure 4.2), although the Nueces River had much higher CH_4 concentrations (NR1: 621.9 ± 89.4 nmol/L from Jan 2019 to June 2019). The exceptionally high CH_4 concentration at NC1 in November 2018 coincided with the largest runoff of the Nueces River during the study period (Figure 4.9), revealing a riverine input from the Nueces River. The positive linear relationship between the monthly Nueces River discharge and synchronic dissolved CH_4 concentration at NC1 illustrated the contribution of the Nueces River to the bay (Figure 4.9). Even in the months with low water discharge, the CH_4 concentration was positively correlated with river runoff (Figure 4.9 Right,

blue line). The porewater CH_4 concentration in the sediment core collected at this site in August 2019 was low (top 14 cm: 17.9~65.3 nmol/L, Figure S4), and the transport of CH_4 at the sediment-water interface was minor (0.054 μmol/m^2·d). Hence, it is most likely that riverine discharge influenced the CH_4 concentration at NC1. Because the CH_4 concentration at NC1 was quite low, riverine input was easily ignored.

In addition to CH_4 concentration, other parameters also showed the influence of rivers. At NC1, salinity exponentially decreased as river discharge increased (R^2=0.79). In the whole bay, salinity increased from the site near the river mouth (NC1) to the site near the Ship channel (NC4) due to less invasion of seawater from the Gulf of Mexico and/or mixing with freshwater discharge from the Nueces River. The CH_4 concentration was also significantly negatively related to salinity, similar to other riverine-dominated estuaries (Dutta et al. 2015). However, due to the low discharge of the Nueces River, the riverine input of CH_4 to the bay was quite limited. No significant relationship was observed between CH_4 concentration and discharge/salinity at site NC2, which was 9.3 km away from NC1.

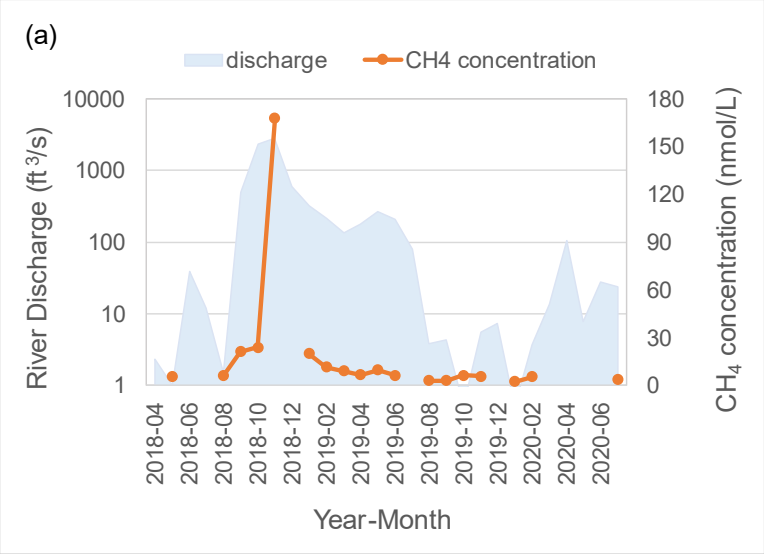

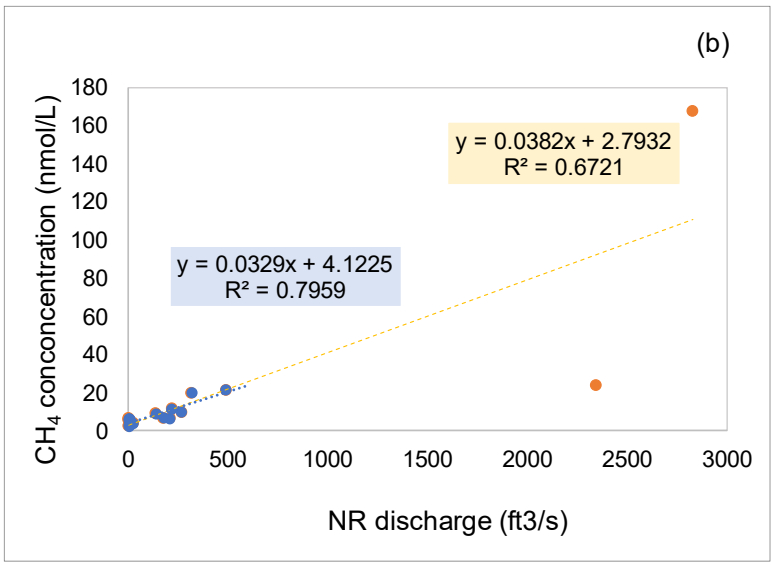

Figure 4.9 (a): Monthly variation in CH_4 concentration at NC1 and Nueces River discharge. (b): Relationship between CH_4 concentration at NC1 and Nueces River discharge.

The orange line represents all data, and the blue line represents the data without outliers in October and November 2018.

4.4.5 Anthropogenic disturbance

4.4.5.1 Channel

Locally, the highest levels of CH_4 concentration and diffusive CH_4 flux were found along the channels, which can be explained by two potential reasons. The first one is pollution. Except in November 2018, CH_4 concentrations at the sites along the maritime channel in Corpus Christi Bay were much higher than those at other sites in the open bay (Figure 4.2, Figure S1). Particularly elevated dissolved CH_4 concentrations were found at the entrance to the canal of the Port of Corpus Christi (64.2±29.3 nmol/L). Although it cannot compare with the high level of CH_4 observed at polluted canals (up to 8378 nmol/L) and harbor areas (1796 nmol/L) in tropical lagoons in Mexico (Chuang et al. 2017), it was higher than that at other sites (17.6±27.6 nmol/L) in the Corpus Christi/Nueces bays.

High CH_4 concentrations can also be attributed to the removal of surface sediment by human activities, e.g., dredging and vessel grounding. The two highest CH_4 concentrations (479.95 nmol/L in August 2019 and 266.1 nmol/L in July 2020) at Upper Laguna Madre were observed in the middle of the intracoastal waterways (LM7). Their $\delta^{13}C$-CH_4 values of -59.5‰ and -59.84‰ suggested a biogenic source rather than a petroleum-related pollution source of CH_4 input. In comparison, the dissolved CH_4 concentration at LM1, the site over seagrass 300 meters away from LM7, was much lower (65.9 nmol/L and 61.7 nmol/L), and $\delta^{13}C$-CH_4 was relatively higher (-57.8‰ to -57.3‰ in August 2019 and -58.7‰ in July 2020). Porewater CH_4 and sulfide concentrations at LM7 in May 2019 were much larger than those in August 2019, up to 800 nmol/L and 2050 μmol/L, respectively (Figure S3). In August, CH_4 concentrations were no more than 100 nmol/L, and sulfide became 0. Such variance was probably caused by human activities that disturbed the surface sediment and released CH_4. Dredging was probably a major reason, considering the annual maintenance of GIWW-T to maintain its transportation capability (Kruse et al. 2016). A study at the Lower Laguna Madre seagrass meadow showed the sedimentation of rich organic matter for months and anoxic sediment with high sulfides for up to 2.5 years after the dredging event (Eldridge et al. 2004). This result indicated the potential of repeat emission of CH_4 from organic-rich sediment along this channel, which can explain the higher frequency of higher CH_4 concentrations in channels than in seagrass.

In comparison, the dissolved CH_4 concentrations in the maritime channel located in NC and GIWW-T in AM were much lower. Fewer organic matter deposits, deeper water depths and less anthropogenic disturbance were probably the main reasons.

4.4.5.2 Pipe leakage

In July and September 2020 and March and May 2021, elevated atmospheric CH_4 concentrations were observed at a pipeline platform (AM14) from 2.75 to 5.32 ppm, much higher than the air CH_4 concentrations over nearby stations (Figure S2). However, dissolved CH_4 concentrations in surface water at AM14 were not higher than others correspondingly, indicating that water was not the source of the high CH_4 concentrations in the atmosphere. The $\delta^{13}C$-CH_4 at AM14 in July 2020 was -43.88‰, higher than that at the nearby site (AM15, -44.89‰) and at the mangrove creek (AM5, -45.19‰), implying that the higher CH_4 concentration at AM14 was probably caused by fossil fuel gas leakage from the pipeline platform (Figure S2b). The ambient CH_4 concentration at AM14 in May 2021 (3.41 ppm) was less than that in July 2020 (5.32 ppm), as were their $\delta^{13}C$-CH_4 values (-44.28‰ and -43.88‰, respectively), proving that the variation in CH_4 concentration was due to leakage. The $\delta^{13}C$-CH_4 of ambient air at AM5 in July 2020 (-45.19‰) was larger than that in August 2019 (-46.41‰), further suggesting that ambient air surrounding the pipeline platform was affected by leakage.

4.4.6 Estimation of regional methane flux and offset to blue carbon

The annual sea-air CH_4 flux from the study area was estimated using CH_4 fluxes in different environments in various seasons due to high spatial and temporal variations in CH_4 concentrations. Both daily flux and annual total flux were highest at LM (Table 4.2). The annual flux at NC was higher than that at AM due to larger areas of bays and channels as well as higher daily flux over channels. Among these estuaries, CH_4 emissions from LM were the majority, accounting for 70%. Annual CH_4 emissions in seagrass meadows were higher than those in mangroves because both coverage and average daily CH_4 flux were larger in seagrass. Hence, in the study region, seagrass was a more significant source of atmospheric CH_4 than mangrove creeks. CH_4 fluxes from the

channel at LM and NC were larger than those at AM, indicating that extensive human disturbance of surface sediment would lead to higher CH_4 emissions. Except for the daily CH_4 fluxes in the open bay in NC and the channel in AM, which were lowest in spring, the other daily CH_4 fluxes were lowest in winter.

Sea-air CH_4 fluxes at mangrove creeks (0.6~395.1 μmol/m^2·d, median: 70.7 μmol/m^2·d) in this study were within the lower range in the current database of CH_4 flux from mangroves globally (-67.3~164588.5 μmol/m^2·d, median: 284.9 μmol/m^2·d) (Al-Haj and Fulweiler 2020). However, CH_4 fluxes over seagrass meadows in this study were 12.3~816.2 μmol/m^2·d (median: 163.7 μmol/m^2·d), over the upper limit of global seagrass meadows (1.2~401.5 μmol/m^2·d, median: 64.8 μmol/m^2·d) (Al-Haj and Fulweiler 2020). Moreover, the offset of CH_4 from mangrove creeks in this study (0.17%) was much lower than the global estimate (~9%), while that from seagrass meadows (1.4%~2.2%) was much higher than the global estimate (i.e., <0.5%) (Al-Haj and Fulweiler 2020). Hence, in comparison with global emissions, local mangrove creeks are weak sources, but seagrass meadows are strong sources of CH_4. Although the annual flux from the channel was not as large as that from seagrass in LM, the daily average CH4 flux was 1.6 times that from seagrass. This result suggested a high risk of more CH_4 emissions once the seagrass sediment was destroyed.

Table 4.2 Sea-air CH_4 fluxes from estuaries in southern Texas

	Area (km^2)	Sea-air CH_4 flux ($\mu mol/m^2d$)					Annual Flux ($10^6 g\ CH_4/yr$)
		spring	summer	autumn	winter	all	
Corpus Christi/Nueces bays							
channel	9.9[1]	95.7±92.9	119.0±83.9	176±228	51.5±35.2	104.7±123.2	6.4
open bay	576[2]	16.8±9.75	23.3±26.9	65.8±122.0	34.8±57.7	36.4±72.1	118.3
Total							124.7
Aransas							
mangrove	33.2[3]	100±114	95.0±43.2	115±95.0	65.8±56.9	94.7±81.3	18.2
channel	7.05[1]	13.4±9.92	56.9±69.7	43.0±27.9	42.2±37.0	39.9±39.0	1.5
open bay	539[4]	13.2±10.4	25.4±29.4	10.0±8.5	5.64±5.32	15.3±18.8	42.7
Total							62.4
Upper Laguna Madre							
seagrass	354[5]	204±180	277±178	274±244	72.4±75.6	221.1±190.7	427.6
channel	2.5[6]	296±250	587±554	435±531	87.6±83.1	354.9±421.1	5.1
Total							432.8
SUM							619.9

[1]calculated using data in (Huang et al. 2012)

[2]data available at https://tpwd.texas.gov/fishing/sea-center-texas/flora-fauna-guide/bays-and-estuaries/bay-habitats/mud-flats-corpus-christi and https://www.gulfbase.org/geological-feature/corpus-christi-bay

[3]data from (Thorhaug et al. 2019); [4]data available at https://www.gulfbase.org/geological-feature/aransas-bay

[5]data from (Onuf 2007); [6]data available at https://tpwd.texas.gov/

Upscaling CH_4 fluxes to all mangroves (3316 ha) and seagrass (94289 ha) along the coast of Texas, annual CH_4 emissions from mangroves and seagrass were 13.6×10^6 gC and 854.3×10^6 gC, respectively. They were approximately 0.0012% and 0.011% of the total stock organic carbon in mangroves (1.12 Tg) and seagrass sediment (7.5 Tg) (Thorhaug et al. 2019). In comparison, seagrass meadows play a more significant role in CH_4 emissions than mangrove creeks along the Texas coast.

4.5 Conclusion

This study provided a rough overview and understanding of CH_4 emissions from southern Texas coastal areas. Although Corpus Christi/Nueces Bays, Aransas Bay and Upper Laguna Madre are connected to form lagoonal estuaries in southern Texas, dissolved CH_4 concentrations and sea-air CH_4 fluxes in this region are highly spatially variable due to the distribution of seagrass, mangroves, channels, and bays. The CH_4 emissions are influenced by vegetation, hydrological conditions, human activities, and extreme weather events.

CH_4 emissions from seagrass meadows were larger than those from mangrove creeks, although porewater CH_4 levels in seagrass sediment were lower than those in mangrove sediment. The tidal processes in mangrove creeks played a crucial role in reducing CH_4 emissions by exporting CH_4 produced inside mangroves to the outside bay during ebbs and diluting CH_4 concentrations in water bodies and pore water during floods. In contrast, located in a relatively isolated lagoon with weak water exchange, CH_4 emissions from seagrass sediment easily accumulated in water bodies.

The anthropogenic impact on CH_4 emissions can be direct or indirect. The highest CH_4 concentrations were observed in the channel, particularly GIWW-T at Upper Laguna Madre. This result indicated that human disturbance of surface sediment by dredging and vessel grounding

could release more CH_4 to the atmosphere from deeper sediment. At Corpus Christi Bay, pollution was another reason that could explain the higher CH_4 concentration in the maritime channel. At Redfish Bay, leakage from the gas pipeline platform has been found in several months to increase atmospheric CH_4 directly.

Extreme cold events that led to the death of mangrove forests at Harbor Island could enhance CH_4 emissions in mangrove creeks because a large amount of organic carbon deposits in mangrove soils and sediment from mangrove debris provided an additional carbon source for methanogenetic production. Heavy precipitation-induced runoff of the Nueces River could dramatically increase dissolved CH_4 concentrations in Nueces Bay by inputting a large amount of CH_4 produced in freshwater. Precipitation could also lead to the increase in CH_4 concentrations in mangrove creeks due to the immersion of upper intertidal sediment and soils.

Annual CH_4 fluxes to the atmosphere were largest at Upper Laguna Madre and lowest at Aransas Bay. CH_4 emissions from mangrove creeks offset 0.16% of buried carbon, only 2% of the global estimate in mangrove forests. CH_4 fluxes to the atmosphere from local seagrass meadows could offset 1.4%~2.2% of the carbon deposited in sediment, over 3 times higher than the global level. This revealed that the utilization of tidal processes is a promising strategy in the restoration of vegetation in coastal regions, which can decrease the emission of greenhouse gases.

Compared with open bays with bare sediment, disturbing the surface sediment of vegetated areas, e.g., seagrass meadow sediment, can release more CH_4. Hence, although vegetation can benefit carbon storage, if it cannot be protected, it can enhance the risk of greenhouse gas emissions. Therefore, it is imperative to protect vegetated areas from disturbance.

CHAPTER V: IMPACT OF ANTHROPOGENIC EMISSIONS ON METHANE OVER INGLESIDE, TEXAS

Abstract

Anthropogenic emissions contribute approximately 60% in the global methane (CH_4) budget. Recent studies have found that CH_4 emissions from urban areas have largely been underestimated. We investigated the atmospheric CH_4 input to the residential area of Ingleside, Texas, through observations at a fixed station from March to August 2021. We also performed aircraft observations focusing on the industrial area in August 2021. The half-year observations at the Ingleside community found seasonal variations in atmospheric CH_4 mixing ratios corresponding to the changes in wind directions. Aircraft observations also acquired elevated CH_4 signals downwind of a tower with smoke located in a refinery plant. Based on a spatially focused box model, CH_4 emission from the tower was estimated to be 590 kg/hr, much larger previous local reports. The CH_4 input to the Ingleside community was up to 1.29×10^6 kg/yr. Estimated a half of CH_4 input (643.3×10^3 kg) was from east, the direction where closely located one of the nation's largest crude oil terminals. Hence, it is most likely fugitive emissions during crude oil loading/offloading operations was a significant contribution of CH_4 to the community. Approximately 30% of CH_4 fluxes came from north, probably related to industrial operations. Among it, 11% corresponded to wind from north-north-west, indicating 142.5×10^3 kg/yr CH_4 originated from the industrial area at Ingleside, which is 2 times the reported emission data (65.2×10^3 kg CH_4) in 2020. This preliminary study showed both the anthropogenic emissions from large facilities in industrial areas and fugitive sources during maritime operations have been largely underestimated.

5.1 Introduction

Methane (CH_4) is the second most abundant greenhouse gas after carbon dioxide (CO_2), with an atmospheric warming potential approximately 28-34 times and 84-86 times that of CO_2 over 100 years and 20 years, respectively (IPCC 2014). Except for its effect on climate change, CH_4 is taken as a precursor of ozone in the lower troposphere, which can influence human health (Fiore et al. 2008). Approximately 60% of global atmospheric CH_4 was estimated from anthropogenic origins (e.g., agriculture, petroleum and natural gas industry, landfill, sewage) (National Academies of Sciences 2018). The CH_4 mixing ratios in the atmosphere increased from ~ 790 ppb before the industrial revolution to over 1800 ppb, which was primarily explained by emissions from the fossil fuel industry. Hence, CH_4 emissions from the fossil fuel industry have long been a concern. In recent years, a few studies have discovered that CH_4 emissions from urban areas have been highly underestimated and poorly characterized (Plant et al. 2022). Moreover, there exists high spatial and temporal variability in urban CH_4 emissions, which can be explained by a variety of sources, e.g., landfills, sewage-treatment plants, and refineries, as well as fugitive release from vehicles and distribution facilities of natural gas (Guha et al. 2020; Huang et al. 2019b; Hugenholtz et al. 2021; Klausner et al. 2020; Lopez-Coto et al. 2020; Sargent et al. 2021; Venturi et al. 2021). A thorough understanding of the anthropogenic CH_4 in urban centers is not only essential to build a more precise global CH_4 budget but also crucial for making realistic, scientific, cost-effective policies for mitigating climate change (Ren et al. 2018).

Currently, large cities are the primary objectives in this study, particularly the metropolitan region of Washington, DC-Baltimore, which has a high population density. Both aircraft and tower observations have found that top-down CH_4 emission rates in this region were over 2 times greater than the rates reported in the EPA inventory (Huang et al. 2019b; Ren et al. 2018). Moreover,

urban natural gas systems could be responsible for ~40-60% of total CH_4 emissions in winter, and landfills accounted for 25±15% (Ren et al. 2018). It also found that there were more emissions in winter than in summer, which was explained by fugitive natural gas sources related to natural gas usage or wetland source impact on background (Huang et al. 2019b; Karion et al. 2020). Daily variation in CH_4 emissions was found to be primarily related to power plants and traffic (Lopez-Coto et al. 2020). Studies in other large cities in the U.S., such as New York, Kansas City, Atlanta, Boston, and San Francisco, all observed more CH_4 emissions than inventory-based estimates, revealing that fugitive emissions from natural gas distribution and end use were highly underestimated (Guha et al. 2020; Plant et al. 2019; Plant et al. 2022; Sargent et al. 2021). Estimated CH_4 emissions from refineries around San Francisco Bay using aircraft observations were also higher than inventory data (Guha et al. 2020). In Europe, CH_4 emissions in Berlin were enhanced by sewage treatment and waste deposition (Klausner et al. 2020). At Florence, high spatial variations in CH_4 levels were caused by various sources, e.g., domestic heating, vehicular exhaust, leakage from underground pipeline networks for natural gas supply, and biogenic emissions from waterways (Venturi et al. 2021). However, anthropogenic CH_4 emissions from urban areas are still quite underestimated, considering numerous middle and small cities, which also play an important role in local and global economic development.

Ingleside is a small city in the coastal area of south Texas and northwest of the Gulf of Mexico. This region provides a potential for clear separation of natural, industrial, and urban CH4 input to the atmosphere. Ingleside-on-the-bay is the coastal part of the city on the north shore of Corpus Christi Bay and at the entrance to the Ship Channel. Its south end is on the maritime channel connecting the Gulf of Mexico and the Port of Corpus Christi, and its west is the La Quinta Channel. The coastline is an intensive seagrass habitat. In recent decades, this area has received

much attention due to its unique advantage for national and international transportation in the rapid development of the petroleum industry and maritime transportation in Texas. Now, it has been surrounded by industrial facilities on its northwest and east directions, and more facilities are being built. This area is also influenced by the development of the port, including an increase in ship traffic, hazardous boating conditions, and maintenance dredging of channels. The local community has been exposed to an elevated risk of air pollution and seagrass habitat loss and more vulnerability to climate changes caused by greenhouse gas emissions. The industrial emissions of greenhouse gases in this region probably have a direct influence on the local climate. Hence, this project will monitor the long-term variations in CH_4 mixing ratios in ambient air, explore the sources of CH_4 and evaluate the influence on local atmospheric CH_4.

5.2 Sampling and Method

5.2.1 Study area

The study area in the city of Ingleside includes Ingleside-on-the-bay (Ingleside community) and the industrial area. They are located along northern Corpus Christi Bay, Texas, USA (Figure 5.1). The maritime channel connecting the Gulf of Mexico and the Port of Corpus Christi passes its south edge. The west edge of this area is the La Quinta Channel. Surrounded this area have been and are being built many plants and facilities, e.g., Moda Ingleside energy center (MODA), EMR Facility (EMR), Chemours Ingleside Plant, Gregory, etc. (Figure 5.1c). In particular, MODA adjacent to the Ingleside community in the east is one of the nation's largest crude export terminals by volume due to its capacity to handle very large crude carriers, its rapid loading rates, and its access to open water via the Port of Corpus Christi.

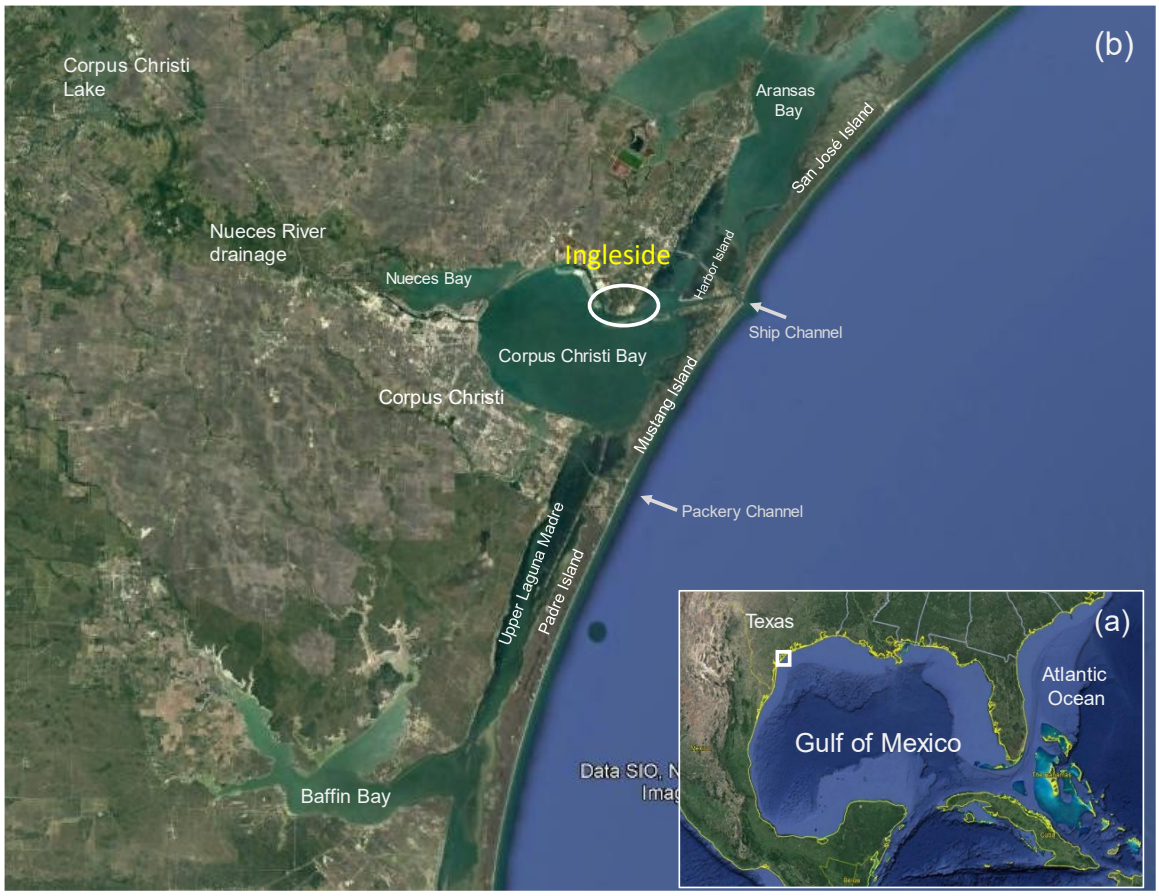
(b)
Corpus Christi Lake
Aransas Bay
San José Island
Nueces River drainage
Ingleside
Nueces Bay
Harbor Island
Ship Channel
Corpus Christi Bay
Corpus Christi
Mustang Island
Packery Channel
Upper Laguna Madre
Padre Island
Baffin Bay
Texas
(a)
Atlantic Ocean
Gulf of Mexico

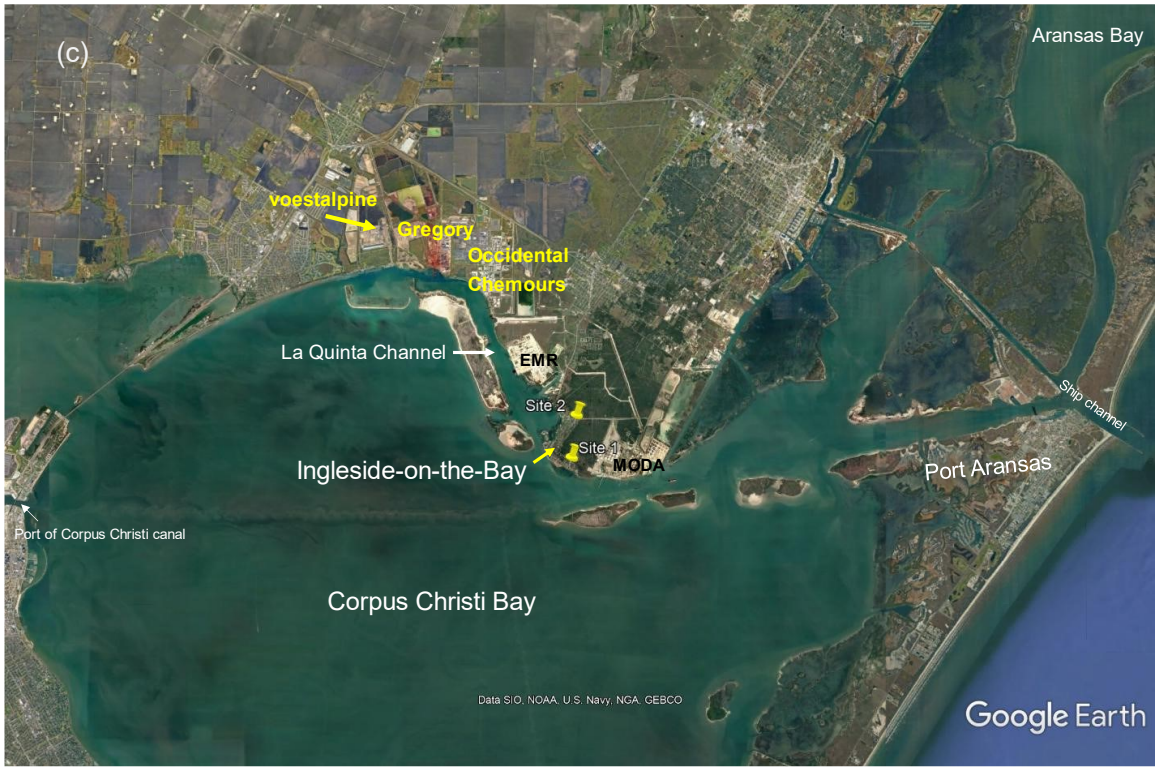
(c)
Aransas Bay
voestalpine
Gregory
Occidental
Chemours
La Quinta Channel
EMR
Site 2
Site 1
MODA
Ingleside-on-the-Bay
Ship channel
Port Aransas
Port of Corpus Christi canal
Corpus Christi Bay
Data SIO, NOAA, U.S. Navy, NGA, GEBCO
Google Earth

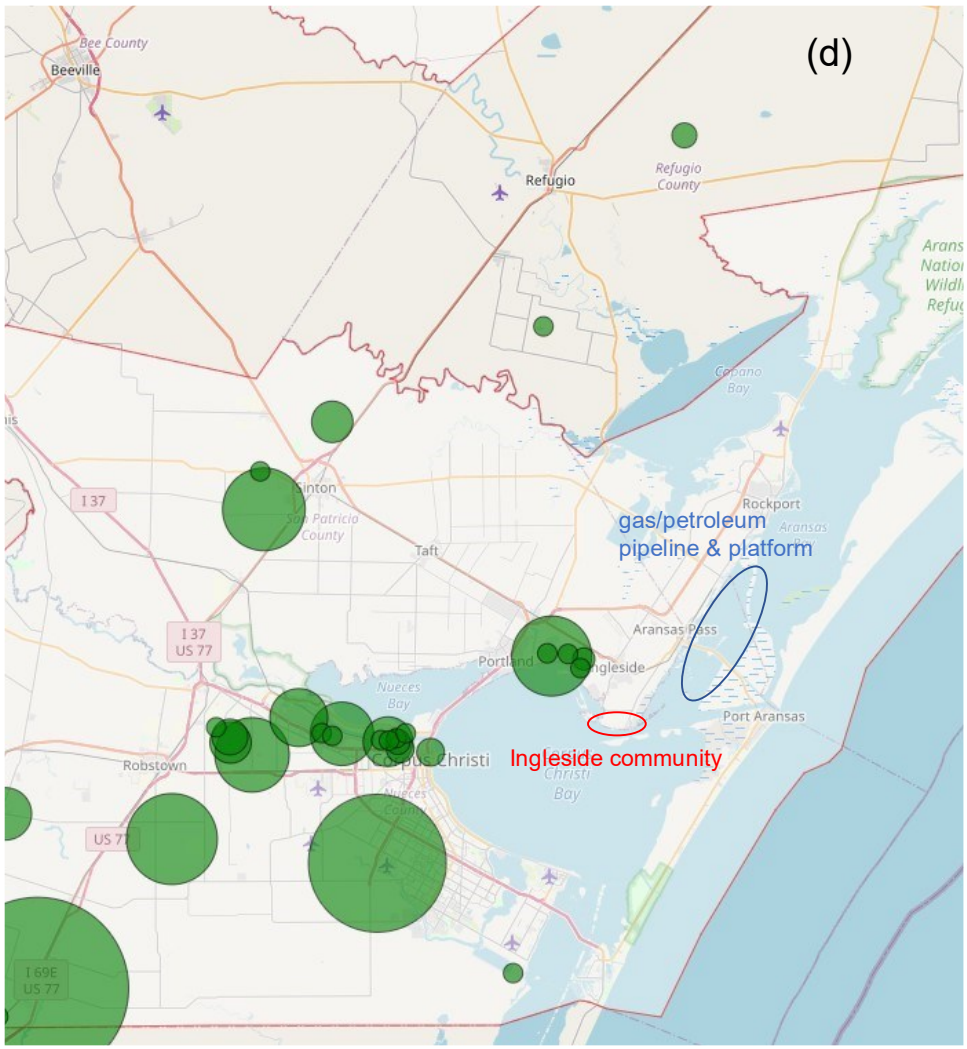

Figure 5.1 Study area.

(a) The study area is located northwest of the Gulf of Mexico, south Texas coast; (b) Surroundings of the study area circled in white; (c) Detailed overview of the study area. Site 1 and Site 2 were sites for long-term observations from March to July 2021 and in August 2021, respectively. Primary companies in the neighborhood are listed on the map. The companies highlighted in yellow are the plants that have large facilities that need to report greenhouse gas emissions to EPA each year. (d) A map marked by known greenhouse gas emissions around the Ingleside community (data available: https://ghgdata.epa.gov/ghgp/main.do#/facility/). Green circles are plants that release greenhouse gases (CO_2, CH_4 and N_2O) from large facilities that need to be reported to the

EPA. The size of the circles represents the relative magnitudes of all emissions (CO_2, CH_4 and N_2O) in 2020. The blue circle is Redfish Bay, where there are some pipelines and platforms. It is located northeast of the Ingleside community.

5.2.2 Long-term observation at fixed stations

From March 11th through August 31st, 2021, a cavity-based spectroscopy, ultraportable greenhouse gas analyzer (UGGA, model 909-0060, ABB Los Gatos Research) was installed at the Ingleside community, Texas (Figure 5.1, Figure 5.2). Tubing (Typgon E-3603 1/8''×1/16'') was used to transport ambient air from 3 meters height to the UGGA. An external filter was connected between the inlet of UGGA and the transport tubing to filter particles in the air before the air entered the analyzer. A pump inside the UGGA drew the air into the sensor at a rate of 0.3~0.5 L/min. Data were measured and collected at a frequency of 1 Hz (1/s). Before the UGGA was installed at Ingleside, certified reference gases CH_4 (1 ppm, 2 ppm, 5 ppm, GASCO Cal Gas) and CO_2 (300 ppm, 650 ppm and 1000 ppm, GASCO Cal Gas) were used to check the status and measurement accuracy of the sensor. During the observation, the running of UGGA was checked each week. Parameters of the lasers and mirror ring-down time were monitored to ensure the accuracy of the measurement. Ambient air samples were collected each week for data comparison. The air samples were measured using gas chromatography at the Isotope Core Lab of TAMUCC. The $\delta^{13}C$-CH_4 of selected air samples were measured at the Stable Isotope Lab of the University of California-Davis, with a precision of ±0.14‰. Hourly and 20-minute wind speed and direction data at the meteorologic station at NOAA Port Aransas Mustang Beach Airport acquired online (https://www.ncdc.noaa.gov/cdo-web/datasets/LCD/stations/WBAN:12995/detail) were applied to calculate CH_4 fluxes and trace potential CH_4 sources.

Figure 5.2 Ultraportable Greenhouse Gas Analyzer.

Upper Left: UGGA (in the container) at Ingleside coastal community; Upper Right: inside overview of the UGGA; Lower Left: outside of UGGA; Lower Right: an external filter connected inlet of UGGA and the air tubing.

5.2.3 Aircraft observation over the whole region

To obtain the greenhouse gas emissions from inland industrial areas, aircraft observations were performed on August 10th, 2021. Considering the safety requirement, we flew parallel to the Ingleside coastline for two sections, over the Corpus Christi Bay and over land (Figure 5.3, upper right). During the flight, the wind direction was SSW (190~210°), and the wind speed was 14~15 mph. Taking into account both wind direction and the coastline shape, we set the flight over the bay upwind and over the land downwind. The flight was performed at the height of 300 feet to 600 feet along the upwind transect and from 500 feet to 1300 feet along the downwind transect with an increment of 100 feet. At each height, the aircraft flew horizontally.

During this flight, a Microportable Greenhouse Gas Analyzer (MGGA, model 909-0050, ABB Los Gatos Research) was installed on a fixed wing aircraft (Pool Glastar 5355, made by Pool Fred W II, Figure 5.3). The MGGA measurement ranges are 0.01-10000 ppm for CH_4 and 100 ppm~10% for CO_2. The precisions for CH_4 are < 9 ppb in 0.1 sec, < 3 ppb in 1 sec and < 1 ppb in 10 sec, and those for CO_2 are < 6 ppm in 0.1 sec, < 2 ppm in 1 sec and < 1 ppm in 10 sec. A tubing (Typgon E-3603 1/8’’×1/16’’) was fixed under a wing to transport ambient air to the MGGA. A pump inside the MGGA drew the air into the sensor at a rate of 1.4~1.5 L/min. Data were measured and collected at a frequency of 10 Hz (10/s). Before each flight, certified reference gases CH_4 (1 ppm, 2 ppm, 5 ppm, GASCO Cal Gas) and CO_2 (300 ppm, 650 ppm and 1000 ppm, GASCO Cal Gas) were used to check the status and measurement accuracy of the sensor. Hourly wind speed and direction data at a downwind meteorologic station, NOAA Campbell Airport, acquired online (https://www.ncdc.noaa.gov/cdo-web/datasets/LCD/stations/WBAN:00365/detail) were applied to calculate CH_4 emission rates.

Figure 5.3 Upper Left: aircraft applied in this study; Upper Right: flight routes; Lower Left: Smoke from a tower (Voestalpine Texas) at the Ingleside industrial area during the flight; tubing was tied under the wing to collect air samples; Lower Right: the assemblies of gas inlet, gas measurement, system control, and data storage of the Microportable Greenhouse Gas Analyzer.

5.2.4 Mass Balance Approach

CH_4 emissions from the Ingleside community and the industrial areas were calculated using the variations in the CH_4 mixing ratio (mole weight) between downwind and upwind sections by a mass balance model (Ren et al. 2018) (Figure 5.4).

$$Emission\ Rate = \int_0^z \int_{-x}^{+x} ([C]_{ij} - [C]_b) \times U_{ij} dx dz \quad (3)$$

$[C]_{ij}$ is the CH_4 mixing ratio at a downwind location (x_i, z_i);

$[C]_b$ is the background CH_4 mixing ratio;

U_{ij} is the perpendicular wind speed at a downwind location (x_i, z_i);

[-x, +x] is the horizontal width of the CH_4 plume from the observation area;

[0, z] is the mixing layer depth.

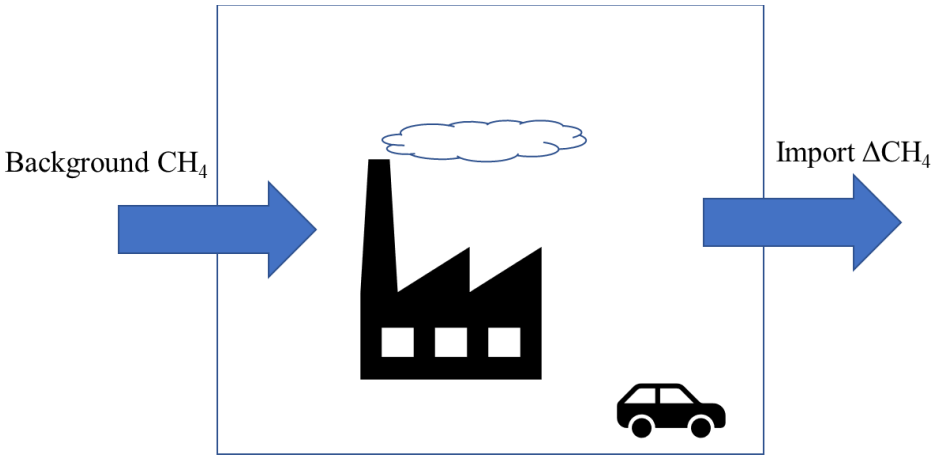

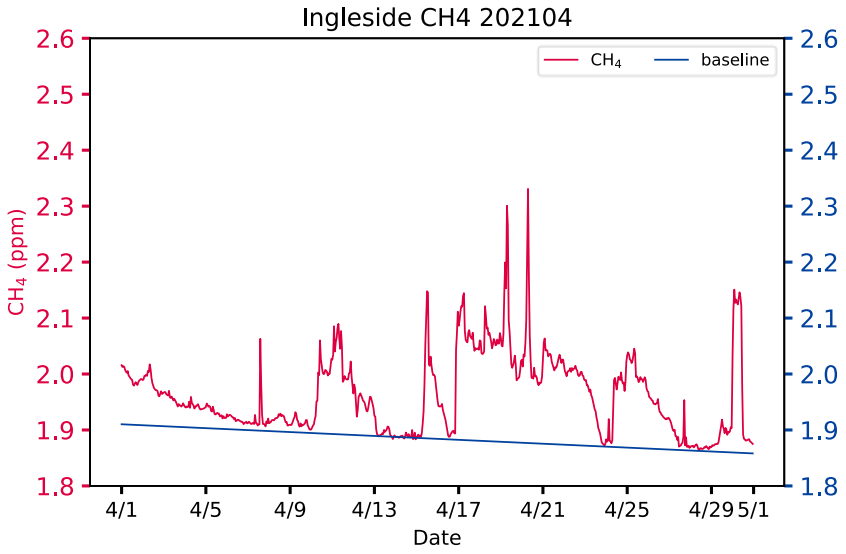

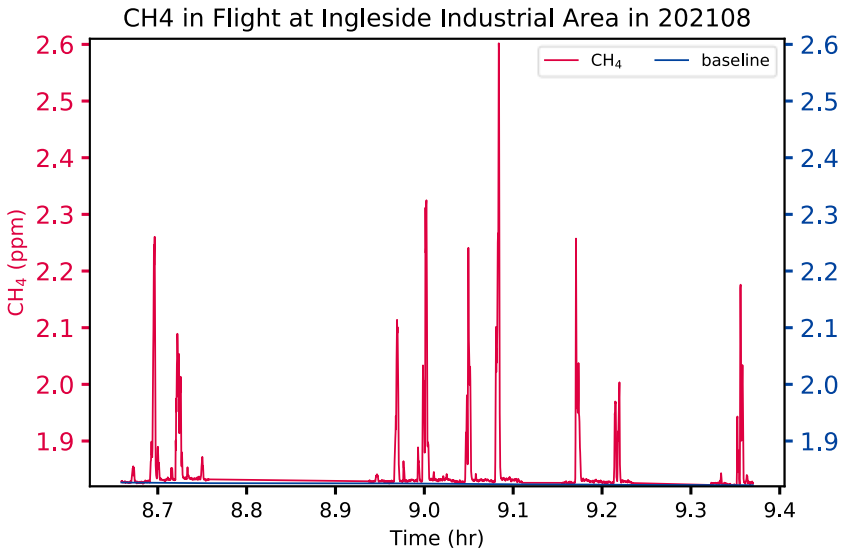

Figure 5.4 Upper: Schematic diagram of the mass balance model; Middle: Hourly average atmospheric CH_4 mixing ratios at the Ingleside community in April as an example; Lower: In situ atmospheric CH_4 mixing ratios during aircraft observation on August 10th, 2021. The blue lines in the lower two plots are baselines that are used as the background CH_4 mixing ratio.

5.3 Results

5.3.1 Temporal variation in atmospheric methane from March to August

During the observations from March to August 2021, both the monthly average atmospheric CH_4 and CO_2 mixing ratios decreased from spring to summer (Table 5.1). The monthly baselines of CH_4 and CO_2 also decreased synchronically, indicating a slight decline in the background greenhouse gases, probably due to less input of CH_4 in the summer or enhanced photodecomposition of CH_4 as the radiation increased. However, the monthly maximum CH_4 mixing ratios were larger in summer (June, July and August) than in spring (March, April and May), probably caused by a stronger temporal input. Furthermore, as Figure 5.5 shows, elevated CH_4 and CO_2 mixing ratios were often coincident with the wind from the north.

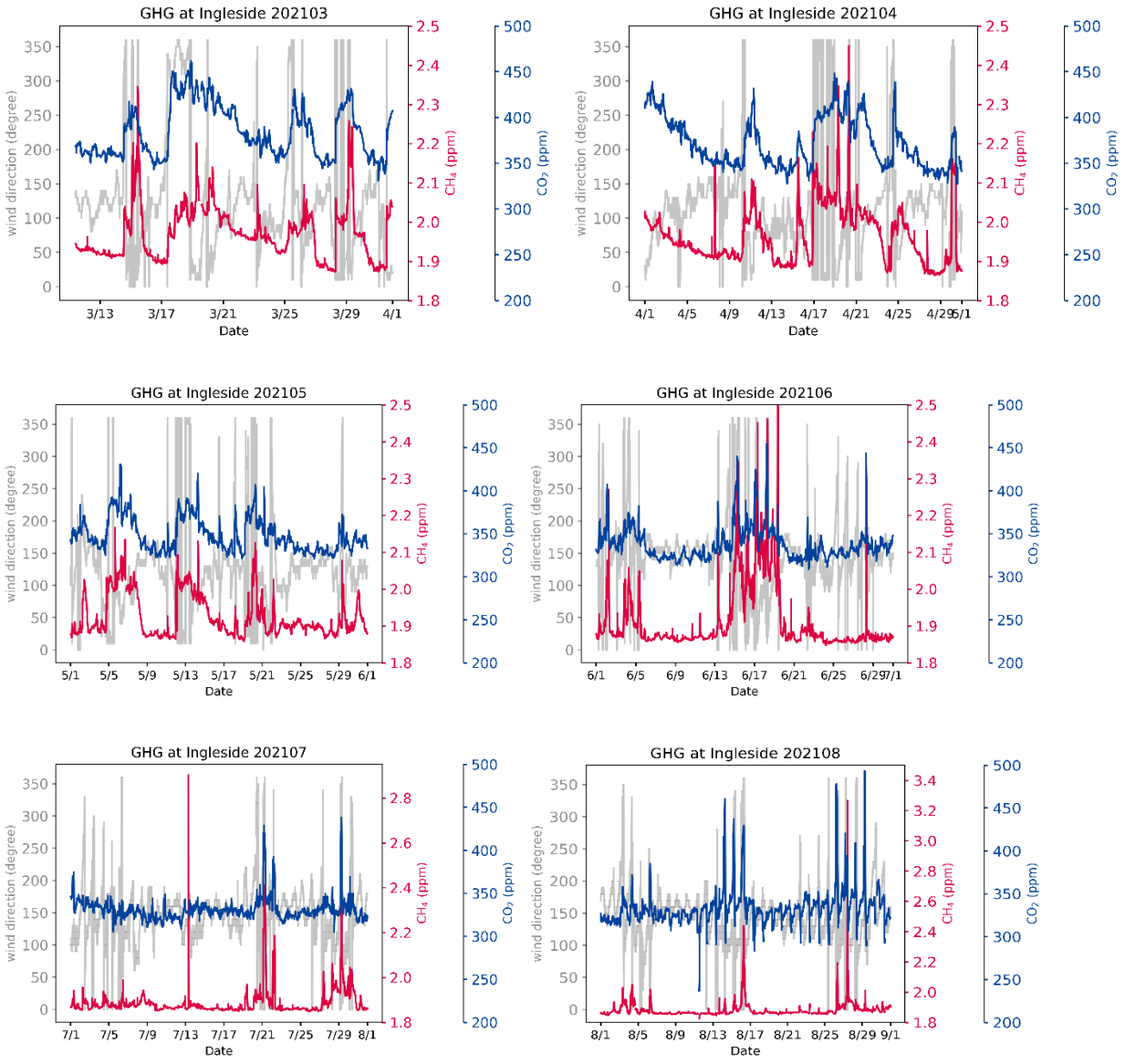

Figure 5.5 Atmospheric CH_4 and CO_2 mixing ratios and wind direction at Ingleside from March to August 2021.

Table 5.1a: Summary of the monthly atmospheric CH_4 mixing ratio and baseline (ppm)

	min	max	median	mean ± sd	baseline* (mean ± sd)
202103	1.874	2.2674	1.965	1.9705±0.0679	1.8883±0.0109
202104	1.864	2.3308	1.9477	1.9631±0.0700	1.8841±0.0151
202105	1.859	2.1295	1.9015	1.9249±0.0557	1.8657±0.0004
202106	1.848	2.531	1.8727	1.9139±0.0932	1.8560±0.0032
202107	1.849	2.5115	1.8681	1.8862±0.0582	1.8527±0.0020

202108**	1.825	2.5882	1.8657	1.8826±0.0539	1.8488±0.0061

* Tolerance of 1e-5

** observation at Site 2, others at Site 1

Table 5.1b: Summary of the monthly atmospheric CO_2 mixing ratio and baseline (ppm)

	min	max	median	mean±sd	baseline (mean±sd)
202103	336.5	459.0	376.0	383.8±28.4	348.4±2.8
202104	329.9	443.2	363.6	371.9±27.2	337.3±3.8
202105	321.4	430.2	342.7	348.5±19.5	324.4±324.4
202106	312.1	450.6	332.6	338±19.7	316.7±0.1
202107	310.7	423.9	329.0	331.1±12.6	314.8±1.5

* Tolerance of 1e-4

5.3.2 Aircraft observations over industrial areas

During the aircraft observations on August 11th, 2021 (Figure 5.6), atmospheric CH_4 mixing ratios downwind of the industrial area (over the land along the north edge of Ingleside, 1.818 ~2.602 ppm from 500 feet to 1300 feet) were higher than those from upwind (over Corpus Christi Bay long the south of Ingleside, 1.813 ~ 1.839 ppm from 300 feet to 600 feet). The background CH_4 (baseline) during flight over the industrial area (1.824±0.002 ppm) was also larger than that over the upwind bay area (1.820±0.004 ppm). Hence, the increase in CH_4 came from industrial emissions, and the influence from upwind can be ignored. Along the downwind direction, an elevated CH_4 mixing ratio appeared close to a tower with smoke at a refinery plant (Voestalpine Texas). The maximum CH_4 (2.602 ppm) occurred at 1000 feet (305 m), while the vertical CH_4 profile showed that the average CH_4 mixing ratio at 800 feet (244 m) was the largest (Figure 5.6). Similar to CH_4, atmospheric CO_2 over the inland industrial area (305~417 ppm) was also higher than that over the upwind area (294~321 ppm), indicating CO_2 input from industrial operations.

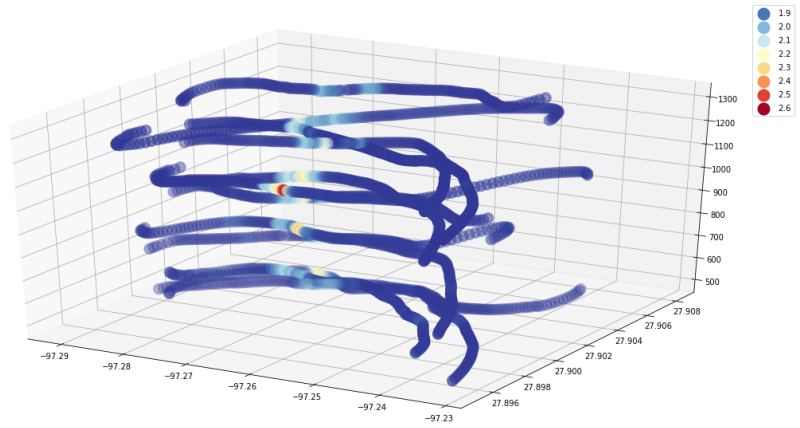

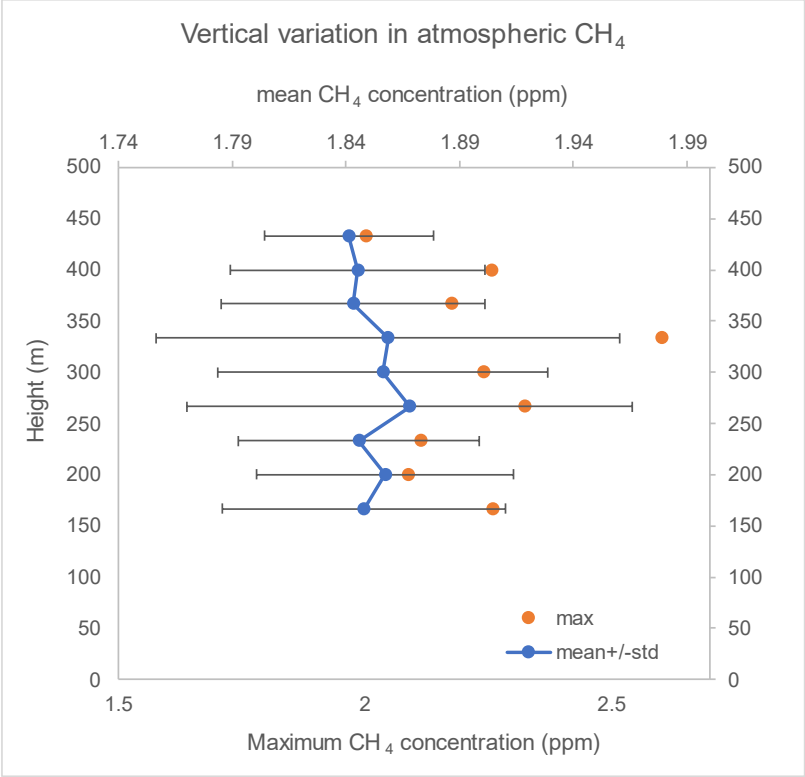

Figure 5.6 Aircraft observation

5.4 Discussion

5.4.1 Relationship between methane and wind parameters at Ingleside community

Figure 5.8 shows that although the dominant wind in the Ingleside community is southeast, there was monthly variation in wind directions. From spring to summer months, the frequency of

wind from the north (northwest and northeast) significantly decreased, but from the south and southeast, it increased. Moreover, the wind speed decreased from spring to summer.

The atmospheric CH_4 and CO_2 mixing ratios in the Ingleside community seemed to be related to wind directions and wind speed considering their coincidence (Figure 5.5). Elevated CH_4 mixing ratios primarily appeared when the wind was from the north in comparison with those from the south, particularly in March and April, when the frequency of the north wind was larger than that in other months. This result is reasonable since the primary industrial area is located northwest of the Ingleside community. In summer, as more wind came from the south and southeast, although the highest CH_4 mixing ratio was still related to the north wind, the relatively higher CH_4 corresponding to the south and southeast winds was probably caused by emissions from maritime exhaust and loading/offloading operations at the dock of the MODA Ingleside Energy Center. Moreover, elevated CH_4 mixing ratios occurred more extensively under wind with low wind speeds rather than high wind speeds. This is probably because the large wind could accelerate the dispersion of gases. Monthly atmospheric CO_2 showed similar patterns as CH_4.

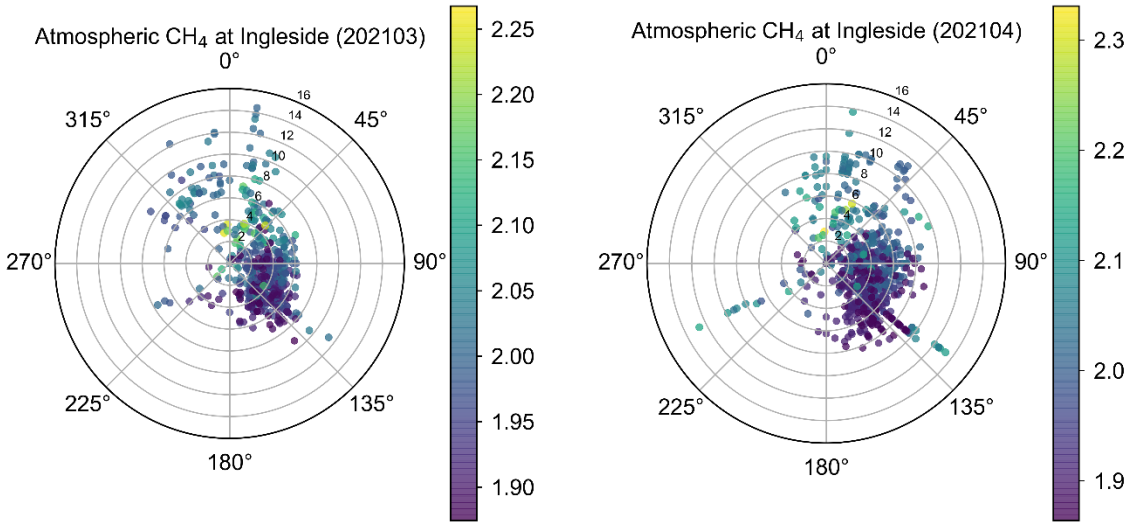

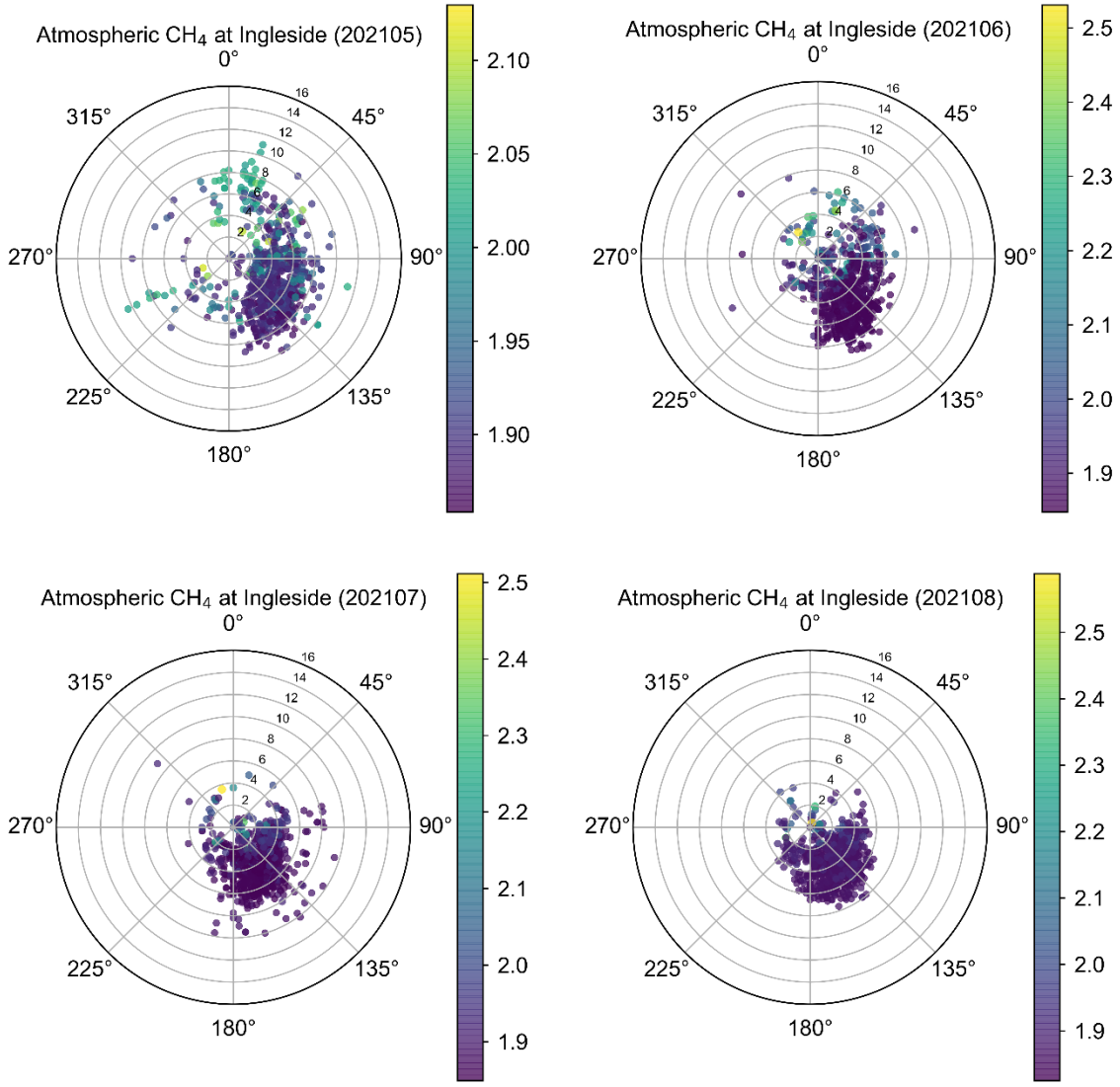

Figure 5.7a: Hourly average atmospheric CH_4 mixing ratios (ppm) with corresponding wind direction (0~360°) and wind speed (m/s, circles).

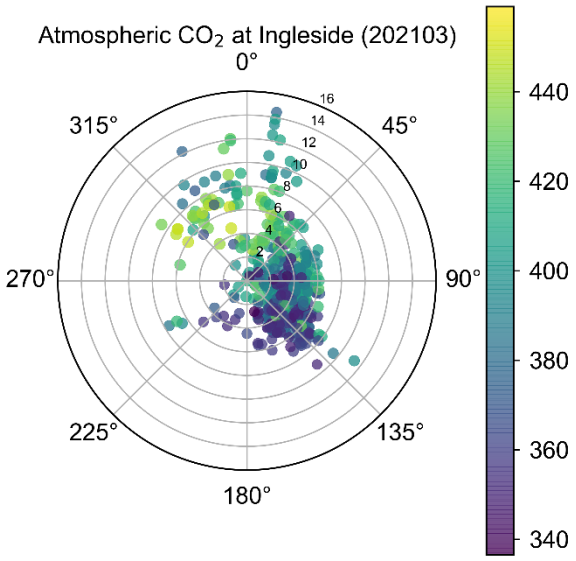
Atmospheric CO2 at Ingleside (202103)
0°
45°
90°
135°
180°
225°
270°
315°
2
4
6
8
10
12
14
16
340
360
380
400
420
440

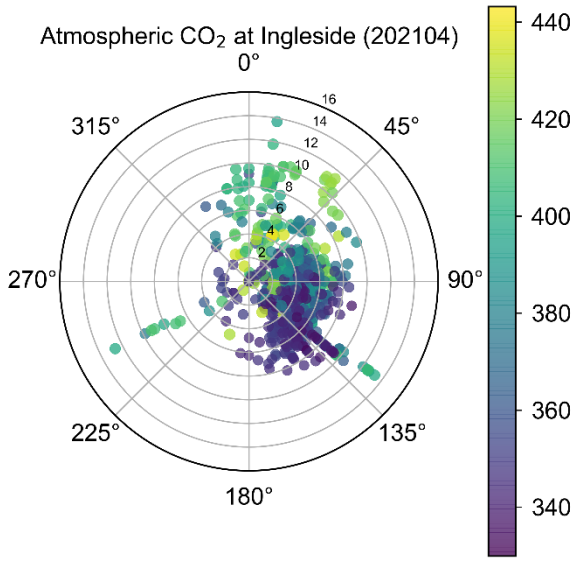
Atmospheric CO2 at Ingleside (202104)
0°
45°
90°
135°
180°
225°
270°
315°
2
4
6
8
10
12
14
16
340
360
380
400
420
440

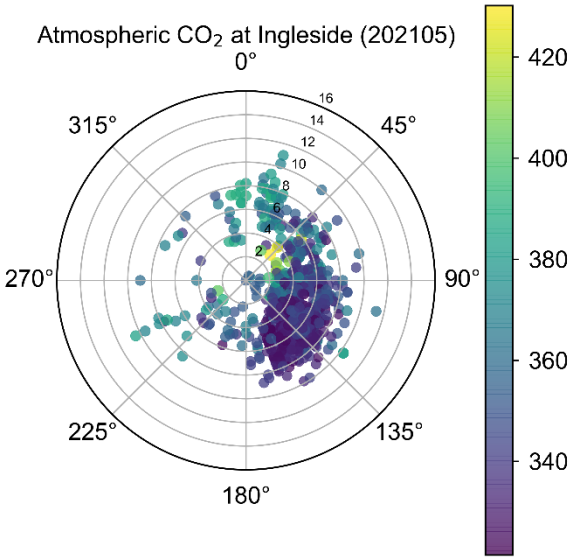
Atmospheric CO2 at Ingleside (202105)
0°
45°
90°
135°
180°
225°
270°
315°
2
4
6
8
10
12
14
16
340
360
380
400
420

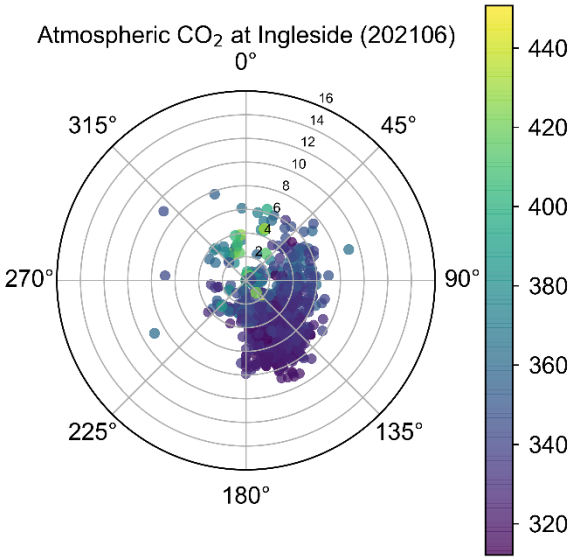
Atmospheric CO2 at Ingleside (202106)
0°
45°
90°
135°
180°
225°
270°
315°
2
4
6
8
10
12
14
16
320
340
360
380
400
420
440

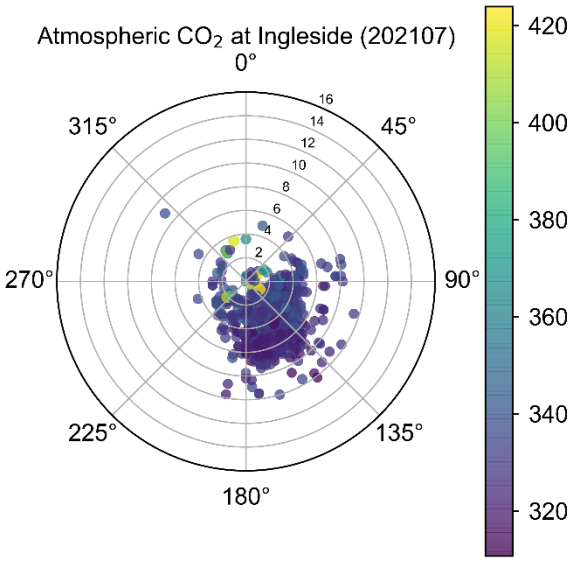

Figure 5.7b: Hourly average atmospheric CO_2 mixing ratios (ppm) with corresponding wind direction (0~360°) and wind speed (m/s, circles).

5.4.2 Relationship between methane and carbon dioxide

As shown in Figure 5.8a, atmospheric CH_4 mixing ratios were significantly correlated with CO_2 in the Ingleside community, indicating that the origins of the two gases were coincident to some extent. However, the ratios between CH_4 and CO_2 (slope) in each month were somewhat different. The ratios of CH_4 and CO_2 were lower in March and April and increased from spring to summer. Elevated ratios of CH_4 and CO_2 in July and August further suggested that the source of CH_4 changed from spring to summer, with more CH_4 proportions in the released gases.

Unlike in the Ingleside community, atmospheric CH_4 and CO_2 during the aircraft observations were not significantly correlated (Figure 5.8b), indicating various gas sources. Below 1100 feet, the CH_4 and CO_2 mixing ratios at each altitude with an interval of 100 feet could be clearly categorized into two groups: a group with higher ratios of CH_4 and CO_2 and a group with lower ratios. The group with higher CH_4/ CO_2 ratios undoubtedly showed the anthropogenic input of CH_4. Since most elevated atmospheric CH_4 during the flight was observed downwind from the

smoke emission from a tower, this group probably could reflect the greenhouse gas emissions from this smoke. Another group with lower CH_4/ CO_2 ratios had low CH_4 mixing ratios. However, since some CO_2 mixing ratios were larger than the maximum CO_2 upwind (321 ppm), this group was most likely another greenhouse gas input from the industrial area.

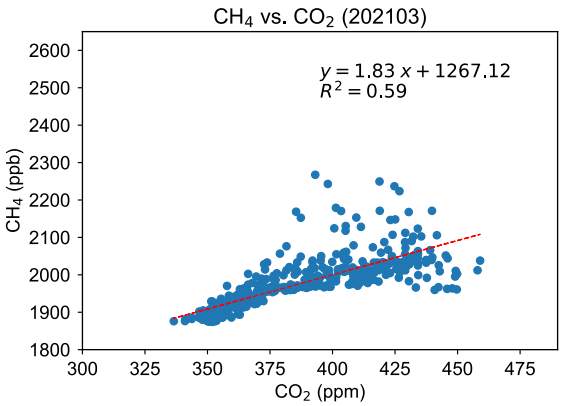

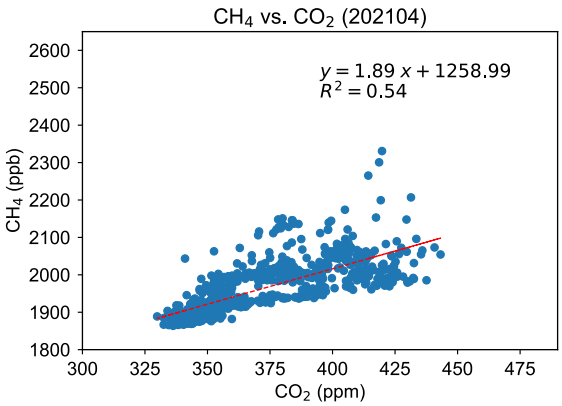

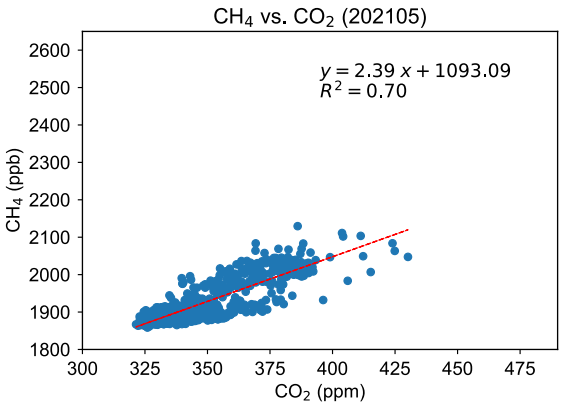

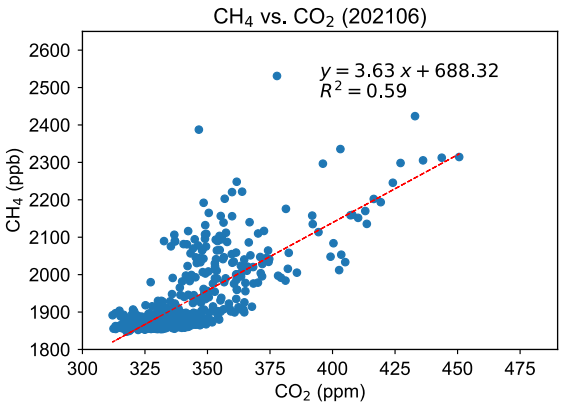

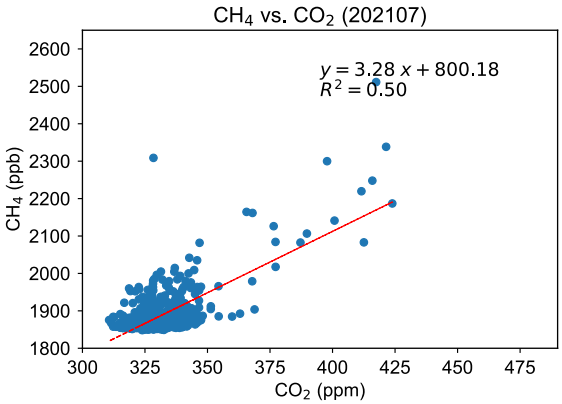

Figure 5.8a: Relationship between CH_4 and CO_2 in the Ingleside community in each month

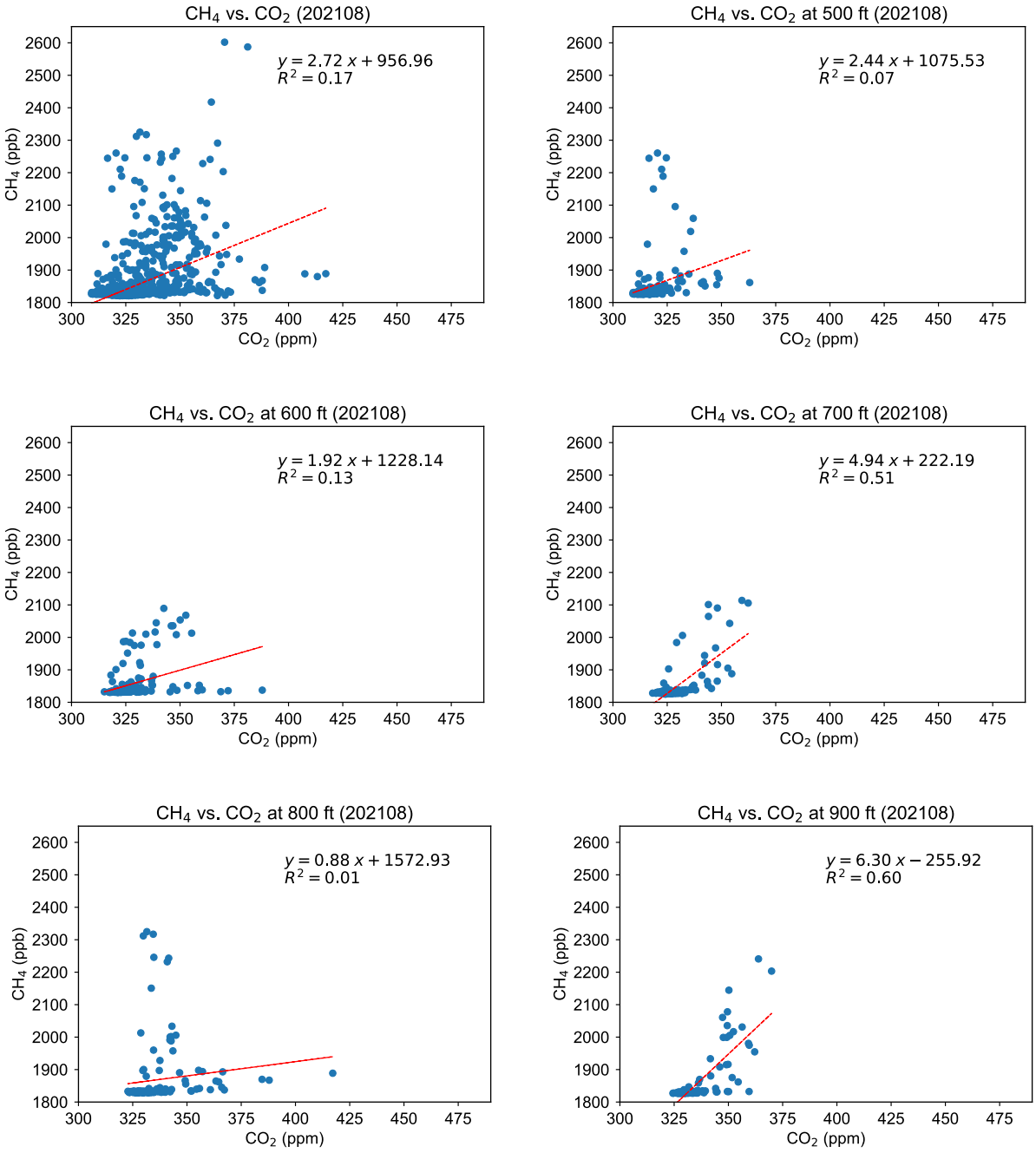

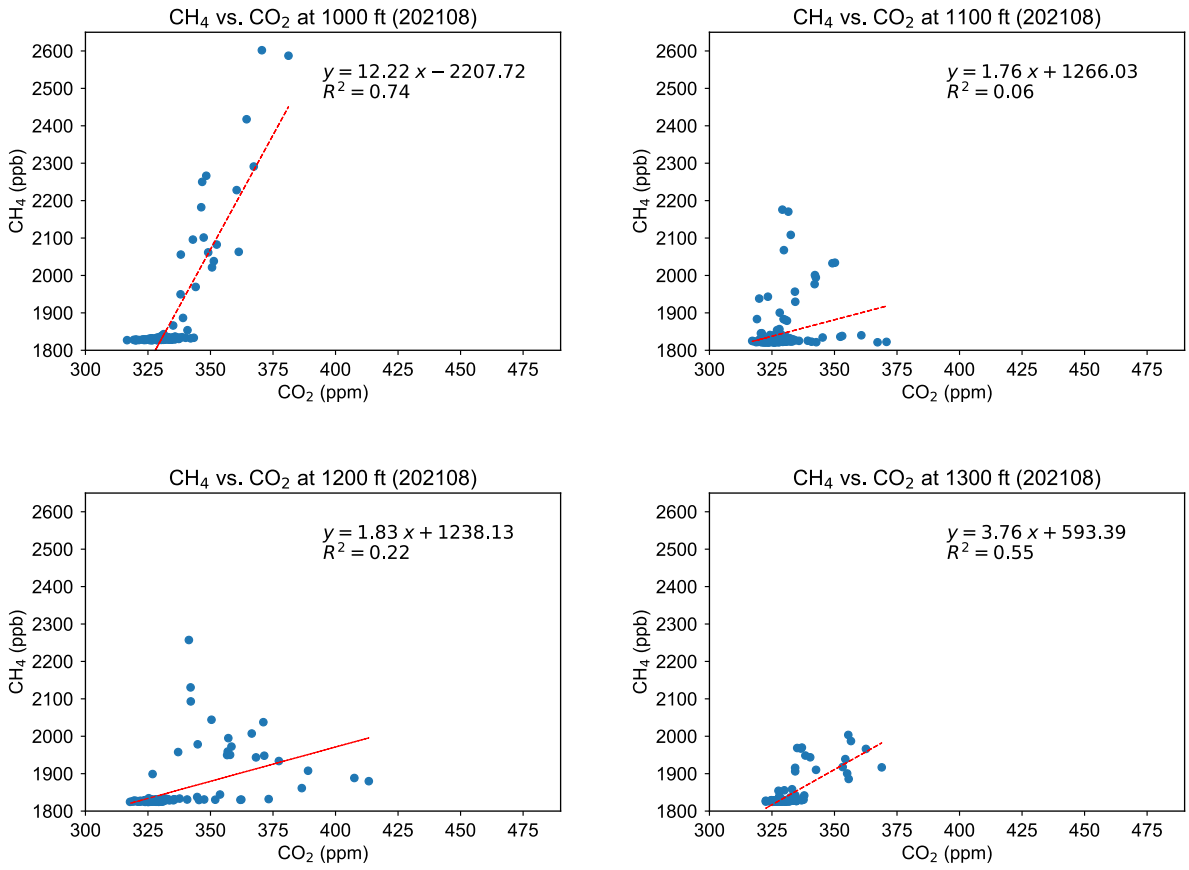

Figure 5.8b: Plots of CH_4 vs CO_2 in the inland industrial area.

5.4.3 Methane emissions rates from industrial areas

Calculated using a box model, the estimated CH_4 emission downwind of the tower was 590 kg/hr (36.9 $\times 10^3$ mol/hr) (Figure 5.9). Since the company (voestalpine) where the tower was located was a refinery plant, we compared this emission rate with those from other refineries. Airborne observations at San Francisco Bay Area found CH_4 emissions from five refineries were 23~1540 kg/hr (Guha et al. 2020). Our estimate was reasonable since it was within this range. However, the EPA inventory data showed that CH_4 emissions reported by facilities from this company were 520 kg/year (13 tons CO_2 equivalent) in 2020, even less than our hourly estimate. Aircraft measurements over refineries at San Francisco Bay Areas also found that the top-down estimates were from 4 to 23 times larger than those reported to regulatory agencies (Guha et al.

2020). However, it is obvious that the discrepancy between our assessment and reported data was much larger. Another refinery at Corpus Christi, Valero, reported that CH_4 emissions from their two plants were 12601 and 7603 tons CO_2 equivalent, respectively, in 2020, which were approximately several hundred to thousand times the data reported by voestalpine (13 tons CO_2 equivalent). Hence, considering several hundred hours of CH_4 emissions in a year in a plant, our estimate could be comparable to data reported by Valero.

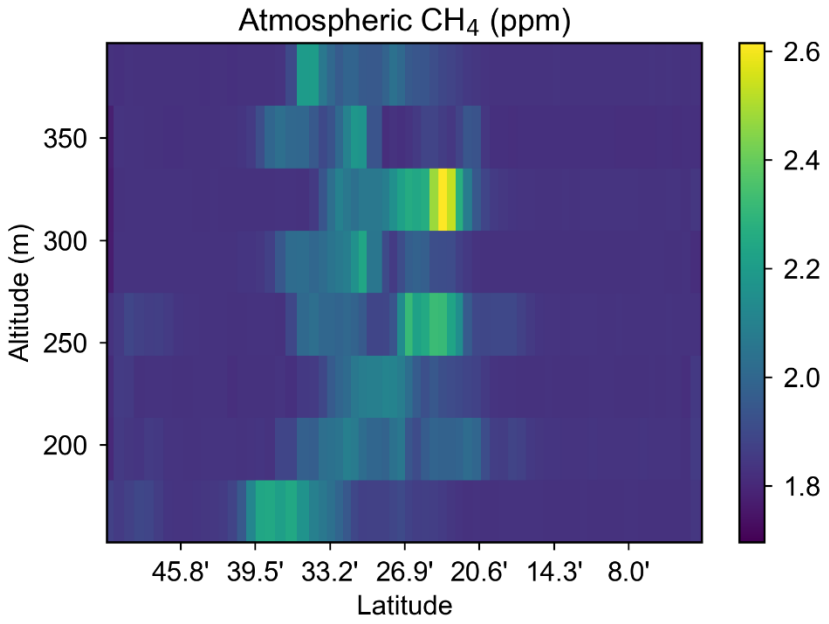

Figure 5.9 Vertical profile of atmospheric CH_4 grids (30 m×30 m) downwind of the smoking tower

5.4.4 Seasonal variation in the methane budget over the inland community

The CH_4 input to the Ingleside community was highest in March 2021 and decreased from spring to summer during the study period (Table 5.2), which is coincident with monthly variations in atmospheric CH_4 mixing ratios. In March, most CH_4 input was from the north (NNW and NNW) and east (ENE and ESE). Then, from spring to summer, CH_4 input from the north (NNW and NNE) decreased. In all months, CH_4 input under wind from the ESE occupied an important

proportion. In July and August, CH_4 fluxes under wind from SSE were highest, up to 40%. The CH_4 inputs under wind from SSW, WSW and WNW were lowest in all months.

Table 5.2 Monthly CH_4 budget in the Ingleside community

	Hourly average flux (mmol/ m^2·hr)	Hours	Monthly budget (mol/m^2·month)
202103	62.87	744*	46.78*
202104	66.95	720	48.20
202105	49.73	744	37.00
202106	30.86	720	22.22
202107	17.60	744	13.09
202108	15.96	744	11.87
SUM (202103-08)			179.17 mol/m^2 2866.7 g/ m^2

* Observation in March 2021 did not last a whole month, and the monthly flux was upscaled by multiplying the hourly average with the total hours in March

Considering the locations of the major industrial area, MODA, platform in the bay and community, it is reasonable that elevated CH_4 fluxes primarily originated from the north and east. Except for the wind from the northwest, which is the major inland industrial area, wind from the northeast seemed to be another input of CH_4 in spring. Viewed from Figure 5.1d, two plants north of the Ingleside community are also potential CH_4 sources, although they are slightly far away since their reported CH_4 emissions exceeded 2500 tons CO_2 equivalent in 2020, 4 times the total reported emissions from four plants in the Ingleside industrial area (65.2 tons CO_2 equivalent). The $\delta^{13}C$-CH_4 of an air sample collected at Ingleside community under north wind in May was -42.93%, suggesting a thermogenic CH_4 input. Redfish Bay is northeast of the Ingleside community, where several fossil fuel or gas platforms have been in operation. We detected CH_4 leakage from a platform in several months from July 2020 to May 2021. It is speculated that fugitive emissions from platforms are another CH_4 input to the Ingleside community. It should be noted that the emissions from ESE occupy a considerable proportion in each month, indicating

that the impact of CH_4 input from fugitive emissions of maritime and loading/offloading on the community was significant. In comparison with greenhouse gases released from industrial facilities, these types of fugitive emissions are easily ignored, although their contributions are significant. The $\delta^{13}C$- CH_4 of an air sample collected at MODA gate on June 24th, 2021, was -44.52‰, indicating a thermogenic source of CH_4 input. Moreover, it is similar to that leaking from the fossil fuel or gas platforms (-44.28‰) in the Redfish Bay. This further verified the existence of fugitive CH_4 exhaust during their loading/offloading operations.

Higher CH_4 emissions in winter than in summer have been reported in Boston and Washington DC-Baltimore, which were explained by consumption-driven losses during extensive natural gas usage in winters (Huang et al. 2019b; Karion et al. 2020; Sargent et al. 2021). Different from these regions, the seasonal variations in the Ingleside community were related to anthropogenic CH_4 input brought by wind from different directions. Considering a small population of approximately 10,000, the CH_4 emissions from local anthropogenic activities such as vehicle exhaust could be ignored.

Upscaling the CH_4 input over Ingleside community from the half year (from March to August) to a whole by doubling the half-year value, the annual CH_4 flux would be 358.34 mol/m^2 (5733.4 g/m^2). Assuming the width of this area is 1.5 km and the height of the atmospheric boundary layer is 150 m, the annual CH_4 budget was 80.6×10^6 mol (1.29×10^6 kg). As shown in Table 5.3, CH_4 input from the east contributed the most, up to 50%, and then from the north 30%. Particularly the input from ESE, the direction where MODA is located was 30%.

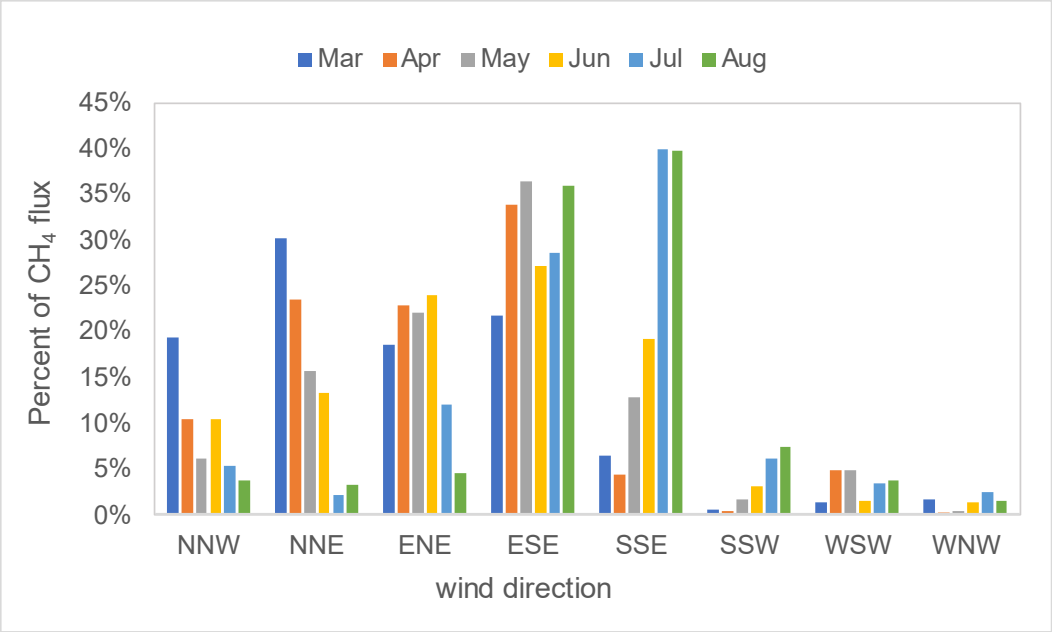

Figure 5.10 Proportion of CH_4 input under different wind directions in each month

Table 5.3 Estimated CH_4 fluxes from different wind directions in a year

Wind direction	CH_4 flux ($\times 10^6$ g/yr)	Wind direction	CH_4 input ($\times 10^6$ g/yr)	Percent of the total flux %
North	393.8	NNW	142.5	11%
		NNE	251.3	19%
East	643.2	ENE	254.3	20%
		ESE	389.0	30%
South	197.2	SSE	173.2	13%
		SSW	24.0	2%
West	55.7	WSW	42.9	3%
		WNW	12.8	1%
TOTAL	1290.0			

5.4.5 Comparison with local inventory emission rates

There are four plants that have large facilities in the industrial area that need to report greenhouse gas emissions to the EPA each year since 2010 (Figure 5.1). They are all located NNW of the Ingleside community. In total, 4.1×10^6 mol/y and 3.9×10^6 mol/y (65.2 and 62.8 tons) of CH_4 emissions were reported from these four companies in 2020 and 2019, respectively, which were

half of the estimated CH_4 flux over the Ingleside community (8.9×10^6 mol/y) under wind from NNW. As previously discussed, another potential CH_4 source from the north is the two plants at Refugio, Texas (Figure 5.1d), since their reported CH_4 emissions in 2020 could reach 2500 tons CO_2 equivalent. However, this needs further study considering its distance to Ingleside. There was no report of greenhouse gas emissions from MODA. However, our measurement found that the CH_4 emissions during its operations were significant. Its contribution to the community was largest among all sources. The CH_4 emissions from local industrial facilities and operations have been largely overlooked.

5.5 Conclusion

During the half-year observations at a fixed station at Ingleside community, we found that the atmospheric CH_4 level was higher in spring than in summer, which was related to the change in wind direction from spring to summer. Calculations based on the box model showed that input of CH_4 from the east was approximately 50%, particularly ESE, where MODA, one of the largest national crude terminals, is located. This result indicated that loading/offloading operations were probably a significant fugitive CH_4 source. Approximately 30% of CH_4 input corresponded to wind from the north, suggesting a contribution from industrial areas. Among these, 11% (8.9×10^6 mol/y) CH_4 was from NNW, where the Ingleside industrial area is located. However, this estimated amount was 2 times the CH_4 emissions reported by companies in this industrial area to the EPA in 2020. The aircraft measurement in August 2021 observed elevated CH_4 emissions downwind of a tower with smoke at a refinery plant. The CH_4 flux was estimated to be 590 kg/hr (36.9×10^3mol/hr), which is much larger than the data reported by this refinery plant. Since our data were within the range of aircraft observations over refineries in the San Francisco Bay area, it is likely that the reported emissions from large facilities in the plant are underestimated. Since our

calculations for CH_4 fluxes used hourly average data of the CH_4 mixing ratio and wind speed, the temporal variation within one hour was ignored. However, both the half-year observations and the aircraft measurements showed that CH_4 emissions from industrial operations and maritime operations have been largely overlooked.

CHAPTER VI: CONCLUDING SUMMARY- METHANE BUDGET AT CORPUS CHRISTI

6.1 Brief summary

This project determined the temporal and spatial CH_4 emissions from the Corpus Christi/Nueces bays, Upper Laguna Madre and Aransas Bay. The annual CH_4 flux at the sea-air interface was largest in Upper Laguna Madre (432.7×10^6g CH_4/yr), followed by Corpus Christi/Nueces bays (124.7×10^6g CH_4/yr), and that from Aransas Bay was lowest (62.4×10^6g CH_4/yr). The high spatial variation in methane (CH_4) emissions was attributed to the distribution of different environmental characteristics, i.e., seagrass, mangroves, channels, and open bays in each estuary. The mechanisms that control CH_4 emissions in different environments are different. Tidal processes, amplitude (spring and neap) and topographic characteristics are crucial factors controlling CH_4 cycling in mangrove estuaries. In seagrass meadows, photosynthetic oxygen transported by seagrass to sediment played a significant role in reducing CH_4 production and transport. The higher daily CH_4 flux in the channels suggested that the disturbance of vegetated sediment could severely enhance CH_4 emissions in comparison with less vegetated sediment.

For hypothesis 1, we observed elevated CH_4 emissions from shallow water of seagrass meadows and mangrove creeks rather than open bay areas with a larger depth. Water incubation experiments showed that the oxidation of CH_4 in the water body was quite limited and that a major portion would be transported to the atmosphere. For hypothesis 2, CH_4 emissions from seagrass meadows at Upper Laguna Madre were larger than those from mangrove creeks, and the corresponding offset to carbon deposits was also larger. This result indicated that the local mangrove ecosystem was a more significant sink of carbon than the seagrass meadow. Tidal processes probably played a crucial role in reducing CH_4 emissions to the air. In comparison, weak

water exchange was most likely to accumulate CH_4 in the water body of the seagrass meadow and caused the elevated CH_4 flux to the atmosphere.

We investigated the atmospheric CH_4 input to the residential area of Ingleside through observations at a fixed station and performed aircraft observations focusing on the industrial area. The CH_4 input to the Ingleside community was up to 1.29×10^9 g/yr, with half the CH_4 input (643.3×10^6g) from fugitive emissions during crude oil loading/offloading operations and approximately 30% of the CH_4 fluxes from industrial operations. The observed results were much larger than the data reported to the EPA. It indicated that the anthropogenic emissions from large facilities in industrial areas and fugitive sources during maritime operations have been largely underestimated (Hypothesis 3).

6.2 Methane emission budget in the Corpus Christi coastal area

CH_4 fluxes to the atmosphere acquired from both bottom-up and top-down approaches are integrated to set up a relatively thorough local CH_4 budget (Figure 6.1). All CH_4 emissions of natural origin were determined in this study. Data on CH_4 emissions from landfills and industries are collected from the EPA inventory database, primarily including landfills and plants in the city of Corpus Christi and the city of Ingleside. Other fugitive CH_4 emissions are acquired based on monitoring in the Ingleside community. The actual anthropogenic emissions should be much larger than these estimates. Our stationery and aircraft observations at Ingleside found that the CH_4 emissions from industrial operations were far greater than the data reported to the EPA and fugitive sources have been overlooked.

Based on the current dataset, it is obvious that anthropogenic emissions are the primary source of atmospheric CH_4 around Corpus Christi, which are 9 times the natural emissions. The proportion of anthropogenic emissions in the local CH_4 budget (90%) is much higher than the

global average (60%). Hence, anthropogenic emissions from coastal areas need more attention. In comparison, coastal wetlands played an important role in carbon sequestration.

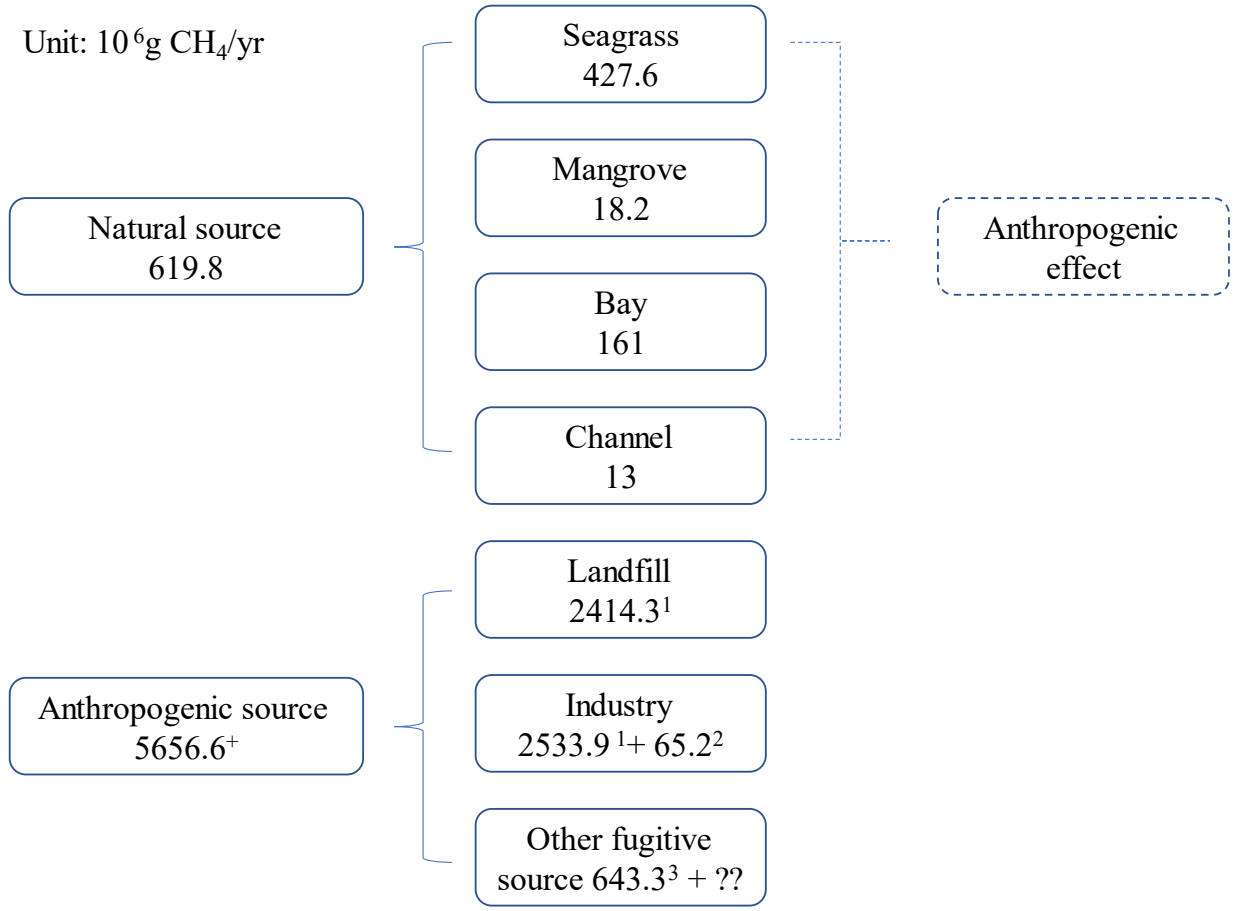

Figure 6.1 CH_4 emission budget in Corpus Christi coastal areas

[1] EPA inventory data of facility emissions at Corpus Christi in 2020; [2] EPA inventory data of facility emissions at Ingleside in 2020; [3] Long-term observation data at the Ingleside community in 2021.

6.3 Problems and future work

In this dissertation research, there still exist some problems that need further work. First, the factors that influence the gas exchange at the water-air interface of estuaries are complicated and no model can describe the gas exchange well to date. However, this question is important because it is crucial to accurately estimate water-air CH_4 fluxes. Second, both our dataset and the

global dataset show that the distribution of CH_4 emissions from coastal areas is not normal. The selection of sampling approaches and spatial analysis methods will determine the precision of upscaling local emissions to the global budget. Then, although we postulated plant-mediation of seagrass on CH_4 emissions, direct evidence is lacking and needs to be pursued. Anthropogenic disturbance on seagrass meadows will not only destroy seagrass ecosystems but bring a high risk to CH_4 emissions. Compared to extensive studies on mangrove ecosystems, seagrass meadows should receive more attention because they are widespread. Last but not least, anthropogenic CH_4 emissions from coastal urban areas should be of highly concern, particularly fugitive emissions.

REFERENCES

Abril, G., M.-V. Commarieu, A. Sottolichio, P. Bretel, and F. Guérin. 2009. Turbidity limits gas exchange in a large macrotidal estuary. Estuarine, Coastal and Shelf Science **83:** 342-348.

Ahmed, N., and S. Thompson. 2019. The blue dimensions of aquaculture: A global synthesis. Science of The Total Environment **652:** 851-861.

Al-Haj, A. N., and R. W. Fulweiler. 2020. A synthesis of methane emissions from shallow vegetated coastal ecosystems. Global Change Biology **26:** 2988-3005.

Allen, D., R. C. Dalal, H. Rennenberg, and S. Schmidt. 2011. Seasonal variation in nitrous oxide and methane emissions from subtropical estuary and coastal mangrove sediments, Australia. Plant Biology **13:** 126-133.

Allen, D. T. and others 2013. Measurements of methane emissions at natural gas production sites in the United States. Proceedings of the National Academy of Sciences **110:** 17768-17773.

Allen, G. and others 2019. The development and trial of an unmanned aerial system for the measurement of methane flux from landfill and greenhouse gas emission hotspots. Waste Management **87:** 883-892.

Alongi, D. M., L. A. Trott, M. C. Undu, and F. Tirendi. 2008. Benthic microbial metabolism in seagrass meadows along a carbonate gradient in Sulawesi, Indonesia. Aquatic Microbial Ecology **51:** 141-152.

Armitage, A. R., W. E. Highfield, S. D. Brody, and P. Louchouarn. 2015. The contribution of mangrove expansion to salt marsh loss on the Texas Gulf Coast. PLoS One **10:** e0125404.

Bahlmann, E. and others 2015. Tidal controls on trace gas dynamics in a seagrass meadow of the Ria Formosa lagoon (southern Portugal). Biogeosciences **12:** 1683-1696.

Banerjee, K., A. Paneerselvam, P. Ramachandran, D. Ganguly, G. Singh, and R. Ramesh. 2018. Seagrass and macrophyte mediated CO_2 and CH_4 dynamics in shallow coastal waters. PLoS One **13:** e0203922.

Bansal, S., B. Tangen, and R. Finocchiaro. 2018. Diurnal Patterns of Methane Flux from a Seasonal Wetland: Mechanisms and Methodology. Wetlands **38:** 933-943.

Barber, T. R., R. A. Burke Jr., and W. M. Sackett. 1988. Diffusive flux of methane from warm wetlands. Global Biogeochemical Cycles **2:** 411-425.

Barber, T. R., and P. R. Carlson. 1993. Effects of seagrass die-off on benthic fluxes and porewater concentrations of $\sum CO_2$, $\sum H_2S$, and CH_4 in florida bay sediments, p. 530-550. *In* R. S. Oremland [ed.], Biogeochemistry of global change. Springer.

Barbosa, P. M. and others 2020. Dissolved methane concentrations and fluxes to the atmosphere from a tropical floodplain lake. Biogeochemistry **148:** 129-151.

Barkley, Z. R. and others 2019. Forward Modeling and Optimization of Methane Emissions in the South Central United States Using Aircraft Transects Across Frontal Boundaries. Geophysical Research Letters **46:** 13564-13573.

Bastviken, D. and others 2010. Methane Emissions from Pantanal, South America, during the Low Water Season: Toward More Comprehensive Sampling. Environmental Science & Technology **44:** 5450-5455.

Beck, V. and others 2012. Methane airborne measurements and comparison to global models during BARCA. Journal of Geophysical Research: Atmospheres **117**.

Berman, E. S. F., M. Fladeland, J. Liem, R. Kolyer, and M. Gupta. 2012. Greenhouse gas analyzer for measurements of carbon dioxide, methane, and water vapor aboard an unmanned aerial vehicle. Sensors and Actuators B: Chemical **169:** 128-135.

Berner, R. A. 1980. Early diagenesis: a theoretical approach. Princeton University Press.

Bianchi, T. S. and others 2013. Historical reconstruction of mangrove expansion in the Gulf of Mexico: Linking climate change with carbon sequestration in coastal wetlands. Estuarine Coastal and Shelf Science **119:** 7-16.

Borges, A. V., W. Champenois, N. Gypens, B. Delille, and J. Harlay. 2016. Massive marine methane emissions from near-shore shallow coastal areas. Scientific Reports **6:** 8.

Borges, A. V. and others 2004. Variability of the gas transfer velocity of CO2 in a macrotidal estuary (the Scheldt). Estuaries **27:** 593-603.

Borum, J., K. Sand-Jensen, T. Binzer, O. Pedersen, and T. M. Greve. 2007. Oxygen movement in seagrasses, p. 255-270. Seagrasses: biology, ecologyand conservation. Springer.

Boudreau, B. P. 1996. The diffusive tortuosity of fine-grained unlithified sediments. Geochimica et Cosmochimica Acta **60:** 3139-3142.

Broecker, W. S., and T.-H. Peng. 1974. Gas exchange rates between air and sea. Tellus **26:** 21-35.

Brownlow, R. and others 2016. Methane mole fraction and δ13C above and below the trade wind inversion at Ascension Island in air sampled by aerial robotics. Geophysical Research Letters **43:** 11,893-811,902.

Burgos, M., T. Ortega, and J. Forja. 2018. Carbon Dioxide and Methane Dynamics in Three Coastal Systems of Cadiz Bay (SW Spain). Estuaries and Coasts **41:** 1069-1088.

Burkholder, J. M., D. A. Tomasko, and B. W. Touchette. 2007. Seagrasses and eutrophication. Journal of Experimental Marine Biology and Ecology **350:** 46-72.

Burkholz, C., N. Garcias-Bonet, and C. M. Duarte. 2020. Warming enhances carbon dioxide and methane fluxes from Red Sea seagrass (Halophila stipulacea) sediments. Biogeosciences **17:** 1717-1730.

Cabezas, A., W. J. Mitsch, C. MacDonnell, L. Zhang, F. Bydałek, and A. Lasso. 2018. Methane emissions from mangrove soils in hydrologically disturbed and reference mangrove tidal creeks in southwest Florida. Ecological Engineering **114:** 57-65.

Call, M. and others 2015. Spatial and temporal variability of carbon dioxide and methane fluxes over semi-diurnal and spring–neap–spring timescales in a mangrove creek. Geochimica et Cosmochimica Acta **150:** 211-225.

Call, M., I. R. Santos, T. Dittmar, C. E. de Rezende, N. E. Asp, and D. T. Maher. 2019. High pore-water derived CO_2 and CH_4 emissions from a macro-tidal mangrove creek in the Amazon region. Geochimica et Cosmochimica Acta **247:** 106-120.

Cavanaugh, K. C. and others 2014. Poleward expansion of mangroves is a threshold response to decreased frequency of extreme cold events. Proceedings of the National Academy of Sciences **111:** 723-727.

Chang, R. Y.-W. and others 2014. Methane emissions from Alaska in 2012 from CARVE airborne observations. Proceedings of the National Academy of Sciences **111:** 16694-16699.

Chanton, J. P., C. S. Martens, C. A. Kelley, P. M. Crill, and W. J. Showers. 1992. Methane transport mechanisms and isotopic fractionation in emergent macrophytes of an Alaskan tundra lake. Journal of Geophysical Research: Atmospheres **97:** 16681-16688.

Che, X., T. Zhang, H. Li, L. Zhang, and J. Liu. Effect of hypoxia on photosystem II of tropical seagrass enhalus acoroides in the dark. Photochemistry and Photobiology **n/a**.

Chuang, P. C., M. B. Young, A. W. Dale, L. G. Miller, J. A. Herrera-Silveira, and A. Paytan. 2016. Methane and sulfate dynamics in sediments from mangrove-dominated tropical coastal lagoons, Yucatán, Mexico. Biogeosciences **13:** 2981-3001.

---. 2017. Methane fluxes from tropical coastal lagoons surrounded by mangroves, Yucatan, Mexico. Journal of Geophysical Research-Biogeosciences **122:** 1156-1174.

Cira, E. K., T. A. Palmer, and M. S. Wetz. 2021. Phytoplankton Dynamics in a Low-Inflow Estuary (Baffin Bay, TX) During Drought and High-Rainfall Conditions Associated with an El Niño Event. Estuaries and Coasts **44:** 1752-1764.

Cline, J. D. 1969. Spectrophotometric determination of hydrogen sulfide in natural waters. Limnology and Oceanography **14:** 454-458.

Clow, J., and J. C. Smith. 2016. Using Unmanned Air Systems to Monitor Methane in the Atmosphere, p. 23. NASA Langley Research Center.

Coffin, R. B. and others 2014. Contribution of Vertical Methane Flux to Shallow Sediment Carbon Pools across Porangahau Ridge, New Zealand. Energies **7:** 5332.

Coffin, R. B., and J. Mueller. 2020. Carbon isotope forensics for methane source identification. Remediation Journal **30:** 55-62.

Coffin, R. B., C. L. Osburn, R. E. Plummer, J. P. Smith, P. S. Rose, and K. S. Grabowski. 2015. Deep Sediment-Sourced Methane Contribution to Shallow Sediment Organic Carbon: Atwater Valley, Texas-Louisiana Shelf, Gulf of Mexico. Energies **8:** 1561-1583.

Coffin, R. B. and others 2013. Spatial variation in shallow sediment methane sources and cycling on the Alaskan Beaufort Sea Shelf/Slope. Marine and Petroleum Geology **45:** 186-197.

Congdon, V. M., C. Bonsell, M. R. Cuddy, and K. H. Dunton. 2019. In the wake of a major hurricane: Differential effects on early vs. late successional seagrass species. Limnology and Oceanography Letters **4:** 155-163.

Davidson, T. A. and others 2018. Synergy between nutrients and warming enhances methane ebullition from experimental lakes. Nature Climate Change **8:** 156-160.

Deborde, J. and others 2010. Methane sources, sinks and fluxes in a temperate tidal Lagoon: The Arcachon lagoon (SW France). Estuarine Coastal and Shelf Science **89:** 256-266.

DeLaune, R. D., C. J. Smith, and W. H. Patrick. 1983. Methane release from Gulf coast wetlands. Tellus B **35B:** 8-15.

DelSontro, T., L. Boutet, A. St-Pierre, P. A. del Giorgio, and Y. T. Prairie. 2016. Methane ebullition and diffusion from northern ponds and lakes regulated by the interaction between temperature and system productivity. Limnology and Oceanography **61:** S62-S77.

Dlugokencky, E. 2021. NOAA/GML (gml.noaa.gov/ccgg/trends_ch4/). NOAA/GML.

Dunton, K. H., L. Cifuentes, P. J. Eldridge, and J. W. Morse. 2003. Effects of dredge deposits on seagrasses: an integrative model for Laguna Madre: concluding report. Volume II, Findings.

Dunton, K. H., and N. E. Reyna. 2019. A long-term seagrass monitoring program for Corpus Christi Bay and Upper Laguna Madre, p. 24. University of Texas at Austin Marine Science Institute.

Dutta, M. K., R. Mukherjee, T. K. Jana, and S. K. Mukhopadhyay. 2015. Biogeochemical dynamics of exogenous methane in an estuary associated to a mangrove biosphere; The Sundarbans, NE coast of India. Marine Chemistry **170:** 1-10.

Eldridge, P. M., J. E. Kaldy, and A. B. Burd. 2004. Stress response model for the tropical seagrassThalassia testudinum: The interactions of light, temperature, sedimentation, and geochemistry. Estuaries **27:** 923-937.

Eldridge, P. M., and J. W. Morse. 2000. A diagenetic model for sediment–seagrass interactions. Marine Chemistry **70:** 89-103.

Engram, M. and others 2020. Remote sensing northern lake methane ebullition. Nature Climate Change **10:** 511-517.

Erftemeijer, P. L. A., and R. R. R. L. III. 2006. Environmental impacts of dredging on seagrasses: A review. Marine Pollution Bulletin **52:** 1553-1572.

Fenwick, L., and P. D. Tortell. 2018. Methane and nitrous oxide distributions in coastal and open ocean waters of the Northeast Subarctic Pacific during 2015–2016. Marine Chemistry **200:** 45-56.

Fiore, A. M., J. J. West, L. W. Horowitz, V. Naik, and M. D. Schwarzkopf. 2008. Characterizing the tropospheric ozone response to methane emission controls and the benefits to climate and air quality. Journal of Geophysical Research: Atmospheres **113**.

Fisher, R. E. and others 2017. Measurement of the 13C isotopic signature of methane emissions from northern European wetlands. Global Biogeochemical Cycles **31:** 605-623.

Fonseca, A. L. D., C. C. Marinho, and F. D. Esteves. 2017. Floating aquatic macrophytes decrease the methane concentration in thewater column of a tropical coastal lagoon: Implications for methane oxidation and emission. Braz. Arch. Biol. Technol. **60:** 16.

Gålfalk, M., D. Bastviken, S. Fredriksson, and L. Arneborg. 2013. Determination of the piston velocity for water-air interfaces using flux chambers, acoustic Doppler velocimetry, and IR imaging of the water surface. Journal of Geophysical Research: Biogeosciences **118:** 770-782.

Gålfalk, M., S. Nilsson Påledal, and D. Bastviken. 2021. Sensitive Drone Mapping of Methane Emissions without the Need for Supplementary Ground-Based Measurements. ACS Earth and Space Chemistry.

Gao, F., S. R. Yates, M. V. Yates, J. Gan, and F. F. Ernst. 1997. Design, Fabrication, and Application of a Dynamic Chamber for Measuring Gas Emissions from Soil. Environmental Science & Technology **31:** 148-153.

Garcias-Bonet, N., and C. M. Duarte. 2017. Methane Production by Seagrass Ecosystems in the Red Sea. Frontiers in Marine Science **4**.

George, R., M. Gullström, M. S. P. Mtolera, T. J. Lyimo, and M. Björk. 2020. Methane emission and sulfide levels increase in tropical seagrass sediments during temperature stress: A mesocosm experiment. Ecology and Evolution **10:** 1917-1928.

Gnanamoorthy, P. and others 2021. Seasonal Variation of Methane Fluxes in a Mangrove Ecosystem in South India: An Eddy Covariance-Based Approach. Estuaries and Coasts.

Golston, L. M. and others 2017. Lightweight mid-infrared methane sensor for unmanned aerial systems. Applied Physics B-Lasers and Optics **123:** 9.

Greatwood, C. and others 2017. Atmospheric Sampling on Ascension Island Using Multirotor UAVs. Sensors **17:** 24.

Guha, A. and others 2020. Assessment of Regional Methane Emission Inventories through Airborne Quantification in the San Francisco Bay Area. Environmental Science & Technology **54:** 9254-9264.

Hartmann, J., M. Gehrmann, K. Kohnert, S. Metzger, and T. Sachs. 2018. New calibration procedures for airborne turbulence measurements and accuracy of the methane fluxes during the AirMeth campaigns. Atmos. Meas. Tech. **11:** 4567-4581.

Hernández, M. E., and D. Junca-Gómez. 2020. Carbon stocks and greenhouse gas emissions (CH_4 and N_2O) in mangroves with different vegetation assemblies in the central coastal plain of Veracruz Mexico. Science of The Total Environment **741:** 140276.

Hicks, D. W., C. P. Onuf, and J. W. Tunnell. 1998. Response of shoal grass, Halodule wrightii, to extreme winter conditions in the Lower Laguna Madre, Texas. Aquatic Botany **62:** 107-114.

Hmiel, B. and others 2020. Preindustrial $^{14}CH_4$ indicates greater anthropogenic fossil CH_4 emissions. Nature **578:** 409-412.

Ho, D. T., N. Coffineau, B. Hickman, N. Chow, T. Koffman, and P. Schlosser. 2016. Influence of current velocity and wind speed on air-water gas exchange in a mangrove estuary. Geophysical Research Letters **43:** 3813-3821.

Ho, D. T., S. Ferrón, V. C. Engel, L. G. Larsen, and J. G. Barr. 2014. Air-water gas exchange and CO2 flux in a mangrove-dominated estuary. Geophysical Research Letters **41:** 108-113.

Horn, C., P. Metzler, K. Ullrich, M. Koschorreck, and B. Boehrer. 2017. Methane storage and ebullition in monimolimnetic waters of polluted mine pit lake Vollert-Sued, Germany. Science of The Total Environment **584-585:** 1-10.

Howarth, R. W. 2019. Ideas and perspectives: is shale gas a major driver of recent increase in global atmospheric methane? Biogeosciences **16:** 3033-3046.

Hu, L., S. A. Yvon-Lewis, J. D. Kessler, and I. R. MacDonald. 2012. Methane fluxes to the atmosphere from deepwater hydrocarbon seeps in the northern Gulf of Mexico. Journal of Geophysical Research: Oceans **117**.

Huang, C.-M., C.-S. Yuan, W.-B. Yang, and L. Yang. 2019a. Temporal variations of greenhouse gas emissions and carbon sequestration and stock from a tidal constructed mangrove wetland. Marine Pollution Bulletin **149:** 110568.

Huang, H., Y. Du, D. Pothina, J. Matsumoto, and S. Negusse. 2012. Corpus Christi Bay Three-Dimensional Hydrodynamics and Salinity Simulations Using Finite-Volume Coastal Ocean Model (FVCOM), p. 46-65. Estuarine and Coastal Modeling (2011).

Huang, Y., E. A. Kort, S. Gourdji, A. Karion, K. Mueller, and J. Ware. 2019b. Seasonally Resolved Excess Urban Methane Emissions from the Baltimore/Washington, DC Metropolitan Region. Environmental Science & Technology **53:** 11285-11293.

Hugenholtz, C. H. and others 2021. Methane emissions from above-ground natural gas distribution facilities in the urban environment: A fence line methodology and case study in Calgary, Alberta, Canada. Journal of the Air & Waste Management Association **71:** 1319-1332.

Huttunen, J. T., T. S. Väisänen, S. K. Hellsten, and P. J. Martikainen. 2006. Methane fluxes at the sediment-water interface in some boreal lakes and reservoirs. Boreal Environment Research **11:** 27-34.

IPCC. 2014. Climate Change 2014: Synthesis Report. Contribution of Working Groups I, II and III to the Fifth Assessment Report of the Intergovernmental Panel on Climate Change, p. 151. *In* C. W. Team, R. K. Pachauri and L. A. Meyer [eds.]. IPCC.

Jackson, R. B. and others 2020. Increasing anthropogenic methane emissions arise equally from agricultural and fossil fuel sources. Environ. Res. Lett. **15:** 071002.

Jacotot, A., C. Marchand, and M. Allenbach. 2018. Tidal variability of CO_2 and CH_4 emissions from the water column within a Rhizophora mangrove forest (New Caledonia). Science of The Total Environment **631-632:** 334-340.

Jeffrey, L. C. and others 2018. The spatial and temporal drivers of pCO_2, pCH_4 and gas transfer velocity within a subtropical estuary. Estuarine, Coastal and Shelf Science **208:** 83-95.

Jeffrey, L. C. and others 2019. Are methane emissions from mangrove stems a cryptic carbon loss pathway? Insights from a catastrophic forest mortality. New Phytologist **224:** 146-154.

Jha, C. S., S. R. Rodda, K. C. Thumaty, A. Raha, and V. K. Dadhwal. 2014. Eddy covariance based methane flux in Sundarbans mangroves, India. Journal of earth system science **123:** 1089-1096.

Jiang, L.-Q., W.-J. Cai, and Y. Wang. 2008. A comparative study of carbon dioxide degassing in river- and marine-dominated estuaries. Limnology and Oceanography **53:** 2603-2615.

Kankaala, P., and I. Bergström. 2004. Emission and oxidation of methane in Equisetum fluviatile stands growing on organic sediment and sand bottoms. Biogeochemistry **67:** 21-37.

Karion, A. and others 2020. Greenhouse gas observations from the Northeast Corridor tower network. Earth Syst. Sci. Data **12:** 699-717.

Kauffman, J. B. and others 2017. The jumbo carbon footprint of a shrimp: carbon losses from mangrove deforestation. Frontiers in Ecology and the Environment **15:** 183-188.

Kauffman, J. B., A. F. Bernardino, T. O. Ferreira, N. W. Bolton, L. E. d. O. Gomes, and G. N. Nobrega. 2018. Shrimp ponds lead to massive loss of soil carbon and greenhouse gas emissions in northeastern Brazilian mangroves. Ecology and Evolution **8:** 5530-5540.

Kelley, C. A., and W. H. Jeffrey. 2002. Dissolved methane concentration profiles and air-sea fluxes from 41 degrees S to 27 degrees N. Global Biogeochemical Cycles **16:** 6.

Kennedy, H. and others 2010. Seagrass sediments as a global carbon sink: Isotopic constraints. Global Biogeochemical Cycles **24**.

Kessler, J. D. and others 2011. A Persistent Oxygen Anomaly Reveals the Fate of Spilled Methane in the Deep Gulf of Mexico. Science **331:** 312-315.

King, G., J. Kostka, T. Hazen, and P. Sobecky. 2015. Microbial responses to the Deepwater Horizon oil spill: from coastal wetlands to the deep sea. Annual review of marine science **7:** 377-401.

Kirschke, S. and others 2013. Three decades of global methane sources and sinks. Nature Geoscience **6:** 813-823.

Klausner, T. and others 2020. Urban greenhouse gas emissions from the Berlin area: A case study using airborne CO_2 and CH_4 in situ observations in summer 2018. Elementa: Science of the Anthropocene **8**.

Kroeger, K. D., S. Crooks, S. Moseman-Valtierra, and J. Tang. 2017. Restoring tides to reduce methane emissions in impounded wetlands: A new and potent Blue Carbon climate change intervention. Scientific Reports **7:** 11914.

Kruse, C. J., D. Ellis, A. Protopapas, N. Norboge, and B. Glover. 2016. Texas Gulf Intracoastal Waterway Master Plan: Technical Report. *In* A. Texas and M. T. Institute [eds.].

Laanbroek, H. J. 2009. Methane emission from natural wetlands: interplay between emergent macrophytes and soil microbial processes. A mini-review. Annals of Botany **105:** 141-153.

Lan, X. and others 2021a. Improved Constraints on Global Methane Emissions and Sinks Using $\delta^{13}C\text{-}CH_4$. Global Biogeochemical Cycles **35:** e2021GB007000.

Lan, X., E. G. Nisbet, E. J. Dlugokencky, and S. E. Michel. 2021b. What do we know about the global methane budget? Results from four decades of atmospheric CH₄ observations and the way forward. Philosophical Transactions of the Royal Society A: Mathematical, Physical and Engineering Sciences **379:** 20200440.

Lee, R. Y., W. P. Porubsky, I. C. Feller, K. L. McKee, and S. B. Joye. 2008. Porewater biogeochemistry and soil metabolism in dwarf red mangrove habitats (Twin Cays, Belize). Biogeochemistry **87:** 181-198.

Lekphet, S., S. Adsavakulchai, S. Towprayoon, A. Chidthaisong, and S. Nitisoravut. 2003. Methane emission from mangrove area in Thailand, p. 18. Proceedings of the 2nd Regional Conference on Energy Technology towards a Clean Environment, Phuket, Thailand.

Lekphet, S., S. Nitisoravut, and S. Adsavakulchai. 2005. Estimating methane emissions from mangrove area in Ranong Province, Thailand. Songklanakarin Journal of Science and Technology **27:** 153-163.

Li, H. Z., M. Mundia-Howe, M. D. Reeder, and N. J. Pekney. 2020a. Gathering Pipeline Methane Emissions in Utica Shale Using an Unmanned Aerial Vehicle and Ground-Based Mobile Sampling. Atmosphere **11:** 716.

Li, H. Z., M. D. Reeder, J. Litten, and N. J. Pekney. 2019. Identifying under-characterized atmospheric methane emission sources in Western Maryland. Atmospheric Environment **219:** 117053.

Li, W. and others 2020b. Carbon isotope fractionation during shale gas transport: Mechanism, characterization and significance. Science China Earth Sciences **63:** 674-689.

Lindsey, R., and M. Scott. 2017. After 2000-era plateu, global methane levels hitting new highs.

Linkhorst, A. and others 2021. Spatially Resolved Measurements in Tropical Reservoirs Reveal Elevated Methane Ebullition at River Inflows and at High Productivity. Global Biogeochemical Cycles **35:** e2020GB006717.

Linto, N., J. Barnes, R. Ramachandran, J. Divia, P. Ramachandran, and R. C. Upstill-Goddard. 2014. Carbon Dioxide and Methane Emissions from Mangrove-Associated Waters of the Andaman Islands, Bay of Bengal. Estuaries and Coasts **37:** 381-398.

Lopez-Coto, I. and others 2020. Wintertime CO_2, CH_4, and CO Emissions Estimation for the Washington, DC–Baltimore Metropolitan Area Using an Inverse Modeling Technique. Environmental Science & Technology **54:** 2606-2614.

Lorenson, T. D., J. Grienert, and R. B. Coffin. 2016. Dissolved methane in the Beaufort Sea and the Arctic Ocean, 1992-2009; sources and atmospheric flux. Limnology and Oceanography **61:** S300-S323.

Lorke, A. and others 2015. Technical note: drifting versus anchored flux chambers for measuring greenhouse gas emissions from running waters. Biogeosciences **12:** 7013-7024.

Lowry, D. and others 2020. Environmental baseline monitoring for shale gas development in the UK: Identification and geochemical characterisation of local source emissions of methane to atmosphere. Science of The Total Environment **708:** 134600.

Lyimo, L. D. and others 2018. Shading and simulated grazing increase the sulphide pool and methane emission in a tropical seagrass meadow. Marine Pollution Bulletin **134:** 89-93.

Macreadie, P. I. and others 2019. The future of Blue Carbon science. Nature Communications **10:** 3998.

Magen, C. and others 2014. A simple headspace equilibration method for measuring dissolved methane. Limnology and Oceanography-Methods **12:** 637-650.

Maher, D. T., K. Cowley, I. R. Santos, P. Macklin, and B. D. Eyre. 2015. Methane and carbon dioxide dynamics in a subtropical estuary over a diel cycle: Insights from automated in situ radioactive and stable isotope measurements. Marine Chemistry **168:** 69-79.

Marbà, N., M. Holmer, E. Gacia, and C. Barron. 2006. Seagrass Beds and Coastal Biogeochemistry, p. 135-157. SEAGRASSES: BIOLOGY, ECOLOGYAND CONSERVATION. Springer Netherlands.

Martens, C. S., and J. Val Klump. 1980. Biogeochemical cycling in an organic-rich coastal marine basin—I. Methane sediment-water exchange processes. Geochimica et Cosmochimica Acta **44:** 471-490.

Matoušů, A., R. Osudar, K. Šimek, and I. Bussmann. 2017. Methane distribution and methane oxidation in the water column of the Elbe estuary, Germany. Aquatic Sciences **79:** 443-458.

McGinnis, D. F. and others 2015. Enhancing Surface Methane Fluxes from an Oligotrophic Lake: Exploring the Microbubble Hypothesis. Environmental Science & Technology **49:** 873-880.

McMillan, C. 1979. Differentiation in response to chilling temperatures among populations of three marine spermatophytes, Thalassia testudinum, Syringodium filiforme and Halodule wrightii. American Journal of Botany **66:** 810-819.

Miller, S. M. and others 2016. A multiyear estimate of methane fluxes in Alaska from CARVE atmospheric observations. Global Biogeochemical Cycles **30:** 1441-1453.

Montagna, P. A., J. Brenner, J. Gibeaut, and S. Morehead. 2011. Coastal impacts, p. 96-123. *In* J. Schmandt, G. R. North and J. Clarkson [eds.], The impact of global warming on Texas. University of Texas Press.

Morin, J., and J. W. Morse. 1999. Ammonium release from resuspended sediments in the Laguna Madre estuary. Marine Chemistry **65:** 97-110.

Myllykangas, J.-P., S. Hietanen, and T. Jilbert. 2020. Legacy Effects of Eutrophication on Modern Methane Dynamics in a Boreal Estuary. Estuaries and Coasts **43:** 189-206.

National Academies of Sciences, E., and Medicine. 2018. Improving Characterization of Anthropogenic Methane Emissions in the United States. The National Academies Press.

Ni, X., and P. M. Groffman. 2018. Declines in methane uptake in forest soils. Proceedings of the National Academy of Sciences **115:** 8587-8590.

Nisbet, E. G. and others 2022. Isotopic signatures of methane emissions from tropical fires, agriculture and wetlands: the MOYA and ZWAMPS flights. Philosophical Transactions of the Royal Society A: Mathematical, Physical and Engineering Sciences **380:** 20210112.

Nisbet, E. G., E. J. Dlugokencky, and P. Bousquet. 2014. Methane on the rise—again. Science **343:** 493-495.

Nisbet, E. G. and others 2016. Rising atmospheric methane: 2007–2014 growth and isotopic shift. Global Biogeochemical Cycles **30:** 1356-1370.

Nisbet, E. G. and others 2019. Very Strong Atmospheric Methane Growth in the 4 Years 2014–2017: Implications for the Paris Agreement. Global Biogeochemical Cycles **33:** 318-342.

O'Connor, D. J., and W. E. Dobbins. 1958. Mechanism of Reaeration in Natural Streams. Transactions of the American Society of Civil Engineers **123:** 641-666.

Onuf, C. P. 2007. Laguna Madre, p. 29-40. *In* L. Handley, D. Altsman and R. DeMay [eds.], Seagrass status and trends in the northern Gulf of Mexico: 1940–2002.

Oremland, R. S. 1975. Methane Production in Shallow-Water, Tropical Marine Sediments. Applied Microbiology **30:** 602-608.

Oremland, R. S., and B. F. Taylor. 1977. Diurnal fluctuations of O_2, N_2, and CH_4 in the rhizosphere of *Thalassia testudinum*. Limnology and Oceanography **22:** 566-570.

Oreska, M. P. J., K. J. McGlathery, L. R. Aoki, A. C. Berger, P. Berg, and L. Mullins. 2020. The greenhouse gas offset potential from seagrass restoration. Scientific Reports **10:** 7325.

Osland, M. J. and others 2018. Mangrove forests in a rapidly changing world: Global change impacts and conservation opportunities along the Gulf of Mexico coast. Estuarine, Coastal and Shelf Science **214:** 120-140.

Padhy, S. R., P. Bhattacharyya, P. K. Dash, C. S. Reddy, A. Chakraborty, and H. Pathak. 2020. Seasonal fluctuation in three mode of greenhouse gases emission in relation to soil labile carbon pools in degraded mangrove, Sundarban, India. Science of The Total Environment **705:** 135909.

Pérez-Estrada, C. J., A. Falcón-Brindis, R. Rodríguez-Estrella, E. Morales-Bojórquez, J. M. Crespo-Domínguez, and F. G. Brun-Murillo. 2021. Seasonal shifts in morphology, physiology and population traits in the seagrass Halodule wrightii (Cymodoceaceae) in a subtropical arid area. Aquatic Botany **172:** 103381.

Phillips, R. C., and E. G. Menez. 1988. Seagrasses. Smithsonian Institution Press.

Plant, G., E. A. Kort, C. Floerchinger, A. Gvakharia, I. Vimont, and C. Sweeney. 2019. Large Fugitive Methane Emissions From Urban Centers Along the U.S. East Coast. Geophys Res Lett **46:** 8500-8507.

Plant, G., E. A. Kort, L. T. Murray, J. D. Maasakkers, and I. Aben. 2022. Evaluating urban methane emissions from space using TROPOMI methane and carbon monoxide observations. Remote Sensing of Environment **268:** 112756.

Prairie, Y. T., and P. A. del Giorgio. 2013. A new pathway of freshwater methane emissions and the putative importance of microbubbles. Inland Waters **3:** 311-320.

Purvaja, R., D. Ganguly, G. Hariharan, K. Arumugam, and R. Ramesh. 2020. In situ Photosynthetic Activities and Associated Biogeochemical Changes in Three Tropical Seagrass Species. Frontiers in Earth Science **8**.

Purvaja, R., R. Ramesh, and P. Frenzel. 2004. Plant-mediated methane emission from an Indian mangrove. Global Change Biology **10:** 1825-1834.

Raymond, P. A., and J. J. Cole. 2001. Gas Exchange in Rivers and Estuaries: Choosing a Gas Transfer Velocity. Estuaries **24:** 312-317.

Reeburgh, W. S. 2007. Oceanic Methane Biogeochemistry. Chemical Reviews **107:** 486-513.

Reese, B. K., D. W. Finneran, H. J. Mills, M.-X. Zhu, and J. W. Morse. 2011. Examination and Refinement of the Determination of Aqueous Hydrogen Sulfide by the Methylene Blue Method. Aquatic Geochemistry **17:** 567.

Ren, X. and others 2019. Methane Emissions from the Marcellus Shale in Southwestern Pennsylvania and Northern West Virginia Based on Airborne Measurements. Journal of Geophysical Research: Atmospheres **124:** 1862-1878.

Ren, X. and others 2018. Methane Emissions From the Baltimore-Washington Area Based on Airborne Observations: Comparison to Emissions Inventories. Journal of Geophysical Research: Atmospheres **123:** 8869-8882.

Ricart, A. M., P. H. York, C. V. Bryant, M. A. Rasheed, D. Ierodiaconou, and P. I. Macreadie. 2020. High variability of Blue Carbon storage in seagrass meadows at the estuary scale. Scientific Reports **10:** 5865.

Rigby, M. and others 2017. Role of atmospheric oxidation in recent methane growth. Proceedings of the National Academy of Sciences **114:** 5373-5377.

Rodriguez, N. D., and R. P. Philp. 2010. Geochemical characterization of gases from the Mississippian Barnett shale, Fort Worth basin, Texas. AAPG bulletin **94:** 1641-1656.

Romero-Uribe, H. M., J. López-Portillo, F. Reverchon, and M. E. Hernández. 2021. Effect of degradation of a black mangrove forest on seasonal greenhouse gas emissions. Environmental Science and Pollution Research.

Rose, P. S. and others 2013. Natural Gas at Seep Site on the UK Continental Shelf, North Sea. Naval Research Laboratory.

Rosentreter, J. A., A. N. Al-Haj, R. W. Fulweiler, and P. Williamson. 2021a. Methane and Nitrous Oxide Emissions Complicate Coastal Blue Carbon Assessments. Global Biogeochemical Cycles **35:** e2020GB006858.

Rosentreter, J. A. and others 2021b. Half of global methane emissions come from highly variable aquatic ecosystem sources. Nature Geoscience **14:** 225-230.

Rosentreter, J. A., D. T. Maher, D. V. Erler, R. Murray, and B. D. Eyre. 2018a. Factors controlling seasonal CO_2 and CH_4 emissions in three tropical mangrove-dominated estuaries in Australia. Estuarine, Coastal and Shelf Science **215:** 69-82.

Rosentreter, J. A., D. T. Maher, D. V. Erler, R. H. Murray, and B. D. Eyre. 2018b. Methane emissions partially offset "blue carbon" burial in mangroves. Science Advances **4:** eaao4985.

Rosentreter, J. A., D. T. Maher, D. T. Ho, M. Call, J. G. Barr, and B. D. Eyre. 2017. Spatial and temporal variability of CO_2 and CH_4 gas transfer velocities and quantification of the CH_4 microbubble flux in mangrove dominated estuaries. Limnology and Oceanography **62:** 561-578.

Sargent, M. R. and others 2021. Majority of US urban natural gas emissions unaccounted for in inventories. Proceedings of the National Academy of Sciences **118:** e2105804118.

Saunders, M. I. and others 2013. Coastal retreat and improved water quality mitigate losses of seagrass from sea level rise. Global Change Biology **19:** 2569-2583.

Saunois, M. and others 2016. The global methane budget 2000–2012. Earth System Science Data (Online)**:** Medium: ED; Size: p. 697-751.

Saunois, M. and others 2020. The Global Methane Budget 2000–2017. Earth System Science Data **12:** 1561-1623.

Scandella, B. P., L. Pillsbury, T. Weber, C. Ruppel, H. F. Hemond, and R. Juanes. 2016. Ephemerality of discrete methane vents in lake sediments. Geophysical Research Letters **43:** 4374-4381.

Schaefer, H. and others 2016. A 21st-century shift from fossil-fuel to biogenic methane emissions indicated by $^{13}CH_4$. Science **352:** 80-84.

Schilder, J., D. Bastviken, M. van Hardenbroek, and O. Heiri. 2016. Spatiotemporal patterns in methane flux and gas transfer velocity at low wind speeds: Implications for upscaling studies on small lakes. Journal of Geophysical Research: Biogeosciences **121:** 1456-1467.

Schroll, M., F. Keppler, M. Greule, C. Eckhardt, H. Zorn, and K. Lenhart. 2020. The stable carbon isotope signature of methane produced by saprotrophic fungi. Biogeosciences **17:** 3891-3901.

Schwietzke, S. and others 2016. Upward revision of global fossil fuel methane emissions based on isotope database. Nature **538:** 88.

Sebacher, D. I., R. C. Harriss, and K. B. Bartlett. 1983. Methane flux across the air-water interface: air velocity effects. Tellus B: Chemical and Physical Meteorology **35:** 103-109.

Seeberg-Elverfeldt, J., M. Schlüter, T. Feseker, and M. Kölling. 2005. Rhizon sampling of porewaters near the sediment-water interface of aquatic systems. Limnology and Oceanography: Methods **3:** 361-371.

Serrano-Silva, N., Y. Sarria-Guzman, L. Dendooven, and M. Luna-Guido. 2014. Methanogenesis and Methanotrophy in Soil: A Review. Pedosphere **24:** 291-307.

Shah, A., J. Pitt, K. Kabbabe, and G. Allen. 2019. Suitability of a Non-Dispersive Infrared Methane Sensor Package for Flux Quantification Using an Unmanned Aerial Vehicle. Sensors **19:** 4705.

Silva, J. P., A. Lasso, H. J. Lubberding, M. R. Peña, and H. J. Gijzen. 2015. Biases in greenhouse gases static chambers measurements in stabilization ponds: Comparison of flux estimation using linear and non-linear models. Atmospheric Environment **109:** 130-138.

Smith, N. P. 1979. Tidal dynamics and low-frequency exchanges in the Aransas Pass, Texas. Estuaries **2:** 218-227.

Solomon, E. A., M. Kastner, I. R. MacDonald, and I. Leifer. 2009. Considerable methane fluxes to the atmosphere from hydrocarbon seeps in the Gulf of Mexico. Nature Geoscience **2:** 561.

Tadić, J. M., S. Miller, V. Yadav, and S. C. Biraud. 2021. Greenhouse gas fluxes from Alaska's North Slope inferred from the Airborne Carbon Measurements campaign (ACME-V). Atmospheric Environment **248:** 118239.

Taillardat, P., B. S. Thompson, M. Garneau, K. Trottier, and D. A. Friess. 2020. Climate change mitigation potential of wetlands and the cost-effectiveness of their restoration. Interface Focus **10:** 20190129.

Thomas, R. M. and others 2015. A Novel UAS Rapid Deployment Platform for Targeted Gas Sampling and Meteorological Soundings at Altitudes up to 2,700 masl. EGU General Assembly Conference Abstracts.

Thorhaug, A. and others 2019. Gulf of Mexico estuarine blue carbon stock, extent and flux: Mangroves, marshes, and seagrasses: A North American hotspot. Science of The Total Environment **653:** 1253-1261.

Thorhaug, A., H. M. Poulos, J. López-Portillo, T. C. W. Ku, and G. P. Berlyn. 2017. Seagrass blue carbon dynamics in the Gulf of Mexico: Stocks, losses from anthropogenic disturbance, and gains through seagrass restoration. Science of The Total Environment **605-606:** 626-636.

Tokoro, T. and others 2008. High gas-transfer velocity in coastal regions with high energy-dissipation rates. Journal of Geophysical Research: Oceans **113**.

Tollefson, J. 2022. Scientists raise alarm over'dangerously fast'growth in atmospheric methane. Nature.

Treude, T., S. Krause, J. Maltby, A. W. Dale, R. B. Coffin, and L. J. Hamdan. 2014. Sulfate reduction and methane oxidation activity below the sulfate-methane transition zone in Alaskan Beaufort Sea continental margin sediments: Implications for deep sulfur cycling. Geochimica et Cosmochimica Acta **144:** 217-237.

Trifunovic, B., A. Vázquez-Lule, M. Capooci, A. L. Seyfferth, C. Moffat, and R. Vargas. 2020. Carbon Dioxide and Methane Emissions From A Temperate Salt Marsh Tidal Creek. Journal of Geophysical Research: Biogeosciences **125:** e2019JG005558.

Tunnell, J., N. Hilburn, and K. Withers. 2002. Comprehensive bibliography of the Laguna Madre of Texas and Tamaulipas. Center for Coastal Studies, Texas A&M University--Corpus Christi for The Nature Conservancy of Texas. Tunnell, JW and FW Judd.

Turner, A. J., C. Frankenberg, P. O. Wennberg, and D. J. Jacob. 2017. Ambiguity in the causes for decadal trends in atmospheric methane and hydroxyl. Proceedings of the National Academy of Sciences **114:** 5367-5372.

Umezawa, T. and others 2014. Variations of tropospheric methane over Japan during 1988–2010. Tellus B: Chemical and Physical Meteorology **66:** 23837.

Umezawa, T., T. Machida, S. Aoki, and T. Nakazawa. 2012. Contributions of natural and anthropogenic sources to atmospheric methane variations over western Siberia estimated from its carbon and hydrogen isotopes. Global Biogeochemical Cycles **26**.

UNFCCC. 2015. United Nations Framework Convention on Climate Change Paris Agreement.

Van Dam, B. R., J. B. Edson, and C. Tobias. 2019. Parameterizing Air-Water Gas Exchange in the Shallow, Microtidal New River Estuary. Journal of Geophysical Research: Biogeosciences **124:** 2351-2363.

Vaughn, D. R., T. S. Bianchi, M. R. Shields, W. F. Kenney, and T. Z. Osborne. 2020. Increased Organic Carbon Burial in Northern Florida Mangrove-Salt Marsh Transition Zones. Global Biogeochemical Cycles **34:** e2019GB006334.

Venturi, S. and others 2021. Near-surface atmospheric concentrations of greenhouse gases (CO_2 and CH_4) in Florence urban area: Inferring emitting sources through carbon isotopic analysis. Urban Climate **39:** 100968.

Wanninkhof, R. 1992. Relationship between wind speed and gas exchange over the ocean. Journal of Geophysical Research: Oceans **97:** 7373-7382.

---. 2014. Relationship between wind speed and gas exchange over the ocean revisited. Limnology and Oceanography: Methods **12:** 351-362.

Wanninkhof, R., W. E. Asher, D. T. Ho, C. Sweeney, and W. R. McGillis. 2009. Advances in Quantifying Air-Sea Gas Exchange and Environmental Forcing. Annual Review of Marine Science **1:** 213-244.

Weber, T., N. A. Wiseman, and A. Kock. 2019. Global ocean methane emissions dominated by shallow coastal waters. Nature Communications **10:** 4584.

Wetz, M. S., K. C. Hayes, K. V. B. Fisher, L. Price, and B. Sterba-Boatwright. 2016. Water quality dynamics in an urbanizing subtropical estuary(Oso Bay, Texas). Marine Pollution Bulletin **104:** 44-53.

Whitfield, A., and M. Elliott. 2011. Ecosystem and Biotic Classifications of Estuaries and Coasts, p. 99-124. *In* E. Wolanski and D. S. McLusky [eds.], Treatise on Estuarine and Coastal Science. Academic Press.

Whiticar, M. J., E. Faber, and M. Schoell. 1986. Biogenic methane formation in marine and freshwater environments: CO2 reduction vs. acetate fermentation—Isotope evidence. Geochimica et Cosmochimica Acta **50:** 693-709.

Whiting, G. J., and J. P. Chanton. 1992. Plant-dependent CH_4 emission in a subarctic Canadian fen. Global Biogeochemical Cycles **6:** 225-231.

Wiesenburg, D. A., and N. L. Guinasso. 1979. Equilibrium solubilities of methane, carbon monoxide, and hydrogen in water and sea water. Journal of Chemical and Engineering Data **24:** 356-360.

Wilson, B. J., B. Mortazavi, and R. P. Kiene. 2015. Spatial and temporal variability in carbon dioxide and methane exchange at three coastal marshes along a salinity gradient in a northern Gulf of Mexico estuary. Biogeochemistry **123:** 329-347.

Wilson, S. S., and K. H. Dunton. 2018. Hypersalinity During Regional Drought Drives Mass Mortality of the Seagrass *Syringodium filiforme* in a Subtropical Lagoon. Estuaries and Coasts **41:** 855-865.

Wilson, S. T. and others 2020. Ideas and perspectives: A strategic assessment of methane and nitrous oxide measurements in the marine environment. Biogeosciences **17:** 5809-5828.

Wofsy, S. C. 2011. HIAPER Pole-to-Pole Observations (HIPPO): fine-grained, global-scale measurements of climatically important atmospheric gases and aerosols. Philosophical Transactions of the Royal Society A: Mathematical,

Physical and Engineering Sciences **369:** 2073-2086.

Wolf, B. and others 2017. THE SCALEX CAMPAIGN Scale-Crossing Land Surface and Boundary Layer Processes in the TERENO-preAlpine Observatory. Bulletin of the American Meteorological Society **98:** 1217-1234.

Wolfe, G. M. and others 2018. The NASA Carbon Airborne Flux Experiment (CARAFE): instrumentation and methodology. Atmospheric Measurement Techniques **11:** 1757-1776.

Worden, J. R. and others 2017. Reduced biomass burning emissions reconcile conflicting estimates of the post-2006 atmospheric methane budget. Nature Communications **8:** 2227.

Yang, H. and others 2020. Enhanced Carbon Uptake and Reduced Methane Emissions in a Newly Restored Wetland. Journal of Geophysical Research: Biogeosciences **125:** e2019JG005222.

Yang, P. and others 2021. Diffusive CH_4 fluxes from aquaculture ponds using floating chambers and thin boundary layer equations. Atmospheric Environment **253:** 118384.

Yang, W.-B., C.-S. Yuan, B.-Q. Huang, C. Tong, and L. Yang. 2018. Emission Characteristics of Greenhouse Gases and Their Correlation with Water Quality at an Estuarine Mangrove Ecosystem – the Application of an In-situ On-site NDIR Monitoring Technique. Wetlands **38:** 723-738.

Yang, W.-B., C.-S. Yuan, C. Tong, P. Yang, L. Yang, and B.-Q. Huang. 2017. Diurnal variation of CO_2, CH_4, and N_2O emission fluxes continuously monitored in-situ in three environmental habitats in a subtropical estuarine wetland. Marine Pollution Bulletin **119:** 289-298.

Yao, H., and X. Hu. 2017. Responses of carbonate system and CO_2 flux to extended drought and intense flooding in a semiarid subtropical estuary. Limnology and Oceanography **62:** S112-S130.

Yao, H., M. R. McCutcheon, C. J. Staryk, and X. Hu. 2020. Hydrologic controls on CO2 chemistry and flux in subtropical lagoonal estuaries of the northwestern Gulf of Mexico. Limnology and Oceanography **65:** 1380-1398.

Ye, W., G. Zhang, W. Zheng, H. Zhang, and Y. Wu. 2019. Methane distributions and sea-to-air fluxes in the Pearl River Estuary and the northern South China sea. Deep Sea Research Part II: Topical Studies in Oceanography **167:** 34-45.

Ye, W. and others 2016. Methane distribution and sea-to-air flux in the East China Sea during the summer of 2013: Impact of hypoxia. Deep Sea Research Part II: Topical Studies in Oceanography **124:** 74-83.

Yu, X. and others 2020. Top-Down Constraints on Methane Point Source Emissions From Animal Agriculture and Waste Based on New Airborne Measurements in the U.S. Upper Midwest. Journal of Geophysical Research: Biogeosciences **125:** e2019JG005429.

Yvon-Lewis, S. A., L. Hu, and J. Kessler. 2011. Methane flux to the atmosphere from the Deepwater Horizon oil disaster. Geophysical Research Letters **38**.

Zang, K. and others 2020. Multiple factors dominate the distribution of methane and its sea-to-air flux in the Bohai Sea in summer and autumn of 2014. Marine Pollution Bulletin **154:** 111049.

Zhang, M. and others 2019. Methane flux dynamics in a submerged aquatic vegetation zone in a subtropical lake. Science of The Total Environment **672:** 400-409.

Ziegler, S., and R. Benner. 1998. Ecosystem metabolism in a subtropical, seagrass-dominated lagoon. Marine Ecology Progress Series **173:** 1-12.

APPENDIX A

SUPPORTING INFORMATION FOR CHAPTER II

SI 1. Artificially unification of monthly average sea-air CH_4 fluxes

Data of different F_{model} and F_{fc} have been compared and F_{W2014} and F_{J2008} matched F_{fc} or closest to F_{fc} as shown in Figure SI 1. In March 2021, F_{W2014} was 2.6 times of F_{fc}, and in May 2021, F_{W2014} was 1.4 times of F_{fc}, and in July 2020 F_{W2014} was 1.3 times of F_{fc}, while in November 2020, F_{W2014} was only 0.8 of F_{fc}. In other months, F_{W2014} or F_{J2008} matched F_{fc} well. Hence, to uniform the CH_4 fluxes, in the months F_{W2014} or F_{J2008} matched Ffc well, we applied data of F_{W2014} or F_{J2008} as final CH_4 flux. In the months F_{W2014} were 0.8 to 2.6 times of Ffc, we applied F_{W2014} divided by 2.6, 1.4, 1.3 and 0.8 in March 2021, May 2021, July 2020 and November 2020, respectively.

Since we have not measured F_{fc} in June 2018, July 2019, January 2021, we applied F_{W2014} in June 2018 and July 2019 and F_{J2008} in January 2021, by comparing tidal process, tidal amplitude, and wind speed in adjacent months.

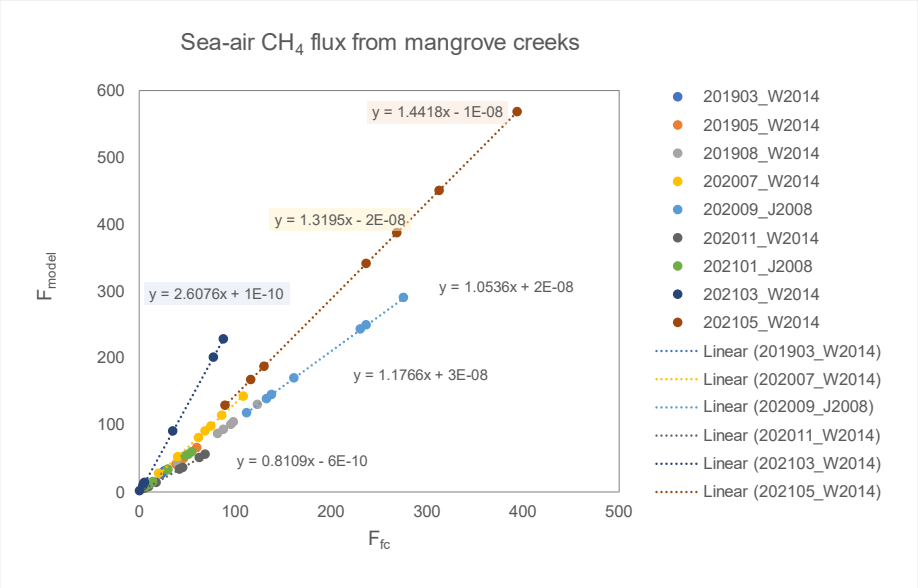

Figure SI1 Comparison of CH_4 fluxes between F_{model} and F_{fc}

Figure S1 Variation in CH_4 concentration during water incubation

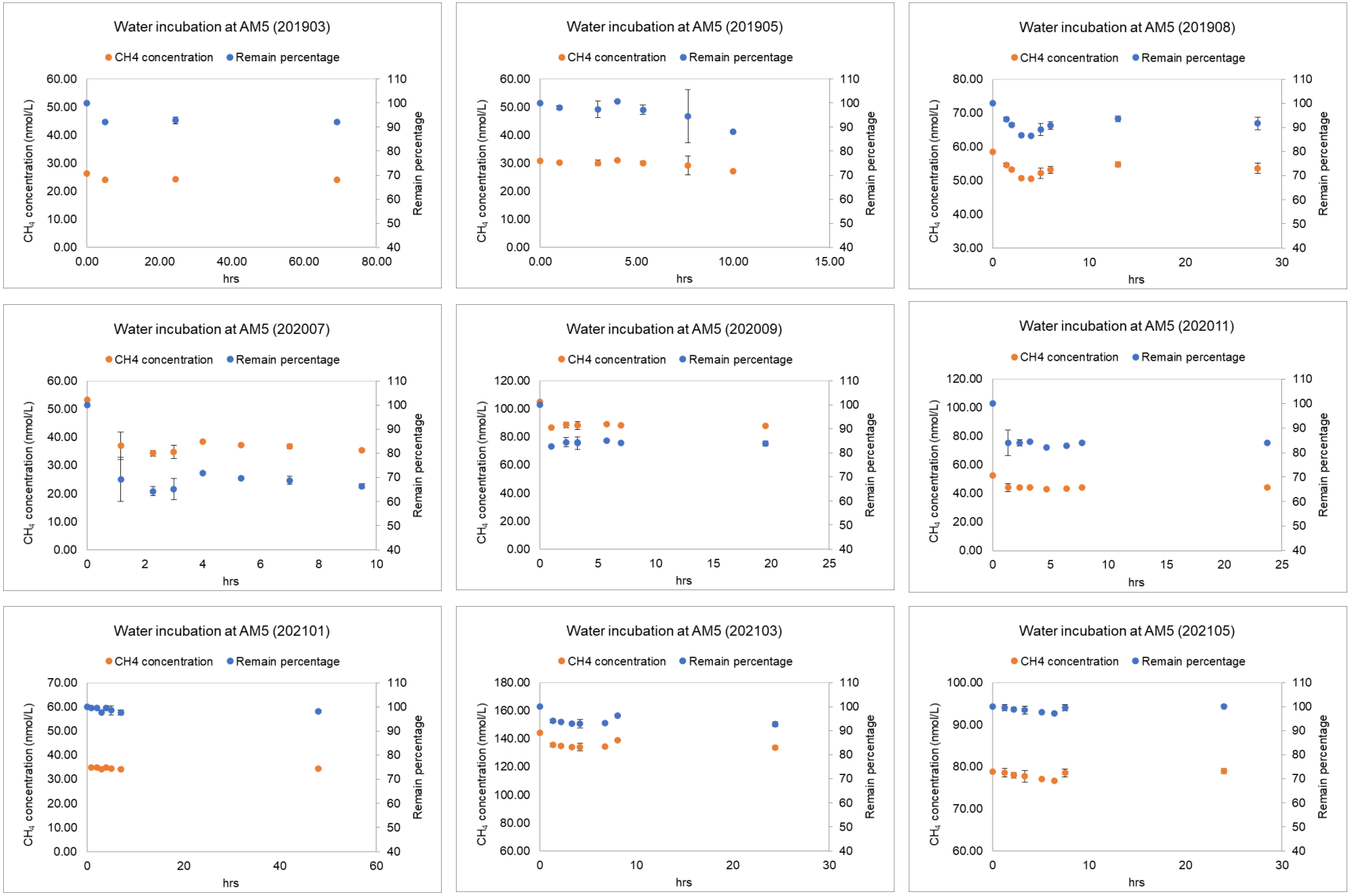

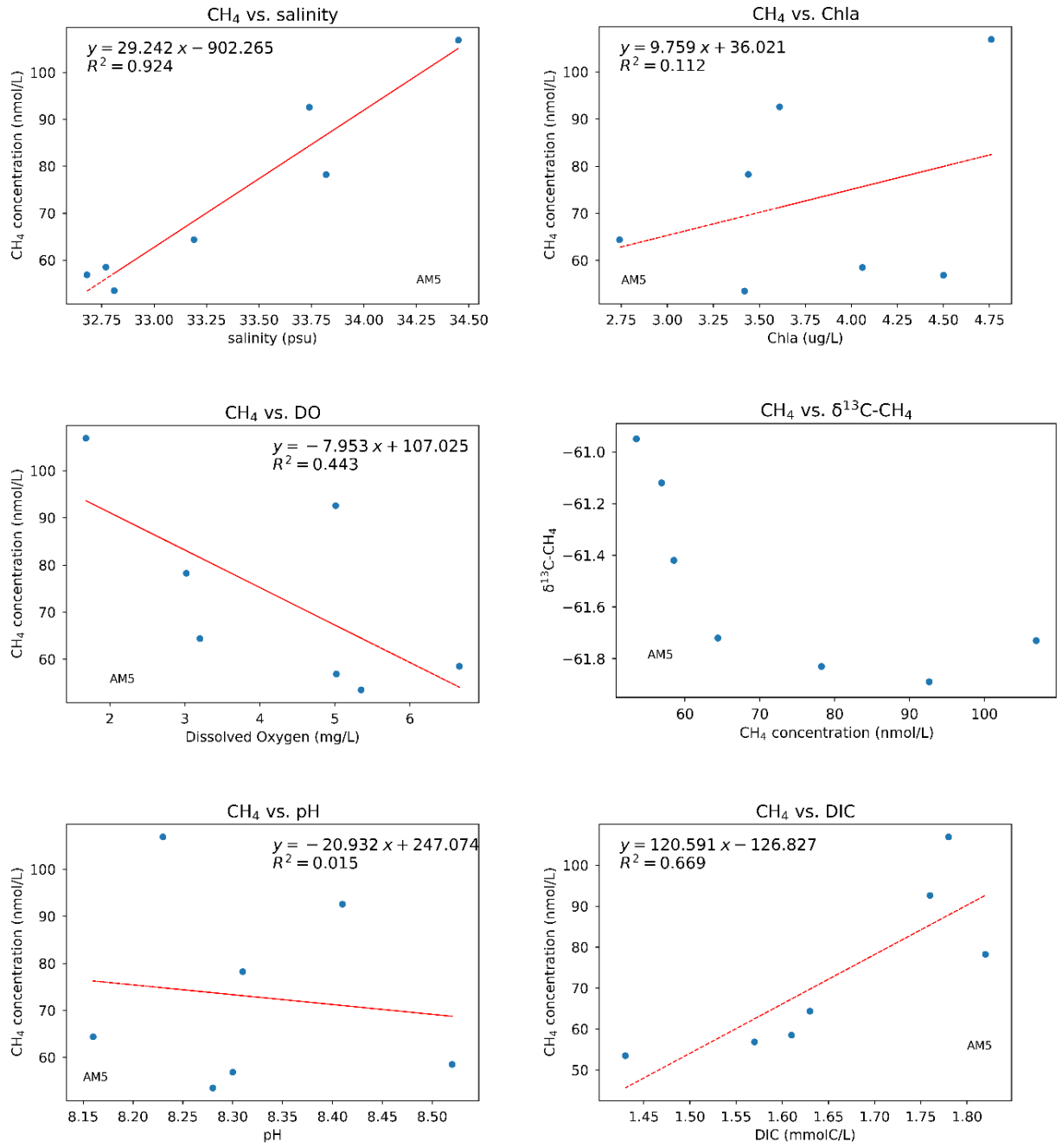

Figure S2. Relationship between CH_4 concentration and other parameters.

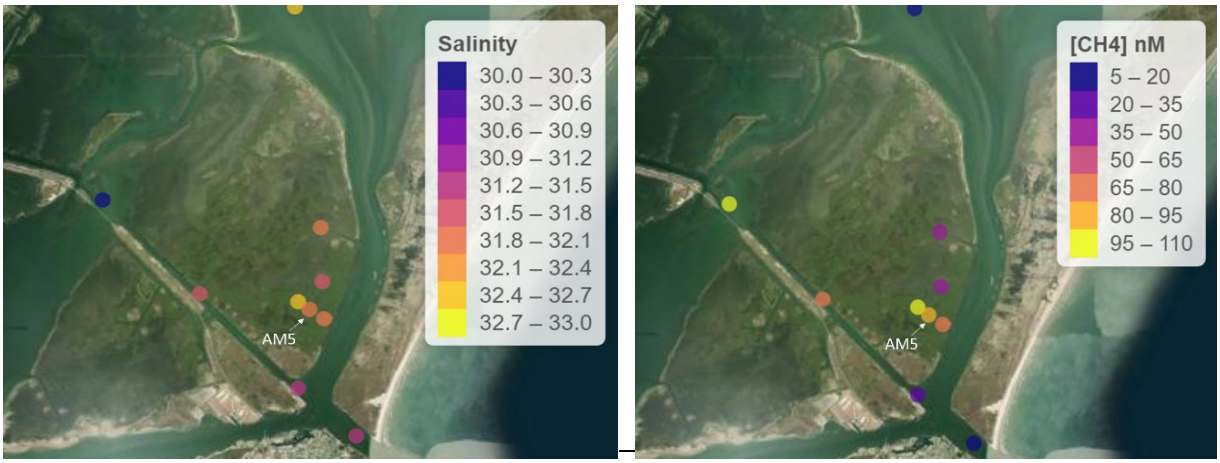

Figure S3. Salinity and dissolved CH_4 concentration at Harbor Island waterways in July 2019.

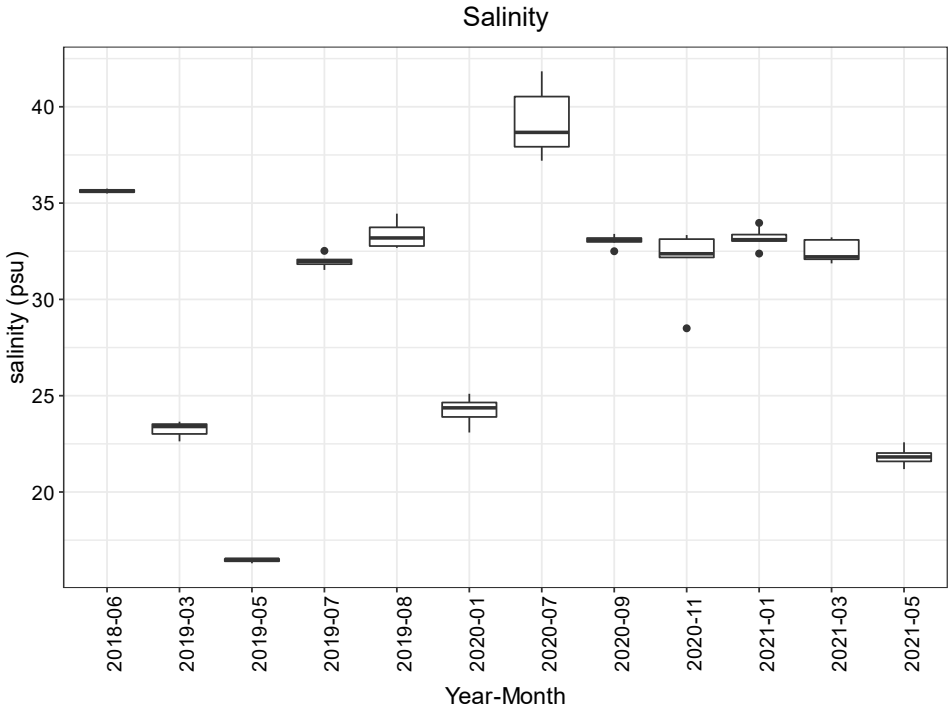

Figure S4. Temporal variation in salinity in Aransas Bay

APPENDIX B

SUPPORTING INFORMATION FOR CHAPTER III

SI1. Detail information about CH_4 cycling in the seagrass meadow

(1) Average hourly variation of CH_4 concentration in the daytime and nighttime and daily variation:

- *In-situ* daytime variation from 9:45 am to 19:05 pm (9.35 hours) was used to calculate the average hourly variation in dissolved CH_4 concentration.

$\Delta[CH_4]_{remain\text{-}daytime}$ = -37.58nM/9.35hr = -4.02 nmol/L·hr

- *In-situ* nighttime variation from 22:00 pm to 5:00 am (7 hours) was used to calculate the average hourly variation in dissolved CH_4 concentration.

$\Delta[CH_4]_{remain\text{-}night}$ = +36.08nM/7hr = +5.15 nmol/L·hr

- The summer day includes13 hours of daytime and 11 hours of nighttime.

$[CH_4]_{remain\text{-}whole\text{-}day}$ = -4.02 nmol/L·hr *13hrs + 5.15 nmol/L·hr *11hrs = + 4.5 nmol/L

Hence, 4.5 nmol/L of dissolved CH_4 was left in the water column during whole-day cycling.

(2) Plant mediation of CH_4 by seagrass

- Daytime: No or few CH_4 was transported by seagrass due to photosynthesis. A decline of dissolved CH_4 in the water column could support this point.
- Nighttime:

An increase of CH_4 in overlying water was used to calculate seagrass transport of CH_4 overnight. Assuming oxygen in sediment chambers was enough to support seagrass survival during the incubation experiment, CH_4 in overlying water increased after sunset like the in-situ conditions.

$[CH_4]_{plant\text{-}mediation}$ = 81.9/11 = 7.4 nmol/L·hr, or 37.66/11=3.4 μmol/m^2·hr

(3) Sediment-water diffusive flux was calculated using Fick's First Law

(4) Water-air CH_4 fluxes in daytime and night were average diffusive fluxes during observation in the day and overnight, respectively.

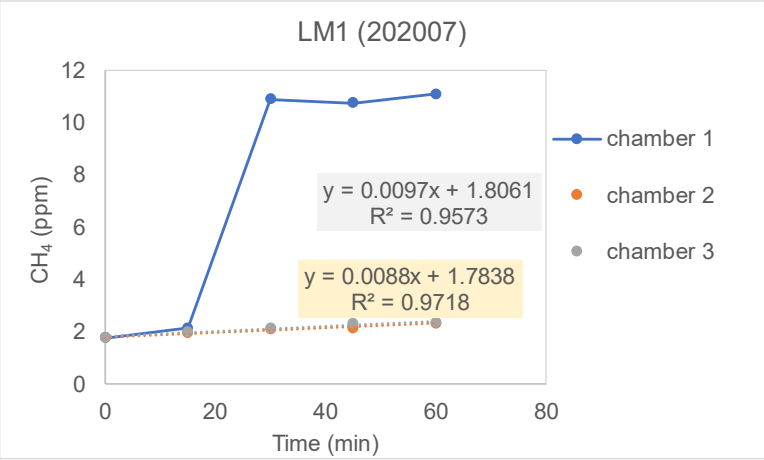

Figure S1 Methane concentration in floating chambers in July 2020.

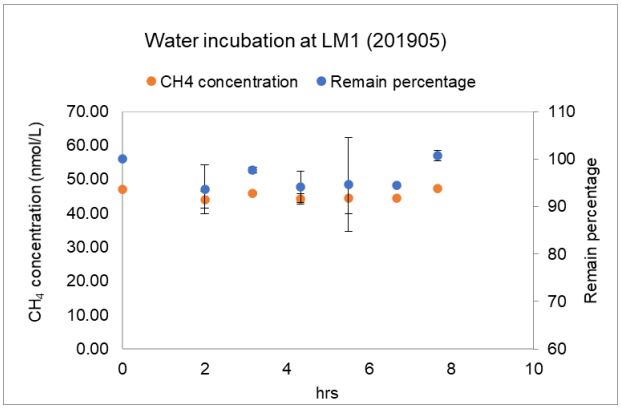
Water incubation at LM1 (201905)
CH4 concentration
Remain percentage
CH4 concentration (nmol/L)
Remain percentage
hrs

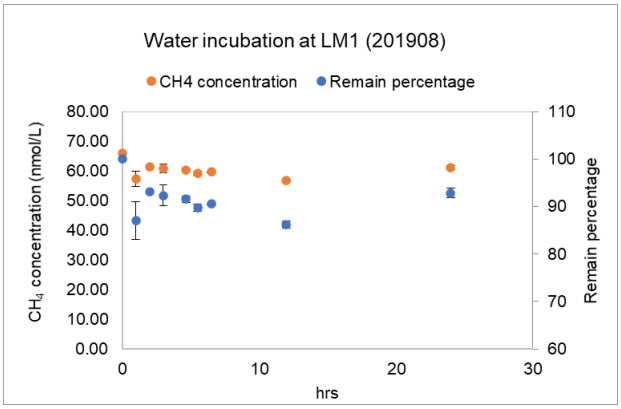
Water incubation at LM1 (201908)
CH4 concentration
Remain percentage
CH4 concentration (nmol/L)
Remain percentage
hrs

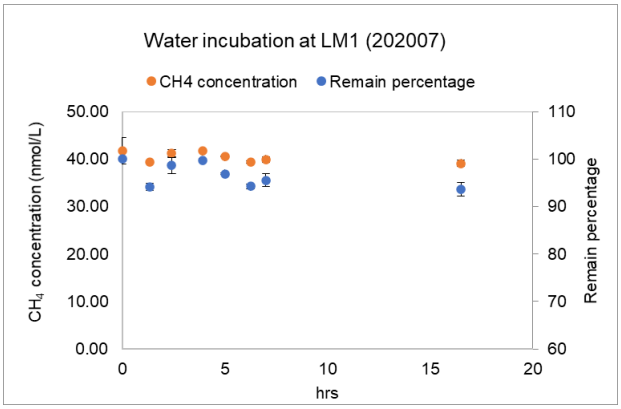
Water incubation at LM1 (202007)
CH4 concentration
Remain percentage
CH4 concentration (nmol/L)
Remain percentage
hrs

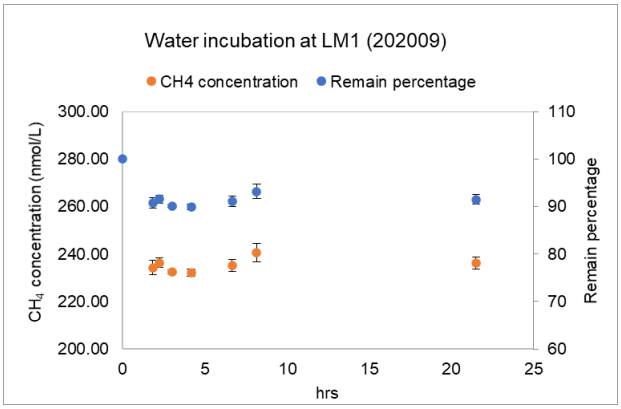
Water incubation at LM1 (202009)
CH4 concentration
Remain percentage
CH4 concentration (nmol/L)
Remain percentage
hrs

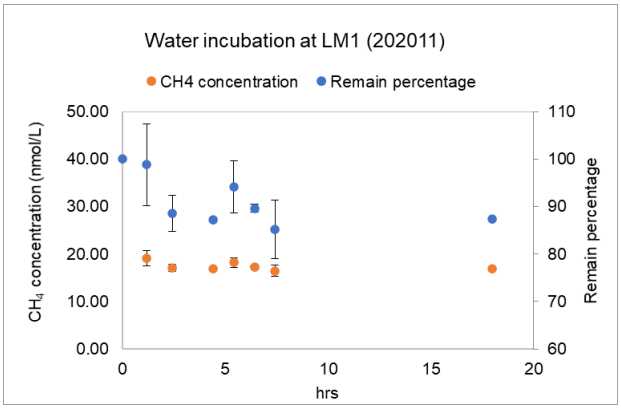
Water incubation at LM1 (202011)
CH4 concentration
Remain percentage
CH4 concentration (nmol/L)
Remain percentage
hrs

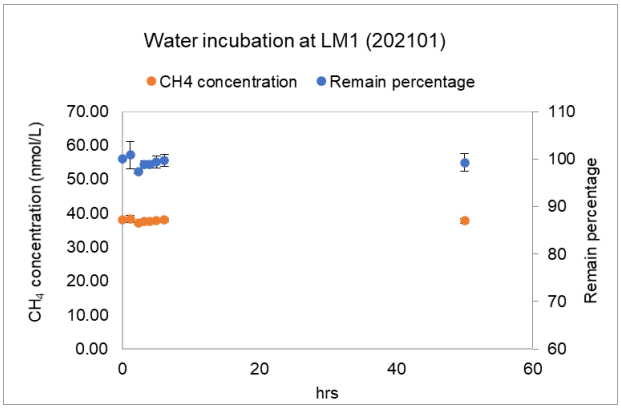
Water incubation at LM1 (202101)
CH4 concentration
Remain percentage
CH4 concentration (nmol/L)
Remain percentage
hrs

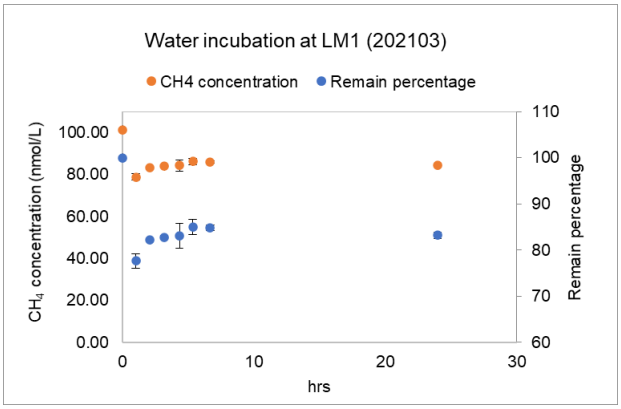
Water incubation at LM1 (202103)
CH4 concentration
Remain percentage
CH4 concentration (nmol/L)
Remain percentage
hrs

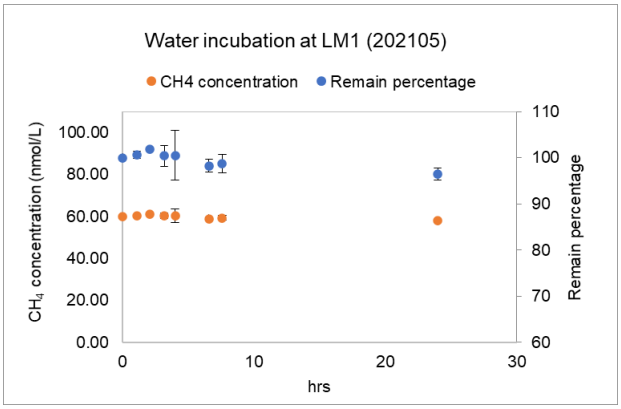
Water incubation at LM1 (202105)
CH4 concentration
Remain percentage
CH4 concentration (nmol/L)
Remain percentage
hrs

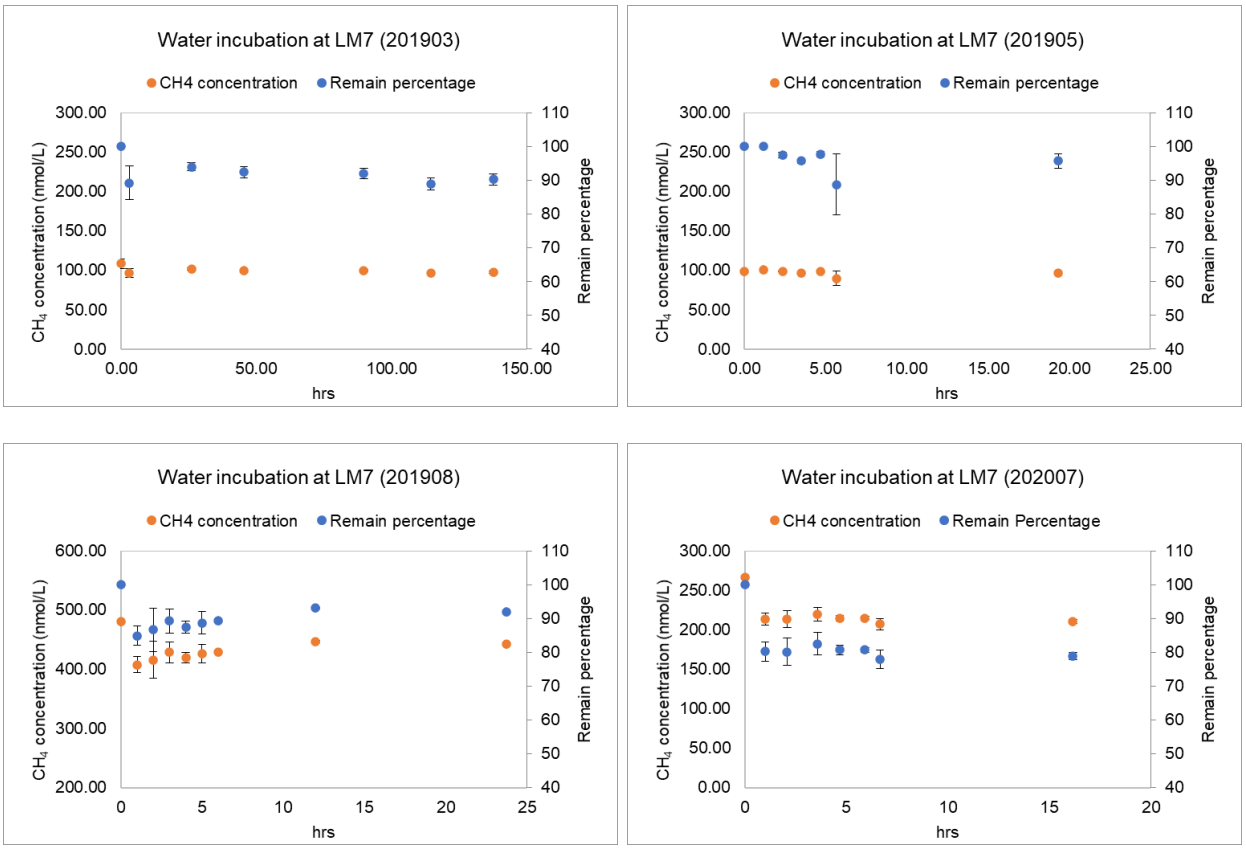

Figure S2 Methane concentration in water incubation experiments

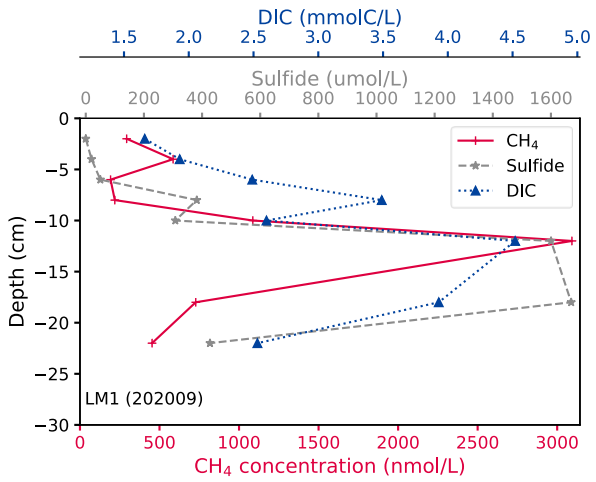
DIC (mmolC/L)
Sulfide (umol/L)
CH4
Sulfide
DIC
Depth (cm)
LM1 (202009)
CH4 concentration (nmol/L)

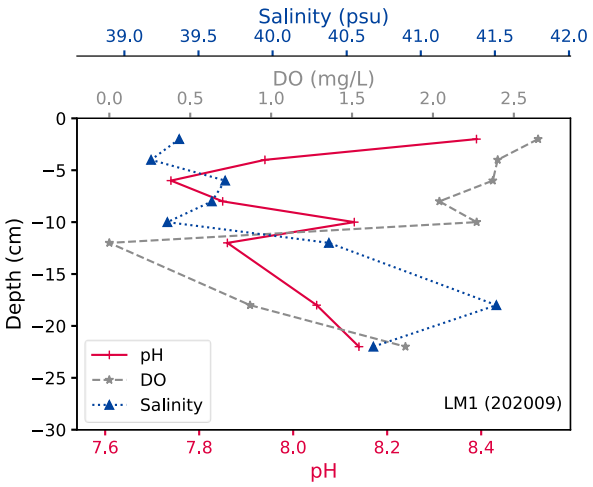
Salinity (psu)
DO (mg/L)
pH
DO
Salinity
Depth (cm)
LM1 (202009)
pH

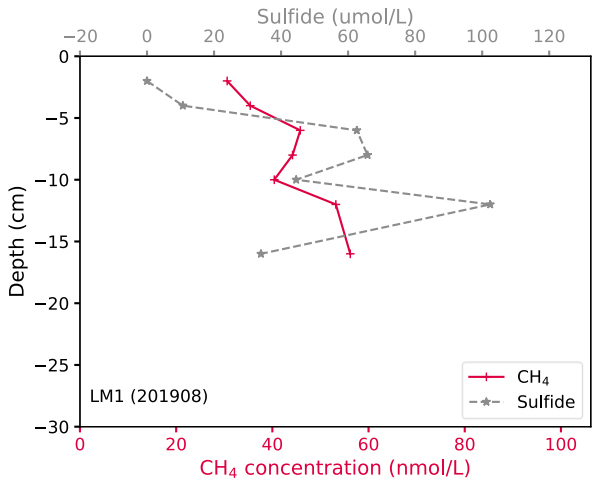
Sulfide (umol/L)
CH4
Sulfide
Depth (cm)
LM1 (201908)
CH4 concentration (nmol/L)

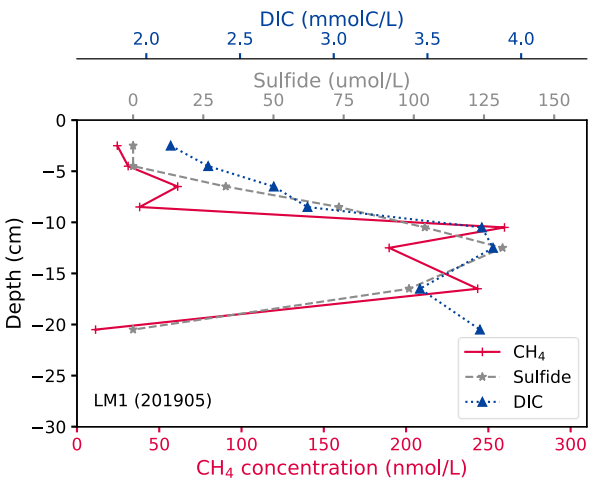
DIC (mmolC/L)
Sulfide (umol/L)
CH4
Sulfide
DIC
Depth (cm)
LM1 (201905)
CH4 concentration (nmol/L)

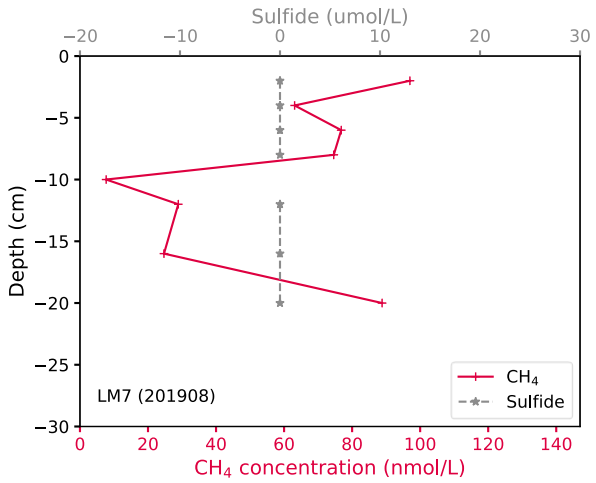
Sulfide (umol/L)
CH4
Sulfide
Depth (cm)
LM7 (201908)
CH4 concentration (nmol/L)

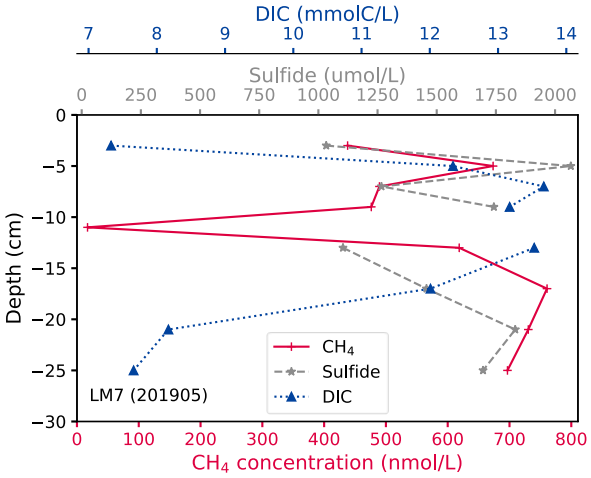
DIC (mmolC/L)
Sulfide (umol/L)
CH4
Sulfide
DIC
Depth (cm)
LM7 (201905)
CH4 concentration (nmol/L)

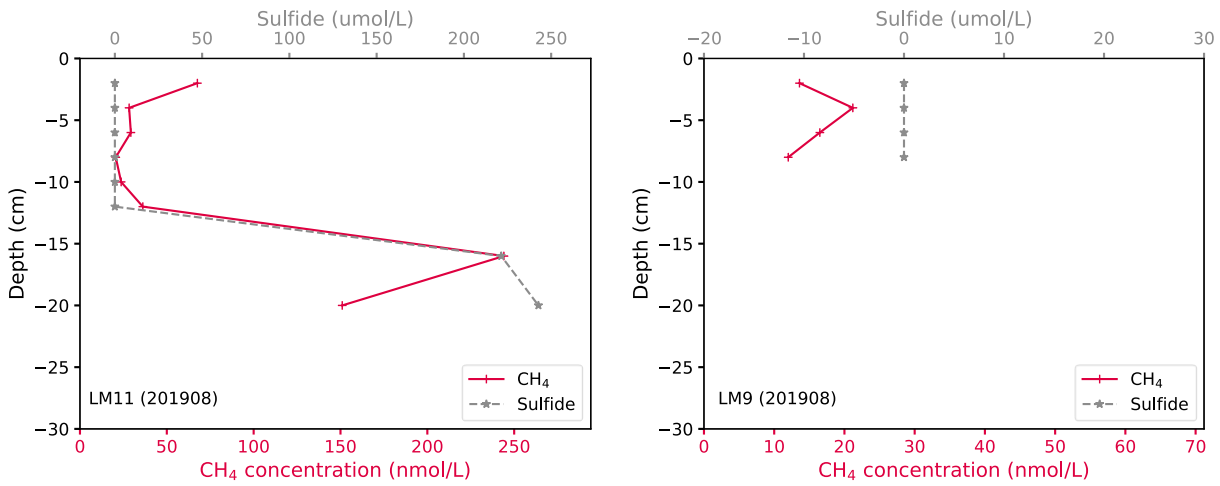

Figure S3 Profile of CH_4, DIC and sulfate in sediment porewater.

APPENDIX C

SUPPORTING INFORMATION FOR CHAPTER IV

SI 1. Quantification of CH_4 variation during the tidal process

Ebb: real time: 16:00 pm ~ 0:00 am (8 hours)

observation time: 16:30 pm ~ 0:00 am (7.5 hours)

[CH4] = (106.9-58.5)/7.5 = +6.45 nmol/L·h

Flood: real time: 0:00 am ~ 16:00 pm (16 hours)

observation time: 0:00 am ~ 11:00 am (11 hours) as flood; 11:00 am ~ 16:30 pm (5.5 hours) as high tide (based on water level at Port Aransas and CH_4 variation at AM5)

[CH4] = (53.5-106.9)/11 = -4.85 nmol/L·h

[CH4] = (58.5-53.5)/5.5 = +0.91 nmol/L·h

For a whole tidal process based on real time: ebb 8 hours; flood 11 hours; high tide 5 hours

+6.45*8 + (-4.85*11) + (+0.91*5) = +2.8 nmo/L·d

Hence, in a whole tidal process dissolved CH_4 concentration at AM5 increased 2.8 nmo/L.

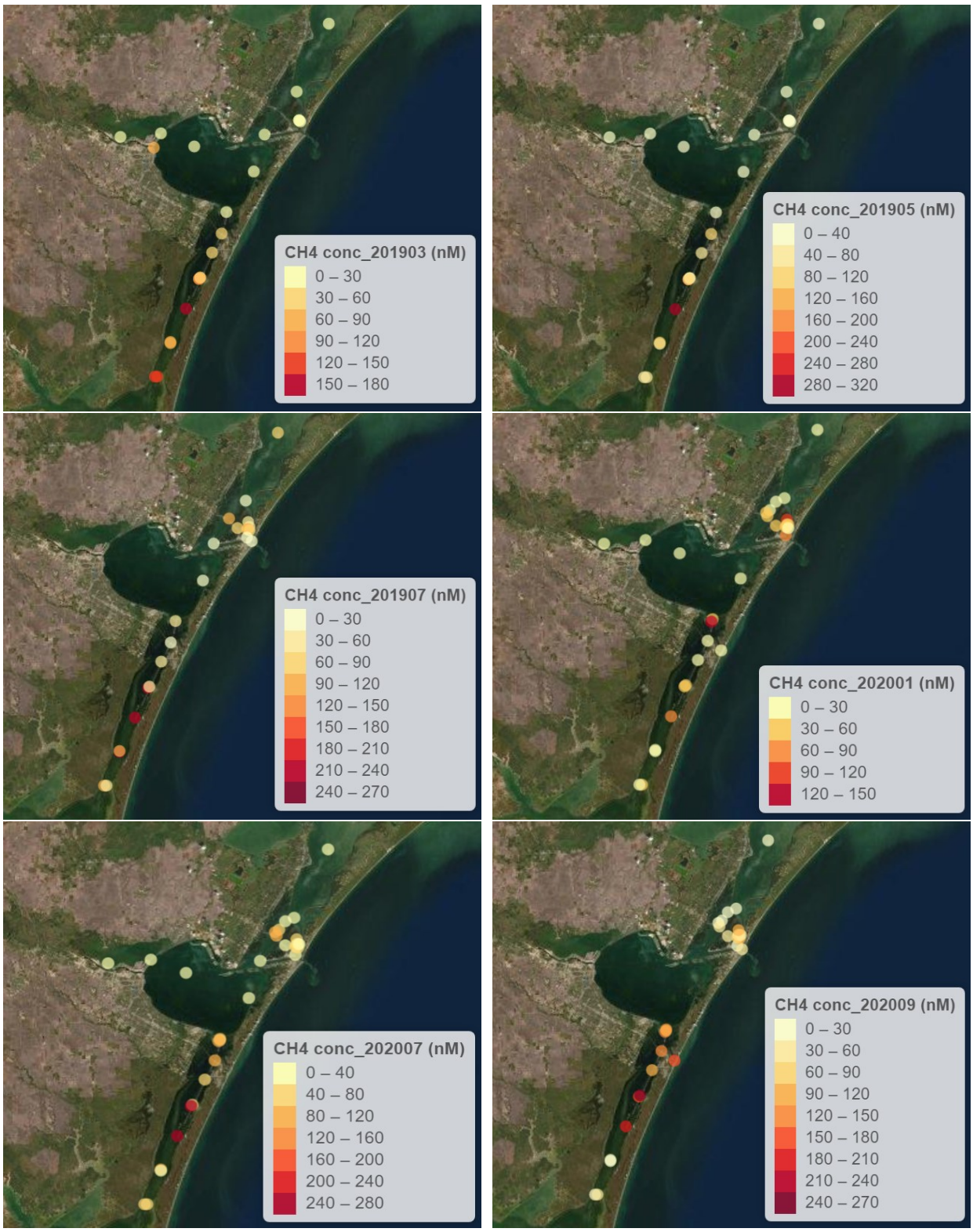
CH4 conc_201903 (nM)
0 – 30
30 – 60
60 – 90
90 – 120
120 – 150
150 – 180
CH4 conc_201905 (nM)
0 – 40
40 – 80
80 – 120
120 – 160
160 – 200
200 – 240
240 – 280
280 – 320
CH4 conc_201907 (nM)
0 – 30
30 – 60
60 – 90
90 – 120
120 – 150
150 – 180
180 – 210
210 – 240
240 – 270
CH4 conc_202001 (nM)
0 – 30
30 – 60
60 – 90
90 – 120
120 – 150
CH4 conc_202007 (nM)
0 – 40
40 – 80
80 – 120
120 – 160
160 – 200
200 – 240
240 – 280
CH4 conc_202009 (nM)
0 – 30
30 – 60
60 – 90
90 – 120
120 – 150
150 – 180
180 – 210
210 – 240
240 – 270

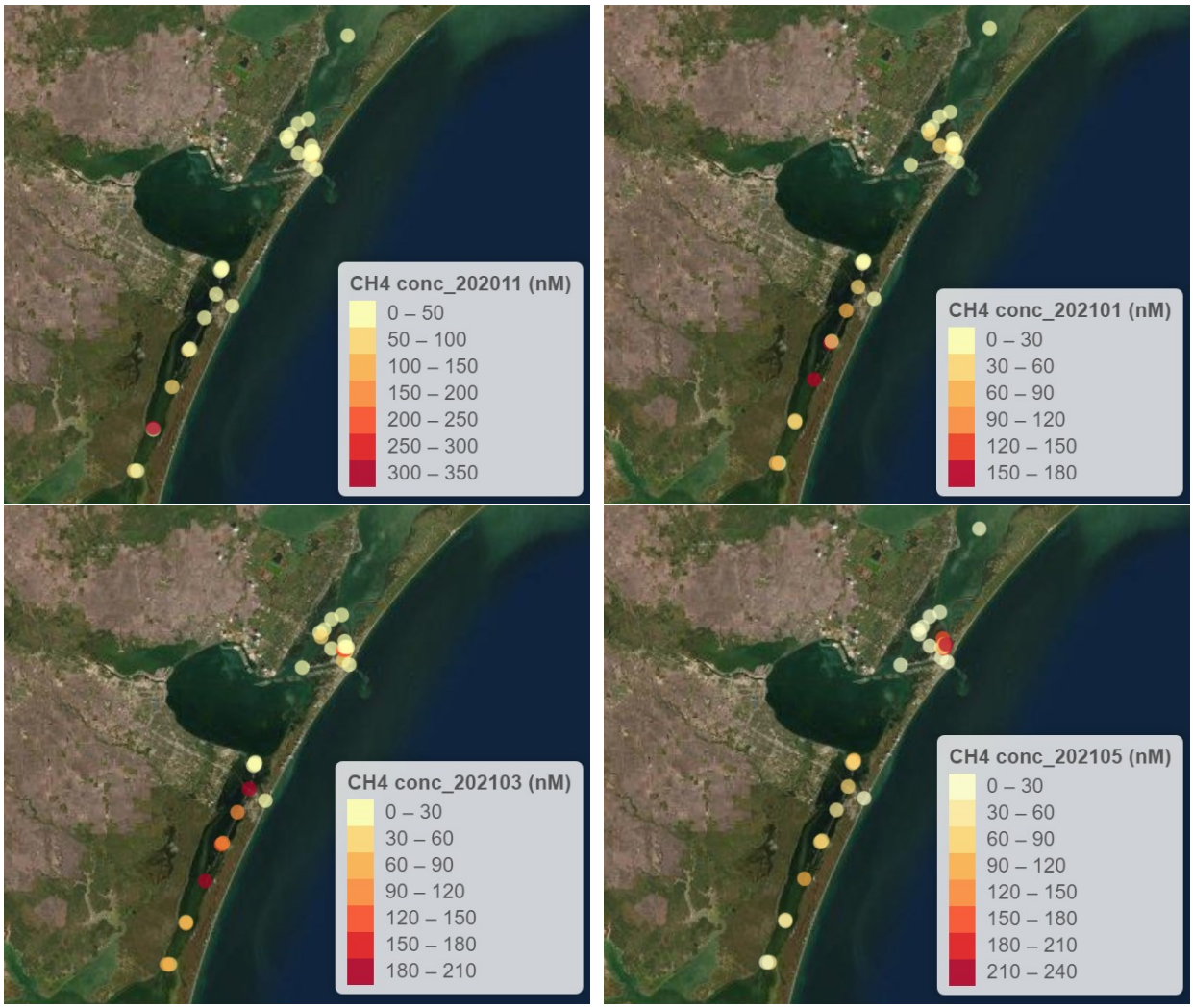

Figure S1 Monthly distribution of CH_4 concentration in whole region


Redfish Bay
Harbor Island
Aransas Pass
Mustang Island
CH4 air_202007 (ppm)
1.7 – 2.1
2.1 – 2.5
2.5 – 2.9
2.9 – 3.3
3.3 – 3.7
3.7 – 4.1
4.1 – 4.5
4.5 – 4.9
4.9 – 5.3
5.3 – 5.7

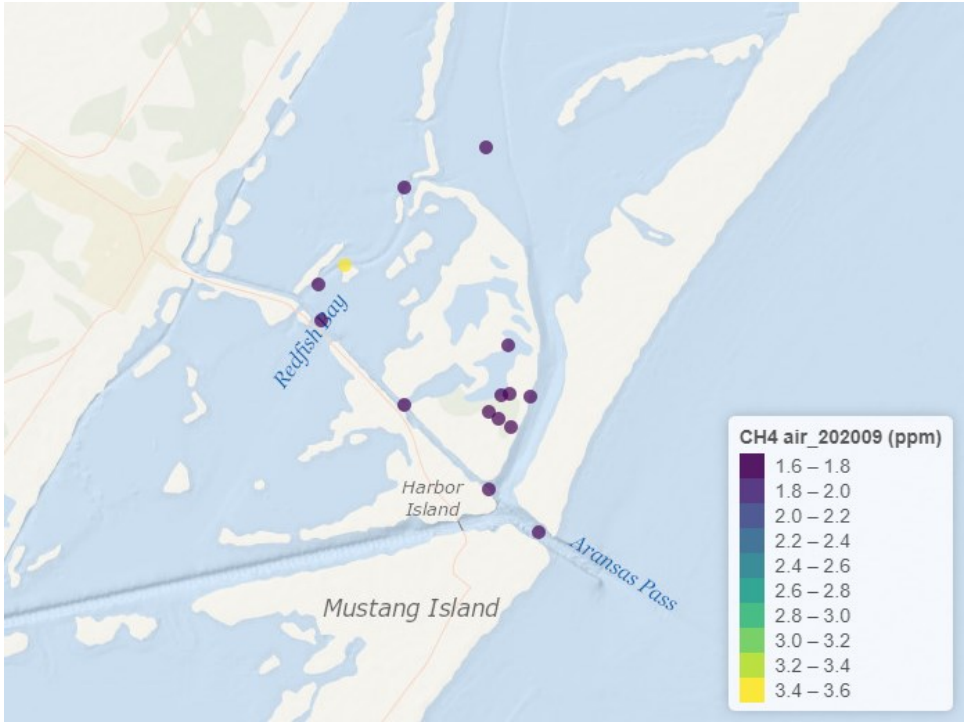
Redfish Bay
Harbor Island
Aransas Pass
Mustang Island
CH4 air_202009 (ppm)
1.6 – 1.8
1.8 – 2.0
2.0 – 2.2
2.2 – 2.4
2.4 – 2.6
2.6 – 2.8
2.8 – 3.0
3.0 – 3.2
3.2 – 3.4
3.4 – 3.6

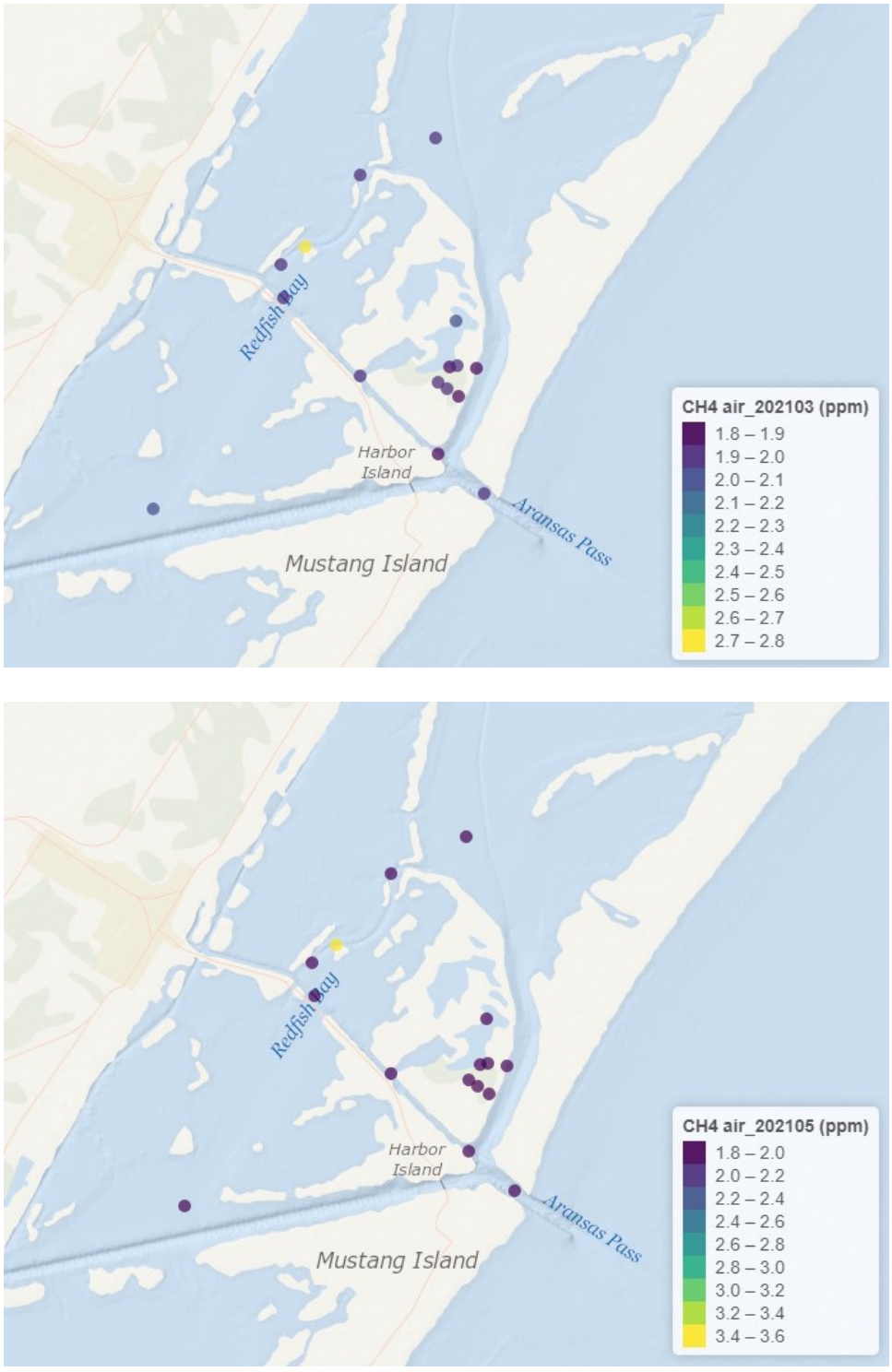

Figure S2a Distribution of CH_4 concentration in atmosphere in July and September 2020 and March and May 2021.

Figure S2b Left: $\delta^{13}C\text{-}CH_4$ at AM14 (-43.88‰), AM15(-44.89‰), and AM5(-45.19‰); Right: platform at AM14

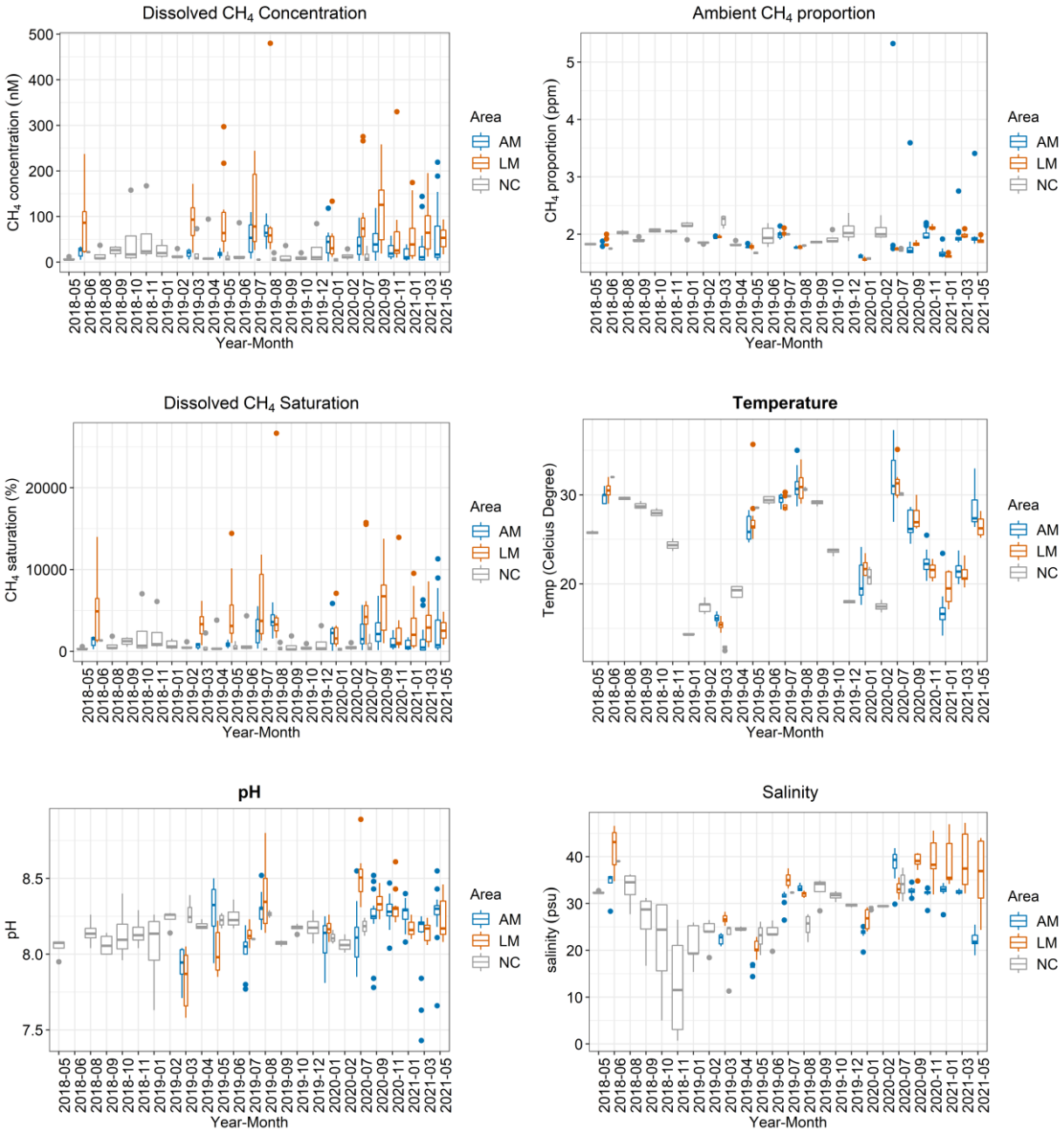
Dissolved CH4 Concentration
CH4 concentration (nM)
Year-Month
Ambient CH4 proportion
CH4 proportion (ppm)
Dissolved CH4 Saturation
CH4 saturation (%)
Temperature
Temp (Celcius Degree)
pH
Salinity
salinity (psu)
Area
AM
LM
NC

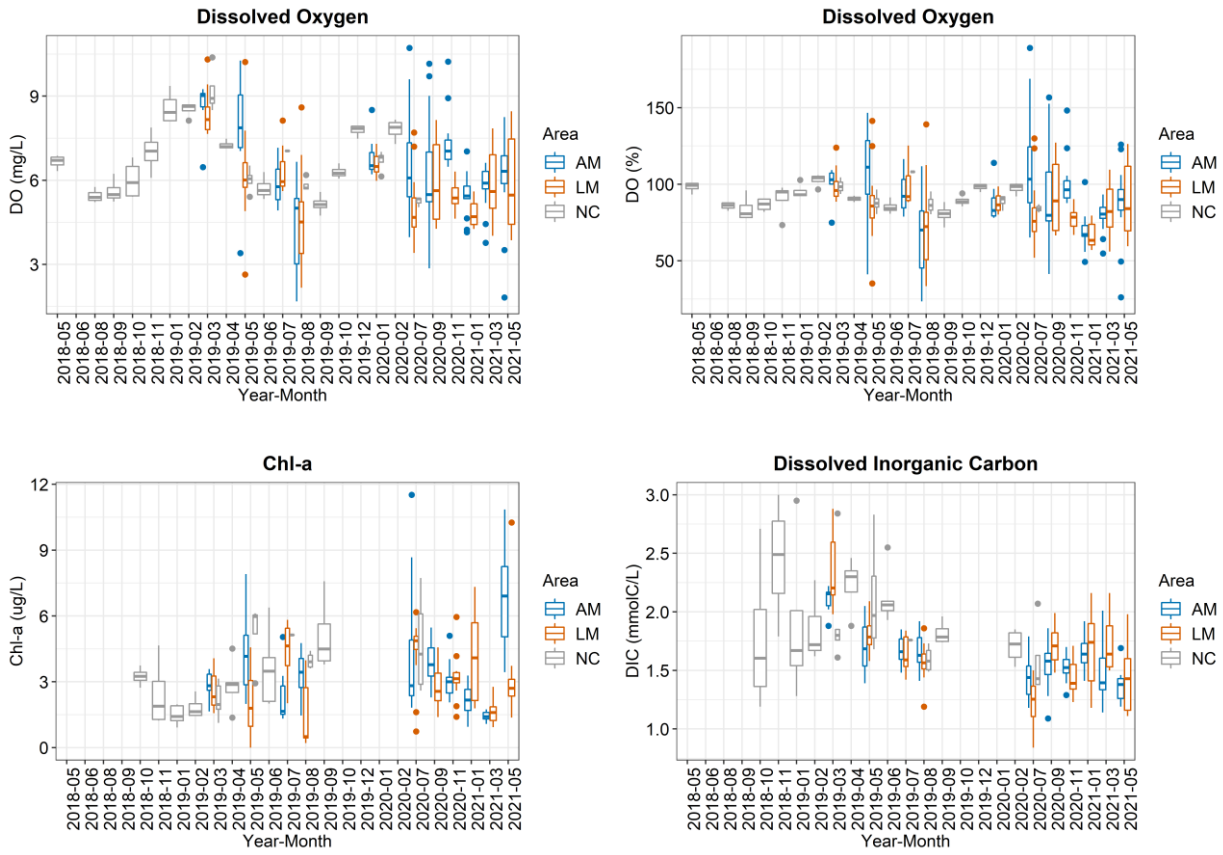

Figure S3 Boxplots of monthly variation in CH_4 and other parameters

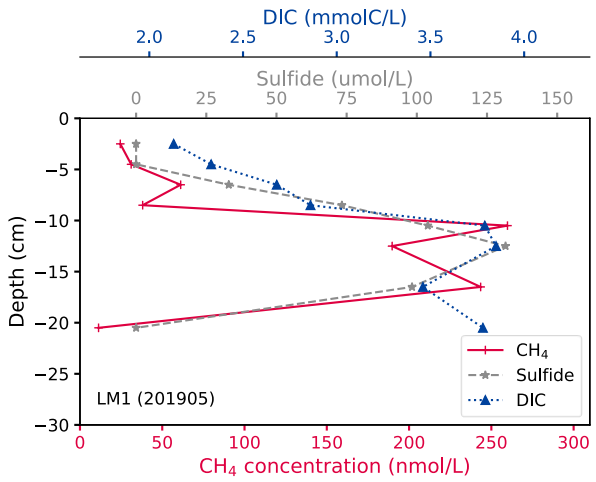
DIC (mmolC/L)
Sulfide (umol/L)
Depth (cm)
CH4
Sulfide
DIC
LM1 (201905)
CH4 concentration (nmol/L)

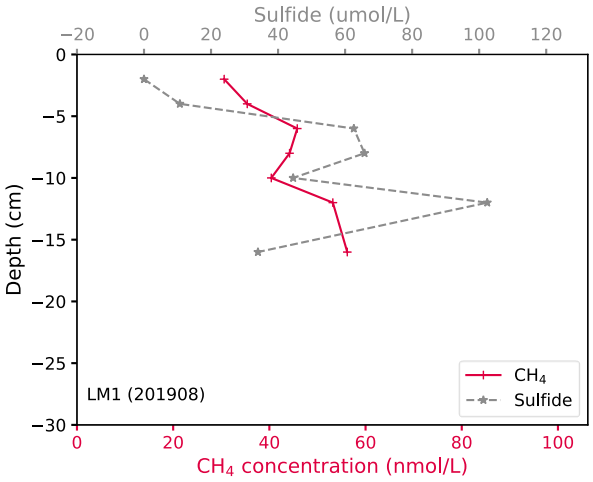
Sulfide (umol/L)
Depth (cm)
CH4
Sulfide
LM1 (201908)
CH4 concentration (nmol/L)

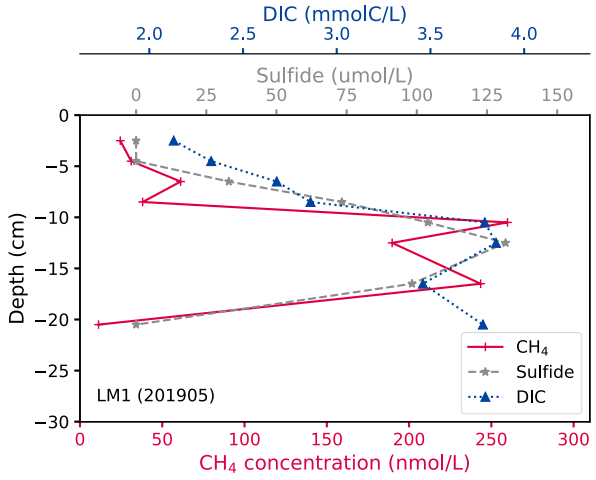
DIC (mmolC/L)
Sulfide (umol/L)
Depth (cm)
CH4
Sulfide
DIC
LM1 (201905)
CH4 concentration (nmol/L)

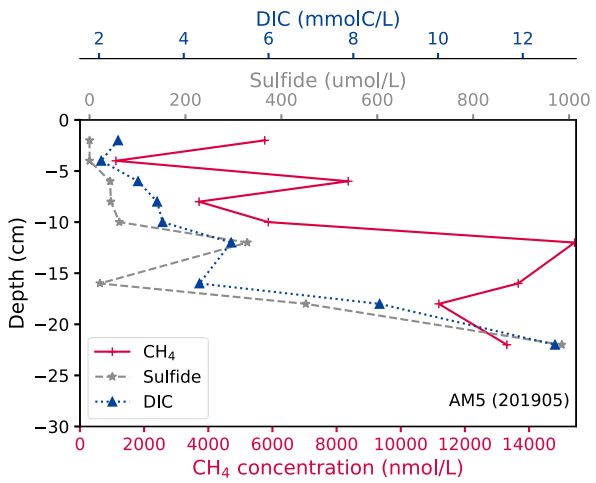
DIC (mmolC/L)
Sulfide (umol/L)
Depth (cm)
CH4
Sulfide
DIC
AM5 (201905)
CH4 concentration (nmol/L)

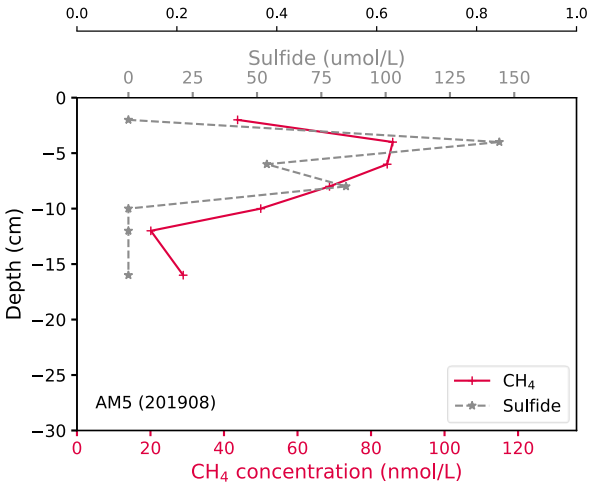
Sulfide (umol/L)
Depth (cm)
CH4
Sulfide
AM5 (201908)
CH4 concentration (nmol/L)

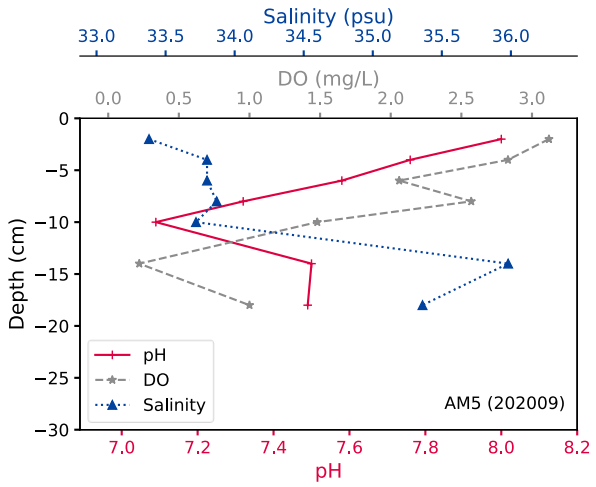
Salinity (psu)
33.0 33.5 34.0 34.5 35.0 35.5 36.0
DO (mg/L)
0.0 0.5 1.0 1.5 2.0 2.5 3.0
Depth (cm)
0 −5 −10 −15 −20 −25 −30
pH
DO
Salinity
AM5 (202009)
7.0 7.2 7.4 7.6 7.8 8.0 8.2
pH

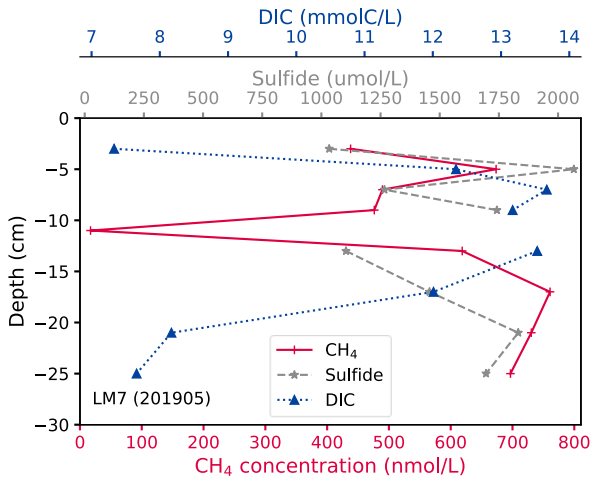
DIC (mmolC/L)
7 8 9 10 11 12 13 14
Sulfide (umol/L)
0 250 500 750 1000 1250 1500 1750 2000
Depth (cm)
0 −5 −10 −15 −20 −25 −30
CH4
Sulfide
DIC
LM7 (201905)
0 100 200 300 400 500 600 700 800
CH4 concentration (nmol/L)

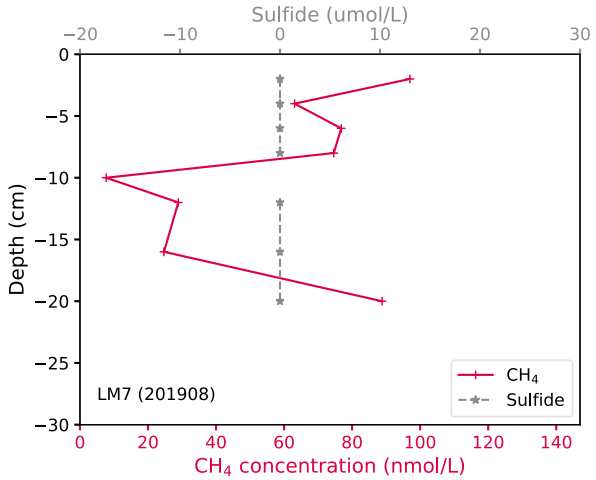
Sulfide (umol/L)
−20 −10 0 10 20 30
Depth (cm)
0 −5 −10 −15 −20 −25 −30
CH4
Sulfide
LM7 (201908)
0 20 40 60 80 100 120 140
CH4 concentration (nmol/L)

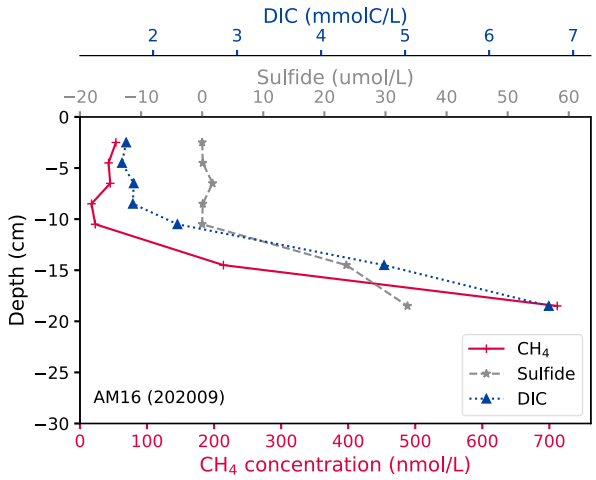
DIC (mmolC/L)
2 3 4 5 6 7
Sulfide (umol/L)
−20 −10 0 10 20 30 40 50 60
Depth (cm)
0 −5 −10 −15 −20 −25 −30
CH4
Sulfide
DIC
AM16 (202009)
0 100 200 300 400 500 600 700
CH4 concentration (nmol/L)

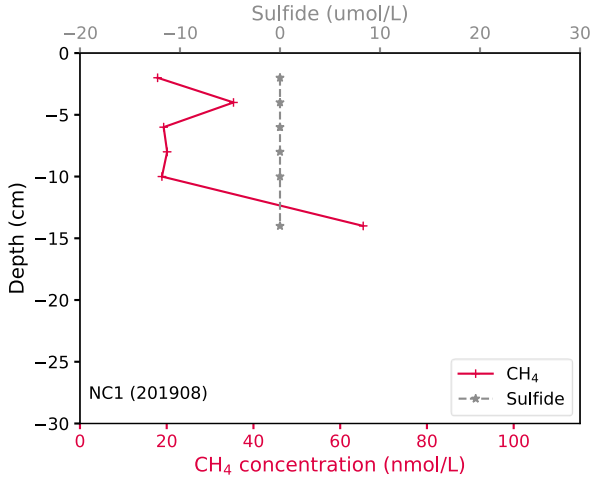
Sulfide (umol/L)
−20 −10 0 10 20 30
Depth (cm)
0 −5 −10 −15 −20 −25 −30
CH4
Sulfide
NC1 (201908)
0 20 40 60 80 100
CH4 concentration (nmol/L)

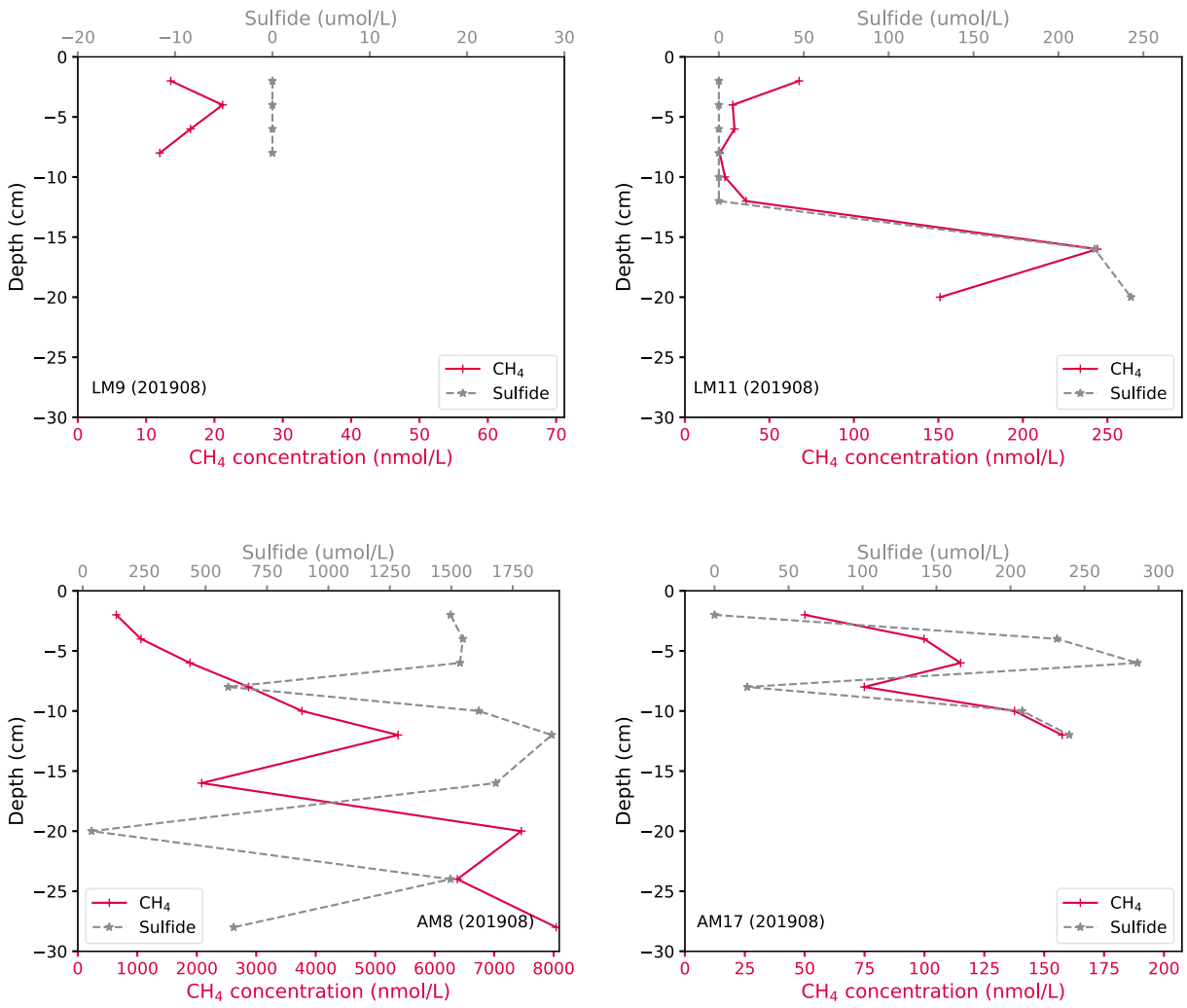

Figure S4 CH_4, DIC and sulfide in sediment porewater